UNIVERSITY OF SOUTHAMPTON

Ultrasonic visco-inertial dissipation in dilute particulate suspensions

Simon David Richards BSc MPhil ARCS DIC MIOA CPhys MInstP

Thesis submitted in partial fulfilment of the requirements for the degree of Doctor of Philosophy of the University of Southampton.

Fluid Dynamics & Acoustics Group,
Institute of Sound and Vibration Research,
Faculty of Engineering and Applied Science,
University of Southampton.

and

Marine Sensors & Environment Group,
Marine & Acoustics Centre,
QinetiQ.

August 2002

UNIVERSITY OF SOUTHAMPTON

ABSTRACT

FACULTY OF ENGINEERING AND APPLIED SCIENCE

INSTITUTE OF SOUND AND VIBRATION RESEARCH

Doctor of Philosophy

ULTRASONIC VISCO-INERTIAL DISSIPATION IN DILUTE PARTICULATE SUSPENSIONS

by Simon David Richards

Coastal seas are often characterized by relatively high concentrations of suspended mineral particles, compared to the open ocean. These suspensions can degrade the performance of high frequency (tens of kHz and above) sonars and other acoustic sensors operating in turbid environments. Existing sonar performance prediction models do not include the effects of suspended particles. There is therefore a requirement to investigate the effects of suspended particles on acoustic propagation and develop techniques for accounting for these effects in sonar performance models.

The purpose of the research described in this thesis was to address that requirement. The effects of suspended solid particles on ultrasonic propagation have therefore been investigated through theory, modelling and laboratory experimentation. The effects considered were: visco-inertial absorption; thermal absorption; scattering; and changes to the phase speed. A numerical model which accounts for each of these effects in suspensions of spherical particles is described. The complexity of this model is such that it obscures physical insight, and more intuitive, approximate models for visco-inertial absorption and scattering have been employed throughout much of this thesis. It is demonstrated that visco-inertial absorption is the dominant effect for most sonar performance applications, with scattering only becoming important at the highest frequencies considered. Furthermore, it is shown that thermal absorption and changes to the speed of sound may usually be neglected in sonar performance studies.

In order to validate the model for visco-inertial absorption by dilute suspensions of spherical particles, and study absorption by more natural particle shapes, a laboratory measurement technique has been developed. Measurement of the absorption due to dilute suspensions in a laboratory-scale experiment was found to be challenging, and a novel experimental configuration was adopted to address these challenges.

The predictions of the models for visco-inertial absorption in suspensions of spherical particles were found to be in very good agreement with measurements made using spherical glass particles. However significant departures from these predictions were observed in measurements made using highly non-spherical particles. Consequently a model for absorption by suspensions of spheroidal particles was employed and the predictions of this model agreed well with measurements made with plate-like kaolin particles. No *a priori* information from the attenuation measurements was required to achieve this agreement. Approximate agreement was obtained between the model predictions and measurements using natural marine sediment particles.

It was determined both theoretically and experimentally that visco-inertial absorption by suspensions can contribute significantly to volume attenuation in the frequency range tens to hundreds of kHz.

The contributions to volume attenuation by visco-inertial absorption and scattering have been incorporated into a high frequency sonar performance model for the first time. This demonstrates the importance of the effects within the context of the other influences on high frequency sonar performance in shallow water. The enhanced sonar model has also been used to explore the possibility of using direct-path acoustic absorption measurements to monitor suspended sediment flux through an estuary.

'ACOUSTICS - A complicated and involved as well as insecure science which has many imponderables. The reader is recommended to read it up first in an encyclopaedia before proceeding to a complete book on the subject', Alan Jefferson in *Inside the Orchestra*, 1974.

© Simon Richards, 2002.

The material contained within this thesis is the intellectual property of QinetiQ Ltd.

Contents

List of Figures

List of Tables

Acknowledgements

The majority of the research described in this thesis was carried out by the author whilst working for the Defence Evaluation and Research Agency (DERA) and, latterly, QinetiQ, which was formed from the greater part of DERA in 2001. This research was funded by the British Ministry of Defence, under the Corporate Research Programme.

I am indebted to my supervisor, friend and colleague, Professor Tim Leighton, for all his advice, support and encouragement during the course of the research described here.

The experimental measurements described in Chapter 6 form a key part of this thesis. These experiments were carried out by a team comprising the author, Dr. Niven Brown and Professor Leighton. I therefore owe a great deal to Niven for all his hard work in developing the technical aspects of the method, and to Tim for proposing the method and for his expertise and advice in guiding its development. I am particularly grateful to both Niven and Tim for the excellent working relationship we enjoyed throughout this project.

I would like to thank Dr. Gary Heald for his encouragement and contributions during the later stages of writing this thesis and also for reading and commenting on the drafts.

I would also like to thank Dr. Tony Heathershaw for proposing and securing funding for the original project from which this thesis arose, and for his assistance and support in the early stages of the research.

I am grateful to Professor Richard Challis (University of Nottingham) and Robert Jack (Malvern Instruments) for useful discussions relating to the Allegra-Hawley model, and also Dr. Andrew Holmes (University of Nottingham) who performed the Allegra-Hawley computations shown in Figures 4.1 and 4.2 for me.

I am also grateful to Professor Chris Morfey for some useful discussions and guidance on the theoretical aspects of this research.

The version of the SEARAY sonar model used, in modified form, to generate the results in Chapter 7 was obtained from the NATO SACLANT Undersea Research Center, La Spezia, Italy, and I am grateful to Mr. Gary Davies and Rear Admiral Jan Spoelstra, Director, SACLANTCEN, for making this model available to me.

The images shown in Figures 1.1 to 1.3 were taken from the NASA space shuttle and are reproduced with the kind permission of the Lunar and Planetary Institute.

The financial support of QinetiQ (formerly DERA) is also gratefully acknowledged.

This thesis was typeset using LaTeX 2_ε.

List of symbols

$\mathbf{A}$	Vector potential in fluid phase
$\mathbf{A}'$	Vector potential in solid phase
A	Azimuthal component of $\mathbf{A}$
A'	Azimuthal component of $\mathbf{A}'$
A_b	Insonified area of the seabed
A_ba	Temperature and salinity dependency of boric acid contribution to attenuation
A_enc	Total sound absorption of an enclosure in m^2
A_{ij}	Coefficients in the calculation of sound speed (Table A.2)
A_ms	Temperature and salinity dependency of magnesium sulphate contribution to attenuation
A_n	Coefficients in series solution of Helmholtz equation for compression waves in fluid
A'_n	Coefficients in series solution of Helmholtz equation for compression waves in solid
A_pw	Temperature and salinity dependency of pure water contribution to attenuation
A_s	Insonified area of the sea surface
A_w	Term used in computing sound speed (Equation A.4)
a	Particle radius
$\bar{a}$	Average Sabine absorptivity
a'	Semi-major axis for oblate spheroids; semi-minor axis for prolate spheroids
a_0	Equilibrium bubble radius
a_i	Coefficient in the calculation of density (Table A.3)
B	Bulk modulus
B_B	Term used in computing bulk modulus (Equation A.14)
B_b	Term used in computing bottom scattering strength (Equation 7.6)
B_h	Horizontal beamwidth in radians
B_{ij}	Coefficients in the calculation of sound speed (Table A.2)
B_n	Coefficients in series solution of Helmholtz equation for thermal waves in fluid
B'_n	Coefficients in series solution of Helmholtz equation for thermal waves in solid
B_s	Bulk modulus of suspension
B_v	Vertical beamwidth in radians
B_w	Term used in computing sound speed (Equation A.5)
b	Damping constant
b'	Semi-minor axis for oblate spheroids; semi-major axis for prolate spheroids
b_1	Term used in the wave equation formulation (Equation 5.43)
b_2	Term used in the wave equation formulation (Equation 5.44)
b_c	Thermal coefficient in fluid (Equation 3.23)
b'_c	Thermal coefficient in solid (Equation 3.30)

b_i	Coefficient in the calculation of density (Table A.3)
b_s	Term used in the partial wave formulation (Equation 3.68)
b_t	Thermal coefficient in fluid (Equation 3.24)
b'_t	Thermal coefficient in solid (Equation 3.31)
C_b	Term used in computing bottom scattering strength (Equation 7.5)
C_{ij}	Coefficients in the calculation of sound speed (Table A.2)
C_n	Coefficients in series solution of Helmholtz equation for shear waves in fluid
C'_n	Coefficients in series solution of Helmholtz equation for shear waves in solid
C_p	Specific heat capacity of fluid
C'_p	Specific heat capacity of solid
C_w	Term used in computing sound speed (Equation A.3)
c	Speed of sound in fluid
c'	Speed of sound in solid
c'_1	Speed of spherical compression waves in solid phase
c_b	Speed of sound in a bubbly liquid
c_i	Coefficient in the calculation of density (Table A.3)
c_ref	Sound speed at reference frequency ω_ref
c_s	Speed of sound in suspension
D	d_0/a, the ratio of mean particle separation (d_0) to particle radius (a)
D_b	Term used in computing bottom scattering strength (Equation 7.7)
D_i	Coefficients in the calculation of sound speed (Table A.2)
D_w	Term used in computing sound speed (Equation A.6)
DI	Directivity index
d	Depth
d_0	Mean inter-particle separation (relative to centres)
d_i	Coefficient in the calculation of density (Table A.3)
d_s	Mean inter-particle separation (relative to surfaces)
d_st	Stokes diameter
$d_\mathrm{st}\|_\mathrm{max}$	Limiting Stokes diameter
E	Energy
E_b	Term used in computing bottom scattering strength (Equation 7.8)
e	Exponential constant, e ≈ 2.718
e_i	Coefficient in the calculation of density (Table A.3)
F	Force on sphere or spheroid oscillating in sound field
F_0	Stokes drag force
f	Frequency
f_ba	Relaxation frequency for boric acid ionic relaxation
f_i	Coefficient in the calculation of density (Table A.3)
f_k	Frequency in kHz
f_ms	Relaxation frequency for magnesium sulphate ionic relaxation
f_n	Generic series function
f_s	Schroeder cut-off frequency
f_∞	Far-field scattering form function
g	Gravitational acceleration, $g \approx 9.81$ ms^{-2}
g_i	Coefficient in the calculation of density (Table A.3)

H	pH of seawater
$H_\nu^{(m)}$	Cylindrical Hankel function
h	Aspect ratio
h_i	Coefficient in the calculation of density (Table A.3)
h_n	Spherical Hankel function ($h_n^{(1)}$)
h_s	Settling distance
i	$\sqrt{-1}$
i_i	Coefficient in the calculation of density (Table A.3)
I	Acoustic plane wave intensity
I_0	Reference intensity
I_amb	Ambient noise intensity
$\Im$	Imaginary part
J_ν	Cylindrical Bessel function
j_i	Coefficient in the calculation of density (Table A.3)
j_n	Spherical Bessel function
K	Thermal conductivity of fluid
K'	Thermal conductivity of solid
K_0	Shape factor
K_1	Constant for large bubbles
K_2	Constant for small bubbles
K_f	Compressibility and density term in high-pass model for form function
$K_{\mathrm{ob},\parallel}$	Shape factor, oblate spheroid, flow parallel to axis of symmetry
$K_{\mathrm{ob},\perp}$	Shape factor, oblate spheroid, flow perpendicular to axis of symmetry
$K_{\mathrm{pr},\parallel}$	Shape factor, prolate spheroid, flow parallel to axis of symmetry
$K_{\mathrm{pr},\perp}$	Shape factor, prolate spheroid, flow perpendicular to axis of symmetry
K_sf	Shape factor
K_α	Compressibility and density term in high-pass model for attenuation
k	Wavenumber
k_b	Compressional wavenumber in a bubbly liquid
k_c	Wavenumber for compression waves in fluid
k'_c	Wavenumber for compression waves in solid
k_e	Wavenumber for turbulent eddies
k_i	Coefficient in the calculation of density (Table A.3)
k_s	Wavenumber for shear waves in fluid
k'_s	Wavenumber for shear waves in solid
k_sus	Wavenumber in suspension
k_t	Wavenumber for thermal waves in fluid
k'_t	Wavenumber for thermal waves in solid
L	Term used in the wave equation formulation (Equation 5.42)
L_b	e-folding depth for small bubbles
L_i	Inertia coefficient
$L_{\mathrm{ob},\parallel}$	Inertia coefficient, oblate spheroid, flow parallel to axis of symmetry
$L_{\mathrm{ob},\perp}$	Inertia coefficient, oblate spheroid, flow perpendicular to axis of symmetry
$L_{\mathrm{pr},\parallel}$	Inertia coefficient, prolate spheroid, flow parallel to axis of symmetry
$L_{\mathrm{pr},\perp}$	Inertia coefficient, prolate spheroid, flow perpendicular to axis of symmetry

l_i	Coefficient in the calculation of density (Table A.3)
M	Mass concentration of suspended particles
M_v	$\sqrt{2}a/\delta_\mathrm{v}$, a parameter proportional to the ratio of the particle radius (a) to the viscous skin depth (δ_v)
m	Mass of fluid displaced by particle
m'	Mass of particle
m_b	Bottom type
m_i	Induced mass
N	Number density of suspended particles
NL	Total noise level
NL_f	Flow noise level
NL_p	Propeller noise level
NL_r	Receiver noise level
n	Order in partial wave expansion
n_b	Number density of bubbles
n_n	Spherical Neumann function
P	Term used in the partial wave formulation (Equation 3.64)
P_B	Term used in computing bulk modulus (Equation A.12)
P_ba	Pressure dependency of boric acid contribution to attenuation
P_ms	Pressure dependency of magnesium sulphate contribution to attenuation
P_n	Legendre polynomial
P_n^1	Associated Legendre polynomial of the first kind
P_pw	Pressure dependency of pure water contribution to attenuation
P_w	Term used in computing bulk modulus (Equation A.15)
p	Hydrostatic pressure
p_0	Reference acoustic pressure
p_b	Equilibrium gas pressure in a bubble
p_i	Instantaneous incident acoustic pressure
p_s	Instantaneous scattered acoustic pressure
p_sus	Acoustic pressure in a suspension
Q	Term used in the partial wave formulation (Equation 3.65)
Q_B	Term used in computing bulk modulus (Equation A.13)
Q_{ij}	Coefficients in the calculation of viscosity (Table A.1)
Q_w	Term used in computing bulk modulus (Equation A.16)
R	Term used in the partial wave formulation (Equation 3.66)
R_k	Coefficients in the calculation of viscosity (Table A.1)
$\Re$	Real part
Re	Reynolds number
RL	Total reverberation level
RL_b	Bottom reverberation level
RL_s	Surface reverberation level
RL_v	Volume reverberation level
r	Radial coordinate
r_c	Radial distance from the axis in a centrifuge
r_r	Range along a ray

S	Salinity (measured on the practical salinity scale)
S_b	Bottom backscattering strength
S_enc	Surface area of an enclosure
S_s	Surface backscattering strength
S_v	Volume scattering strength
SL	Source level
SNR	Signal to noise ratio
s	Coefficient of frictional component of force on particle
T	Temperature of fluid in degrees Kelvin
T'	Temperature of solid in degrees Kelvin
TL	Transmission loss
TS	Target strength
t	Time
t_{60}	Reverberation time
t'_{60}	Reverberation time for a volume of particulate-laden water
$\mathbf{u}$	Displacement vector
u	Relative velocity between particle and fluid
u_0	Magnitude of sinusoidal relative velocity oscillations
V	Volume
V'	Volume of particles in suspension
V_enc	Volume of an enclosure
V_v	Insonified volume
$\mathbf{v}$	Velocity vector
v	Instantaneous velocity of fluid
v'	Instantaneous velocity of particle
v_0	Magnitude of sinusoidal velocity oscillations
v_p	Platform speed
v_s	Free-fall velocity
w	Wind speed in knots
x_c	Size parameter for compression waves in fluid
x'_c	Size parameter for compression waves in solid
x_s	Size parameter for shear waves in fluid
x'_s	Size parameter for shear waves in solid
x_t	Size parameter for thermal waves in fluid
x'_t	Size parameter for thermal waves in solid
z	Cartesian z-coordinate
z_0	Reference z-coordinate
z_1	Generic complex argument
α	Plane wave attenuation coefficient in dB m^{-1}
α_0	Term used in computing the inertia coefficient (Equation 5.81)
α_b	Attenuation coefficient in a bubbly liquid
α_g	Bottom type parameter in GESMA model
α_n	Term used in the partial wave formulation (Equation 2.41)
α_s	Attenuation coefficient due to scattering
α_t	Thermal absorption coefficient

α_v	Visco-inertial absorption coefficient
α_vt	$\alpha_\mathrm{v} + \alpha_\mathrm{t}$, sum of visco-inertial and thermal absorption coefficients
α_w	Attenuation coefficient in clear seawater
α_τ	Attenuation coefficient due to turbulence
β	Reciprocal of shear wave skin depth
β_g	Bottom type parameter in GESMA model
β_n	Term used in the partial wave formulation (Equation 2.42)
β_s	Term used in the partial wave formulation (Equation 3.62)
Γ	Term used in computing the surface scattering strength (Equation 7.15)
Γ_n	Term used in the partial wave formulation (Equation 3.67)
γ	Ratio of specific heat at constant pressure to that at constant volume in fluid
γ'	Ratio of specific heat at constant pressure to that at constant volume in solid
γ_0	Term used in computing the inertia coefficient (Equation 5.89)
γ_1	Term used in computing the inertia coefficient (Equation 5.93)
γ_κ	Compressibility contrast
γ_ρ	Density contrast
ΔV_tot	Total volume change of suspension
δ_n	Term used in the partial wave formulation (Equation 2.40)
δ_t	Thermal wave skin depth in fluid
δ'_t	Thermal wave skin depth in solid
δ_v	Shear wave skin depth in fluid
δ'_v	Shear wave skin depth in solid
ϵ	Volume fraction of suspended particles
ϵ_d	Dissipation rate of turbulent kinetic energy
ε	Eccentricity
ζ	Plane wave attenuation coefficient in Npm^{-1}
ζ_s	$(1 + \mathrm{i}x_\mathrm{s})^{-1}$, parameter used in the partial wave formulation
η	Molecular viscosity of ambient fluid
η'	Molecular viscosity of fluid spheres
η_k	Kolmogorov length scale
η_n	Phase shift of nth partial wave in partial wave expansion
Θ	Temperature in degrees Celsius
Θ_0	Reference temperature in degrees Celsius
θ	Polar coordinate
θ_d	Grazing angle in degrees
θ_g	Grazing angle in radians
ϑ	Coefficient of thermal expansion of fluid
ϑ'	Coefficient of thermal expansion of solid
κ	Bulk compressibility of fluid
κ'	Bulk compressibility of solid
κ_i	Imaginary part of dynamic compressibility
κ_r	Real part of dynamic compressibility
κ_s	Bulk compressibility of suspension
κ_v	Volume averaged bulk compressibility
Λ_n	Term used in the partial wave formulation (Equation 3.60)

λ	Acoustic wavelength
λ'	Lamé constant
μ'	Shear modulus
μ_0	Lambert's parameter
ν	Kinematic viscosity
Ξ	Term used in computing the damping constant for bubbles (Equation 7.23)
ξ	Adjustable parameter in high-pass model
ξ_n	Term used in the partial wave formulation (Equation 3.61)
π	pi, $\pi \approx 3.14159$
ρ	Density of fluid
ρ'	Density of solid
ρ_s	Density of suspension
ρ_v	Volume averaged density
ρ_w	Density of pure water with $p = 0$ (Equation A.9)
σ	Density ratio
τ	Coefficient of inertial component of force on particle
Φ	Thermal scaling factor
Φ_n	Term used in the partial wave formulation (Equation 2.43)
ϕ	Azimuthal coordinate
$\overline{\phi}$	$\phi_\mathrm{c} + \phi_\mathrm{t}$, sum of scalar potentials for compression and thermal waves in fluid
$\overline{\phi}'$	$\phi'_\mathrm{c} + \phi'_\mathrm{t}$ sum of scalar potentials for compression and thermal waves in solid
ϕ_0	Scalar potential for incident wave
ϕ_c	Scalar potential for compression wave in fluid
ϕ'_c	Scalar potential for compression wave in solid
ϕ_r	Scalar potential for scattered compression wave
ϕ_t	Scalar potential for thermal wave in fluid
ϕ'_t	Scalar potential for thermal wave in solid
φ	Phase
χ	Thermal diffusivity of fluid
χ'	Thermal diffusivity of solid
χ_g	Gas thermal diffusivity
Ψ_n	Term used in the partial wave formulation (Equation 3.59)
ω	Angular frequency
ω'	Integration variable in integrals over frequency
ω_0	Resonant frequency of a bubble of equilibrium radius a_0
ω_c	Rotation speed of a centrifuge
ω_ref	Reference frequency

List of abbreviations

AH	Allegra and Hawley
APL:UW	Applied Physics Laboratory, University of Washington
ARL:UT	Advanced Research Laboratory, University of Texas
ASW	Anti-submarine warfare
BASIC	Beginners' All-purpose Symbolic Instruction Code
B&K	Brüel and Kjær
DAC	Digital-to-analogue converter
DERA	Defence Evaluation and Research Agency
ECCI	English China Clay International
DSO	Digital storage oscilloscope
GESMA	Group d'Etudes Sous-Marines de l'Atlantique
GPIB	General purpose interface bus
IIR	Integrated impulse response
ISVR	Institute of Sound and Vibration Research
LSS	Light scattering sensor
NAG	Numerical Algorithms Group
NASA	National Aeronautical and Space Administration
NATO	North Atlantic Treaty Organisation
NCSC	Naval Coastal Systems Center
PC	Personal computer
SACLANT	Supreme Allied Commander, Atlantic
SACLANTCEN	NATO SACLANT Centre for undersea research
SEM	Scanning electron microscope / micrograph
SSP	Sound speed profile

Chapter 1

Introduction

1.1 Introduction to this thesis

This thesis describes research carried out by the author on the subject of ultrasonic attenuation in water containing suspended solid particles.

In writing this thesis it was the intention that, as far as possible, it should be self contained and no specialist knowledge of the subject matter should be required of the reader, other than a graduate level knowledge of physics. For this reason derivations of key results obtained by previous researchers have been included. It has been made clear in the text where this is the case, and the original papers have been cited and included in the list of references.

1.2 Background

Sonar performance prediction modelling has classically focused on the long-range, low frequency, antisubmarine warfare (ASW) scenarios in the deep ocean (so-called 'blue water'), well away from any coastal influences. More recently, there has been increased interest in the use of high frequency (tens to hundreds of kHz) sonar in shallow coastal environments. Anecdotal evidence suggests that current sonar performance prediction models are incapable of predicting with any accuracy the variability in high frequency sonar performance observed in such environments.

Many coastal marine environments are characterized by high concentrations of suspended particulate matter relative to the open ocean. Such material may arise from rivers or estuaries discharging their sediment load to coastal seas, through the action of waves and tidal currents in stirring up bottom sediment, or through anthropogenic activity such as the dredging of navigation channels, for example.

This thesis will demonstrate that the presence of suspended solid particles can have a significant effect on the performance of high frequency sonars and other acoustic sensors operating at similar frequencies. The primary effect for typical marine suspensions (with grain sizes in the range 0.1 to 100 μm) is an increase in the acoustic attenuation through the processes of visco-inertial absorption and scattering, although suspended particles can also have an influence on the sound speed.

Figures 1.1, 1.2 and 1.3 show evidence of coastal turbidity along the coast of the Gulf of Mexico in the United States. These figures were chosen simply because these images were easily available

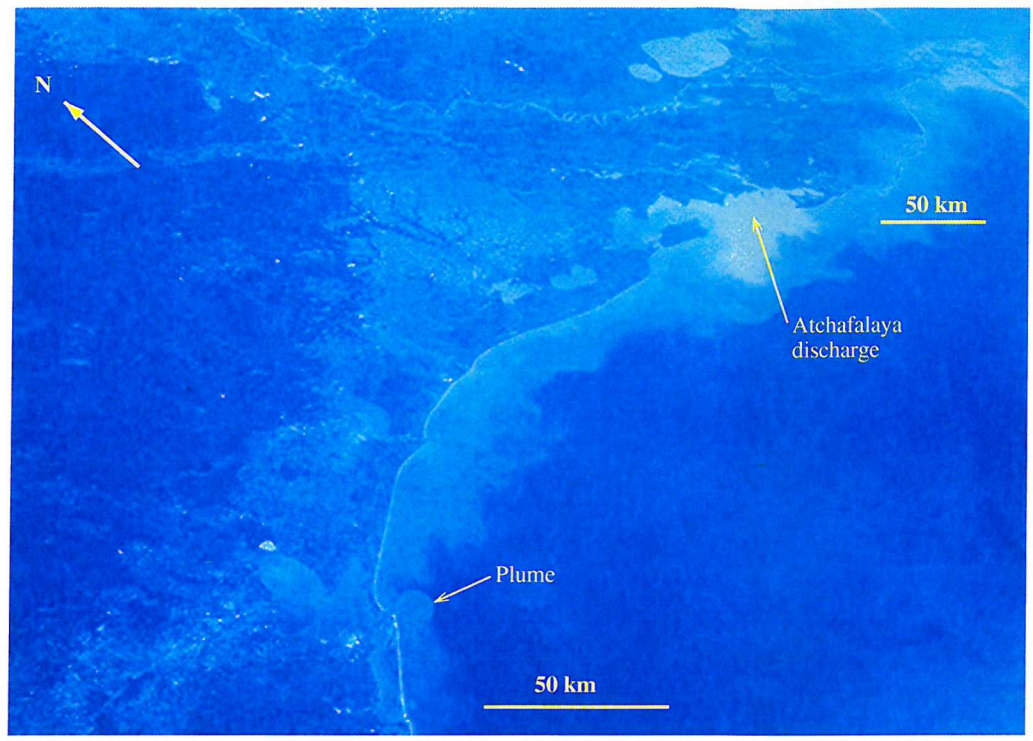

Figure 1.1. Photograph of the Louisiana & Texas Gulf Coast showing coastal turbidity. (The scale and orientation indicators are approximate. The two scale bars indicate the perspective arising from the oblique viewing angle.) Source: NASA, reproduced with the permission of the Lunar and Planetary Institute.

and not because they depict extraordinary features. Similar examples of coastal turbidity can be found in coastal regions throughout the world.

Figure 1.1 shows a synoptic oblique view of part of the Texas and Louisiana coastline of the Gulf of Mexico, extending from west of Galveston Bay in the lower central region of the picture, eastwards towards the Mississippi Delta in the upper right corner of the figure (Source : NASA Space Shuttle, STS-41C, April 1984, Picture #13-51-2422). The light coloured patch to the west of the Mississippi Delta shows sediment discharging from the Atchafalaya River into the Gulf of Mexico through Atchafalaya Bay. It is noticeable that the sediment discharge from the Atchafalaya River is much greater than that from the Mississippi. It is also evident that the sediment plume from Atchafalaya Bay is being advected along the coast by a westward longshore current. A balloon-shaped sediment plume can also be seen discharging from the Trinity River into the Gulf through Trinity Bay / Galveston Bay.

Figure 1.2 shows a larger scale photograph of the Trinity Bay and Galveston Bay area (Source : NASA Space Shuttle, STS-51D, April 1985, Picture #23-40-019). Note that this picture was taken a year later than Figure 1.1. A sediment plume can clearly be seen streaming out of the inlet of the bay into the Gulf. This plume only flows straight for a short distance before being turned westwards by the longshore current.

Figure 1.3 shows the Mississippi Delta (Source : NASA Space Shuttle, STS-61A, October - November 1985, Picture #61A-42-051). In this picture the sediment discharge plume from the major western distributary can be seen flowing freely into the Gulf, as it is flowing with the

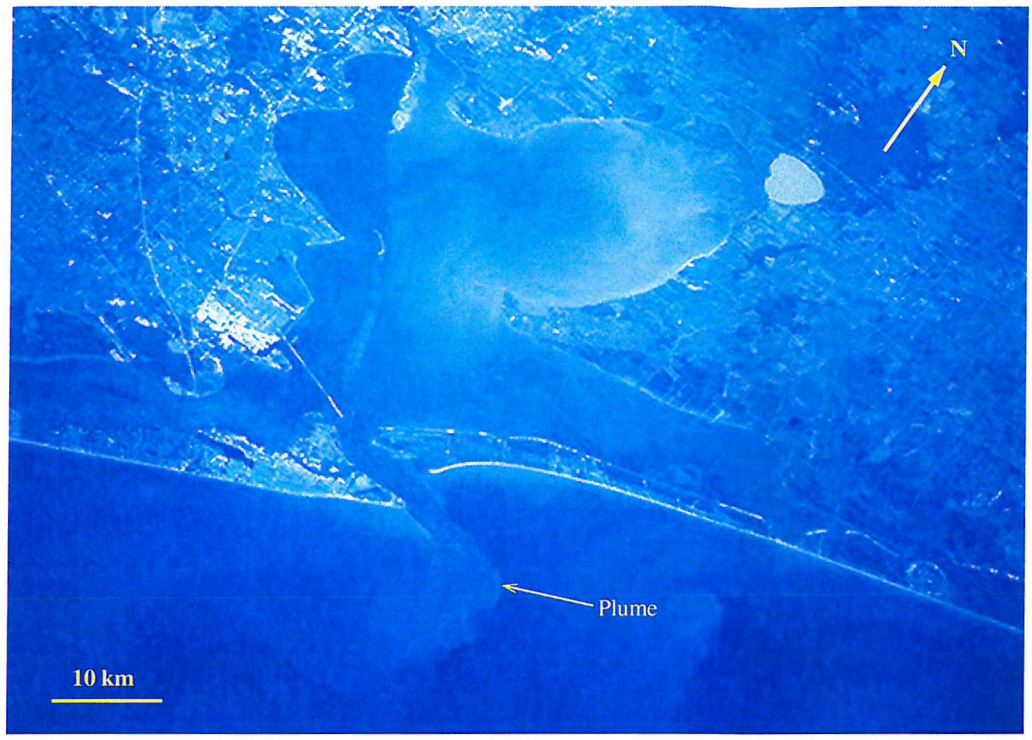

Figure 1.2. Photograph of Trinity Bay / Galveston Bay, Texas Gulf Coast, showing a turbidity plume from the Trinity River. (The scale and orientation indicators are approximate.) Source: NASA, reproduced with the permission of the Lunar and Planetary Institute.

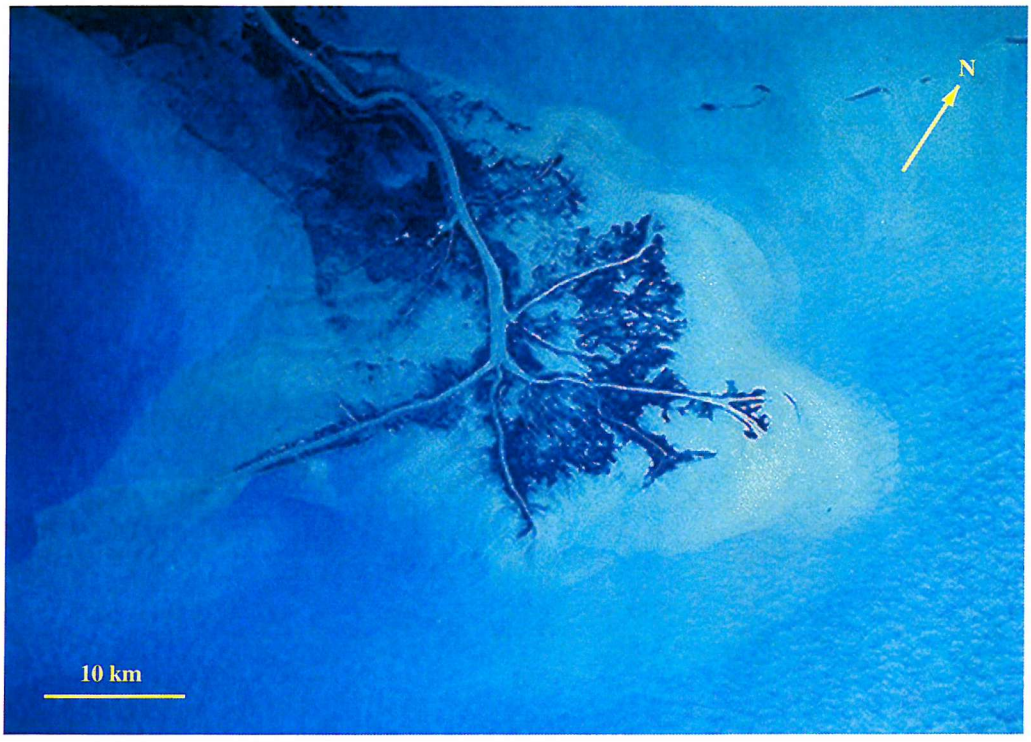

Figure 1.3. Photograph of the Mississippi Delta showing sediment discharge. (The scale and orientation indicators are approximate.) Source: NASA, reproduced with the permission of the Lunar and Planetary Institute.

westerly longshore current. The sediment plumes on the eastern side of the delta, on the other hand, are being turned sharply to the south and west by wind-driven long-shore current in the open Gulf. Wind-induced choppy waves can be seen in the bottom-right of the picture, contrasting with the relatively calm water to the west of the delta.

Although there is a great deal of similar evidence of turbidity in coastal waters, very little work appears to have been done to assess the impact of coastal turbidity on sonar performance. The research presented in the remainder of this thesis addresses this shortfall.

1.3 Purpose of the research

The purpose of the research described in this thesis is to elucidate the physics of, and provide a methodology for enabling quantitative predictions of the effects of dilute suspensions of marine particles on high frequency (tens to hundreds of kHz) sonars.

The problem of developing a model which is capable of accurately predicting sonar performance in shallow water environments is a highly complex one in which many different phenomena should be considered. Such a model would require detailed data regarding the bottom bathymetry, geoacoustic properties of the seabed, acoustic properties of the water column, physical properties and distributions of suspended particulate matter, ambient bubble populations, sea surface scattering properties, etc.

The research described in this thesis is therefore confined to the study of one particular aspect of the larger problem. The other factors influencing the performance of high frequency active sonars operating in shallow, coastal environments should each be investigated to a similar level of detail in order to produce a model which is capable of accurate predictions of sonar performance in such environments.

1.4 Thesis plan and original contributions

Very little previous work has been carried out on the effect of turbidity on the performance of high frequency sonars and acoustic sensors, and the primary contribution of this thesis is to address this issue.

Chapter 2 describes the physics of absorption and scattering by dilute particulate suspensions. Models for the contributions to the volume absorption coefficient are presented and their applicability to the problem of attenuation by marine suspensions at sonar frequencies in the range from a few tens of kHz to 1 MHz is discussed. The independent formulations for absorption and scattering described in Chapter 2 have the benefit of facilitating physical insight into the phenomena, but they are based on a number of approximations and assumptions.

A more complete, rigorous, theoretical model for scattering of plane waves by a thermally conducting, elastic sphere suspended in a thermally conducting viscous fluid is described in Chapter 3. This may be viewed as the benchmark solution to the problem and it is in this capacity that it has been employed here for validation of the formulations of Chapter 2.

In Chapter 4 the predictions of the different models are compared. It is shown that the approaches described in Chapter 2 are a reasonable approximation to the more complete model

described in Chapter 3 for particle sizes to be found in suspension in the sea and at practical sonar frequencies below 1 MHz. For the first time results are presented which demonstrate the magnitude of the increased attenuation for practical sonar applications and the important parameter dependencies.

Chapter 5 discusses the effect of suspended particles on the sound speed in turbid water, and presents a wave equation for sound propagation in suspensions. This chapter shows that the change in sound speed due to the presence of suspended particles is small over the parameter range of interest. The attenuation may also be obtained from the complex wave number in the wave equation, and the attenuation coefficient obtained by this method is shown to be equivalent to the models presented in Chapter 2. The wave equation formulation facilitates the inclusion of the effects of particle shape, and this is demonstrated in Chapter 5 by employing a shape factor and inertia coefficient to obtain the attenuation coefficient and sound speed in suspensions of non-spherical particles.

In order to have confidence in the theoretical models experimental validation is required. Whilst a significant amount of previous experimental work has been done on scattering by particulate suspensions, little or no work appears to have been done on experimental measurements of visco-inertial absorption in dilute suspension at frequencies in the range tens to hundreds of kHz. Chapter 6 describes a novel laboratory technique for measuring the ultrasonic absorption coefficient in dilute suspensions. Although the attenuation due to dilute suspensions can be significant in the sea over propagation ranges of hundreds of meters, it is a very challenging quantity to measure in a laboratory scale experiment. The development of the method is described and new results are presented showing the measured attenuation for a number of particulate suspensions over the frequency range 50 kHz to 150 kHz. These measurements are compared with the predictions of the models discussed in Chapter 2. Some of the measurements were made in suspensions of highly non-spherical particles and these results are compared with the predictions of the model of attenuation by suspensions of spheroidal particles described in Chapter 5. It is thought to be the first time that results have been presented showing the comparison between: predictions of a model for visco-inertial absorption in suspensions of spheroids; and laboratory measurements of attenuation at sonar-relevant frequencies in suspensions of the kind found in the sea.

For the first time the effects of suspended particulate matter have been incorporated into a sonar performance prediction model and this work is described in Chapter 7. Within the framework of this model the relative importance of the suspended particles has been compared with the other phenomena influencing sonar performance. New results are presented which show that the detection range of a high frequency active sonar may be significantly reduced by the presence of suspended particles in the water.

The dependence of volume attenuation on the concentration of suspended particulate matter presents the possibility of inverting sonar transmission measurements to infer sediment concentration across, say, a river mouth or estuary. This approach is proposed here for the first time and the sonar performance model described in Chapter 7 has been employed to model an example scenario of this nature.

The additional attenuation contributions depend on the density, viscosity and sound speed in the water, all of which depend on the ambient temperature, pressure and salinity. Appendix A

therefore presents an original investigation into the effect of temperature, pressure and salinity on the acoustic attenuation coefficient in seawater containing suspended particulate matter. This investigation shows that the ambient temperature in particular can have a significant effect on the attenuation, and the local temperature should therefore be taken into account in the calculation of the attenuation.

The Kramers-Kronig relations may be used to relate the attenuation to the dispersion in dispersive media. This presents the possibility of inferring absorption from measurements of dispersion, and this is discussed in Appendix B.

A number of publications arose from the research described in this thesis, and these are listed on Page 143 *et seq.*

Chapter 2, starting overleaf, introduces the physics of absorption and scattering as relevant to the problem of high frequency sonar performance in turbid coastal waters.

Chapter 2

The physics of absorption and scattering

2.1 Introduction

This chapter introduces the basic physics of absorption and scattering of sound in seawater containing a suspension of mineral particles. Models for calculating the visco-inertial absorption and scattering contributions to the attenuation are discussed and the validity of the dilute approximation is examined in each case.

2.2 Attenuation

Sound propagating through seawater containing suspended particulate matter is attenuated by several mechanisms. These include physico-chemical absorption by the seawater, thermo-viscous absorption and scattering by suspended particulate matter, geometric spreading of the acoustic wavefronts, and losses due to interactions with the seabed and sea surface.

Considering for the moment just the plane wave attenuation, the sound intensity after propagation over distance z may be given by

$$I = I_0 \mathrm{e}^{-2\zeta z} \tag{2.1}$$

where I_0 is the sound intensity at some reference range $z = 0$ and ζ is the attenuation coefficient of the medium in Nepers m^{-1}.

In sonar research it is convenient to express attenuation in terms of dBm^{-1} and these are the units used in the remainder of this thesis. The relationship between the attenuation coefficient α in dBm^{-1} and the coefficient ζ in Npm^{-1} is given by

$$\alpha = 10 \log \left(\mathrm{e}^2\right) \zeta \tag{2.2}$$

The total volume attenuation coefficient α in seawater containing suspended particles may be considered as the linear sum of the attenuation due to clear seawater, α_w, and that due to visco-inertial absorption, α_v and scattering , α_s by suspended particles. The attenuation coefficient may therefore be written

$$\alpha = \alpha_{\mathrm{w}} + \alpha_{\mathrm{v}} + \alpha_{\mathrm{s}} \tag{2.3}$$

These three contributions to the attenuation are discussed in the following sections. In fact there is a fourth contribution to the attenuation which may be referred to as thermal absorption. This effect, which will be discussed in Chapter 3, may generally be neglected for mineral particles in seawater at sonar frequencies (below 1 MHz) and will therefore not be discussed further in this chapter.

2.3 Sound absorption in seawater

The absorption of sound in clear seawater is considered as the sum of the contributions from pure water, and two ionic relaxation processes involving magnesium sulphate ($MgSO_4$) and boric acid ($B(OH)_3$). Contributions from other ionic reactions are small and are neglected. Several empirical expressions exist for calculating the absorption in seawater (e.g. Fisher and Simmons [1], Thorpe [2], Shulkin and Marsh [3]) but the one that appears to be the most complete is that of Francois and Garrison [4,5]. Their expression yields the total attenuation resulting from the three contributions as a function of frequency, pressure, temperature, salinity and pH, and may be written as

$$\alpha_{\mathrm{w}} = 10^{-3}\left[\frac{A_{\mathrm{ba}}P_{\mathrm{ba}}f_{\mathrm{ba}}f^2}{f^2+f_{\mathrm{ba}}^2} + \frac{A_{\mathrm{ms}}P_{\mathrm{ms}}f_{\mathrm{ms}}f^2}{f^2+f_{\mathrm{ms}}^2} + A_{\mathrm{pw}}P_{\mathrm{pw}}f^2\right] \quad \mathrm{dBm}^{-1} \tag{2.4}$$

where A_{ba}, A_{ms} and A_{pw} represent the temperature and salinity dependencies, P_{ba}, P_{ms} and P_{pw} are the pressure dependencies, f_{ba} and f_{ms} are the relaxation frequencies and the subscripts ba, ms and pw refer to the boric acid, magnesium sulphate and pure water contributions respectively. These terms are given below [4].

Boric acid contribution

$$A_{\mathrm{ba}} = \frac{8.86}{c}\cdot 10^{(0.78H-5)} \quad \mathrm{dBkm}^{-1}\mathrm{kHz}^{-1} \tag{2.5}$$

$$P_{\mathrm{ba}} = 1 \tag{2.6}$$

$$f_{\mathrm{ba}} = 2.8(S/35)^{0.5}10^{(4-1245/(\Theta+273))} \quad \mathrm{kHz} \tag{2.7}$$

where c is the sound speed (ms^{-1}), H is the pH, Θ is the temperature (degrees Celsius) and S is the salinity, measured on the practical salinity scale[1].

[1] The Practical Salinity Scale 1978 was introduced to address problems with the traditional chlorinity-conductivity relationship used to establish salinity [6–8]. Salinity is now expressed in the dimensionless units psu or practical salinity units.

Magnesium sulphate contribution

$$A_{\mathrm{ms}} = 21.44(S/c)(1 + 0.025\Theta) \quad \mathrm{dBkm^{-1}kHz^{-1}} \tag{2.8}$$

$$P_{\mathrm{ms}} = 1 - 1.37 \cdot 10^{-4} d + 6.2 \cdot 10^{-9} d^2 \tag{2.9}$$

$$f_{\mathrm{ms}} = \frac{8.17 \cdot 10^{(8-1990/(\Theta+273))}}{1 + 0.0018(S - 35)} \quad \mathrm{kHz} \tag{2.10}$$

where d is the depth (m).

Pure water contribution

$$P_{\mathrm{pw}} = 1 - 3.83 \cdot 10^{-5} d + 4.9 \cdot 10^{-10} d^2 \tag{2.11}$$

For $\Theta \leq 20°\mathrm{C}$,

$$\begin{aligned} A_{\mathrm{pw}} &= 4.937 \cdot 10^{-4} - 2.59 \cdot 10^{-5}\Theta \\ &\quad + 9.11 \cdot 10^{-7}\Theta^2 - 1.50 \cdot 10^{-8}\Theta^3 \quad \mathrm{dBkm^{-1}kHz^{-1}} \end{aligned} \tag{2.12}$$

For $\Theta > 20°\mathrm{C}$,

$$\begin{aligned} A_{\mathrm{pw}} &= 3.964 \cdot 10^{-4} - 1.146 \cdot 10^{-5}\Theta \\ &\quad + 1.45 \cdot 10^{-7}\Theta^2 - 6.5 \cdot 10^{-10}\Theta^3 \quad \mathrm{dBkm^{-1}kHz^{-1}} \end{aligned} \tag{2.13}$$

2.4 Visco-inertial absorption

Visco-inertial absorption arises as a result of the phase lag between the motions of suspended particles or droplets and the suspending fluid in response to an acoustic wave. Unless the particles or droplets are of the same density as the ambient fluid (i.e. they are neutrally buoyant) their inertia will differ from that of the fluid they displace. As a result there will be a phase lag between the particle and fluid oscillations, which means that there is a boundary layer at the surface of the particle in which there is a velocity gradient. This velocity gradient results in the conversion of energy to heat as a consequence of the viscosity of the suspending fluid.

The absorption of sound in a suspension of small particles was considered theoretically by Sewell [9] in 1910, and more recently by Epstein [10]. Sewell considered the case of small, rigid, spherical particles which are taken to be immobile in that they do not oscillate in the sound field. He was interested in the propagation of sound in fogs and clouds, and the assumption of immobile particles is valid for water droplets in air at audio frequencies. However, in the case of aqueous suspensions at megahertz and sub-megahertz frequencies, the particles do respond to the acoustic field and Sewell's theory breaks down.

Lamb [11] extended Sewell's theory to the case of rigid, incompressible particles that are free to move in the sound field. His approach was to obtain an expression for the velocity potential of the waves scattered by such a particle and to obtain the absorption by finding the average rate at which work is done over a large spherical surface surrounding the particle.

Urick [12] obtained the same result as Lamb by employing the expressions for the viscous drag developed by Stokes [13], and this derivation is reproduced here. Stokes investigated theoretically the effect of viscosity on the period of a spherical pendulum bob swinging in a viscous fluid. He found that the force F exerted by the fluid on a sphere of radius a oscillating with angular frequency ω is

$$F = -\tau m \frac{\mathrm{d}u}{\mathrm{d}t} - sm\omega u \tag{2.14}$$

where τ and s are defined as

$$\tau = \frac{1}{2} + \frac{9}{4\beta a} \tag{2.15}$$

and

$$s = \frac{9}{4\beta a}\left(1 + \frac{1}{\beta a}\right) \tag{2.16}$$

The velocity u is the instantaneous velocity of the sphere, $m = \frac{4}{3}\pi a^3 \rho$ is the mass of ambient fluid of density ρ displaced by the sphere and $\beta = \sqrt{\omega/2\nu}$. In fact, β is the inverse of the scale length over which the viscous shear waves are damped in the fluid, the skin depth δ_v, i.e.

$$\delta_\mathrm{v} = \sqrt{\frac{2\nu}{\omega}} \tag{2.17}$$

Equation 2.14 may be compared with Equation 5.15 in Section 5.3.1 which considers the more general case of suspensions of viscous spheres. Equation 5.15 reduces to Equation 2.14 in the case of rigid particles.

The first term on the right of Equation 2.14 represents an addition to the inertia of the sphere, while the second is a frictional, or drag, force proportional to velocity. The velocity u can be considered as the relative velocity between particle and fluid, i.e.

$$u = v' - v \tag{2.18}$$

For a particle of density ρ' with mass $m' = \frac{4}{3}\pi a^3 \rho'$ the equation of motion is then

$$m' \frac{\mathrm{d}v'}{\mathrm{d}t} = -\tau m \frac{\mathrm{d}u}{\mathrm{d}t} - sm\omega u + m \frac{\mathrm{d}v'}{\mathrm{d}t} \tag{2.19}$$

where $m\mathrm{d}v'/\mathrm{d}t$ is the external force produced by the sound field if both the particle size and its displacement are small compared with a wavelength. On replacing $\mathrm{d}v'/\mathrm{d}t$ by $\mathrm{d}u/\mathrm{d}t + \mathrm{d}v/\mathrm{d}t$, and writing $\sigma = m'/m$ $(= \rho'/\rho$, the ratio of particle density to fluid density), this becomes for sinusoidal motion

$$(\sigma+\tau)\frac{\mathrm{d}u}{\mathrm{d}t}+s\omega u = -(\sigma-1)\frac{\mathrm{d}v}{\mathrm{d}t}$$
$$= -\mathrm{i}\omega(\sigma-1)v_0\mathrm{e}^{\mathrm{i}\omega t} \tag{2.20}$$

This has the solution

$$u = u_0\mathrm{e}^{\mathrm{i}(\omega t-\varphi)} \tag{2.21}$$

where

$$u_0 = \frac{\sigma-1}{[s^2+(\sigma+\tau)^2]^{1/2}}v_0 \tag{2.22}$$

and

$$\tan\varphi = \frac{s}{\sigma+\tau} \tag{2.23}$$

Since the drag force on a single particle is

$$F = -sm\omega u \tag{2.24}$$

the instantaneous rate of energy loss is

$$\frac{\mathrm{d}E}{\mathrm{d}t} = Fu = -sm\omega u^2 \tag{2.25}$$

The average rate is therefore

$$\left(\frac{\mathrm{d}E}{\mathrm{d}t}\right)_{\mathrm{Av}} = -\tfrac{1}{2}sm\omega u_0^2 \tag{2.26}$$

If there are N particles per unit volume then the rate of energy loss per unit area of the beam, or intensity lost after propagating a distance $rmdz$, is

$$\mathrm{d}I = -\tfrac{1}{2}sm\omega u_0^2 N\mathrm{d}z \tag{2.27}$$

where the z-direction is defined as being along the axis of the beam and plane waves are assumed. Introducing the relationship $I = \frac{1}{2}\rho c v_0^2$ where c is the speed of sound, we obtain

$$\frac{\mathrm{d}I}{I} = -\frac{sm\omega}{\rho c}\left(\frac{u_0}{v_0}\right)^2 N\mathrm{d}z \tag{2.28}$$

Introducing the volume concentration $\epsilon = Nm/\rho$ and the acoustic wavenumber $k = \omega/c$ yields

$$\frac{\mathrm{d}I}{I} = -\epsilon k s\left(\frac{u_0}{v_0}\right)^2 \mathrm{d}z \tag{2.29}$$

Integrating this equation gives

$$I = I_0 \exp\left[-\epsilon k s \left(\frac{u_0}{v_0}\right)^2\right] \tag{2.30}$$

Comparing this expression with Equations 2.1 and 2.2, in which the attenuation coefficient α was defined, we see that the visco-inertial absorption coefficient is given by

$$\frac{\alpha_v}{10\log e^2} = \frac{\epsilon k s}{2}\left(\frac{u_0}{v_0}\right)^2 = \frac{\epsilon k(\sigma-1)^2}{2}\left[\frac{s}{s^2+(\sigma+\tau)^2}\right] \tag{2.31}$$

The visco-inertial absorption coefficient therefore depends upon the square of the ratio of the velocity difference between particles and fluid to the velocity of the fluid.

Implicit in Equations 2.29 to 2.31 is the assumption that the absorption coefficient in a suspension of similar particles is linearly proportional to the volume fraction, ϵ, i.e. the process is linearly additive. This assumption is valid for dilute suspensions, in which inter-particle interactions may be neglected. Urick showed experimentally [12] that this linear relationship between the viscous absorption coefficient and concentration holds for volume fractions of up 8–9% for kaolin particles at MHz frequencies. Note that a volume fraction of 8% corresponds to a mass concentration of approximately 200 kgm^{-3} for these particles.

Departing from Urick's work, it is instructive to estimate theoretically the concentrations at which particle interaction effects may become important. We may proceed with this by comparing the mean inter-particle separation with the scale length over which the viscous shear waves are damped in the fluid. This scale length is the skin depth, which was given by Equation 2.17

$$\delta_\mathrm{v} = \sqrt{\frac{2\nu}{\omega}} \tag{2.32}$$

For water, having a kinematic viscosity of $\nu = 10^{-6}\ \mathrm{m^2 s^{-1}}$, at a frequency of 100 kHz, this yields $\delta_\mathrm{v} = 1.78\ \mu\mathrm{m}$.

Now, turning to the estimation of the mean inter-particle separation, the volume fraction is given by

$$\epsilon = \frac{M}{\rho'} \tag{2.33}$$

where M is the mass concentration and ρ' is the density of the particles.

The number density, N, is then

$$N = \frac{\epsilon}{V} \tag{2.34}$$

where $V = \frac{4}{3}\pi a^3$ is the volume of the (spherical) particles.

The mean inter-particle separation may then be estimated to be $N^{-1/3}$. Note that this is the mean separation between the centres of the particles, and it is important to take the finite size of the particle into account. A more appropriate separation to use is therefore

$$d_s = N^{-1/3} - 2a \tag{2.35}$$

Taking as an example a mass concentration of 1 kgm^{-3}, a particle radius of 1 μm and a particle density of 2600 kgm^{-3}, the mean separation d_s is found to be 20.1 μm. Since this separation is much greater than the skin depth of the shear waves the inter-particle effects may be neglected in this case.

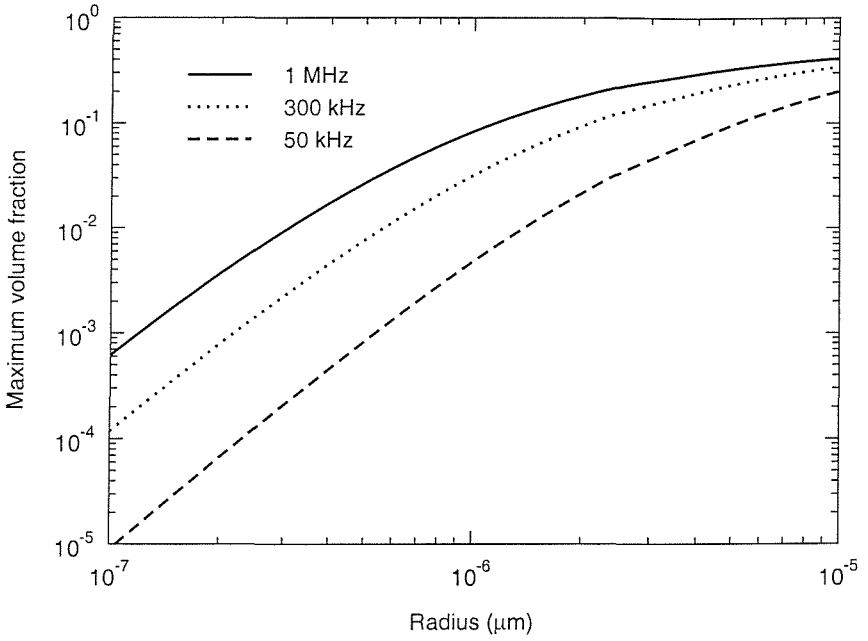

Figure 2.1. Estimates of the maximum concentration at which the effects of inter-particle interactions on attenuation may be neglected, as a function of particle radius, for 3 different frequencies.

More generally we can calculate the maximum volume fraction for which the effects of inter-particle interactions on the attenuation may be neglected for a given frequency and particle size. Let us assume that we may neglect these inter-particle effects if the mean inter-particle separation is greater than three times the skin depth, by which distance the amplitude of the shear waves will have been attenuated by about 95%. We can then calculate the maximum volume fraction for which this condition is satisfied, as a function of particle size, for different frequencies. Figure 2.1 shows the results of such a calculation for quartz particles and frequencies of 50, 300 and 1000 kHz. This shows that the maximum volume concentration for which inter-particle effects may be ignored increases as the particle size increases. This is because for a given mass concentration the number density reduces as the particle mass increases, and hence the inter-particle separation increases. As the frequency increases the viscous skin depth decreases, explaining the increase in the maximum concentration for which inter-particle effects may be neglected as frequency increases. The figure shows that for 1 μm particles at a frequency of 1 MHz, particle interactions should be taken into account for volume fractions above about 8-9%, which is in agreement with Urick's observations [12]. Note that this corresponds to a mass concentration of the order of 200 kgm^{-3}, which is far higher than concentrations to be found in the sea, except perhaps in the sediment boundary layer at the seabed. The experimental measurements presented in Chapter 6 were made with a maximum volume fraction of less than

0.1%, and are therefore consistent with the dilute approximation.

2.5 Scattering

Acoustic plane waves incident on inhomogeneities in the medium through which they are propagating will be scattered in all directions. Energy which is scattered, whilst remaining part of the total acoustic field, represents a contribution to the attenuation of the forward propagating wave.

In the spherical polar coordinate system, (r, θ, ϕ) shown in Figure 2.2 the instantaneous acoustic pressure p_i at time t due to a plane wave travelling along the polar axis is given by the real part of

$$p_\mathrm{i} = p_0 \exp\left[\mathrm{i}\left(k_c r \cos\theta - \omega t\right)\right] \tag{2.36}$$

where p_0 is the source pressure, ω is the angular frequency of the incident compression wave, $k_c = \omega/c$ is the wavenumber and c is the sound speed of the compression wave.

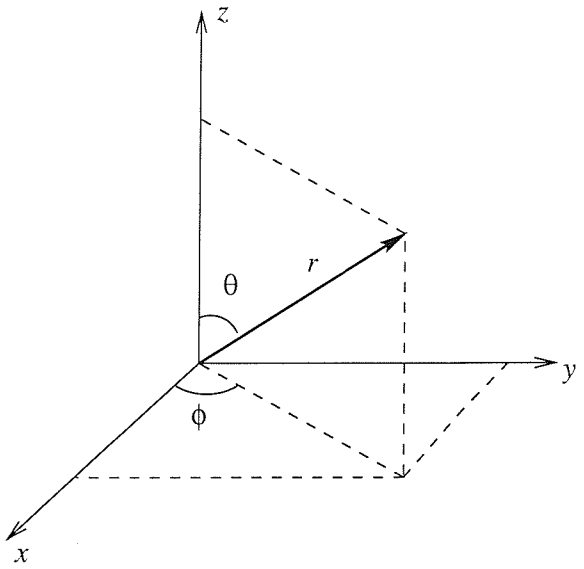

Figure 2.2. Schematic showing the spherical polar coordinate system.

The instantaneous pressure p_s due to a wave scattered from a particle, at any point (r, θ, ϕ) in the far-field of the particle, in the absence of attenuation, is given by

$$p_\mathrm{s} = p_\mathrm{i}\left\{\frac{a f_\infty(\theta)}{2r}\right\}\exp\left[\mathrm{i}\left(k_c r - \omega t\right)\right] \tag{2.37}$$

where a is the particle radius, f_∞ is the far-field scattering form function, θ is the scattering angle and r is the radial distance from the particle.

Employing a partial wave expansion as used by Faran [14], the far-field scattering form function for spheres may be written [14, 15]

$$f_\infty(\theta) = -\frac{2}{x_c}\sum_{n=0}^{\infty}(2n+1)\sin\eta_n \exp(-i\eta_n)\, P_n(\cos\theta) \tag{2.38}$$

where η_n is the phase shift of the nth partial wave and P_n is the Legendre polynomial of order n. The size parameter x_c is defined as the product of the wavenumber in the ambient fluid and the particle radius, $x_c = k_c a$.

The elastic properties of the scatterer enter the problem through the phase shifts η_n, which are given by [14]

$$\tan\eta_n = \tan\delta_n(x_c)\frac{[\tan\alpha_n(x_c) + \tan\Phi_n(x_c', x_s')]}{[\tan\beta_n(x_c) + \tan\Phi_n(x_c', x_s')]} \tag{2.39}$$

where

$$\tan\delta_n(x_c) = -j_n(x_c)/n_n(x_c) \tag{2.40}$$

$$\tan\alpha_n(x_c) = -x_c j_n'/j_n(x_c) \tag{2.41}$$

$$\tan\beta_n(x_c) = -x_c n_n'/n_n(x_c) \tag{2.42}$$

in which $x_c' = k_c' a$ and $x_s' = k_s' a$ where k_c' and k_s' are the wavenumbers of the compression and shear waves in the scatterer. The functions j_n and n_n are the spherical Bessel and Neumann functions, and primes on these functions denote differentiation with respect to the argument. The elastic properties of the scatterer are contained solely within the $\tan\Phi_n$ term, given by

$$\begin{aligned}\tan\Phi_n = \frac{\rho x_s'^2}{2\rho'}\Bigg\{&\Bigg(\frac{\tan\alpha_n(x_c')}{\tan\alpha_n(x_c')+1} \\ &- \frac{(n^2+n)}{(n^2+n-1) - x_s'^2/2 + \tan\alpha_n(x_s')}\Bigg) \\ &\times \Bigg[\Bigg(\frac{n^2+n-x_s'^2/2+2\tan\alpha_n(x_c')}{\tan\alpha_n(x_c')+1} \\ &- \frac{(n^2+n)\,[\tan\alpha_n(x_s')+1]}{(n^2+n-1) - x_s'^2/2 + \tan\alpha_n(x_s')}\Bigg)\Bigg]^{-1}\Bigg\}\end{aligned} \tag{2.43}$$

The attenuation coefficient due to scattering, α_s may be obtained from the far-field scattering form function through the expression

$$\frac{\alpha_s}{10\log e^2} = \frac{3\epsilon}{4a}\left\{\frac{\Im[f_\infty(0)]}{x_c}\right\} \tag{2.44}$$

where $\epsilon = M/\rho'$ is the volume concentration of suspended particles, M is the mass concentration and ρ' is the density of the solid.

As in the case of the viscous absorption expression (Equation 2.31) this expression contains the implicit assumption that the attenuation coefficient depends linearly on the volume concentration, ϵ. This implies that multiple scattering may be neglected.

Bjørnø and Bjørnø [16] looked at the problem of multiple scattering in suspensions both experimentally and theoretically, following the theoretical approach of Gaunaurd *et al.* [17]. In their summary of the analysis of the numerical solutions they state that the two main parameters governing the interaction between two rigid spheres of radius a are ka and the ratio $D = d_0/a$, where d_0 is the distance between the centres of the spheres. The analysis also suggests that the effects of multiple scattering should become important when $ka = d_0/a$. Their experimental approach was to measure the backscattered intensity from a pair of stainless steel spheres suspended by fine nylon lines in the far field of a transducer. The measurements were made at frequencies in the range 300 - 1200 kHz, and with spheres giving ka in the range 5 - 30. They found that the form function for a pair of spheres exhibits significant angular dependence, as expected, and also that interaction between the two spheres can be significant for separations up to $D = 10$ for certain angles.

We can now calculate the maximum volume fraction for which the effects of multiple scattering on the attenuation may be neglected. This may be calculated as a function of particle size, for different frequencies, as was done for viscous absorption on page 13. The result of such a calculation is shown in Figure 2.3, which shows the volume fraction at which $ka = 0.1D$. This shows that the effects of multiple scattering may be neglected at all practical concentrations over the ranges of particle radius and frequency of interest. The effects of multiple scattering begin to become significant at lower concentrations as both the frequency and the particle size increase, i.e. as ka increases.

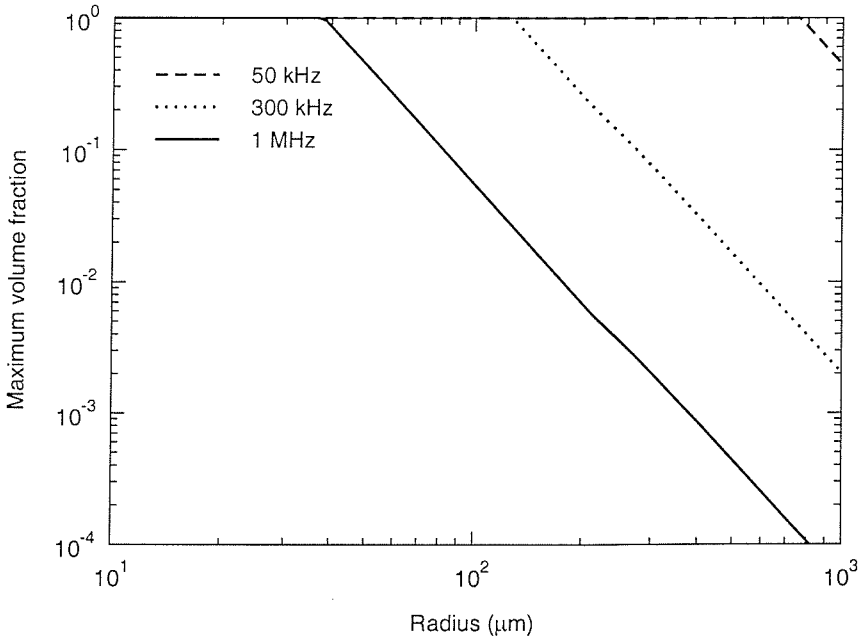

Figure 2.3. Estimated maximum concentration at which the effect of multiple scattering on the attenuation may be neglected, as a function of particle radius, for 3 different frequencies.

Johnson [18] introduced the high pass model for backscattered intensity from a fluid sphere. A simple polynomial is used to represent the general x_c-dependence of the scattering form function approximately by requiring that it fits the form of f_∞ exactly in the Rayleigh (small x_c) and geometric (large x_c) regimes.

Sheng and Hay [19] extended Johnson's model to include the angular dependence, and their expression takes the form

$$|f_\infty(\theta)| = \frac{K_\mathrm{f} x_\mathrm{c}^2}{1 + K_\mathrm{f} x_\mathrm{c}^2} \tag{2.45}$$

where

$$K_\mathrm{f} = \frac{2}{3} |\gamma_\kappa + \gamma_\rho \cos\theta| \tag{2.46}$$

and γ_κ and γ_ρ are the compressibility and density contrasts, given by

$$\gamma_\kappa = \frac{\kappa' - \kappa}{\kappa} \tag{2.47}$$

$$\gamma_\rho = \frac{3\,(\rho' - \rho)}{2\rho' + \rho} \tag{2.48}$$

For small x_c, Equation 2.45 has the required Rayleigh dependence ($f_\infty \propto x_\mathrm{c}^2$) and for large x_c, $|f_\infty(\pi)|$ goes to unity as required.

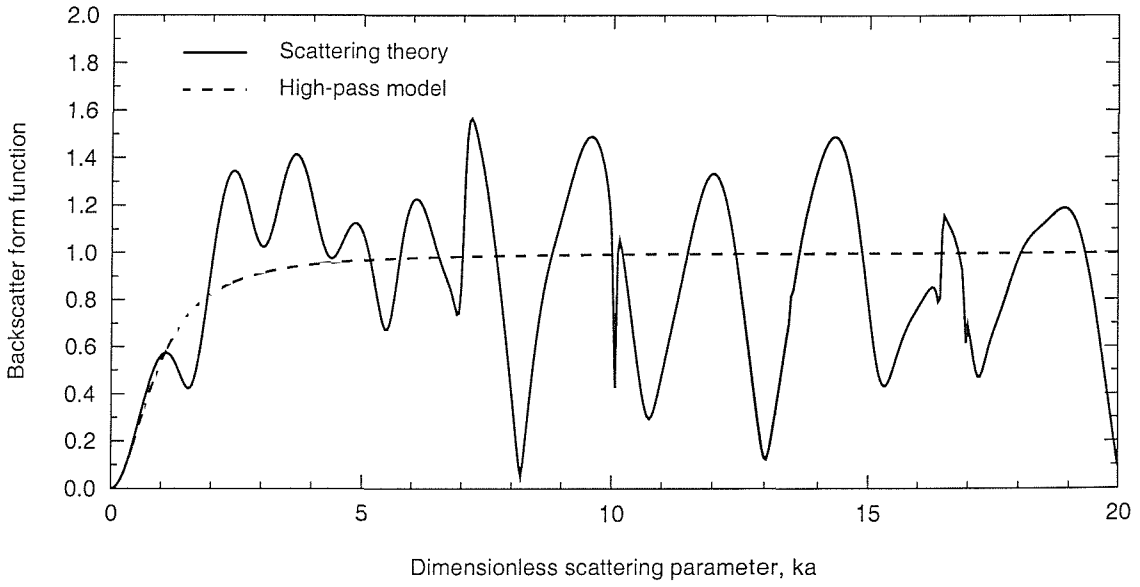

Figure 2.4. Far-field backscattering form function for an elastic, movable quartz sphere: Comparison between scattering theory and high-pass model.

Figure 2.4 shows the far-field amplitude backscattering form function as a function of ka, computed using Faran's model as described above. This was calculated using compression and shear wave speeds representative of those of quartz. Also shown is the approximate form function calculated using the high pass model. A great deal of structure is observed in the full form function and this is due to resonances of the normal modes of the sphere. These normal modes are each characterized by a wavelength which fits into the circumference of the sphere an integer number of times. The zeroth order mode ($n = 0$) is known as the monopole or breathing mode in which the surface moves radially in and out, $n = 1$ is the dipole mode in which the body moves

rigidly to and fro, and the $n = 2$ mode is the quadrupole mode in which the shape oscillates between prolate and oblate spheroids, etc. Rayleigh's observations on the significance of these modes, or terms in the partial wave expansion, are discussed in Section 3.2. All of these motions represent standing waves which may be resolved into pairs of surface waves travelling in opposite directions. The modal series may be transformed, by means of the Watson transformation (see e.g. [20]), into a series of *creeping* surface waves which fall into a number of distinct categories. These include Rayleigh waves, whispering gallery waves, Stonely waves and Franz waves. See Reference [20] for a discussion of these various types of surface wave.

Whilst the scattered field from a monodisperse suspension of spheres will be characterized by this complex resonant structure, it has been shown [21] that a distribution of particle sizes leads to the smoothing out of this structure. This results in a form function which has a profile similar to the high pass filter response, as represented by the high pass model.

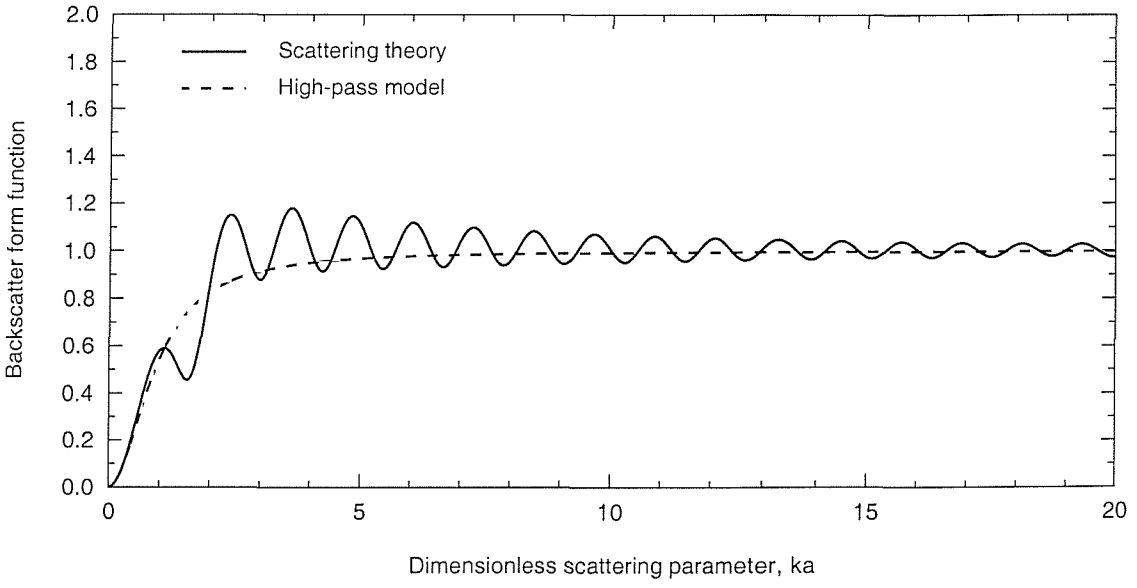

Figure 2.5. Far-field backscattering form function for a rigid, movable quartz sphere: Comparison between scattering theory and high-pass model.

Figure 2.5 shows the form function for a rigid, mobile sphere. In this calculation the compression and shear wave speeds in the solid have been made artificially high, to approximate to the rigid limit. The complicated resonance structure observed in the elastic case is not manifested in the rigid case, since most of the surface waves are not supported by the impenetrable, rigid sphere. Only one type of surface wave still exists in the rigid case and that is the Franz wave, which propagates solely in the fluid and arises as a result of the curved geometry. The interference between the circumferentially propagating Franz waves and the backscattered wave is responsible for the oscillations in the form function for rigid spheres. Whilst this phenomenon may be explained in terms of these creeping Franz waves, it may be realized that it is nothing more than simple diffraction due to an impenetrable sphere.

This form function is once again compared with the high pass model, shown by the dashed curve. It is clear from this figure that the high pass model has the same general x_c dependence as the rigid form function, as required. The characteristic oscillations in the form function due to

diffraction are not, of course, represented by the high pass model. As described above, this structure will be different for each particle size in a distribution of sizes and will thus be smeared out in the ensemble average over all particles contributing to the total scattering.

Clearly the elastic resonances that are excited at certain x_c values can have a significant effect on the scattering form function. It might be expected that the elastic model for the form function would yield the best agreement with experimental measurements with real (i.e. elastic) particles. For measurements made with a monodisperse population of spheres this is indeed the case. However, for measurements made with natural sand grains the rigid models and the high pass model have been shown to provide a better fit to measurements [19]. This implies either that resonant excitation does not occur, or at that it not significant. This is partly due to the smoothing effect of the size distribution, and partly because natural sand grains are irregular in shape and inhomogeneous in composition. The importance of waves travelling on the surface of the particle has already been discussed in the context of resonant scattering, and the circuit times of these surface waves at a resonance must be an integral dividend of the incident wave period. It appears likely that in natural sand grains the irregularities in shape are such that the surface waves do not have well-defined circuit times and many of the resonance structures are not therefore observed in the form function [22]. Scattering measurements made with irregular particles [22] do show some evidence of structure arising from surface waves, principally the Rayleigh wave, but the ensemble averaging over many shapes, sizes and orientations smears these features out in the mean form function.

The high pass model of Equation 2.45 may therefore be considered appropriate for approximating the form function in natural suspensions.

Sheng and Hay have also constructed a high pass model for the attenuation coefficient which can be written as

$$\frac{\alpha_s}{10 \log e^2} = \frac{\epsilon K_\alpha x_c^4}{a\left(\frac{4}{3} K_\alpha x_c^4 + \xi x_c^2 + 1\right)} \tag{2.49}$$

where

$$K_\alpha = \frac{1}{6}\left(\gamma_\kappa^2 + \frac{\gamma_\rho^2}{3}\right) \tag{2.50}$$

and ξ is an adjustable constant ≥ 1. The ξ term allows the form of the polynomial to be adjusted to improve the fit to experimental data for intermediate x_c values.

2.6 Summary and conclusions

In this chapter the key areas of physics relating to the attenuation of sound in dilute suspensions of solid particles have been introduced and discussed. Urick's model [12] has been introduced to calculate the visco-inertial absorption contribution to the attenuation and Sheng and Hay's high-pass model has been introduced to calculate the contribution due to scattering. The validity of the dilute approximation in the cases of absorption and scattering has been examined, and it was shown that at practical sonar frequencies below 1 MHz the dilute approximation is valid for naturally occurring suspensions.

The contribution to the attenuation due to viscous absorption can be modelled using considerations based on the viscous drag experienced by a particle oscillating in a sound field. This approach was taken by Urick [12], and his model was discussed in section 2.4. This model calculates the acoustic energy dissipated by a single spherical particle. To calculate the total attenuation by a collection of particles the single particle result is multiplied by the number density of suspended particles. i.e. the total attenuation is assumed to be the linear summation of the attenuation due to each particle. This is only valid for dilute suspensions where inter-particle interactions may be neglected, and the maximum concentration for which such an assumption is valid was investigated using simple arguments based on mean inter-particle separation. This investigation showed that over the range of frequency, particle size and concentration of interest in the present study, the assumption that particle interactions may be ignored is valid. Urick [12] measured the attenuation at 1 MHz in a suspension of kaolin particles as a function of particle concentration and found a linear dependence up to a volume fraction of around 8% – 9%, and the calculations of the concentrations at which particle interactions become important presented here are in agreement with this observation.

Section 2.5 discussed a method for calculating the scattering form function of an elastic sphere suspended in an inviscid fluid based on a partial wave expansion. Although the intensity scattering form functions can be complicated as a result of resonance excitation the general trend is to obey a $(ka)^4$ dependence for $ka \ll 1$ (Rayleigh scattering) and to tend to unity for $ka \gg 1$ (geometric scattering). This behaviour permits a considerable simplification, as the form function can be approximated by a fourth-order polynomial in $x = ka$. This approach is known as the high-pass model.

Calculations of the scattering form function for a homogeneous quartz sphere suspended in water showed the expected complexity due to resonance excitation, with large departures from the predictions of the high-pass model for large ka. However, natural sand grains are not found to exhibit strong resonances, for the reasons discussed in this chapter. The high-pass model is therefore believed to be an adequate model for calculating the attenuation due to scattering by natural particles. In fact, for the present study, the small ka regime is of the most interest, where the $(ka)^4$ dependence of the high-pass model represents the scattering form function very well.

As with the viscous absorption calculations, a linear dependence on particle concentration has been assumed in the scattering models, thus ignoring multiple scattering. By employing arguments similar to those used in the case of absorption, the maximum concentration for which such an assumption is valid was calculated. It was found that the effects of multiple scattering may be neglected at all practical concentrations over the ranges of particle radius and frequency of interest.

The following chapter introduces a rigorous theoretical treatment of absorption and scattering by an elastic, thermally conducting spherical particle suspended in a viscous, thermally conducting fluid. This model will be used as a benchmark model against which the models presented in this chapter may be compared.

Chapter 3

A model of a spherical scatterer in a thermo-viscous fluid

3.1 Introduction

In this chapter a rigorous theoretical treatment for the attenuation of sound by elastic, thermally conducting spheres suspended in a viscous, thermally conducting fluid is introduced. This approach constitutes a benchmark solution to the problem and results from this model will be compared with the results of the models discussed in Chapter 2.

3.2 Complete theory

A unified model to describe the attenuation of an acoustic wave propagating through a fluid containing suspended particulate matter is conceptually preferable to the independent explicit models for absorption and scattering described in Chapter 2. Although these models have the advantage of simplicity, it is important to compare them with a more complete physical description of the effects over the parameter range of interest.

The problem of sound attenuation by suspensions of small spherical particles has been the subject of a number of studies, originating with Rayleigh's [23] discussions of the disturbance of plane waves produced by small obstacles. He observed that the magnitude of the zero-order term in a partial wave expansion of the disturbed field is a manifestation of the compressibility difference between the particle and the suspending fluid. This is apparent as the zero-order or monopole term describes radial pulsations of the sphere, and is often referred to as the breathing mode, as described in Section 2.5 on Page 17. Rayleigh further observed that the first-order or dipole term is determined by the density difference. Section 2.5 discussed how this term describes rigid, translational motion of the particle. It is therefore clearly associated with relative motion of the particle and fluid, and hence the viscous drag losses described in Section 2.4.

It was previously stated that Sewell's treatment [9] of the absorption of sound in a suspension of small particles considered the particles to be rigid and immobile. Lamb [11] removed the restriction that the particles be immobile and Epstein [10] refined the theory to include elastic particles. In this latter treatment, the spherical objects representing the particles in suspension were attributed the properties of viscous fluids or elastic solids. Urick [12] derived a result equivalent to that of Lamb and Epstein using simple arguments based on viscous drag, as

described in section 2.4.

Isakovich [24] noted that sound propagation in a suspension can produce temperature gradients at the particle-fluid interface, due to the adiabatic character of acoustic waves and may result in significant attenuation via thermal diffusion. Epstein and Carhart [25] independently deduced the thermal loss contribution in a detailed theoretical examination of the problem. Their work was primarily aimed at attenuation in aerosols, although the bulk of their analysis may also be applied to dispersions in condensed media.

Allegra and Hawley [26] (hereafter referred to as AH), closely following the derivation of Epstein and Carhart, have extended the theory to include the case of elastic, heat-conducting, solid spheres suspended in a viscous, heat-conducting fluid. The AH formulism has been used here, and the fundamentals of the theory are summarized below. For a more complete description the interested reader is referred to the original papers [25,26].

The attenuation of a sound wave propagating in an inhomogeneous medium is defined as the sum of scattering and absorption losses. In the inviscid, non-conducting case three waves are required to describe adequately the response of the fluid-solid system to an incident compression wave. These are the scattered compression wave in the fluid and compression and shear waves in the solid. When viscous effects are included an additional viscous shear wave in the fluid arises, and considering thermal effects requires that thermal waves in both the fluid and the solid be taken into account.

Mathematically the increased absorption of the incident wave in the presence of the scatterer is due to the damping of these additional waves. Physically, energy loss arising from thermal conduction is due to the differences in amplitude and phase of the acoustically driven temperature fluctuations in the fluid and particle. This leads to a heat flux between the fluid and particle. Viscous losses arise from a momentum flux between the fluid and particle due to the relative motion of the fluid and the particle. The viscous losses reach a maximum when the viscous shear wavelength is approximately the same as the particle size. Similarly, the thermal losses are at a maximum when the wavelength of the thermal wave is comparable to the size of the particle. At low frequencies the temperature difference between the particle and fluid will equilibrate in the time of the passage of the wave, whilst at high frequencies only a small fraction of the particle volume near the surface will participate in the thermal conduction process.

These heat and momentum fluxes are large where the temperature and velocity gradients are large. This is the case in the boundary layers surrounding the particles. The thicknesses of the boundary layers are defined as the skin depths of the viscous and thermal waves, i.e. the distances over which the amplitudes of the waves are damped by a factor of 1/e. They are given by

$$\delta_{\mathrm{v}} = \sqrt{\frac{2\nu}{\omega}} \quad \text{and} \quad \delta_{\mathrm{t}} = \sqrt{\frac{2\chi}{\omega}} \tag{3.1}$$

where ν is the kinematic viscosity of the fluid and χ is the thermal diffusivity , given by

$$\chi = \frac{K}{\rho C_{\mathrm{p}}} \tag{3.2}$$

where K here is the thermal conductivity of the fluid, and C_{p} is its specific heat capacity. Similarly, a skin depth for the thermal wave within the solid particle may be defined as

$$\delta'_{\mathrm{t}} = \sqrt{\frac{2\chi'}{\omega}} \tag{3.3}$$

with

$$\chi' = \frac{K'}{\rho' C'_{\mathrm{p}}} \tag{3.4}$$

where the primed symbols indicate the respective physical properties of the solid.

The first step in calculating the attenuation is to obtain the wave equations for the propagation of the compression, shear and thermal waves in the two media. The wave equations are obtained from the conservation laws , a stress-strain relation, and two thermodynamic equations of state. The wave equations are then solved in spherical coordinates in terms of series expansions involving spherical Bessel and Hankel functions and series of unknown coefficients. From the boundary conditions at the fluid-particle interface six simultaneous equations are obtained which may be solved to give the unknown coefficients. The attenuation of the primary wave may be related to these coefficients.

The amplitude of the sound wave is taken to be sufficiently small that nonlinear effects can be ignored[1]. In this case the deviation of a variable from its mean value is also small, and products of such deviations are negligible. Dropping these terms, and time and space derivatives of mean quantities, the conservation equations together with the equations of state are reduced to two coupled equations. Using the identity $\partial/\partial t \equiv -\mathrm{i}\omega$ these equations may be written [27] as follows for the fluid

$$\omega^2 \mathbf{v} + \left(\frac{c^2}{\gamma} - \frac{\mathrm{i}\omega\eta}{3\rho}\right) \boldsymbol{\nabla}(\boldsymbol{\nabla} \cdot \mathbf{v}) + \frac{\mathrm{i}\omega c^2 \vartheta}{\gamma} \boldsymbol{\nabla} T - \frac{\mathrm{i}\omega\eta}{\rho} \nabla^2 \mathbf{v} = 0 \tag{3.5}$$

and

$$\left[\frac{\gamma - 1}{\vartheta}\right] \boldsymbol{\nabla} \cdot \mathbf{v} - \mathrm{i}\omega T - \gamma\chi \nabla^2 T = 0 \tag{3.6}$$

where $\mathbf{v}$ is the velocity vector, c is the sound speed of compression waves in the fluid, T is the absolute temperature and η is the molecular viscosity of the fluid.

In a solid the equivalent equations are

$$\omega^2 \mathbf{u} + \left(\frac{c_1'^2}{\gamma'} + \frac{\mu'}{3\rho'}\right) \boldsymbol{\nabla}(\boldsymbol{\nabla} \cdot \mathbf{u}) - \frac{c_1'^2 \vartheta'}{\gamma'} \boldsymbol{\nabla} T' + \frac{\mu' \nabla^2 \mathbf{u}}{\rho'} = 0 \tag{3.7}$$

and

$$(-\mathrm{i}\omega)\left[\frac{\gamma' - 1}{\vartheta'}\right] \boldsymbol{\nabla} \cdot \mathbf{u} - \mathrm{i}\omega T' - \gamma'\chi' \nabla^2 T' = 0 \tag{3.8}$$

where T is the temperature, $\mathbf{u}$ is the displacement vector, c'_1 is the sound speed of spherical compression waves in the solid and μ' is the shear modulus of the solid.

[1] The acoustic amplitude used in the experiments described in Chapter 6 is far too small for finite amplitude effects to be significant.

The other variables in these equations are

γ = ratio of specific heat at constant pressure to that at constant volume in the fluid
ρ = density of the fluid
ϑ = thermal expansion coefficient of the fluid
χ = thermal diffusivity $\equiv K/\rho C_\mathrm{p}$ of the fluid
K = thermal conductivity of the fluid
C_p = specific heat capacity of the fluid

and primed quantities refer to the respective physical properties of the solid.

The velocity field in the fluid and displacement field in the solid are represented by scalar potentials $\overline{\phi}$ and vector potentials $\mathbf{A}$ such that

$$\mathbf{v} = -\boldsymbol{\nabla}\overline{\phi} + \boldsymbol{\nabla} \times \mathbf{A} \tag{3.9}$$

$$\mathbf{u} = -\boldsymbol{\nabla}\overline{\phi}' + \boldsymbol{\nabla} \times \mathbf{A}' \tag{3.10}$$

where $\boldsymbol{\nabla} \cdot \mathbf{A} = 0$ and

$$\overline{\phi} = \phi_\mathrm{c} + \phi_\mathrm{t} \tag{3.11}$$

in which ϕ_c and ϕ_t are the scalar potentials for the compression and thermal waves.

In the fluid

$$\phi_\mathrm{c} = \phi_0 + \phi_\mathrm{r} \tag{3.12}$$

where ϕ_0 and ϕ_r are the scalar potentials for the incident and scattered compression waves.

The Helmholtz equations for the three potentials - compressional, ϕ_c, thermal, ϕ_t, and viscous, $\mathbf{A}$, may be written in the form

$$\left(\nabla^2 + k_\mathrm{c}^2\right)\phi_\mathrm{c} = 0 \tag{3.13}$$

$$\left(\nabla^2 + k_\mathrm{t}^2\right)\phi_\mathrm{t} = 0 \tag{3.14}$$

$$\left(\nabla^2 + k_\mathrm{s}^2\right)\mathbf{A} = 0 \tag{3.15}$$

in the fluid, and

$$\left(\nabla^2 + k_\mathrm{c}'^2\right)\phi_\mathrm{c}' = 0 \tag{3.16}$$

$$\left(\nabla^2 + k_{\mathrm{t}}'^2\right)\phi_{\mathrm{t}}' = 0 \tag{3.17}$$

$$\left(\nabla^2 + k_{\mathrm{s}}'^2\right)\mathbf{A}' = 0 \tag{3.18}$$

in the solid.

The wavenumbers of the compression, thermal and shear waves in the fluid medium are given by

$$k_{\mathrm{c}}^2 = \left(\frac{\omega^2}{c^2}\right)\left\{1 - \left(\frac{\mathrm{i}\omega}{c^2}\right)\left[\frac{4\eta}{3\rho} + (\gamma - 1)\chi\right]\right\}^{-1} \tag{3.19}$$

$$k_{\mathrm{t}}^2 = \frac{\mathrm{i}\omega}{\chi} \tag{3.20}$$

$$k_{\mathrm{s}}^2 = \frac{\mathrm{i}\omega\rho}{\eta} \tag{3.21}$$

provided the temperature is given by

$$T = \frac{b_{\mathrm{c}}\phi_{\mathrm{c}} + b_{\mathrm{t}}\phi_{\mathrm{t}}}{-\mathrm{i}\omega} \tag{3.22}$$

where

$$b_{\mathrm{c}} = \left(\frac{-\gamma}{c^2\vartheta}\right)\left[\omega^2 - \left(\frac{c^2}{\gamma} - \frac{4\mathrm{i}\omega\eta}{3\rho}\right)k_{\mathrm{c}}^2\right] \tag{3.23}$$

$$b_{\mathrm{t}} = \left(\frac{-\gamma}{c^2\vartheta}\right)\left[\omega^2 - \left(\frac{c^2}{\gamma} - \frac{4\mathrm{i}\omega\eta}{3\rho}\right)k_{\mathrm{t}}^2\right] \tag{3.24}$$

Note that 3.19 and 3.20 are only valid if $|k_{\mathrm{c}}/k_{\mathrm{t}}| \ll 1$, $|k_{\mathrm{c}}| \sim \omega/c$ and

$$\omega \ll \frac{3\rho c^2}{4\eta\gamma} \quad \text{or} \quad \left|\frac{k_{\mathrm{c}}}{k_{\mathrm{s}}}\right| \ll 1 \tag{3.25}$$

For water, Equation 3.25 requires that the frequency be much less than 10^{11} Hz, i.e. this is not a practical limitation in this case.

In the solid the wavenumbers are given by

$$k_{\mathrm{c}}'^2 = \frac{\omega^2}{c'^2}\left(1 - \frac{\mathrm{i}\omega\chi'}{c'^2}(\gamma' - 1)\frac{\lambda' + 2\mu'/3}{\lambda' + 2\mu'}\right)^{-1} \tag{3.26}$$

where λ' is the Lamé constant ,

$$k_{\mathrm{t}}'^2 = \frac{\mathrm{i}\omega}{\chi'} \tag{3.27}$$

$$k_{\mathrm{s}}'^2 = \frac{\rho'\omega^2}{\mu'} \tag{3.28}$$

provided

$$T' = b_{\mathrm{c}}'\phi_{\mathrm{c}}' + b_{\mathrm{t}}'\phi_{\mathrm{t}}' \tag{3.29}$$

where

$$b_{\mathrm{c}}' = \frac{-\gamma'}{c_1'^2\vartheta'}\left[\omega^2 - \left(\frac{c_1'^2}{\gamma'} + \frac{4\mu'}{3\rho'}k_{\mathrm{c}}'^2\right)\right] \tag{3.30}$$

$$b_{\mathrm{t}}' = \frac{-\gamma'}{c_1'^2\vartheta'}\left[\omega^2 - \left(\frac{c_1'^2}{\gamma'} + \frac{4\mu'}{3\rho'}k_{\mathrm{t}}'^2\right)\right] \tag{3.31}$$

Again, the equations for k_{c}' and k_{t}' hold only if $|k_{\mathrm{c}}'| \sim \omega/c'$ and $|k_{\mathrm{c}}'|/k_{\mathrm{t}}' \ll 1$. This does not impose a restriction on the frequency, as was the case in the ambient fluid, but requires that in the solid γ' must be very close to 1.

Note that the equations for fluid and solid media are identical if $\partial\mathbf{u}/\partial t = \mathbf{v}$, $(\mathbf{v} = -i\omega\mathbf{u})$, $\mu' = -i\omega\eta'$ and $c_1' = c'$ provided

$$\omega \ll \frac{\rho' c^2}{\eta'} \tag{3.32}$$

which is equivalent to Equation 3.25

It is now possible to solve the problem of a plane compression wave impinging on a solid sphere of radius a suspended in a fluid medium. The presence of the sphere gives rise to a reflected compression wave in the fluid, a compression wave in the sphere, and thermal and viscous shear waves inside and outside the sphere.

The series solutions of the wave equations in spherical polar coordinates with symmetry about the polar axis, and which remain finite at the origin and at infinity are given by

$$\phi_0 = \sum_{n=0}^{\infty} \mathrm{i}^n(2n+1)j_n(x_{\mathrm{c}})P_n(\cos\theta) \tag{3.33}$$

$$\phi_{\mathrm{r}} = \sum_{n=0}^{\infty} \mathrm{i}^n(2n+1)A_n h_n(x_{\mathrm{c}})P_n(\cos\theta) \tag{3.34}$$

$$\phi_{\mathrm{t}} = \sum_{n=0}^{\infty} \mathrm{i}^n(2n+1)B_n h_n(x_{\mathrm{t}})P_n(\cos\theta) \tag{3.35}$$

$$A = \sum_{n=0}^{\infty} \mathrm{i}^n(2n+1)C_n h_n(x_{\mathrm{s}})P_n^1(\cos\theta) \tag{3.36}$$

$$\phi_{\mathrm{c}}' = \sum_{n=0}^{\infty} \mathrm{i}^n(2n+1)A_n' j_n(x_{\mathrm{c}}')P_n(\cos\theta) \tag{3.37}$$

$$\phi'_{\mathrm{t}} = \sum_{n=0}^{\infty} \mathrm{i}^n (2n+1) B'_n j_n(x'_{\mathrm{t}}) P_n(\cos\theta) \tag{3.38}$$

$$A' = \sum_{n=0}^{\infty} \mathrm{i}^n (2n+1) C'_n j_n(x'_{\mathrm{s}}) P_n^1(\cos\theta) \tag{3.39}$$

where A and A' represent the non-vanishing azimuthal components of $\mathbf{A}$ and $\mathbf{A}'$. The j_n are the spherical Bessel functions and the h_n are the spherical Hankel functions (actually $h_n^{(1)}$ but written h_n here for convenience). The functions P_n and P_n^1 are the Legendre functions and the associated Legendre functions. The arguments of the Bessel and Hankel functions are $x_{\mathrm{c}} = k_{\mathrm{c}} a$, $x_{\mathrm{t}} = k_{\mathrm{t}} a$ and $x_{\mathrm{s}} = k_{\mathrm{s}} a$ for the fluid and their primed equivalents for the solid.

The values of the unknown coefficients A_n, B_n, C_n, A'_n, B'_n, C'_n are determined by the boundary conditions at the surface of the sphere. These conditions are that the radial velocity, tangential velocity, temperature, heat flux, radial stress and tangential stress be continuous [25,26]. The boundary conditions yield six simultaneous equations which may be solved for the six unknown coefficients.

These equations are

(a) continuous radial velocity

$$\begin{aligned} &x_{\mathrm{c}} j'_n(x_{\mathrm{c}}) + x_{\mathrm{c}} A_n h'_n(x_{\mathrm{c}}) + t B_n h'_n(x_{\mathrm{t}}) - C_n n(n+1) h_n(x_{\mathrm{s}}) \\ &= (-\mathrm{i}\omega) \left[x'_{\mathrm{c}} A'_n j'_n(x'_{\mathrm{c}}) + x'_{\mathrm{t}} B'_n j'_n(x'_{\mathrm{t}}) - C'_n n(n+1) j_n(x'_{\mathrm{s}}) \right] \end{aligned} \tag{3.40}$$

(b) no-slip condition (continuous tangential velocity)

$$\begin{aligned} &j_n(x_{\mathrm{c}}) + A_n h_n(x_{\mathrm{c}}) + B_n h_n(x_{\mathrm{t}}) - C_n \left[h_n(x_{\mathrm{s}}) + x_{\mathrm{s}} h'_n(x_{\mathrm{s}}) \right] \\ &= (-\mathrm{i}\omega) \left\{ A'_n j_n(x'_{\mathrm{c}}) + B'_n j_n(x'_{\mathrm{t}}) - C'_n \left[j_n(x'_{\mathrm{s}}) + x'_{\mathrm{s}} j'_n(x'_{\mathrm{s}}) \right] \right\} \end{aligned} \tag{3.41}$$

(c) continuous temperature

$$b_{\mathrm{c}} \left[j_n(x_{\mathrm{c}}) + A_n h_n(x_{\mathrm{c}}) \right] + b_{\mathrm{t}} B_n h_n(x_{\mathrm{t}}) = (-\mathrm{i}\omega) \left[b'_{\mathrm{c}} A'_n j_n(x'_{\mathrm{c}}) + b'_{\mathrm{t}} B'_n j_n(x'_{\mathrm{t}}) \right] \tag{3.42}$$

(d) continuous heat flux

$$K \left\{ b_{\mathrm{c}} \left[x_{\mathrm{c}} j'_n + A_n x_{\mathrm{c}} h'_n(x_{\mathrm{c}}) \right] + B_n b_{\mathrm{t}} h'_n(x_{\mathrm{t}}) \right\} = (-\mathrm{i}\omega) K' \left[A'_n b'_{\mathrm{c}} x'_{\mathrm{c}} j'_n(x'_{\mathrm{c}}) + B'_n b'_{\mathrm{t}} x'_{\mathrm{t}} j'_n(x'_{\mathrm{t}}) \right] \tag{3.43}$$

(e) continuous radial stress

$$\begin{aligned} &\eta \left\{ \left[\left(x_{\mathrm{s}}^2 - 2x_{\mathrm{c}}^2 \right) j_n(x_{\mathrm{c}}) - 2x_{\mathrm{c}}^2 j''_n(x_{\mathrm{c}}) \right] \right. \\ &+ A_n \left[\left(x_{\mathrm{s}}^2 - 2x_{\mathrm{c}}^2 \right) h_n(x_{\mathrm{c}}) - 2x_{\mathrm{c}}^2 h''_n(x_{\mathrm{c}}) \right] \\ &\left. + B_n \left[\left(x_{\mathrm{s}}^2 - 2x_{\mathrm{t}}^2 \right) h_n(x_{\mathrm{t}}) - 2x_{\mathrm{t}}^2 h''_n(x_{\mathrm{t}}) \right] + C_n 2n(n+1) \left[x_{\mathrm{s}} h'_n(x_{\mathrm{s}}) - h_n(x_{\mathrm{s}}) \right] \right\} \\ &= A'_n \left[\left(\omega^2 \rho' a^2 - 2\mu' x_{\mathrm{c}}'^2 \right) j_n(x'_{\mathrm{c}}) - 2\mu' x_{\mathrm{c}}'^2 j''_n(x'_{\mathrm{c}}) \right] \\ &+ B'_n \left[\left(\omega^2 \rho' a^2 - 2\mu' x_{\mathrm{t}}'^2 \right) j_n(x'_{\mathrm{t}}) - 2\mu' x_{\mathrm{t}}'^2 j''_n(x'_{\mathrm{t}}) \right] + C_n 2\mu' n(n+1) \left[x'_{\mathrm{s}} j'_n(x'_{\mathrm{s}}) - j_n(x'_{\mathrm{s}}) \right] \end{aligned} \tag{3.44}$$

(f) continuous tangential stress

$$\begin{aligned}
&\eta\left\{x_{\mathrm{c}}j_n'(x_{\mathrm{c}}) - j_n(x_{\mathrm{c}}) + A_n\left[x_{\mathrm{c}}h_n'(x_{\mathrm{c}}) - h_n(x_{\mathrm{c}})\right]\right.\\
&\left.+B_n\left[x_{\mathrm{t}}h_n'(x_{\mathrm{t}}) - h_n(x_{\mathrm{t}})\right] - C_n\left[x_{\mathrm{s}}^2h_n''(x_{\mathrm{s}}) - (n^2+n-2)h_n(x_{\mathrm{s}})\right]/2\right\}\\
&= \mu'\left\{A_n'\left[x_{\mathrm{c}}'j_n'(x_{\mathrm{c}}') - j_n(x_{\mathrm{c}}')\right] + B_n'\left[x_{\mathrm{t}}'j_n'(x_{\mathrm{t}}') - j_n(x_{\mathrm{t}}')\right]\right.\\
&\left.-C_n'\left[x_{\mathrm{s}}'^2j_n''(x_{\mathrm{s}}') - (n^2+n-2)j_n(x_{\mathrm{s}}')\right]/2\right\}
\end{aligned} \tag{3.45}$$

where the primes on the spherical Bessel and Hankel functions denote differentiation with respect to the argument.

In the thermally non-conducting case the conditions on temperature and heat flux are dropped.

The attenuation of sound in suspensions and emulsions arises from energy scattered by the sphere to infinity, i.e. distances r with $k_{\mathrm{c}}r \gg 1$, as well as the energy absorbed in the vicinity of the particle. The scattered energy is just that contained in the reflected compression wave, ϕ_{r}. The viscous shear and thermal waves that are produced at the fluid-particle interface are damped close to the boundary, (recall from page 22 that the e-folding length for these waves is the thickness of the boundary layer) and do not contribute to the scattered field at large distances from the particle.

The energy absorbed can be obtained by writing the total velocity potential at infinity in terms of incoming and outgoing waves. Then the difference in the energy carried by these waves yields the energy absorbed by the medium.

In this way the attenuation of the incident wave is found to depend explicitly on the coefficients of the reflected compression wave, A_n, only [26]. The attenuation coefficient due to viscous absorption, thermal absorption and scattering, expressed in dB m^{-1} may be written

$$\alpha_{\mathrm{v}} + \alpha_{\mathrm{t}} + \alpha_{\mathrm{s}} = \left(10\log \mathrm{e}^2\right)\left\{-\frac{3\epsilon}{2k_{\mathrm{c}}^2a^3}\sum_{n=0}^{\infty}(2n+1)\Re(A_n)\right\} \tag{3.46}$$

where ϵ is the volume fraction of suspended particles. More generally, both the attenuation and phase speed may be evaluated from the single scattering equation

$$\left(\frac{k_{\mathrm{sus}}}{k_{\mathrm{c}}}\right)^2 = 1 + \frac{3\epsilon}{\mathrm{i}k_{\mathrm{c}}^3a^3}\sum_{n=0}^{\infty}(2n+1)A_n \tag{3.47}$$

where k_{sus} is the complex wavenumber for the suspension. The total attenuation coefficient, $\alpha = \alpha_{\mathrm{v}} + \alpha_{\mathrm{t}} + \alpha_{\mathrm{s}}$, and the phase speed, c_{s}, may be determined from the imaginary and real parts of the complex wavenumber respectively.

$$k_{\mathrm{sus}} = \frac{\omega}{c_{\mathrm{s}}} + \frac{\mathrm{i}\alpha}{10\log \mathrm{e}^2} \tag{3.48}$$

3.3 Multiple scattering

This thesis is concerned with acoustics in dilute suspensions in which the effects of particle interaction and multiple scattering are not significant. The validity of the dilute approximation was examined in Sections 2.4 and 2.5. However, it is interesting to see how one might proceed in more concentrated suspensions in which the dilute approximation is not valid.

A number of multiple scattering equations exist, the simplest of which is that of Waterman and Truell [28]. For values of n from 0 to 2 this gives

$$\left(\frac{k_{\mathrm{sus}}}{k_{\mathrm{c}}}\right)^2 = 1 + \frac{3\epsilon}{\mathrm{i}k_{\mathrm{c}}^3 a^3}\left(A_0 + 3A_1 + 5A_2\right) - \frac{27\epsilon^2}{k_{\mathrm{c}}^6 a^6}\left(A_0 A_1 + 5A_1 A_2\right) \tag{3.49}$$

Lloyd and Berry [29] also give a multiple scattering equation, which differs from Equation 3.49 in that it contains an additional term in ϵ^2

$$\begin{aligned}\left(\frac{k_{\mathrm{sus}}}{k_{\mathrm{c}}}\right)^2 = 1 + \frac{3\epsilon}{\mathrm{i}k_{\mathrm{c}}^3 a^3}\left(A_0 + 3A_1 + 5A_2\right) - \frac{27\epsilon^2}{k_{\mathrm{c}}^6 a^6}\left(A_0 A_1 + 5A_1 A_2\right) \\ - \frac{54\epsilon^2}{k_{\mathrm{c}}^6 a^6}\left(A_1^2 + \frac{5}{3}A_0 A_2 + 3A_1 A_2 + \frac{115}{21}A_2^2\right)\end{aligned} \tag{3.50}$$

3.4 Simplifications

For the case of mineral particles suspended in water the thermal losses are negligible, as shown by the result in Figure 4.2 on Page 36. Therefore heat conduction may be ignored and k_{s}' and k_{c}' are purely real. In contrast both k_{s} and k_{c} are complex. However, it is clear from Equation 3.19 that the imaginary part of k_{c} is negligibly small for all practical frequencies and k_{c} may therefore be considered to be real. On the other hand the real and imaginary parts of k_{s} are equal.

Now, from Equation 3.21, the magnitude of the scattering parameter for the shear waves in the ambient fluid may be written

$$|x_{\mathrm{s}}| = \left(\frac{c\rho a x_{\mathrm{c}}}{\eta}\right)^{1/2} \tag{3.51}$$

Hay and Mercer [15] simplified the algebraic solution of the AH equations in the absence of thermal conduction by employing the asymptotic form of the spherical Hankel function of argument x_{s}, i.e.

$$h_n(x_{\mathrm{s}}) = (1/x_{\mathrm{s}})\exp\left[\mathrm{i}\left[x_{\mathrm{s}} - (n+1)\pi/2\right]\right] \tag{3.52}$$

The condition for the use of this form of the spherical Hankel function may be written

$$|x_{\mathrm{s}}| > n(n+1)/2 \tag{3.53}$$

From Equation 3.51 it may be determined that this condition is not satisfied for very fine particles ($O(1\ \mu\mathrm{m})$) suspended in water at the lowest frequencies of interest ($O(10\ \mathrm{kHz})$). In this

regime the full AH solution would be required. However, for the case of larger particles, such as sand grains ($O(100\ \mu\text{m})$), use of the asymptotic approximation is appropriate.

Hay and Mercer proceeded with a partial wave method as described in Section 2.5, recognizing the following relationship between the partial wave phase shift, η_n, and the coefficient A_n of the AH theory

$$A_n = -\mathrm{i}\sin\eta_n \mathrm{e}^{-\mathrm{i}\eta_n} = -\mathrm{i}\tan\eta_n/(1+\mathrm{i}\tan\eta_n) \tag{3.54}$$

Hay and Mercer employed the standard recursion relations for the spherical Bessel and Hankel functions to eliminate the second derivatives of these functions in the AH equations. They then proceeded to reduce these equations to the forms shown below (correcting a typographic error in their paper).

The phase shift η_n of the nth partial wave is given by (c.f. Equation 2.39)

$$\tan\eta_n = \tan\delta_n(x_\mathrm{c})\frac{[\tan\alpha_n(x_\mathrm{c}) + \tan\Psi_n(x'_\mathrm{c}, x'_\mathrm{s})]}{[\tan\beta_n(x_\mathrm{c}) + \tan\Psi_n(x'_\mathrm{c}, x'_\mathrm{s})]} \tag{3.55}$$

where

$$\tan\delta_n(x_\mathrm{c}) = -j_n(x_\mathrm{c})/n_n(x_\mathrm{c}) \tag{3.56}$$

$$\tan\alpha_n(x_\mathrm{c}) = -x_\mathrm{c}j'_n/j_n(x_\mathrm{c}) \tag{3.57}$$

$$\tan\beta_n(x_\mathrm{c}) = -x_\mathrm{c}n'_n/n_n(x_\mathrm{c}) \tag{3.58}$$

and the properties of the materials enter the problem through the term $\tan\Psi_n$, defined as

$$\tan\Psi_n = \frac{\zeta_\mathrm{s}(n^2+n)b_\mathrm{s}\tan\Lambda_n - \beta_\mathrm{s}\left[\zeta_\mathrm{s}\Gamma_n(x_\mathrm{s})+1\right]\tan\xi_n}{1+\beta_\mathrm{s}\left(2\tan\Lambda_n - \tan\xi_n\right)} \tag{3.59}$$

where

$$\begin{aligned}\tan\Lambda_n = &\left(\frac{\tan\alpha_n(x'_\mathrm{c}) + \zeta_\mathrm{s}(n^2+n)}{\tan\alpha_n(x'_\mathrm{c}) + 1 - \beta_\mathrm{s}\zeta_\mathrm{s}\Gamma_n(x_\mathrm{s})} - \frac{(n^2+n)\left[P(x'_\mathrm{s}) - \zeta_\mathrm{s}\right]}{Q(x'_\mathrm{s}) + \beta_\mathrm{s}\zeta_\mathrm{s}\Gamma_n(x_\mathrm{s})}\right)\\ &\times\left(\frac{(n^2+n)\left[1-\beta_\mathrm{s}\zeta_\mathrm{s}(1-\mathrm{i}x_\mathrm{s})\right] - x'^2_\mathrm{s}/2 + 2\tan\alpha_n(x'_\mathrm{c})}{\tan\alpha_n(x'_\mathrm{c}) + 1 - \beta_\mathrm{s}\zeta_\mathrm{s}\Gamma_n(x_\mathrm{s})}\right.\\ &\left.-\ (n^2+n)\frac{R(x'_\mathrm{s}) + \beta_\mathrm{s}\zeta_\mathrm{s}(1-\mathrm{i}x_\mathrm{s})}{Q(x'_\mathrm{s}) + \beta\zeta\Gamma_n(x_\mathrm{s})}\right)^{-1}\end{aligned} \tag{3.60}$$

and

$$\begin{aligned}\tan\xi_n = &\left\{\left((n^2+n)\frac{R(x'_s)+\beta_s\zeta_s(1-\mathrm{i}x_s)}{Q(x'_s)+\beta\zeta\Gamma_n(x_s)}\right)\left(\frac{\tan\alpha_n(x'_c)+\zeta_s(n^2+n)}{\tan\alpha_n(x'_c)+1-\beta_s\zeta_s\Gamma_n(x_s)}\right)\right.\\ &\left.-\left(\frac{(n^2+n)\left[P(x'_s)-\zeta_s\right]}{Q(x'_s)+\beta_s\zeta_s\Gamma_n(x_s)}\right)\left(\frac{(n^2+n)\left[1-\beta_s\zeta_s(1-\mathrm{i}x_s)\right]-x'^2_s/2+2\tan\alpha_n(x'_c)}{\tan\alpha_n(x'_c)+1-\beta_s\zeta_s\Gamma_n(x_s)}\right)\right\}\\ &\times\left\{\left(\frac{(n^2+n)\left[1-\beta_s\zeta_s(1-\mathrm{i}x_s)\right]-x'^2_s/2+2\tan\alpha_n(x'_c)}{\tan\alpha_n(x'_c)+1-\beta_s\zeta_s\Gamma_n(x_s)}\right.\right.\\ &\left.\left.-(n^2+n)\frac{R(x'_s)+\beta_s\zeta_s(1-\mathrm{i}x_s)}{Q(x'_s)+\beta\zeta\Gamma_n(x_s)}\right)\right\}^{-1}\end{aligned} \tag{3.61}$$

with

$$\beta_s = \mathrm{i}\omega\eta/\mu' = \left(\rho x'^2_s\right)/\left(\rho' x^2_s\right) \tag{3.62}$$

$$\zeta_s^{-1} = 1+\mathrm{i}x_s \tag{3.63}$$

$$P(x'_s) = \left[1-\tan\alpha_n(x'_s)\right]^{-1} \tag{3.64}$$

$$Q(x'_s) = P(x'_s)\left[\tan\alpha_n(x'_s)+(n^2+n-1)-x'_s/2\right] \tag{3.65}$$

$$R(x'_s) = P(x'_s)\left[\tan\alpha_n(x'_s)+1\right] \tag{3.66}$$

$$\Gamma_n(x_s) = (n^2+n-1-x_s/2-\mathrm{i}x_s) \tag{3.67}$$

$$b_s = \rho x'^2_s/2\rho' + \beta_s(n^2+n)[1+\zeta_s(1-\mathrm{i}x_s)] \tag{3.68}$$

The $\tan\Psi_n$ are the analog of the $\tan\Phi_n$ discussed in Section 2.5, but include the effects of viscosity. In the inviscid limit they become identical, i.e.

$$\lim_{\eta\to 0}\tan\Psi_n(x', x'_s, x_s) = \tan\Phi_n(x', x'_s) \tag{3.69}$$

As with the AH model, the total attenuation coefficient is given by (c.f. Equation 3.46, neglecting thermal absorption);

$$\alpha_v+\alpha_s = \left(10\log\mathrm{e}^2\right)\left\{-\frac{3\epsilon}{2k_c^2a^3}\sum_{n=0}^{\infty}(2n+1)\Re(A_n)\right\} \tag{3.70}$$

whilst the scattering and viscous absorption components respectively are given by [26]

$$\alpha_s = \left(10\log\mathrm{e}^2\right)\left\{\frac{3\epsilon}{2k_c^2a^3}\sum_{n=0}^{\infty}(2n+1)|A_n|^2\right\} \tag{3.71}$$

$$\alpha_v = \left(10\log\mathrm{e}^2\right)\left\{-\frac{3\epsilon}{2k_c^2a^3}\sum_{n=0}^{\infty}(2n+1)\left[|A_n|^2+\Re(A_n)\right]\right\} \tag{3.72}$$

3.5 Numerical methods

The AH model for scattering of plane waves from a thermally conducting, elastic sphere in a thermally conducting viscous fluid has been implemented in Fortran. The six simultaneous equations derived from the boundary conditions (Equations 3.40 to 3.45) are formulated as a matrix equation, and the complex spherical Bessel and Hankel functions $j_n(z_1)$ and $h_n^{(1)}(z_1)$ are evaluated from their cylindrical counterparts $J_\nu(z_1)$ and $H_\nu^{(1)}(z_1)$ using the defining expressions [30]

$$j_n(z_1) = \sqrt{\frac{\pi}{2z_1}} J_{n+1/2}(z_1) \tag{3.73}$$

and

$$h_n^{(m)}(z_1) = \sqrt{\frac{\pi}{2z_1}} H_{n+1/2}^{(m)}(z_1) \qquad (m = 1, 2) \tag{3.74}$$

Note that for $n = 0$ Equations 3.41 and 3.45 are not valid and the problem reduces to four simultaneous equations. Similarly the terms in C_n vanish because of the factor $n(n+1)$. Physically this is to be expected because the transverse waves should not enter into the problem for the spherically symmetric $n = 0$ mode.

The Bessel and Hankel functions of complex argument and non-integer order are evaluated in double precision using standard subroutines[2] from the Numerical Algorithms Group (NAG) Fortran subroutine library.

The first and second derivatives of the spherical Bessel and Hankel functions are calculated using the following expressions [30]

$$f_n'(z_1) = \frac{n}{z_1} f_n(z_1) - f_{n+1}(z_1) \tag{3.75}$$

and

$$f_n'' = \frac{n(n-1)}{z_1^2} f_n(z_1) - \frac{2n+1}{z_1} f_{n+1}(z_1) + f_{n+2}(z_1) \tag{3.76}$$

where $f_n(z_1)$ may be $j_n(z_1)$ or $h_n^m(z_1)$.

As a check on the accuracy of the spherical Bessel and Hankel functions and their first and second derivatives the Wronskian determinants are calculated and compared with their expected values. The Wronskian determinant for $j_n(z_1)$ and $h_n(z_1)$ and their first derivatives is given by [30]

$$\begin{vmatrix} j_n(z_1) & j_n'(z_1) \\ h_n^{(1)}(z_1) & h_n^{(1)\prime}(z_1) \end{vmatrix} = \frac{\mathrm{i}}{z_1^2} \tag{3.77}$$

The Wronskian determinant for the second derivatives may be obtained analytically from the sine and cosine representations of the zero order spherical Bessel and Hankel functions, i.e.,

[2] Subroutines S17DEF and S17DLF.

$$j_0(z_1) = \frac{\sin z_1}{z_1} \tag{3.78}$$

and

$$h_0^{(1)}(z_1) = \frac{\sin z_1}{z_1} - \frac{\mathrm{i}\cos z_1}{z_1} \tag{3.79}$$

Differentiating these twice and evaluating the determinant yields

$$\begin{vmatrix} j_n(z_1) & j_n''(z_1) \\ h_n^{(1)}(z_1) & h_n^{(1)\prime\prime}(z_1) \end{vmatrix} = \frac{-2\mathrm{i}}{z_1^3} \tag{3.80}$$

The complex double precision matrix equation which is formed from the six simultaneous equations derived from the boundary conditions is solved to give the values of the unknown coefficients using a standard NAG routine[3], after having first been LU factorized by another NAG routine[4]. The process of LU factorization is a numerical technique to facilitate the solution of the matrix equation. The matrix is factorized into a lower triangular matrix, an upper triangular matrix and a diagonal matrix.

Thermal dissipation can be turned off in the model by dropping the boundary conditions on temperature and heat flux, and solving the remaining four simultaneous equations.

There are a number of difficulties associated with the numerical solution of the AH equations:

- There are typographic errors in the papers
- Very large amplitudes may arise in the Bessel and Hankel functions
- The matrix is ill-conditioned

Whilst the implementation of the AH model described above generally yields a good solution over the parameter range considered, some numerical artefacts were observed due to these issues. Other researchers have spent many years addressing these problems and it was therefore felt pragmatic to use one of the well developed and tested models.

3.6 Other models

In Chapter 2 a method was described for deriving the visco-inertial absorption coefficient, based on simple energy balancing arguments. Also described was a partial wave expansion for computing the attenuation due to scattering and a simple heuristic approximation to this. In this chapter a model for attenuation by a thermally-conducting, elastic sphere suspended in a thermally-conducting, viscous fluid was described. Chapter 5 will discuss the derivation of a wave equation for propagation in suspensions, using an approach similar to that employed in Chapter 2.

Other researchers have adopted different theoretical approaches to the problem and those of note are simply mentioned here for completeness.

[3] F07ASF
[4] F07ARF

Temkin and Dobbins [31] describe the viscous and thermal losses in terms of relaxation phenomena, using equations which take the same form as the equations for molecular relaxation due to a sound wave.

Morfey [32] extended Temkin & Dobbins' analysis to include compressible particles (or bubbles). This leads to an additional relaxation mechanism in which pulsations of the suspended particles are resisted by the shear viscosity of the surrounding fluid.

There exists a category of model collectively known as coupled phase models. These, in common with the wave equation approach discussed in Chapter 5, are continuum models. They are based on the same set of equations as the scattering models i.e. the conservation equations and equations of state. These are then 'coupled' via a momentum transfer term in the momentum equations and a heat transfer term in the energy equation. The fact that the two phases occupy the same volume of space is accounted for by means of volume averaged variables, which has the effect of coupling the continuity equations. Coupled phase theories fall into two categories. The first [33, 34] assumes an incompressible particular phase and allows for heat transfer between the phases. The second [35–37] allows for a compressible particulate phase but neglects heat transfer. A coupled phase theory which accounts for both a compressible particulate phase and heat transfer has also now been developed [38].

Several other researchers have published treatments which are derivatives or special cases of theories which are covered elsewhere in this thesis or mentioned above and these are not discussed further.

The model which contains the fewest number of assumptions and approximations is the Allegra and Hawley model discussed in this chapter. Therefore this model has been chosen as the benchmark against which to compare the predictions of the models discussed in Chapter 2.

3.7 Summary and conclusions

In this chapter a rigorous method was introduced for calculating the attenuation due to scattering and absorption by a suspension of spheres. In this treatment the spheres are elastic and thermally conducting, and are free to move in a viscous and thermally conducting fluid. This approach implicitly includes visco-inertial absorption, thermal absorption and scattering, and represents the benchmark solution to the problem for dilute suspensions of spheres.

In Chapter 4 the predictions of the models presented in Chapter 2 will be compared against the results of the treatment discussed in this chapter. Chapter 4 then goes on to use the models to calculate the magnitude of the effects under investigation and to study the importance of the relevant physical parameters.

Chapter 4

Model results

Pluralitas non est ponenda sine neccesitate.
William of Ockham (ca. 1285-1349)

Physics should be made as simple as possible, but not simpler.
Albert Einstein (1879-1955)

4.1 Results

4.1.1 Introduction

In this chapter results from the models described in Chapters 2 and 3 will be presented and compared. These results will show how the scattering and absorption models discussed in Chapter 2 compare to the benchmark model discussed in Chapter 3 over the parameter range of interest. Further results will be presented to show how the magnitude of the absorption varies with the key parameters.

4.1.2 Comparison of models

Figure 4.1 shows the results of calculating the attenuation for a suspension of quartz-like spheres in pure water using the AH model presented in Section 3.2 and the explicit models for absorption and scattering presented in Sections 2.4 and 2.5. Thermal absorption was included in the AH calculation, but no explicit model for thermal absorption has been included. The figure shows results for calculations at frequencies of 1 MHz and 100 kHz and the attenuation has been normalized with respect to mass concentration of the suspended material. The attenuation in dBm^{-1} can thus be obtained from this plot by reading the normalized attenuation off the vertical axis and multiplying by the sediment concentration in kgm^{-3}. The results from the AH model presented in Figures 4.1 and 4.2 were calculated for the author by Dr. Andrew Holmes of Nottingham University [39]

As can be seen from the figure, there is excellent agreement between the models, with the two curves at each frequency overlaying almost exactly. It will be noted however that in the 1 MHz

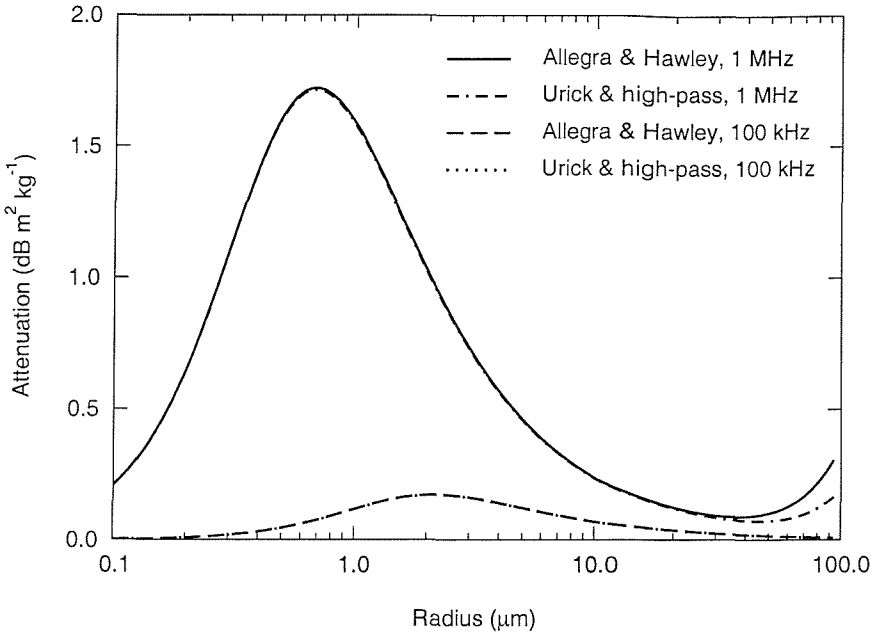

Figure 4.1. Comparison of attenuation calculations for a suspension of quartz-like spheres using the AH model and the explicit models.

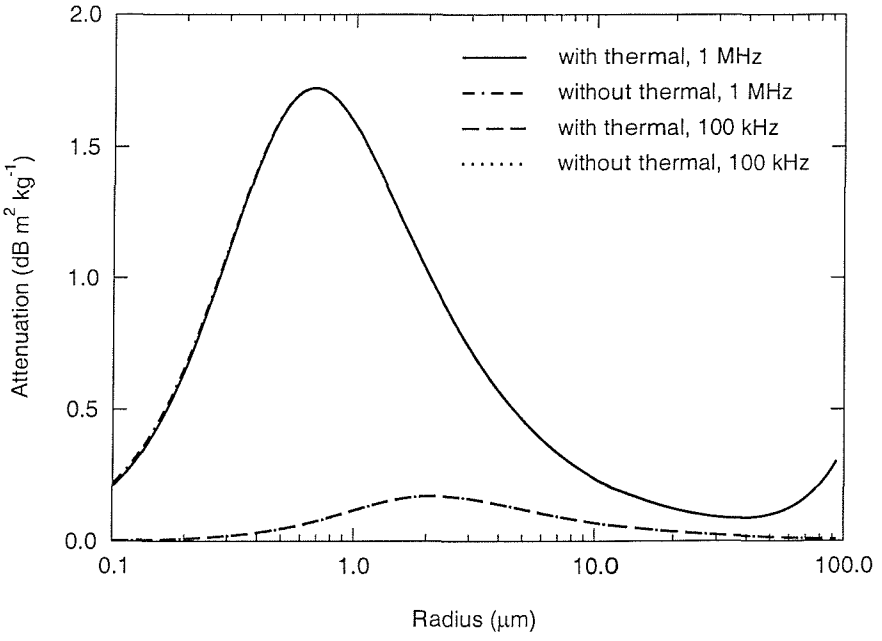

Figure 4.2. Calculated attenuation for a suspension of quartz-like spheres, with and without thermal losses.

case the two models begin to depart at the upper end of the particle size range. This is where scattering begins to be important and there is some disagreement between the AH model and the high-pass model in this area. This region is characterized by intermediate values of ka and agreement between the models could be improved by adjusting the value of ξ in the high-pass model. In this calculation the default value of $\xi = 1$ has been used.

Figure 4.2 shows the effect of thermal losses at 1 MHz and 100 kHz for quartz-like spheres suspended in water. The figure shows the results of running the AH model twice, once with thermal effects included and once without. Again the curves at each frequency overlay each other almost exactly indicating that thermal losses are negligible in these cases.

These two figures clearly demonstrate that the magnitude of the thermal absorption is very much smaller than the magnitude of the visco-inertial absorption for quartz-like particles suspended in water. The thermal effects can therefore be ignored for quartz-like particles suspended in water, as suggested by the good agreement between the non-thermal AH calculation and the Urick calculation shown in Figure 4.1.

For other materials, however, the thermal effects may be more significant and may even be the dominant absorption mechanism, as is the case for polystyrene spheres suspended in water [26]. The important factor in determining the thermal losses is the difference in the ratio $\beta/(\rho C_p)$ for the solid and suspending fluid. The absorption depends upon the square of this difference [26] which is an order of magnitude greater for polystyrene in water than for quartz in water. Additionally, the density of polystyrene is close to that of water, so the visco-inertial contribution is very much smaller for polystyrene than for quartz. Whilst polystyrene is clearly not relevant to the present study, it is likely that organic material might have a density close to that of water, and the thermal properties might be such that thermal effects become important. Where there is a large density contrast between phases, as for mineral particles suspended in water, the visco-inertial term is dominant.

These results demonstrate that Urick's equation for visco-inertial absorption agrees well with the more complete AH model over the parameter range of interest, and the simpler model will therefore be used in the remainder of this thesis.

4.1.3 Attenuation calculations

The results presented in this section were calculated using Urick's equation for visco-inertial absorption (Equation 2.31) and the high pass model for scattering (Equation 2.45).

Except where otherwise stated, the physical parameters of the sediment material and the suspending fluid are as shown in Table 4.1. These parameters are representative of quartz particles suspended in seawater [40]. Quartz has been used as a generic mineral material for the purposes of example calculations throughout much of this thesis.

	Density, ρ $\mathrm{kgm^{-3}}$	Compressibility, κ $\mathrm{Pa^{-1}}$	Kinematic viscosity, ν $\mathrm{m^2s^{-1}}$
solid	2600	2.71×10^{-11}	—
fluid	1028	4.31×10^{-10}	1.478×10^{-6}

Table 4.1. Physical parameters of sediment particles and ambient fluid [40].

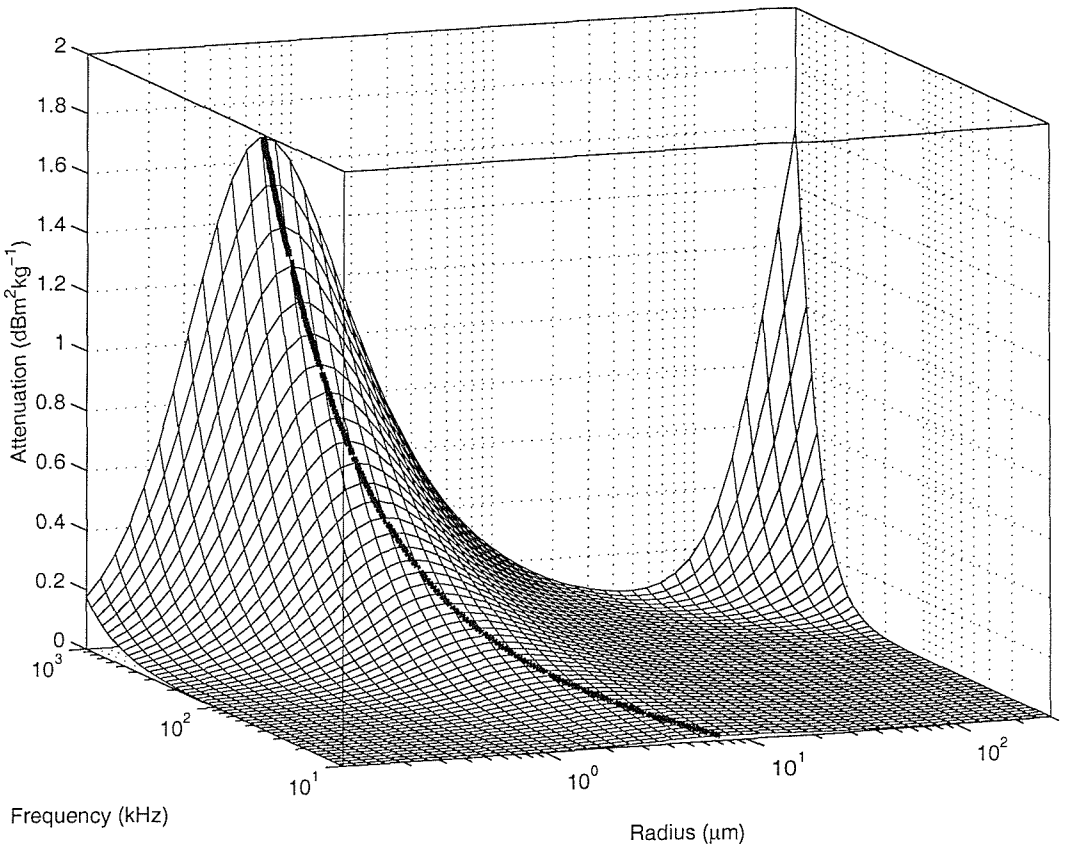

Figure 4.3. Calculated attenuation coefficient for quartz particles suspended in seawater.

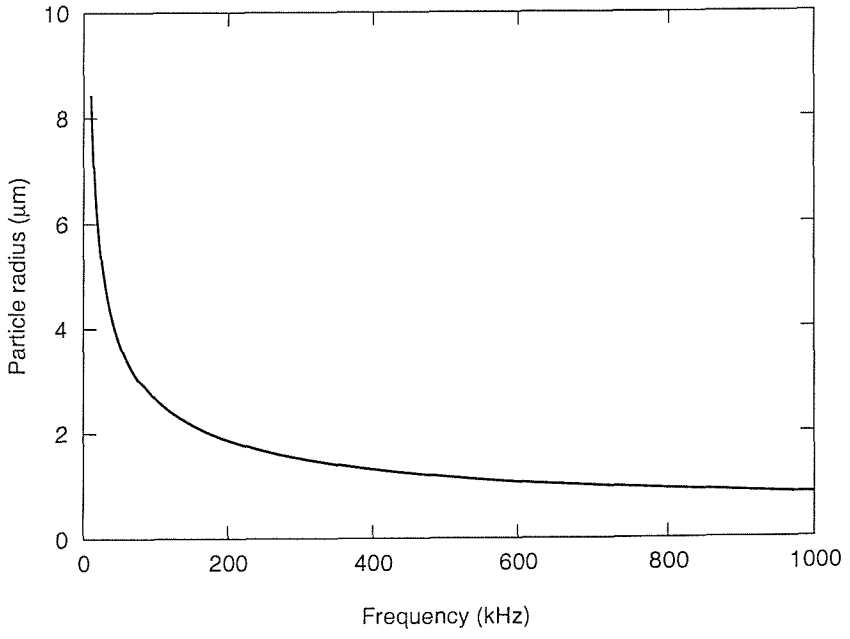

Figure 4.4. Locus of viscous absorption peak in the frequency-size domain for quartz particles suspended in seawater.

Figure 4.3 shows the calculated attenuation as a function of frequency and particle radius for a suspension of quartz particles in seawater.

The peak in the high frequency and large particle size region of Figure 4.3 is the contribution due to scattering, which becomes important in this region of parameter space due to the increase in the scattering parameter, ka.

The peak in the high frequency and small particle size region of Figure 4.3 is the peak due to the visco-inertial absorption contribution, which achieves a maximum as a result of the relative effects of particle mass and surface area. This peak moves to larger particle sizes as the acoustic frequency is reduced. This behaviour is shown by the bold curve on the plot, which is the locus of the visco-inertial absorption peak. The locus of the peak in the frequency-size domain is shown in Figure 4.4.

4.1.4 Comparison with clear water attenuation

Figure 4.5 shows the total attenuation due to seawater and suspended sediment. The attenuation due to the suspended sediment was calculated using Equations 2.31 and 2.45, assuming quartz particles of radius 3 μm and a concentration of 0.2 kgm^{-3}. The particle size was chosen to be 3 μm as this gives the largest attenuation at 100 kHz (see Figure 4.4), a frequency in the range of interest for high frequency sonar applications. The contribution due to the seawater was calculated using the Francois & Garrison expression (Equation 2.4), assuming a temperature of 4°C, salinity of 35, pH of 8, and a pressure of 1 atmosphere (i.e. near surface).

The solid bold curve in the figure is the total attenuation for seawater containing the sediment, whilst the lighter solid curve shows the total attenuation for clear seawater. The broken curves are the individual contributions due to particles (scattering and absorption), pure water and the boric acid and magnesium sulphate relaxation processes. From Figure 4.5 it can be seen that in the frequency range of interest (50 kHz – 300 kHz) the total acoustic attenuation coefficient is significantly greater than that due to seawater alone, with the difference being approximately 0.03 dBm^{-1} at 100 kHz. This means, for example, that for a total propagation path length of 200 m, the additional attenuation due to the presence of a suspension of 3 μm quartz particles with a concentration of 0.2 kgm^{-3} would be 6 dB for a sonar system operating at 100 kHz. This corresponds to reducing the intensity at the receiver by a factor of 4, and is thus significant.

Figure 4.5 also demonstrates that the total attenuation approaches the pure water attenuation asymptotically at very high frequencies ($f > 1$ MHz), and at very low frequencies ($f < 100$ Hz) the boric acid relaxation is the dominant process.

4.1.5 Effect of particle size distributions

The results presented thus far have all been obtained assuming that all particles in the suspension have the same radius (i.e. a monodisperse suspension). However, in the natural environment we know that there will be some distribution of particle sizes. It is therefore useful to investigate the effects that such distributions would have on the acoustic losses.

In-situ measurements of suspended particle size distributions in estuaries [41] have shown that such distributions often follow a log-normal curve, sometimes with a 'tail' of fine particles. Figure 4.6 shows log-normal distributions with and without this tail, where both distributions

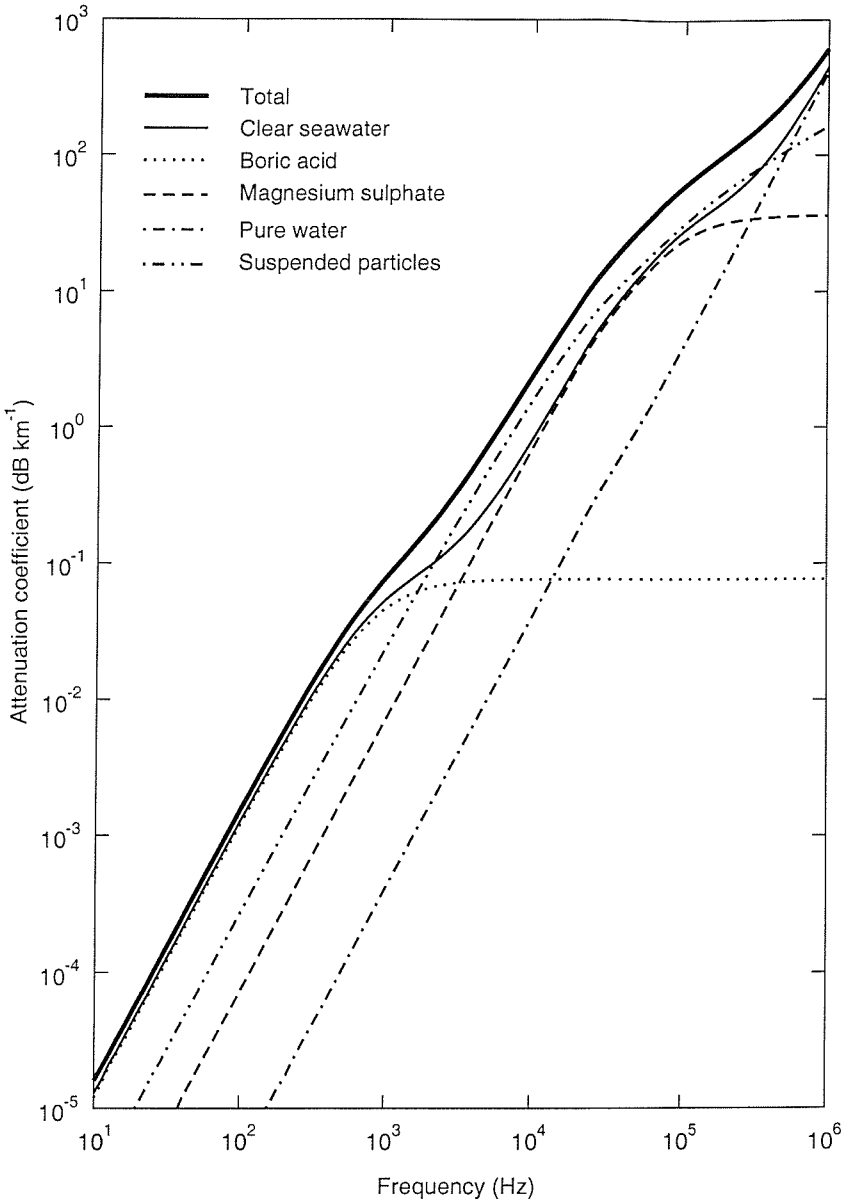

Figure 4.5. Attenuation coefficient for seawater containing suspended quartz particles, using Equations 2.31 and 2.45 with the solid parameters given in Table 4.1, and Equation 2.4 with $\Theta = 4°\text{C}$, $S = 35$, $p = 1$ atm, and a pH of 8.

have the same total concentrations of 0.2 kgm^{-3}.

The simplest method of calculating the attenuation arising from a distribution of particle sizes is to integrate over a series of single-size calculations of the form presented above, using a series of particle sizes and concentrations to represent the complete distribution. Figures 4.7 and 4.8 show the results of such a calculation for the distributions shown in Figure 4.6. In these calculations the particle size distributions have been represented by 100 regularly spaced bins.

Figure 4.7 shows the attenuation due to the distributions shown in Figure 4.6. The solid line here refers to the attenuation due to the log-normal distribution, and the dashed line refers to the distribution with a tail of fine particles, consistent with the notation of Figure 4.6. The dotted

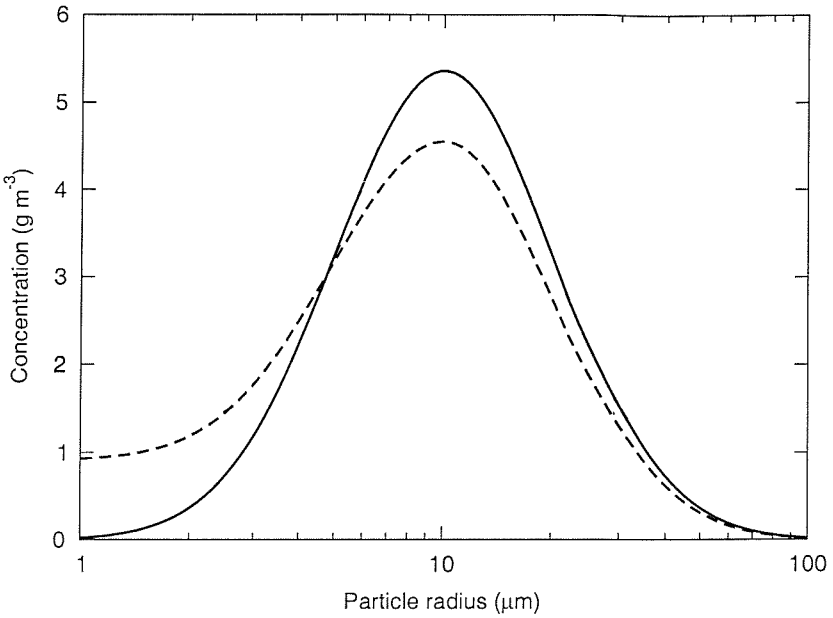

Figure 4.6. Typical idealized particle size distributions.

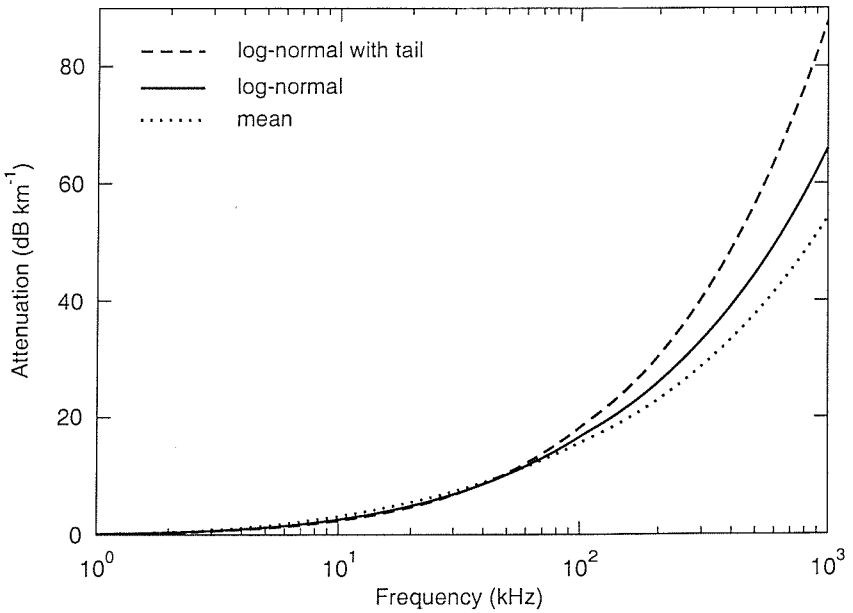

Figure 4.7. Attenuation due to the particle size distributions of Figure 4.6, calculated using Equations 2.31 and 2.45.

line represents the calculated attenuation for a suspension of particles which all have the same radius of 10 μm.

Figure 4.8 shows the *difference* between the calculated attenuation coefficients due to the distributions shown in Figure 4.6, and the attenuation coefficient calculated for a single mean particle size of 10 μm.

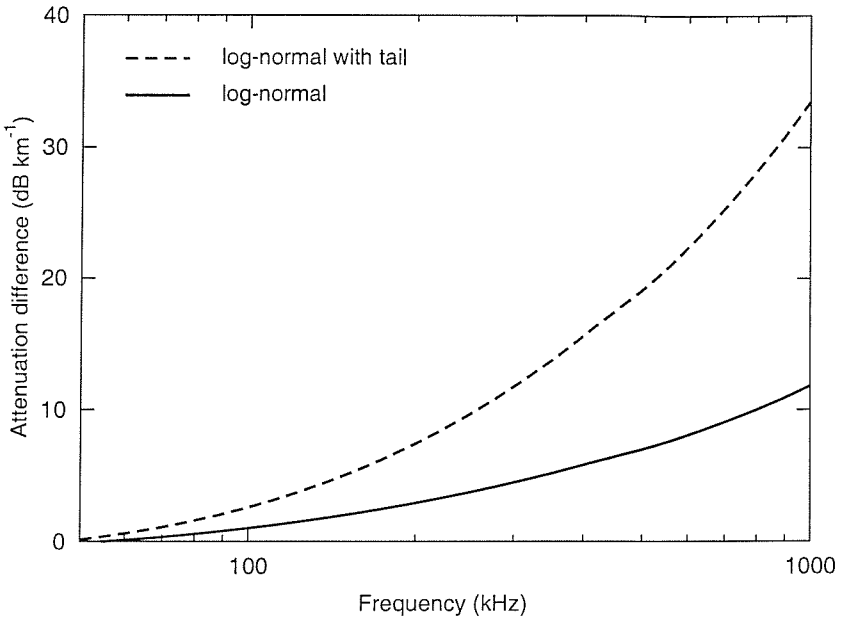

Figure 4.8. Difference in attenuation due particle size distributions of Figure 4.6 and single mean particle size of 10 μm.

The results shown in Figure 4.8 clearly demonstrate that for the case considered here, performing the attenuation calculations for just the mean particle size would significantly underestimate the actual attenuation due to the full distribution. Similarly, the tail of fine particles contributes significantly to the attenuation coefficient.

Let us now apply these results to the prediction of the performance of an active sonar operating at 300 kHz, for a target at range 250 m, corresponding to a total straight-line propagation path of 500 m. If the real suspended sediment particle size distribution was given by the log-normal distribution with a tail of fine particles shown in Figure 4.6, then assuming the log-normal distribution would underestimate the propagation loss by 3.75 dB, and assuming all particles had the same radius of 10 μm would underestimate the loss by 6 dB, a factor of 4 in intensity.

It should also be realized that, in some circumstances, assumption of a single mean particle size could lead to an overestimate of the attenuation. For example, if the attenuation was calculated for a particle radius lying on the peak of the viscous absorption curve in Figure 4.3 at some frequency, then some distribution centred on this mean (or modal) particle size would give a lower attenuation for the same total concentration.

It is instructive to perform a check on whether a sufficiently large number of bins was used to represent the distributions in these calculations. Figure 4.9 shows the peak error in the calculation of attenuation due to the log-normal distribution of Figure 4.6 as a function of the number of bins. The error here is defined as being the difference between the attenuation

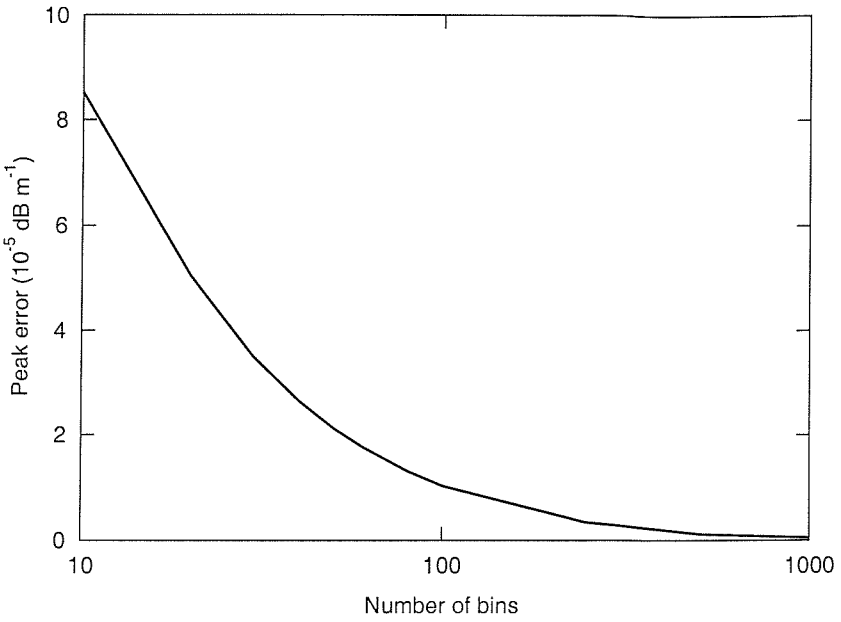

Figure 4.9. Peak error in the calculated attenuation as a function of the number of bins used to represent the size distribution.

calculated with a given number of bins and that calculated with 1000 bins. As expected, the error approaches zero as the number of bins becomes large. With 100 bins used to represent the distribution the peak error is about 10^{-5} dBm^{-1}, as compared with a maximum attenuation of about 0.066 dBm^{-1} (Figure 4.7). This represents a fractional error of only 0.015%, suggesting that, in this case, the distribution could have been represented by far fewer than 100 bins. However, since the computational requirement for these calculations is fairly trivial 100 bins were retained.

4.1.6 Effect of particle density

In addition to considering the effects of particle size distributions on the attenuation, it is also interesting to look at the nature of the particles themselves. In the natural environment, particularly in estuaries where fresh water flows into more saline water, small clay or mineral particles have a tendency to flocculate as a result of biogeochemical processes. Development of a rigorous mathematical treatment of the absorption and scattering by such flocs is a complex problem, and even an approximate method for dealing with them will require much further work (absorption by simple non-spherical bodies is discussed in Section 5.4). However, since we know that the average density of a floc must be lower than that of the homogeneous particles considered so far, it may be useful to investigate the effects of particle density on the attenuation coefficient.

Figure 4.10 shows the calculated attenuation coefficient as a function of particle radius, at a frequency of 200 kHz, for three different particle densities. This shows that reducing the density reduces the attenuation. This is the expected result because as the density of the particle approaches the density of the ambient fluid, the difference between the inertia of the particles and that of the fluid decreases, and the velocity difference between the particles and fluid, from which the viscous absorption arises, therefore decreases. The figure also shows that the

absorption peak moves to larger particles as the density is reduced. This may be explained by the fact that for a particle of a given mass (and thus inertia), the lower the density the larger the particle must be. The scattering term is not apparent in Figure 4.10 because for the range of particle sizes plotted scattering is negligible at 200 kHz.

Figure 4.11 presents the effects of particle density in an alternative way. This figure shows the calculated attenuation as a function of particle density for three different particle sizes and two different frequencies.

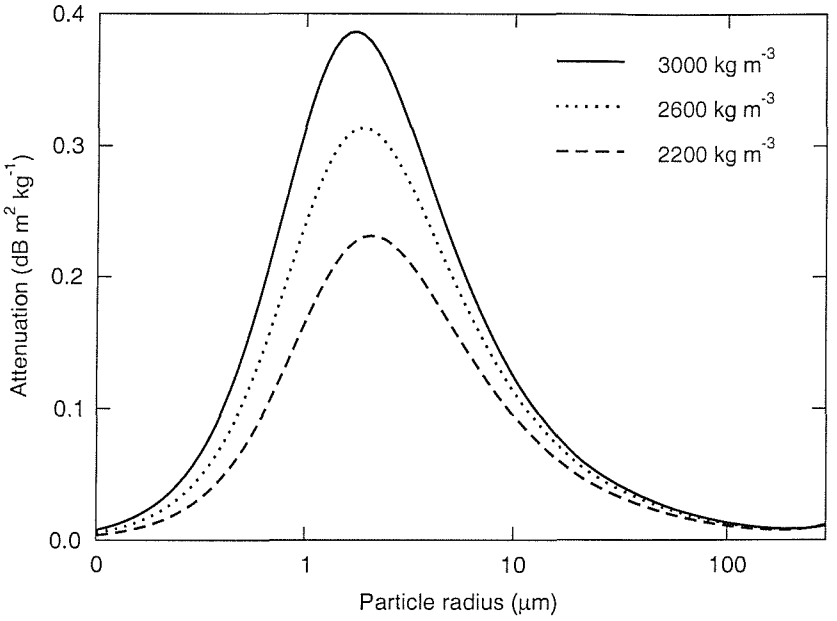

Figure 4.10. Effect of particle density on attenuation.

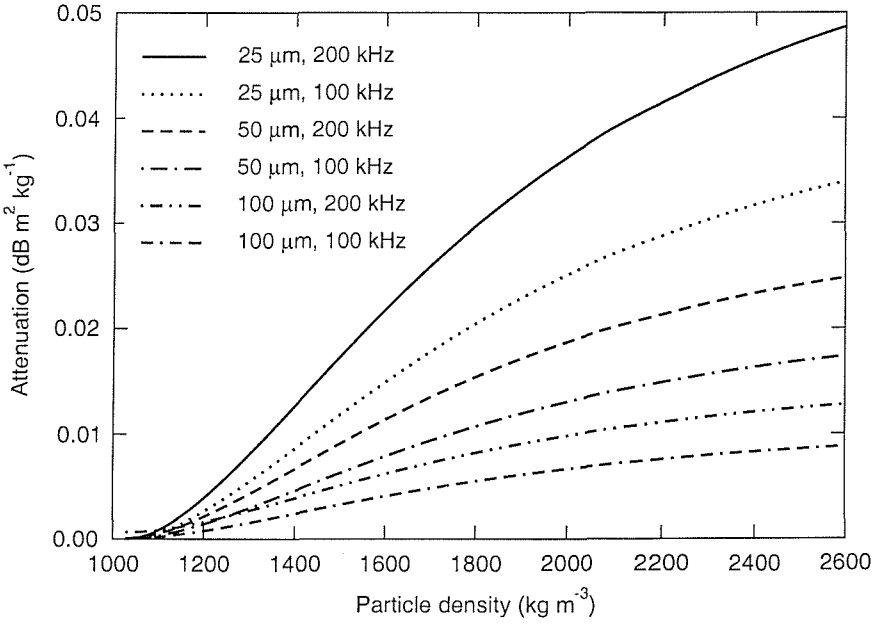

Figure 4.11. Attenuation as a function of particle density for three particle sizes at 100 kHz and 200 kHz.

4.1.7 Effect of sediment concentration

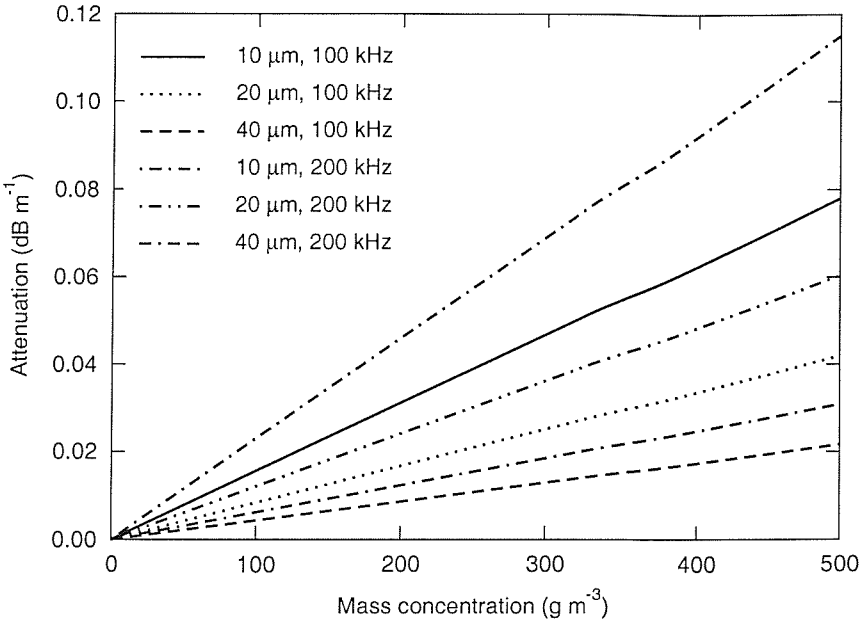

Figure 4.12. Attenuation as a function of mass concentration for three particle sizes at 100 kHz and 200 kHz.

Figure 4.12 shows the calculated attenuation as a function of sediment mass concentration for three different particle sizes and two different frequencies. The linear dependence on concentration is an assumption of the models, as discussed in Chapter 2. It was demonstrated there that this assumption, which implies that interparticle effects may be neglected, is valid for all concentrations and parameter ranges considered here.

4.2 Summary and conclusions

In this chapter results are presented from the models of ultrasonic absorption discussed in Chapters 2 and 3.

It was realized that the assumption of an inviscid fluid in the scattering models was inconsistent with the viscous absorption model. In order to address this issue and provide some validation of the independent models for absorption and scattering the AH model was employed. This model, which was described in Chapter 3, includes the effects of scattering, viscous absorption and thermal absorption which was not considered in the simple models at all. The results of the AH model were compared with the predictions of the simpler models, and found to be in very good agreement over the parameter range of interest. It was also shown that the thermal absorption contribution was not significant for the cases considered.

The generally good agreement between the AH model and Equations 2.31 and 2.45, over the parameter ranges considered in this thesis, led to the use of the Urick model for viscous absorption combined with the high pass model for scattering for the parameter sensitivity study presented in this chapter and the remainder of the thesis.

The results presented demonstrate that the attenuation coefficient of seawater, at frequencies in the range tens to hundreds of kHz, may be significantly increased by a suspension of mineral particles at concentrations typically observed in turbid coastal environments. The effect of distributions of particle sizes was investigated by integrating the attenuation calculations over the size distribution. In this way it was demonstrated that significant errors in the estimation of the attenuation coefficient could result if calculations were carried out using a mean or modal particle size, as opposed to taking the full distribution into account.

It was found that, over the parameter range of interest to the present study, viscous absorption is the dominant attenuation mechanism associated with the presence of suspended particles. Since the density of the particles is a key parameter governing this phenomenon, the sensitivity of the attenuation to density was investigated, the results showing how the attenuation depends on density.

Finally, although a linear dependence on suspension concentration is implicit in the models used, the attenuation as a function of concentration for two frequencies and three particle sizes was presented.

In addition to the additional attenuation discussed theoretically in Chapters 2 and 3, and investigated numerically in this chapter, suspended particles may also modify the sound speed. The next chapter discusses the calculation of sound speed in suspensions, and describes a model based on the formulation of the wave equation for sound propagation in suspensions. This formulation also yields the attenuation in such a way as to facilitate the treatment of non-spherical particles. This will also be discussed in the next chapter.

Chapter 5

The wave equation, complex wavenumber and non-spherical particles

5.1 Introduction

In this chapter the wave equation for sound propagation in dilute suspensions is introduced. This formulation allows the phase speed to be inferred from the wavenumber and, since the wavenumber is complex, the attenuation may also be obtained.

In addition to increasing the attenuation, the presence of suspended mineral particles may also affect the sound speed in suspensions.

It might be expected that estimates of the sound speed in a suspension may be obtained by simply considering that a fraction of the volume of the water has been replaced with solid particles with a higher bulk modulus and density. It is shown in this chapter that this bulk averaging approach does not always predict the correct sound speed, and a different technique must be employed.

Using simple considerations of mass and momentum balances on a sufficiently small, homogeneous and compressible volume element of a suspension, Ahuja [42, 43] has formulated a wave equation for the propagation of sound in suspensions or emulsions. This approach has been used here to calculate the sound speed in aqueous suspensions, and the main elements of his derivation are reproduced in Section 5.3.2. This approach is generic to both suspensions and emulsions in that the suspended particles are assumed to be spheres of viscous fluid. Rigid particles are accounted for by employing a very large viscosity.

In addition to the sound speed the formulation of the wave equation for sound propagation through suspensions yields the attenuation coefficient through the the complex wavenumber. It will be shown that the visco-inertial absorption derived in this way is equivalent to the expression due to Urick (Equation 2.31) presented in Chapter 2. The wave equation formulation facilitates the task of considering attenuation by non-spherical particles by employing correct expressions for the drag force acting on non-spherical bodies. This approach will be used to model the attenuation due to suspensions of oblate and prolate spheroids.

5.2 Speed of sound - bulk averaging approach

The speed of sound in a fluid is given by

$$c = \sqrt{\frac{B}{\rho}} \tag{5.1}$$

where ρ is the ambient density of the fluid and B is the bulk modulus, defined as the fractional volume change $\mathrm{d}V$ resulting from a pressure change $\mathrm{d}p$, i.e.

$$B = -V\frac{\mathrm{d}p}{\mathrm{d}V} \tag{5.2}$$

From Equations 5.1 and 5.2 we have

$$\frac{\mathrm{d}V}{V} = -\frac{\mathrm{d}p}{c^2\rho} \tag{5.3}$$

So, for a pressure increase of Δp the volume change is given by

$$\Delta V = -\frac{V\Delta p}{c^2\rho} \tag{5.4}$$

In an aqueous suspension consisting of a volume V of water of density ρ with sound speed c and a volume V' of solid particles of density ρ' with sound speed c' the volume changes of the water and solid components resulting from a pressure increase of Δp are therefore given by

$$\Delta V = -\frac{V\Delta p}{c^2\rho} \tag{5.5}$$

and

$$\Delta V' = -\frac{V'\Delta p}{c'^2\rho'} \tag{5.6}$$

The total change in the volume of the suspension is then $\Delta V_{\mathrm{tot}} = \Delta V + \Delta V'$, and from Equation 5.2 the effective bulk modulus of the suspension is given by

$$B_{\mathrm{s}} = -V_{\mathrm{tot}}\frac{\Delta p}{\Delta V_{\mathrm{tot}}} = -(V+V')\frac{\Delta p}{\Delta V + \Delta V'} \tag{5.7}$$

Substituting for ΔV and $\Delta V'$ yields

$$B_{\mathrm{s}} = (V+V')\frac{\Delta p}{\left(\frac{V\Delta p}{c^2\rho}\right) + \left(\frac{V'\Delta p}{c'^2\rho'}\right)} \tag{5.8}$$

Rearranging, we have

$$B_s = \left[\left(\frac{V}{V+V'}\right)\left(\frac{1}{c^2\rho}\right) + \left(\frac{V'}{V+V'}\right)\left(\frac{1}{c'^2\rho'}\right)\right]^{-1} \tag{5.9}$$

This may be rewritten in terms of the volume fraction, ϵ, recognizing that

$$\epsilon = \frac{V'}{V+V'} \qquad \text{and} \qquad 1-\epsilon = \frac{V}{V+V'} \tag{5.10}$$

i.e.

$$B_s = \left[\left(\frac{1-\epsilon}{c^2\rho}\right) + \left(\frac{\epsilon}{c'^2\rho'}\right)\right]^{-1} \tag{5.11}$$

Now, turning to the density, the average bulk density of the suspension may be written

$$\rho_s = \frac{\rho V + \rho' V'}{V+V'} \tag{5.12}$$

Again, writing in terms of ϵ, we have

$$\rho_s = (1-\epsilon)\rho + \epsilon\rho' \tag{5.13}$$

Finally, from Equation 5.1, the sound speed in the suspension is given by

$$c_s = \sqrt{\frac{B_s}{\rho_s}} \tag{5.14}$$

5.3 Formulation of the wave equation

The propagation speed for compression waves travelling through a suspension can be obtained, together with the attenuation coefficient, by formulating the wave equation for propagation through the medium. This was done by Ahuja [43], and his formulation is used here.

5.3.1 Equation of motion

The passage of an acoustic plane wave through a suspension or an emulsion causes the suspended particles to pulsate and oscillate. Assume that the acoustic wavelength is large compared to the particle radius ($k_c a \ll 1$) and consider the region of fluid in the vicinity of the particle ($k_c r \ll 1$). Under these conditions it may be shown [44] that, to second order in $k_c a$, the acoustic wave equation reduces to $\nabla^2 p = 0$. This is Laplace's equation for incompressible potential flow and the fluid in the vicinity of the particle may therefore be considered to be incompressible under the above assumptions. As discussed in Chapter 2, viscous effects are important within the skin depth of the viscous shear waves, δ_v, given by Equation 3.1.

Assuming then that the amplitude of the particle oscillation is very small compared with its size, the linearized Navier-Stokes equations apply for the unsteady incompressible viscous flow in the fluid surrounding the particle. If the molecular viscosity of the particle, η', is at least one order of magnitude greater than that of the surrounding fluid, η, then the linearized Navier-Stokes equation can be applied for the steady, incompressible flow inside the particle.

The pulsations of the particle are neglected and the following boundary conditions at the surface of the particle are employed:

- zero radial velocity inside and outside the particle
- continuity of tangential velocity
- continuity of tangential stress

The complex drag force experienced by a spherical particle of radius a may then be written (c.f. Equation 2.14)

$$F = -\tau m \frac{\mathrm{d}u}{\mathrm{d}t} - sm\omega u \tag{5.15}$$

where u is the instantaneous particle velocity and is defined as $v' - v$, where v' is the velocity of the centre of the particle and v is the velocity of the fluid at the centre of the particle if the particle were absent. The quantity $m = \frac{4}{3}\pi a^3 \rho$ is the mass of ambient fluid displaced by the particle ω is the angular frequency of the acoustic wave and τ and s are given by

$$\tau = \frac{1}{2} + \frac{\delta_\mathrm{v}}{4a}\left\{\frac{(2\eta + 3\eta')^2}{[(\eta + \eta') + a\eta/3\delta_\mathrm{v}]^2 + (a\eta/3\delta_\mathrm{v})^2}\right\} \tag{5.16}$$

$$s = \frac{3}{4}\left\{(2\eta + 3\eta')\left(\frac{\delta_\mathrm{v}}{a}\right)^2 \frac{(1 + a/\delta_\mathrm{v})\left[(\eta + \eta') + a\eta/3\delta_\mathrm{v}\right] + (\eta/3)\,(a/\delta_\mathrm{v})^2}{[(\eta + \eta') + a\eta/3\delta_\mathrm{v}]^2 + (a\eta/3\delta_\mathrm{v})^2}\right\} \tag{5.17}$$

Equation 5.15 is valid for viscous spherical particles with $\eta'/\eta \geq 10$. In the limiting case of rigid particles, $\eta'/\eta \to \infty$, and Equation 5.15 reduces to that derived by Stokes (Equation 2.14).

As discussed in Section 2.4, the first term on the right hand side of Equation 5.15 represents the inertial contribution to the complex drag force, and the second term represents the viscous contribution .

Now, the equation of motion of the sphere oscillating in the sound field is

$$\rho' \frac{\mathrm{d}v'}{\mathrm{d}t} = \rho \frac{\mathrm{d}v}{\mathrm{d}t} + \rho \frac{F}{m} \tag{5.18}$$

which is equivalent to Equation 2.19. Using Equation 5.15 and the relation $u = v' - v$, the equation of motion may be written

$$(\sigma + \tau)\frac{\mathrm{d}v'}{\mathrm{d}t} + s\omega v' = (\tau + 1)\frac{\mathrm{d}v}{\mathrm{d}t} + s\omega v \tag{5.19}$$

where $\sigma = \rho'/\rho$.

Again, it was shown in Section 2.4 that, assuming a sinusoidal time dependence, the equation of motion may be solved to give the instantaneous particle velocity as

$$u = u_0 \mathrm{e}^{\mathrm{i}(\omega t - \varphi)} \tag{5.20}$$

where

$$u_0 = \frac{\sigma - 1}{[s^2 + (\sigma + \tau)^2]^{1/2}} v_0 \tag{5.21}$$

and

$$\tan\varphi = \frac{s}{\sigma + \tau} \tag{5.22}$$

Note that Equations 5.20 to 5.22 are equivalent to Equations 2.21 to 2.23 in Section 2.4.

5.3.2 Formulation of the wave equation - continuum approach

The treatment presented here is based on the analysis of sufficiently small volume elements which may be considered to be homogeneous with respect to the acoustic field. For this to be valid the volume elements must be small compared with the wavelength and large enough to contain many particles.

In order to determine the range of parameters over which this condition is satisfied, consider a cubic volume element with sides equal to one tenth of the acoustic wavelength in water and assume that this volume element must contain at least 100 particles. It is then straightforward to calculate the minimum volume fraction of suspended particles required to meet these criteria as a function of particle radius for different frequencies. Figure 5.1 shows the results of such a calculation for particle radii in the range 1 μm to 100 μm, at 30 kHz, 100 kHz and 300 kHz.

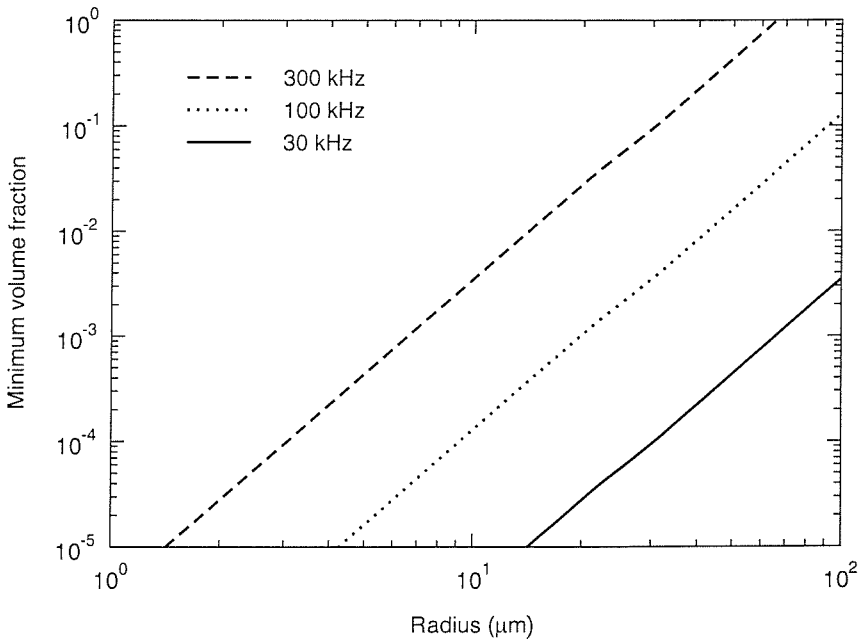

Figure 5.1. Minimum volume fraction necessary to satisfy the homogeneity condition at three frequencies (see text).

This figure clearly shows that, as the particle size increases, greater concentrations are required to satisfy the condition of homogeneity. This is to be expected since, for a given volume fraction, the number of particles in a volume element decreases as the particle size is increased. The figure also shows that, as the frequency is increased (and hence the wavelength is reduced) higher volume fractions are required to meet the homogeneity condition as expected. Numerically it can be seen that, at 100 kHz, the homogeneity condition is only satisfied for volume fractions ϵ greater than

about $\epsilon = 10^{-4}$ for particles smaller than about 10 μm, and that at lower concentrations or with larger particles the condition is not satisfied according to the criteria specified above. Of course, in practice there will not be a sharp cut-off delimiting regions of parameter space for which the present treatment does or does not apply, and it may be expected that the formulism will give reasonable predictions for slightly lower concentrations and larger particles.

Assuming then that the above condition is satisfied or nearly satisfied, a volume element of the suspension may be replaced, in the first approximation, by a homogeneous and continuous fluid of temporally and spatially independent volume-averaged bulk density given by

$$\rho_{\mathrm{v}} = (1 - \epsilon)\rho + \epsilon\rho' \tag{5.23}$$

and volume-averaged bulk compressibility given by

$$\kappa_{\mathrm{v}} = (1 - \epsilon)\kappa + \epsilon\kappa' \tag{5.24}$$

Now consider an acoustic plane wave propagating in the positive z-direction and consider a volume $\mathrm{d}z$ of the suspension, containing many particles, bounded by unit areas of the planes $z = z_0$ and $z = z_0 + \mathrm{d}z$ and the planes perpendicular to these. As described above, the suspension in this volume element is replaced with a homogeneous and continuous fluid. Now, in response to the passage of the acoustic disturbance the density, pressure and temperature of the fluid undergo fluctuations as functions of both z and time, t. It is assumed that these fluctuations are small with respect to the equilibrium values of the quantities involved.

In a thermally non-conducting medium the acoustic compressions are adiabatic and the pressure and density fluctuations are in phase. In this case the density fluctuation, $\Delta\rho$ satisfies

$$\Delta\rho = \rho\kappa p \tag{5.25}$$

where p is the acoustic pressure.

If there is a contrast between the thermodynamic properties of the suspended particles and the suspending fluid then their temperature fluctuations will be different, as discussed in Chapter 3. This leads to a temperature gradient in a boundary layer surrounding the particle, with a thermal skin depth of

$$\delta_{\mathrm{t}} = \sqrt{\frac{2K}{\rho C_{\mathrm{p}}\omega}} \tag{5.26}$$

(see Equations 3.1 and 3.2), where K is the thermal conductivity of the suspending fluid and C_{p} is the specific heat capacity at constant pressure. Since thermal energy can flow between the suspension components there is a net flow of energy from the acoustic field into heat (dissipation) and the compressibility in the thermal boundary layer therefore becomes a complex quantity. This complex compressibility of the suspension may be derived from scattering theory, and can be expressed as

$$\kappa_{\mathrm{s}} = \kappa_{\mathrm{v}} + \Delta\kappa \tag{5.27}$$

with

$$\Delta\kappa = \kappa\left\{\tfrac{3}{2}\epsilon\left(\gamma-1\right)\left(1-\frac{\vartheta'\rho C_{\mathrm{p}}}{\vartheta\rho' C'_{\mathrm{p}}}\right)^{2}\left(\frac{\delta_{\mathrm{t}}}{a}\right)\right.$$
$$\left. + \mathrm{i}\left[\tfrac{3}{2}\epsilon\left(\gamma-1\right)\left(1-\frac{\vartheta'\rho C_{\mathrm{p}}}{\vartheta\rho' C'_{\mathrm{p}}}\right)^{2}\left(\frac{\delta_{\mathrm{t}}}{a}\right)\left(1+\frac{\delta_{\mathrm{t}}}{a}\right)\right]\right\} \tag{5.28}$$

where γ is the ratio of specific heats at constant pressure and volume and ϑ is the coefficient of thermal expansion.

It is now assumed that the homogeneous, continuous fluid representing the suspension has a bulk compressibility given by Equation 5.28. In the first approximation the linear relationship between density and pressure fluctuations holds (strictly only true in a lossless medium) so that

$$\Delta\rho = \rho_{\mathrm{v}}\kappa_{\mathrm{s}}p_{\mathrm{sus}} \tag{5.29}$$

where p_{sus} is the acoustic pressure in the suspension.

It is further assumed that, in the sound field, the homogeneous and continuous fluid enters the volume element $\mathrm{d}z$ at volume-averaged values of velocity and momentum.

We may now proceed with the derivation of the wave equation by formulating the continuity equation and momentum equation in the usual way.

Beginning with the equation of mass continuity, the mass flux entering the volume element at section $z = z_0$ is

$$\left\{\left(\rho_{\mathrm{v}}+\Delta\rho\right)\left[\left(1-\epsilon\right)v+\epsilon v'\right]\right\}_{z_0} \tag{5.30}$$

and the mass flux leaving the volume element at section $z = z_0 + \mathrm{d}z$ is

$$\left\{\left(\rho_{\mathrm{v}}+\Delta\rho\right)\left[\left(1-\epsilon\right)v+\epsilon v'\right]\right\}_{z_0+\mathrm{d}z} \tag{5.31}$$

The net mass of fluid leaving the element per unit time is therefore

$$\frac{\partial}{\partial z}\left\{\left(\rho_{\mathrm{v}}+\Delta\rho\right)\left[\left(1-\epsilon\right)v+\epsilon v'\right]\right\}\mathrm{d}z \tag{5.32}$$

The decrease in mass in the volume element with time may be written

$$-\frac{\partial}{\partial t}\left(\rho_{\mathrm{v}}+\Delta\rho\right)\mathrm{d}z \tag{5.33}$$

so equating this with Equation 5.32 yields

$$-\frac{\partial}{\partial t}\left(\rho_{\mathrm{v}}+\Delta\rho\right) = \frac{\partial}{\partial z}\left\{\left(\rho_{\mathrm{v}}+\Delta\rho\right)\left[\left(1-\epsilon\right)v+\epsilon v'\right]\right\} \tag{5.34}$$

This equation may be linearized to give

$$-\frac{\partial(\Delta\rho)}{\partial t} = \rho_{\mathrm{v}}\frac{\partial}{\partial z}\left[v + \epsilon\left(v' - v\right)\right] \tag{5.35}$$

Now, substituting for $\Delta\rho$ from Equation 5.29 and employing Equation 5.21 gives

$$-\kappa_{\mathrm{s}}\frac{\partial p_{\mathrm{sus}}}{\partial t} = \left(1 - \epsilon\frac{(\sigma-1)\exp(-\mathrm{i}\varphi)}{\left[(\sigma+\tau)^2 + s^2\right]^{1/2}}\right)\frac{\partial v}{\partial z} \tag{5.36}$$

Turning to the momentum equation, balancing the total time derivative of the volume-averaged momentum by the acoustic pressure gradient yields

$$\frac{\mathrm{d}}{\mathrm{d}t}\left[(1-\epsilon)\rho v + \epsilon\rho' v'\right] = -\frac{\partial p_{\mathrm{sus}}}{\partial z} \tag{5.37}$$

The total time derivative may be written in terms of partial derivatives as

$$\frac{\partial}{\partial t}\left[(1-\epsilon)\rho v + \epsilon\rho' v'\right] + (1-\epsilon)\rho v\frac{\partial v}{\partial z} + \epsilon\rho' v'\frac{\partial v'}{\partial z} \tag{5.38}$$

from which the second and third terms, being of higher order, may be neglected to leave

$$\frac{\partial}{\partial t}\left[(1-\epsilon)\rho v + \epsilon\rho' v'\right] = -\frac{\partial p_{\mathrm{sus}}}{\partial z} \tag{5.39}$$

Substituting from Equations 5.19 and 5.20 gives

$$\rho\frac{\partial v}{\partial t} + \rho\epsilon\left(\tau\frac{\partial v}{\partial t} + \omega s v\right)\frac{(\sigma-1)\exp(-\mathrm{i}\varphi)}{\left[(\sigma+\tau)^2\right]^{1/2}} = -\frac{\partial p_{\mathrm{sus}}}{\partial z} \tag{5.40}$$

Finally, differentiating the continuity equation (Equation 5.36) with respect to z and the momentum equation (Equation 5.40) with respect to t and eliminating the non-linear term $\partial^2 p_{\mathrm{sus}}/\partial z\partial t$ gives the wave equation for acoustic plane waves propagating in suspensions:

$$\frac{\partial^2 v}{\partial z^2} = \left(\frac{1 + \epsilon L\left(\tau + \mathrm{i}s\right)\exp(-\mathrm{i}\varphi)}{\rho\kappa\left(b_1 + \mathrm{i}b_2\right)\left[1 - \epsilon L\exp(-\mathrm{i}\varphi)\right]}\right)\frac{\partial^2 v}{\partial t^2} \tag{5.41}$$

where

$$L = \frac{(\rho'/\rho - 1)}{\left[(\rho'/\rho + \tau)^2 + s^2\right]^{1/2}} \tag{5.42}$$

$$b_1 = 1 - \epsilon\left(1 - \frac{\kappa'}{\kappa}\right) + \tfrac{3}{2}\epsilon\left(\gamma - 1\right)\left(1 - \frac{\vartheta'\rho C_p}{\vartheta\rho' C_p'}\right)^2\left(\frac{\delta_{\mathrm{t}}}{a}\right) \tag{5.43}$$

$$b_2 = \tfrac{3}{2}\epsilon\left(\gamma - 1\right)\left(1 - \frac{\vartheta'\rho C_p}{\vartheta\rho' C_p'}\right)^2\left(\frac{\delta_{\mathrm{t}}}{a}\right)\left(1 + \frac{\delta_{\mathrm{t}}}{a}\right) \tag{5.44}$$

and

$$\kappa_s = \kappa\,(b_1 + \mathrm{i}b_2) \tag{5.45}$$

Since the suspension is represented by a homogeneous fluid, the wave equation may be written

$$\frac{\partial^2 v}{\partial z^2} = \left(\frac{k_{\mathrm{sus}}}{\omega}\right)\frac{\partial^2 v}{\partial t^2} \tag{5.46}$$

where k_{sus} is the wavenumber for sound waves of frequency ω propagating in the suspension. As the fluid representing the suspension is dispersive, the wavenumber may be written

$$k_{\mathrm{sus}} = \frac{\omega}{c_s} + \frac{\mathrm{i}\alpha_{\mathrm{vt}}}{10\log \mathrm{e}^2} \tag{5.47}$$

where c_s is the phase speed of sound propagating in the suspension and α_{vt} is the sum of the viscous absorption and thermal absorption coefficients.

Having derived the wave equation and complex wavenumber, it is now possible to extract expressions for the sound speed and attenuation coefficients. Recognizing that $c^2 = 1/\kappa\rho$ we have

$$\left(\frac{\omega}{c_s} + \frac{\mathrm{i}\alpha_{\mathrm{vt}}}{10\log \mathrm{e}^2}\right)^2 = \left(\frac{\omega}{c}\right)^2 (b_1 + \mathrm{i}b_2)\,\frac{1 - \epsilon L\,(\tau + \mathrm{i}s)\exp(-\mathrm{i}\varphi)}{1 - \epsilon L\exp(-\mathrm{i}\varphi)} \tag{5.48}$$

We now use the Euler relation

$$\exp(-\mathrm{i}\varphi) = \cos\varphi - \mathrm{i}\sin\varphi \tag{5.49}$$

and the binomial formula (for $|\epsilon L\exp(-\mathrm{i}\varphi)| \ll 1$)

$$\frac{1}{1 - \epsilon L\exp(-\mathrm{i}\varphi)} \sim 1 + \epsilon L\exp(-\mathrm{i}\varphi) \tag{5.50}$$

to give

$$\begin{aligned}\left(\frac{\omega}{c_s} + \frac{\mathrm{i}\alpha_{\mathrm{vt}}}{10\log \mathrm{e}^2}\right)^2 \sim{}& \left(\frac{\omega}{c}\right)^2 (b_1 + \mathrm{i}b_2)\,[1 + \epsilon L\cos\varphi - \mathrm{i}\epsilon L\sin\varphi] \\ &\times\,[1 + \epsilon L\,(\tau\cos\varphi + s\sin\varphi) \\ &+\mathrm{i}\epsilon L\,(s\cos\varphi - \tau\sin\varphi)]\end{aligned} \tag{5.51}$$

Neglecting higher order terms in φ this becomes

$$\begin{aligned}\left(\frac{\omega}{c_s} + \frac{\mathrm{i}\alpha_{\mathrm{vt}}}{10\log \mathrm{e}^2}\right)^2 \sim{}& \left(\frac{\omega}{c}\right)^2 b_1\,\{1 + \epsilon L\,[(\tau + 1)\cos\varphi + s\sin\varphi]\} \\ &+ \mathrm{i}\left(\frac{\omega}{c}\right)^2 \{\epsilon L b_1\,[s\cos\varphi - (\tau + 1)\sin\varphi] + b_2\}\end{aligned} \tag{5.52}$$

Taking the square root of both sides and using the binomial formula again gives

$$\left(\frac{\omega}{c_\mathrm{s}}+\frac{\mathrm{i}\alpha_\mathrm{vt}}{10\log\mathrm{e}^2}\right)\sim\left(\frac{\omega}{c}\right)b_1^{1/2}\left\{1+\tfrac{1}{2}\epsilon L\left[(\tau+1)\cos\varphi+s\sin\varphi\right]\right\}$$
$$+\,\mathrm{i}\left(\frac{\omega}{c}\right)\left\{\epsilon L b_1\left[s\cos\varphi-(\tau+1)\sin\varphi\right]+b_2\right\} \tag{5.53}$$

Since the sound speed depends only on the real part of the wavenumber, we can equate the real parts of Equation 5.53 and substitute the expressions for b_1 and b_2 to give

$$\frac{1}{c_\mathrm{s}}\sim\left(\frac{1}{c}\right)\left[1-\epsilon\left(1-\frac{\kappa'}{\kappa}\right)+\tfrac{3}{2}\epsilon\left(\gamma-1\right)\left(1-\frac{\vartheta'\rho C_\mathrm{p}}{\vartheta\rho' C'_\mathrm{p}}\right)^2\left(\frac{\delta_\mathrm{t}}{a}\right)\right]^{1/2}$$
$$\times\left\{1+\tfrac{1}{2}\epsilon L\left[(\tau+1)\cos\varphi+s\sin\varphi\right]\right\} \tag{5.54}$$

The speed of sound propagation in suspensions is finally obtained by taking the reciprocal of both sides, substituting the expressions for L and φ and using the binomial formula yet again. The result may be written

$$c_\mathrm{s}\sim c\left(1+\tfrac{1}{2}\epsilon\left(1-\frac{\kappa'}{\kappa}\right)+\tfrac{3}{4}\epsilon\left(\gamma-1\right)\left(1-\frac{\vartheta'\rho C_\mathrm{p}}{\vartheta\rho' C'_\mathrm{p}}\right)^2\left(\frac{\delta_\mathrm{t}}{a}\right)\right.$$
$$\left.-\;\frac{1}{2}\epsilon\frac{(\sigma-1)\left[(\sigma+\tau)(1+\tau)+s^2\right]}{(\sigma+\tau)^2+s^2}\right) \tag{5.55}$$

The attenuation arises from the imaginary parts of the wavenumber, so equating the imaginary components of Equation 5.53 we have

$$\frac{\alpha_\mathrm{vt}}{10\log\mathrm{e}^2}\sim\left(\frac{\omega}{2c}\right)\left\{\epsilon L b_1\left[s\cos\varphi-(\tau+1)\sin\varphi\right]+b_2\right\} \tag{5.56}$$

Substituting expressions for b_1, L and ϕ and neglecting higher order terms in ϵ gives

$$\frac{\alpha_\mathrm{vt}}{10\log\mathrm{e}^2}\sim\frac{\omega}{2c}\left(\frac{\epsilon(\sigma-1)^2 s}{(\sigma+\tau)^2+s^2}+b_2\right) \tag{5.57}$$

As stated previously, the total attenuation coefficient, $\alpha_\mathrm{vt}=\alpha_\mathrm{v}+\alpha_\mathrm{t}$, is the sum of the visco-inertial attenuation coefficient and the thermal attenuation coefficient. On examination, it is clear that the thermal effects are contained within the b_2 term, such that the visco-inertial absorption coefficient may be written

$$\frac{\alpha_\mathrm{v}}{10\log\mathrm{e}^2}=\frac{\epsilon\omega(\sigma-1)^2}{2c}\left[\frac{s}{s^2+(\sigma+\tau)^2}\right] \tag{5.58}$$

It may be noted that Equation 5.58 for the visco-inertial absorption coefficient is identical to Urick's expression (Equation 2.31) on page 12.

5.3.3 Simplification

It was shown in Chapter 4 that the effects of thermal dissipation are not significant for mineral particles suspended in water, and this permits considerable simplification of the expression for the sound speed in such a suspension.

Letting $\delta_t \rightarrow 0$ in Equation 5.54, rearranging and ignoring terms in ϵ^2 yields.

$$c_s^2 \sim c^2 \left\{ \left[1 - \epsilon \left(1 - \frac{\kappa'}{\kappa} \right) \right]^{-1} \frac{1 - \epsilon L \cos\varphi}{1 + \epsilon L \left\{ (\tau + 1) \cos\varphi + s \sin\varphi \right\}} \right\} \tag{5.59}$$

Using the binomial formula once again and neglecting ϵ^2 terms we have

$$c_s^2 \sim c^2 \left\{ \frac{1 - \epsilon L \cos\varphi}{\left[1 - \epsilon \left(1 - \kappa'/\kappa \right) \right] \left[1 + \epsilon L \left(\tau \cos\varphi + s \sin\varphi \right) \right]} \right\} \tag{5.60}$$

This is the expression derived by Ahuja in Reference [42], in which he did not take thermal dissipation into account.

5.3.4 Results

Using the bulk averaging approach described in Section 5.2 the sound speed may be calculated as a function of volume fraction and the results of such a calculation for quartz particles are presented in Figure 5.2.

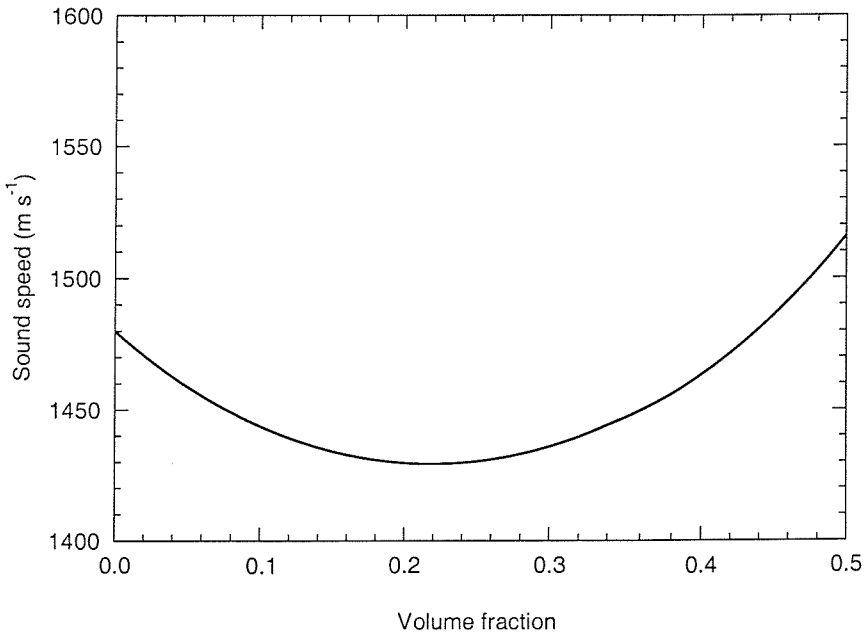

Figure 5.2. Sound speed in an aqueous suspension of quartz spheres as a function of volume fraction, calculated using the bulk averaging approach.

This figure demonstrates that at low concentrations the sound speed is reduced as the concentration increases, indicating that the increasing density dominates, whilst at higher concentrations the sound speed increases with increasing concentration, indicating that the

increasing bulk modulus has become the dominant effect. As the volume fraction approaches unity the sound speed tends towards the sound speed in the solid as expected (not shown in this figure).

Figure 5.2 may be compared with Figure 5.3, which shows the results of calculating the sound speed at a frequency of 100 kHz, for spherical particles with density and bulk compressibility comparable to those of quartz, as a function of volume fraction for four different particle radii. These curves were calculated using Equation 5.59 rather than Equation 5.60, i.e. without the final use of the binomial approximation and omission of ϵ^2 terms. It was found that, whilst Equation 5.60 is generally a good approximation to Equation 5.59, it does diverge slightly for the smallest particles.

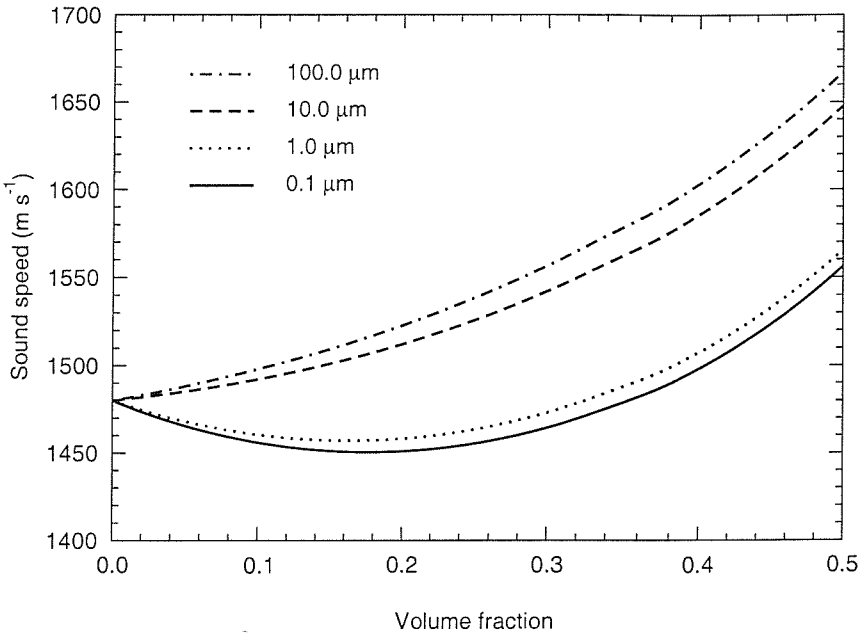

Figure 5.3. Sound speed in an aqueous suspension of quartz spheres as a function of volume fraction for three different particle sizes, calculated using Equation 5.59.

It is clear from these two figures that the bulk averaging approach of Section 5.2, which does not include any dependence on particle size, does not generally predict the correct sound speed for propagation in suspensions.

Investigating the dependence on particle size further, it is interesting to plot the sound speed as a function of particle radius for a fixed concentration. Figure 5.4 shows such a plot for a volume fraction of 0.01, with the prediction of the bulk averaging model shown for comparison. Clearly there is a significant dependence on the particle size over this range. However, the sound speed becomes independent of particle size for very small and very large particles, and the two methods converge when the particle size becomes very small.

The reason that the sound speed depends on the particle size is that, in fact, it is determined not only by the compressibilities of the suspension components, but also by the inertial part of the complex drag experienced by the oscillating particle. The fact that the sound speed becomes independent of particle size for very small and very large particles may be explained in terms of the phase lag between the particles and the fluid oscillating in the acoustic field. Very small

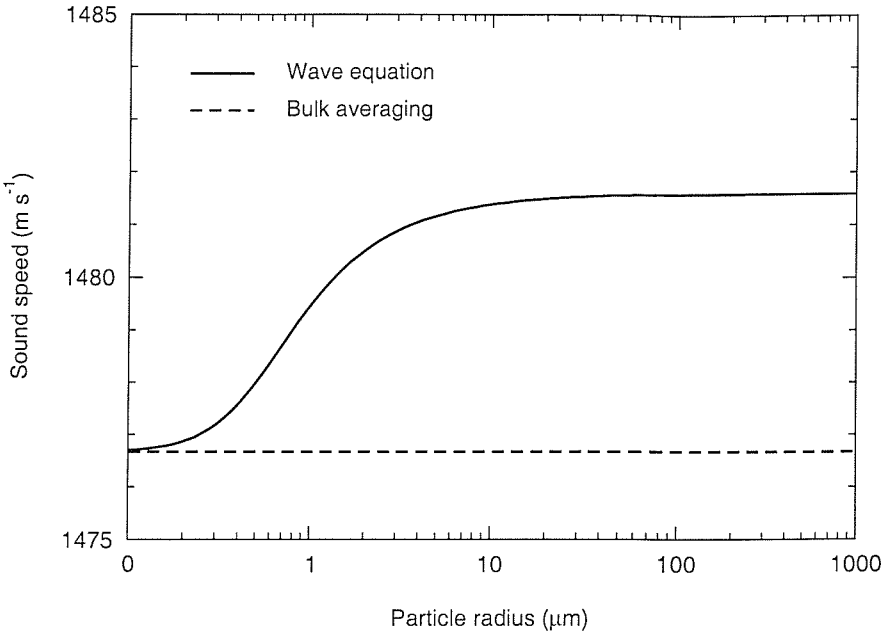

Figure 5.4. Sound speed as a function of particle size, calculated using Equation 5.14 and Equation 5.59.

particles have little inertia, and can therefore oscillate in phase with the acoustic field, whilst very large particles have a large inertia and do not therefore respond to the acoustic field. In each case the phase lag becomes independent of the particle size, and consequently so does the sound speed. It may be seen from this result that, in order to calculate the sound speed over the range of particle sizes and frequencies of interest, the bulk averaging method will not be sufficient, and the wave equation approach is required.

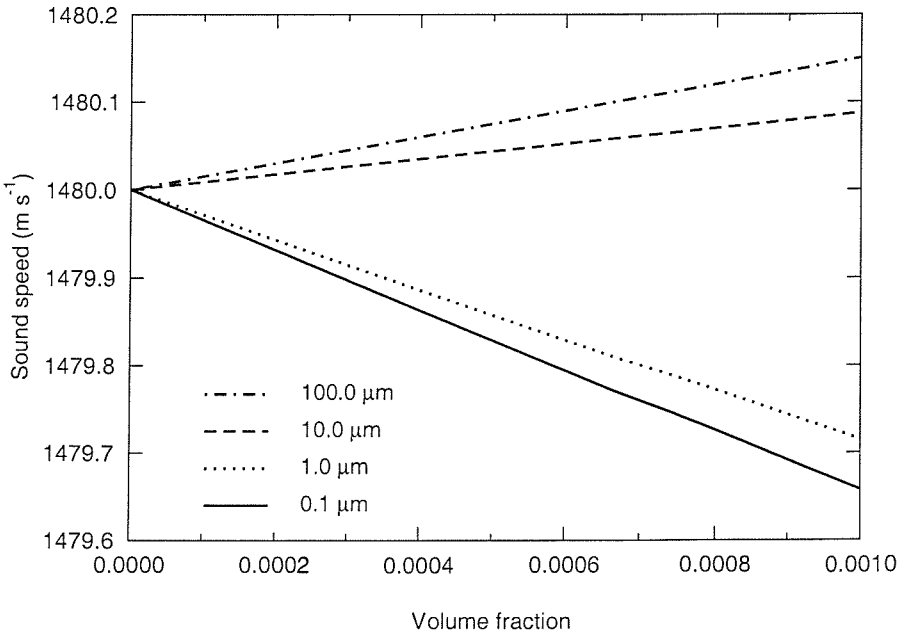

Figure 5.5. Sound speed in an aqueous suspension of glass spheres over the volume fraction range of interest for the laboratory experiments of Chapter 6.

Finally, Figure 5.5 shows sound speed as a function of volume fraction over the range of interest for the experimental measurements discussed in Section 6. This result shows that the variation in sound speed caused by the introduction of the particles into the experiment is very small (typically less than 0.01%).

5.4 Non-spherical particles - visco-inertial absorption and phase speed

5.4.1 Introduction

Thus far only spherical particles have been considered. Natural marine particles are not, of course, spherical (see Section 6.4.3) and an approach is required to estimate the absorption due to non-spherical particles in suspension. To attempt this by employing scattering theory involves significant additional complication and the problem rapidly becomes intractable. However the formulation of the wave equation for acoustic propagation in suspensions, presented in Section 5.3, allows non-spherical particles to be accounted for by employing correct expressions for the drag force acting on non-spherical bodies [45].

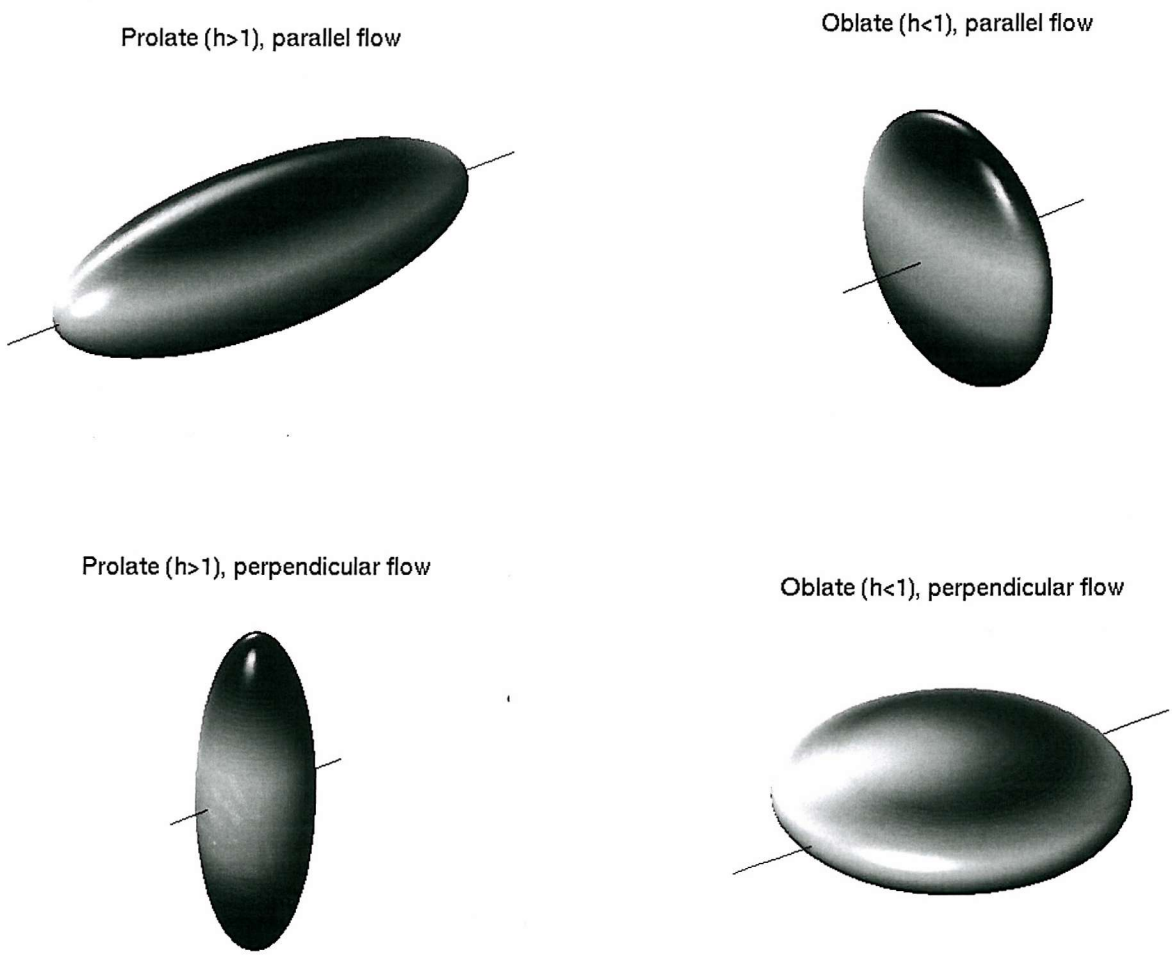

Figure 5.6. Oblate and prolate spheroids oriented with their axes of symmetry parallel or perpendicular to the direction of motion through the fluid. The motion is parallel to the axis plotted.

The non-spherical particles considered in this analysis are oblate and prolate spheroids, together with their degenerate forms of circular disks and cylindrical needles. Reference [45] gives results for spheres and oblate and prolate spheroids with the same volume, and the same examples are also used here. Figure 5.6 shows oblate and prolate spheroids orientated with their axes of symmetry parallel or perpendicular to the direction of motion.

5.4.2 Theory

In this analysis only visco-inertial absorption is considered and the dilute approximation is assumed.

The drag on an axisymmetric body oscillating along its axis of symmetry in a viscous fluid is given by [46]

$$F = F_0 \left[1 + \frac{F_0}{6\sqrt{2}\pi\eta a' u_0} (1 + \mathrm{i}) M_\mathrm{v} + O(M_\mathrm{v}^2) \right] \mathrm{e}^{-\mathrm{i}\omega t} \tag{5.61}$$

where F_0 is the Stokes drag, η is the molecular viscosity of the suspending fluid, a' is the radius perpendicular to the axis of symmetry, u_0 is the magnitude of the instantaneous velocity of the particle and $M_\mathrm{v} = \sqrt{2}a'/\delta_\mathrm{v}$ where δ_v is the shear wave skin depth.

Strictly Equation 5.61 is derived for axisymmetric unsteady flow, but Reference [46] argues that this may be applied to unsteady flow parallel to any principal axis of a body provided that correct forms are employed for the Stokes drag, as below.

For spheroids the Stokes drag may be written

$$F_0 = 6\pi\eta K_\mathrm{sf} a' u_0 \tag{5.62}$$

(noting that this is stated incorrectly in Reference [45]) and Equation 5.61 may be written

$$\begin{aligned} F = & -\rho \left(\frac{4}{3}\pi a'^2 b' \right) \left(\frac{9}{4}\frac{\delta}{b'} K_\mathrm{sf}^2 \right) \left(\frac{\mathrm{d}u}{\mathrm{d}t} \right) \\ & -\rho \left(\frac{4}{3}\pi a'^2 b \right) \left(\frac{9}{4}\frac{\delta}{b'} K_\mathrm{sf}^2 \right) \left(1 + \frac{1}{K_\mathrm{sf}}\frac{\delta}{a'} \right) \omega u \end{aligned} \tag{5.63}$$

where K_sf is a shape factor (see Table 5.1) and a' and b' are, respectively, the semi-major and semi-minor axes for oblate spheroids and the semi-minor and semi-major axes for prolate spheroids.

As $\omega \to 0$ (i.e. as the flow becomes steady), the $\mathrm{d}u/\mathrm{d}t$ term in Equation 5.61 vanishes and the u terms tends to $6\pi\eta a' u_0$, such that the total drag force tends to the Stokes drag. However, as $\delta \to 0$ (ideal fluid) in the unsteady flow $F \to 0$. This is incorrect as the drag on a body moving at nonuniform velocity in an ideal fluid is given by

$$F = -m_\mathrm{i} \left(\frac{\mathrm{d}u}{\mathrm{d}t} \right) \tag{5.64}$$

where m_i is the induced mass of the body. For a sphere of radius a oscillating in a fluid of density

ρ the induced mass is

$$m_{\mathrm{i}} = \frac{1}{2}\left(\frac{4}{3}\pi a^3 \rho\right) \tag{5.65}$$

where $\frac{4}{3}\pi a^3 \rho$ is the mass of the displaced fluid and $\frac{1}{2}$ is the inertia coefficient [11], which depends on the particle shape and orientation to the acoustic field. For the spheroids considered here the induced mass is given by

$$m_{\mathrm{i}} = L_{\mathrm{i}}\left(\frac{4}{3}\pi a'^2 b' \rho\right) \tag{5.66}$$

where L_{i} is the inertia coefficient.

Combining Equations 5.63, 5.64 and 5.66 yields the following expression for the drag on spheroids oscillating in a viscous fluid

$$F = -\rho\left(\frac{4}{3}\pi a'^2 b'\right)\tau\left(\frac{\mathrm{d}u}{\mathrm{d}t}\right) - \rho\left(\frac{4}{3}\pi a'^2 b'\right)\omega s u \tag{5.67}$$

where

$$\tau = L_{\mathrm{i}} + \frac{9}{4}\left(\frac{\delta}{b'}\right)K_{\mathrm{sf}}^2 \tag{5.68}$$

and

$$s = \frac{9}{4}\left(\frac{\delta}{b'}\right)K_{\mathrm{sf}}^2\left[1 + \left(\frac{1}{K_{\mathrm{sf}}}\right)\left(\frac{\delta}{a'}\right)\right] \tag{5.69}$$

Proceeding to formulate the wave equation, as in Section 5.3, yields expressions for the speed of sound (Equation 5.55) which, ignoring thermal conduction, may be written

$$c_{\mathrm{s}} = c\left[1 + \frac{1}{2}\epsilon\left(1 - \frac{\kappa'}{\kappa}\right) - \frac{1}{2}\epsilon\frac{(\sigma-1)\left[(\sigma+\tau)(1+\tau)+s^2\right]}{(\sigma+\tau)^2+s^2}\right] \tag{5.70}$$

and the visco-inertial absorption coefficient (Equation 5.58)

$$\frac{\alpha_{\mathrm{v}}}{10\log \mathrm{e}^2} = \frac{\epsilon\omega(\sigma-1)^2}{2c}\left[\frac{s}{s^2+(\sigma+\tau)^2}\right] \tag{5.71}$$

5.4.3 Shape factor and inertia coefficient

Shape factors for oblate and prolate spheroids with flow parallel and perpendicular to the axis of symmetry are given in [47] and inertia coefficients are given in [11].

5.4.3.1 Shape factor

The shape factor for oblate spheroids with $h = b'/a' < 1$, for flow parallel to the axis of symmetry is given by

$$K_{\mathrm{ob},\parallel} = \frac{8}{3}\left\{\frac{2h}{1-h^2} + \frac{2(1-2h^2)}{(1-h^2)^{3/2}}\tan^{-1}\left[\frac{(1-h^2)^{1/2}}{h}\right]\right\}^{-1} \tag{5.72}$$

In the limiting case of a thin circular disk moving broadside on, $h \to 0$ and

$$K_{\mathrm{ob},\parallel} = \frac{8}{3\pi} \tag{5.73}$$

The shape factor for prolate spheroids with $h = b'/a' > 1$, for flow parallel to the axis of symmetry is given by

$$K_{\mathrm{pr},\parallel} = \frac{8}{3}\left\{-\frac{2h}{h^2-1} + \frac{2h^2-1}{(h^2-1)^{3/2}}\ln\left[\frac{h+(h^2-1)^{1/2}}{h-(h^2-1)^{1/2}}\right]\right\}^{-1} \tag{5.74}$$

In the limiting case of a long cylindrical needles moving end on, $h \gg 1$ and

$$K_{\mathrm{pr},\parallel} \approx \frac{2h}{3(\ln 2h - 0.5)} \tag{5.75}$$

It will be noted that as $a' \to 0$ and $h \to \infty$, $K_{\mathrm{pr},\parallel} \to \infty$, but the Stokes drag, F_0, correctly tends to zero.

For oblate spheroids with $h = b'/a' < 1$ and flow perpendicular to the axis the shape factor is

$$K_{\mathrm{ob},\perp} = \frac{8}{3}\left\{-\frac{h}{1-h^2} - \frac{2h^2-3}{(1-h^2)^{3/2}}\sin^{-1}(1-h^2)^{1/2}\right\}^{-1} \tag{5.76}$$

In the limiting case of a thin circular disk moving edgewise, $h \to 0$ and

$$K_{\mathrm{ob},\perp} \approx \frac{16}{9\pi} \tag{5.77}$$

For prolate spheroids with $h = b'/a' > 1$ moving perpendicularly the shape factor is

$$K_{\mathrm{pr},\perp} = \frac{8}{3}\left\{\frac{h}{h^2-1} + \frac{2h^2-3}{(h^2-1)^{3/2}\ln\left[h+(h^2-1)^{1/2}\right]}\right\}^{-1} \tag{5.78}$$

In the limiting case of a cylindrical needle moving broadside on, $h \gg 1$ and

$$K_{\mathrm{pr},\perp} \approx \frac{4h}{3(\ln 2h + 0.5)} \tag{5.79}$$

Again, as $a' \to 0$ and $h \to \infty$, $K_{\mathrm{pr},\perp} \to \infty$, but the Stokes drag, F_0, correctly tends to zero.

5.4.3.2 Inertia coefficient

The inertia coefficient for oblate spheroids moving parallel to their axis of symmetry is given by

$$L_{\mathrm{ob},\parallel} = \frac{\alpha_0}{2-\alpha_0} \tag{5.80}$$

where

$$\alpha_0 = \left(\frac{2}{\varepsilon^2}\right)\left[1 - \sqrt{1-\varepsilon^2}\left(\frac{\sin^{-1}\varepsilon}{\varepsilon}\right)\right] \tag{5.81}$$

with the eccentricity ε given by

$$\varepsilon = \sqrt{1 - \frac{b'^2}{a'^2}} \tag{5.82}$$

In the limiting case of a thin circular disk moving broadside on, $\varepsilon \longrightarrow 1$ and

$$\alpha_0 \rightarrow 2 - \pi\sqrt{1-\varepsilon^2} \tag{5.83}$$

such that $\alpha_0 \rightarrow 2$ and $L_{\mathrm{pr},\parallel} \rightarrow \infty$. However in the limiting case of $\varepsilon = 1$, a direct calculation for a thin circular disk moving broadside on yields the inertial coefficient $L_{\mathrm{i}} = 2/\pi$ [11].

The inertia coefficient for prolate spheroids moving parallel to their axis of symmetry is given by

$$L_{\mathrm{pr},\parallel} = \frac{\alpha_0}{2 - \alpha_0} \tag{5.84}$$

where

$$\alpha_0 = \left[\frac{2(1-\varepsilon^2)}{\varepsilon^3}\right]\left\{\frac{1}{2}\ln\left[\frac{1+\varepsilon}{1-\varepsilon}\right] - \varepsilon\right\} \tag{5.85}$$

and the eccentricity is

$$\varepsilon = \sqrt{1 - \frac{a'^2}{b'^2}} \tag{5.86}$$

In the limiting case of a long cylindrical needle moving end on, $\varepsilon \longrightarrow 1$ and

$$\alpha_0 \rightarrow 2\left(\frac{a'}{b'}\right)^2\left[\ln\frac{2b'}{a'} - 1\right] \tag{5.87}$$

Under this limiting approximation, as $\varepsilon \rightarrow 1$ so $\alpha_0 \rightarrow 0$ and $L_{\mathrm{pr},\parallel} \longrightarrow 0$.

For fluid motion perpendicular to the axis of symmetry the inertia coefficient for an oblate spheroid is

$$L_{\mathrm{ob},\perp} = \frac{\gamma_0}{2 - \gamma_0} \tag{5.88}$$

where

$$\gamma_0 = \frac{\sqrt{1-\varepsilon^2}}{\varepsilon^3}\sin^{-1}\varepsilon - \left[\frac{1-\varepsilon^2}{\varepsilon^2}\right] \tag{5.89}$$

with

$$\varepsilon = \sqrt{1 - \frac{b'^2}{a'^2}} \tag{5.90}$$

In the limiting case of a thin circular disk moving edgewise $\varepsilon \to 1$ and

$$\gamma_0 \to \left(\frac{\pi}{2}\right)\sqrt{1-\varepsilon^2} \tag{5.91}$$

In the limit as $\varepsilon \to 1$ so $\gamma_0 \to 1$ and $L_{\mathrm{ob},\perp} \to 0$.

Finally, the inertia coefficient for a prolate spheroid with fluid motion perpendicular to the axis of symmetry is

$$L_{\mathrm{pr},\perp} = \frac{\gamma_1}{2-\gamma_1} \tag{5.92}$$

where

$$\gamma_1 = \left(\frac{1}{\varepsilon^2}\right)\left\{1 - \left[\frac{1-\varepsilon^2}{2\varepsilon}\right]\ln\left[\frac{1+\varepsilon}{1-\varepsilon}\right]\right\} \tag{5.93}$$

with

$$\varepsilon = \sqrt{1 - \frac{a'^2}{b'^2}} \tag{5.94}$$

In the limiting case of a long cylindrical needle moving broadside on, $\varepsilon \to 1$ and

$$\gamma_1 \to 1 - \left(\frac{a'}{b'}\right)^2 \ln\left(\frac{2b'}{a'}\right) \tag{5.95}$$

Again considering the limit as $\varepsilon \to 1$ so $\gamma_1 \to 1$ and $L_{\mathrm{pr},\perp} \to 1$

5.4.4 Results

In order to illustrate the effects of particle shape on the propagation parameters in suspensions, examples are chosen from Reference [45]. These examples were initially chosen to validate the code by comparing the predictions with the results presented in Reference [45], but for the purposes of this chapter they also serve as illustrative examples. The geometric parameters of these bodies are given in Table 5.1.

Figures 5.7 to 5.10 show the results of calculating the attenuation coefficients for the particles of Table 5.1 using the approach described in Sections 5.4.3 and 5.4.2. The frequency range for these calculations was extended up to 10 MHz for comparison with the results presented in Reference [45].

Figure 5.7 shows the calculated attenuation, normalized with respect to concentration, for the oblate spheroids of Table 5.1. The attenuation for the equivalent volume sphere is also shown for comparison. This result demonstrates that particle orientation has a significant effect on the absorption. At low frequencies the attenuation for oblate spheroids orientated edgewise to the flow is close to that for spheres, whilst at higher frequencies the attenuation becomes greater

Particle	Dimensions (μm)	Orientation to acoustic field	Shape factor K_{sf}	Inertia coefficient L_i
Sphere	Radius $a = 2.75$		1	0.5
Oblate spheroid	Major radius $a' = 4.36$	Broadside	0.868	2.374
	Minor radius $b' = 1.1$	Edgewise	0.682	0.174
Prolate spheroid	Major radius $b' = 6.9$	Broadside	2.057	0.872
	Minor radius $a' = 1.7$	End on	1.598	0.0816
Circular disk	Diameter $2a' = 5.5$	Broadside	0.849	0.627
	Thickness $2b' = 0.055$	Edgewise	0.571	0.008
Cylindrical needle	Diameter $2a' = 0.055$	Broadside	23.0	1
	Length $2b' = 5.5$	End on	13.894	0

Table 5.1. Shape factors and inertia coefficients for a variety of simple particle shapes.

than the attenuation by spheres. The attenuation for oblate spheroids oriented broadside to the flow is consistently lower than the both the attenuation for the orthogonal orientation and that of spheres of the same volume.

Figure 5.8 shows the equivalent result for prolate spheroids. Once again particle orientation has an effect, although the difference in attenuation for the two orthogonal orientations is smaller in the case of prolate spheroids than for oblate spheroids.

Figures 5.9 and 5.10 show the attenuation for the degenerate forms of oblate and prolate spheroids, i.e. disks and needles. These show again the effects of orientation on the attenuation. The attenuation for the spheres is shown again in these figures for comparison, but it should be noted that the disks and needles do not have the same volume as these spheres.

The results for the spheroids are summarized in Figure 5.11, which shows the ratio of the absorption coefficient for spheroids to that of spheres of equivalent volume.

Figure 5.12 shows the ratio of the phase speed in a suspension of particles to that in the suspending fluid. Results are shown for spheres, oblate spheroids and their degenerate form, disks. Figure 5.13 shows the corresponding result for prolate spheroids and needles. It may be noted from these figures that the degenerate forms of both the oblate and prolate spheroids appear to exhibit very little dispersion compared to either spheres or spheroids. However it must be remembered that the degenerate examples have a much smaller volume than the spherical or spheroidal examples.

The cases examined in this section should be viewed merely as illustrative examples of the calculation of attenuation and phase speed in suspensions of oblate and prolate spheroids. The examples were chosen to be the same as in Reference [45] in order to validate the computer model which implements the theory described in that reference. These examples do, however, serve to demonstrate that both particle shape and orientation do have an effect on the visco-inertial dissipation and should be considered when dealing with non-spherical particles. The model described in this section will be applied to the interpretation of absorption measurements made with suspensions of non-spherical particles in Chapter 6.

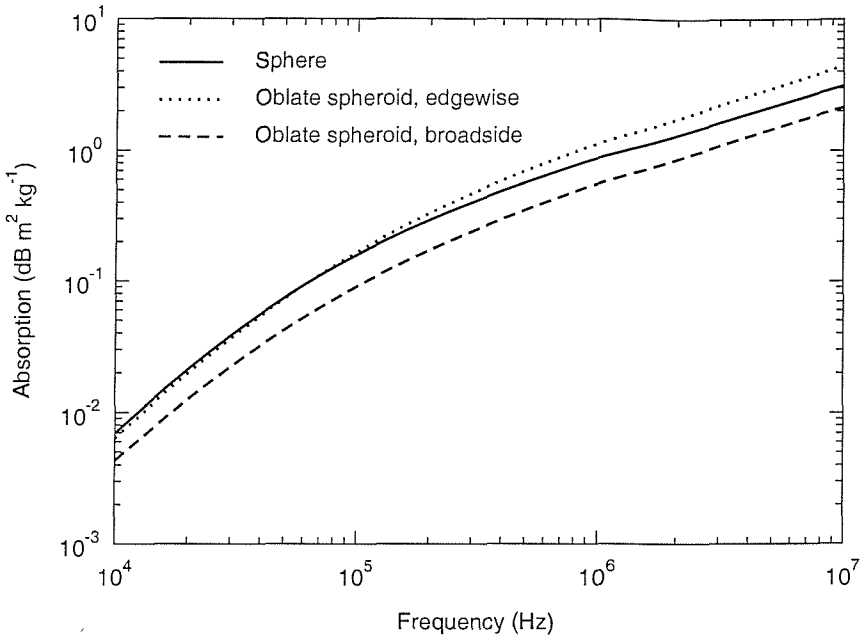

Figure 5.7. Attenuation coefficient for the spheres and oblate spheroids of Table 5.1.

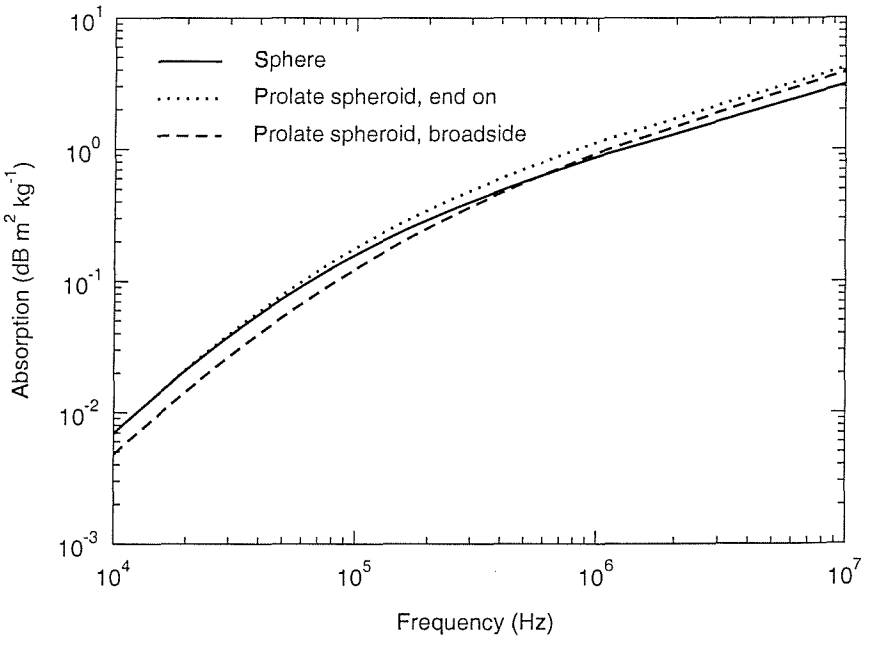

Figure 5.8. Attenuation coefficient for the spheres and prolate spheroids of Table 5.1.

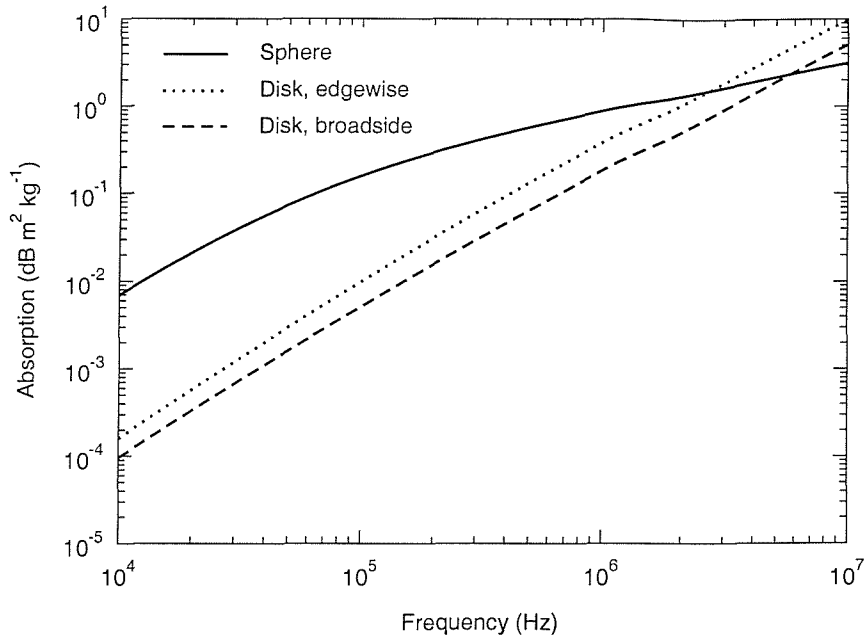

Figure 5.9. Attenuation coefficient for the spheres and disks of Table 5.1.

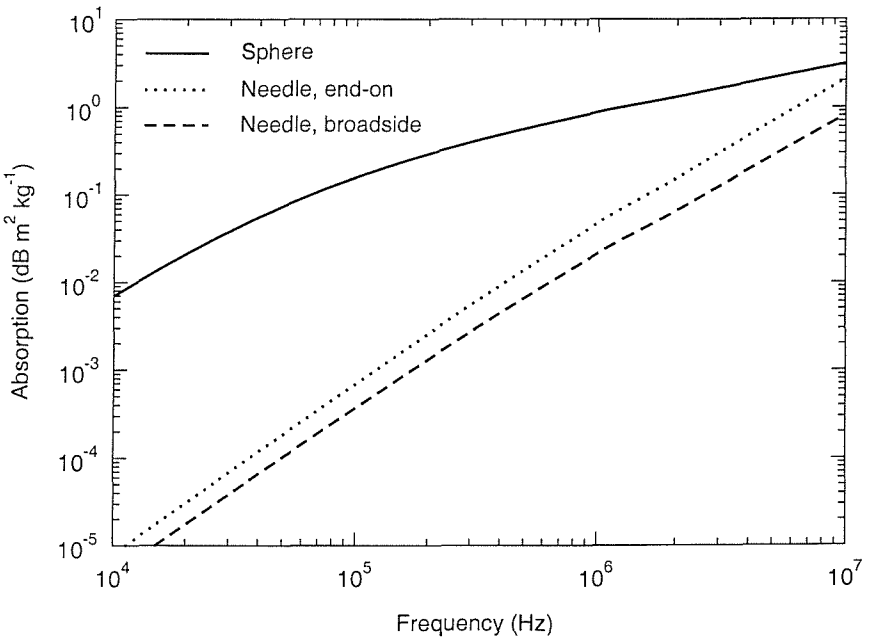

Figure 5.10. Attenuation coefficient for the spheres and needles of Table 5.1.

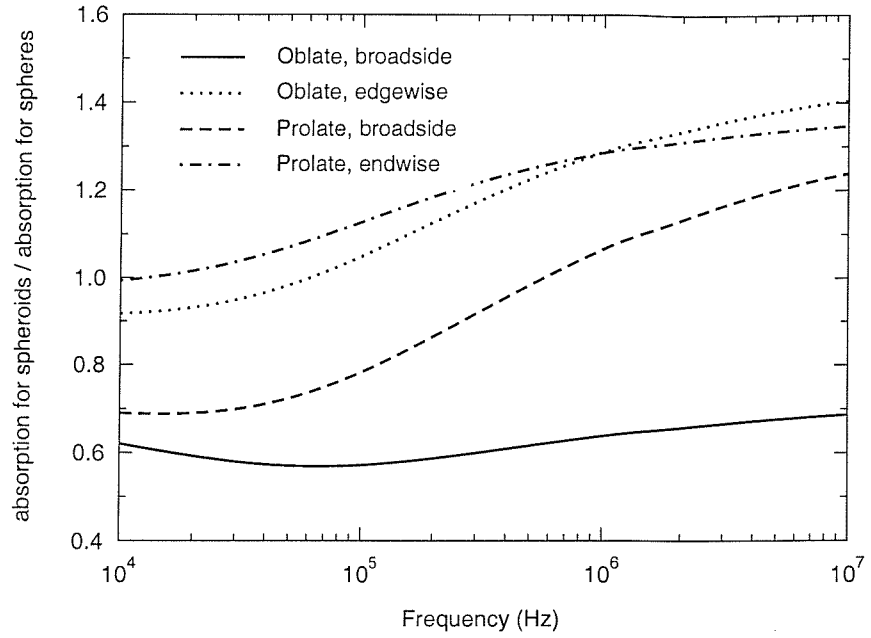

Figure 5.11. Ratio of the attenuation coefficient for the spheroids of Table 5.1 to that of spheres.

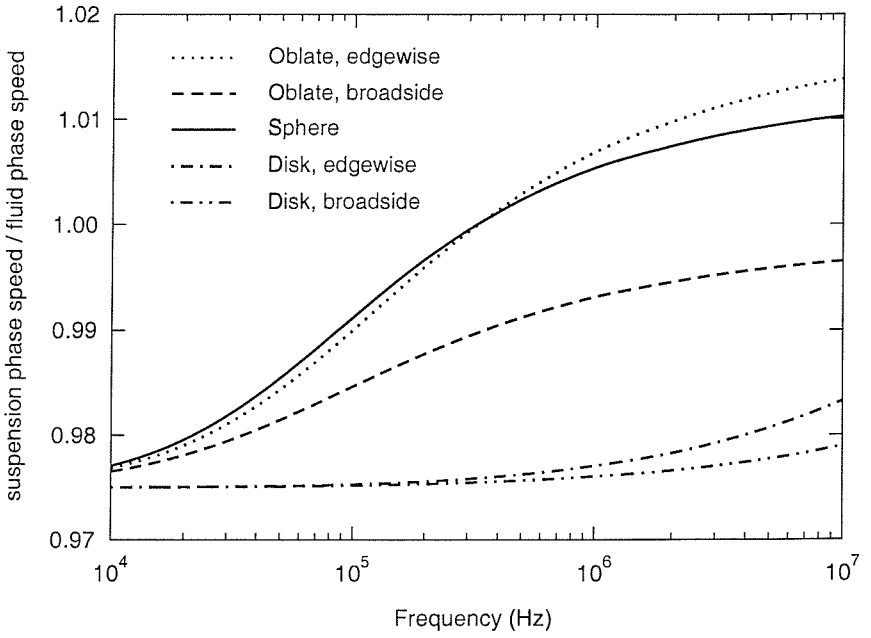

Figure 5.12. Sound speed ratios for the oblate spheroids, spheres and disks of Table 5.1.

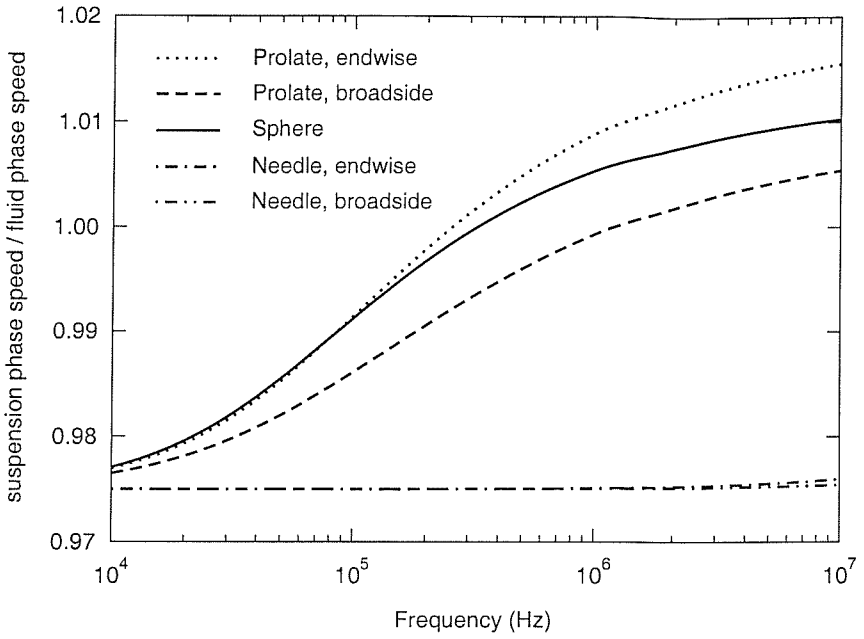

Figure 5.13. Sound speed ratios for the prolate spheroids, spheres and needles of Table 5.1.

5.5 Summary and conclusions

In addition to increasing the acoustic attenuation, the presence of particles in suspension can also influence the sound speed.

In this chapter a simple method for calculating the sound speed in suspensions, based on replacing a fraction of the volume of fluid with material of different density and bulk modulus, was described. An alternative method was also described in which the sound speed was obtained by formulating the wave equation for propagation in suspensions.

Results presented in this chapter demonstrated that, although the bulk averaging approach gives the correct result in the limit of very small particles, the expression derived from the wave equation is required in general. This is because the sound speed in the suspension depends not only on the sound speed in each suspension component, but also on the inertial part of the complex drag experienced by the oscillating particle.

The attenuation coefficient may be obtained from the imaginary part of the complex wavenumber in the wave equation, and the viscous absorption coefficient obtained in this was was shown to be identical to the expression obtained by Urick as described in Section 2.4. This was to be expected as a similar approach was taken in the derivation of both the wave equation and the Urick expression.

The results presented here show that, for dilute suspensions of mineral particles, the change in the sound speed is relatively small, and will have little effect on refraction of sound at the relatively short ranges of interest for high frequency sonars. The change in sound speed resulting from bubble populations in shallow, coastal waters is likely to be far more significant. At very high concentrations, such as may be found in the muddy boundary layer near the seabed, the change in sound speed due to particles in suspension may become significant.

Finally, a method for calculating the absorption and phase speed in suspensions of oblate and prolate spheroids was discussed. Example results from this model showed that the absorption by suspensions of spheroids may be significantly different from absorption by spheres of equivalent volume. It was also shown that the orientation of the spheroid with respect to the sound field is important.

Theoretical models of visco-inertial absorption by suspensions of both spheres and spheroids have now been discussed. Results from these models will be compared with measurements in the next chapter, which introduces a laboratory technique for measuring absorption in dilute suspensions at low ultrasonic frequencies.

Chapter 6

Experimental investigations

6.1 Introduction

The preceding chapters discussed the theory of sound absorption and scattering by solid particles suspended in water, and included results of calculations based on these theories. In order both to validate this theoretical work and to gain a deeper physical insight into the phenomena of interest, it is important to investigate the physical processes experimentally.

The literature contains numerous examples of measurements of scattering in suspensions and emulsions, e.g. [21, 48–50]. Acoustic backscattering techniques are also becoming common for the measurements of suspensions in the sea, as reviewed by Thorne and Hanes [51]. Furthermore, measurements have also been made of the scattering form function of suspended cubes [52, 53] and polyhedra, to address the issue of scattering by angular, faceted, non-spherical bodies. However, there is a lack of laboratory measurements of the absorption coefficient in dilute aqueous suspensions of mineral particles over the frequency range extending from tens to hundreds of kHz.

To address this a series of experimental investigations has been carried out. This work was carried out by a team which comprised the author, Dr. Niven Brown and Prof. Tim Leighton. This team was jointly responsible for the design and development of the experimental technique. Dr. Brown performed most of the technical work in building and setting up the apparatus and he carried out the measurements made with spherical particles, the results of which are shown on Page 88 *et seq.* The author was responsible for making the measurements with kaolin and calcium carbonate particles, the results of which are given in Figures 6.26 and 6.27 respectively. All three members of the experiment team contributed to the analysis and interpretation of the results.

The development of the experimental technique and the results have been presented in a number of publications by the author and colleagues [54–60].

It should be noted that, in the course of this investigation, the laboratory measurement of absorption by dilute suspensions of mineral particles in small volumes of water at frequencies in the range 50 - 150 kHz was found to be extremely challenging. Whilst the absorption can be significant in the sea, over ranges of order hundreds of metres, the absorption in a laboratory scale experiment is extremely small. The fact that the attenuation by the particles in suspension can be much smaller than both the boundary losses at the walls of the container and the absorption due to the instrumentation means that the absorption being measured was a small part of the total attenuation in the system. In fact it was even found that the measurement was sensitive to small changes (O(mm)) in the length of submerged hydrophone cable. This

illustrates the type of difficulties encountered in making these measurements. Other practical problems include the following: The particles settle out of suspension under the influence of gravity, necessitating some means of resuspension, and the addition of any stirrer into the water to achieve this increases the absorption in the system. In addition natural particles, such as clay particles, may have a tendency to flocculate, severely complicating the effects under study.

6.2 Method

6.2.1 Theory

The experimental method used in the present investigation was to infer the total acoustic loss in a volume of fluid containing suspended particulate matter from measurements of the reverberation time of the system. The attenuation due to the suspended particles may thus be estimated by comparing the reverberation times of the system with and without the particles present. Making measurements relative to the clear water case in this way partially corrects for the effects of the boundary losses and other contributions to the total attenuation in the system. However, it should be noted that when the suspended particles' contribution to the total attenuation is small (i.e. at low concentration) the effect of the relatively large boundary losses will be to give large errors in the relative measurement of the influence of the suspended particles on the reverberation time.

The reverberation time of a reverberating volume is defined as the time taken for the sound pressure level to fall by 60 dB after the sound source is removed and may be given by (e.g. [61])

$$t_{60} = \frac{55.26 V_{\text{enc}}}{c\left(S_{\text{enc}}\bar{a} + 8\zeta V_{\text{enc}}\right)} \tag{6.1}$$

where V_{enc} is the volume of the enclosure, S_{enc} is the surface area, c is the compression wave speed, $\bar{a}$ is the average Sabine absorptivity and ζ is the absorption coefficient of the fluid in Nepers per metre. The average Sabine absorptivity is defined

$$\bar{a} = \frac{A_{\text{enc}}}{S_{\text{enc}}} \tag{6.2}$$

where A_{enc} is the total sound absorption of the enclosure, expressed in units of m^2, such that $\bar{a}$ is dimensionless.

If t_{60} and t'_{60} are the reverberation times of a volume of particulate-free water and water containing particles respectively, then it is clear from Equation 6.1 and Equation 2.2 that the difference in the attenuation coefficients of the two fluids, expressed in dB m^{-1}, is given by

$$\begin{aligned} \Delta\alpha &= \left(10 \log \text{e}^2\right) \frac{55.26}{8c} \left(\frac{1}{t'_{60}} - \frac{1}{t_{60}}\right) \\ &= \frac{60}{c} \left(\frac{1}{t'_{60}} - \frac{1}{t_{60}}\right) \end{aligned} \tag{6.3}$$

provided that the addition of the particles does not significantly affect:

- the sound speed in the medium;
- the volume of fluid;
- the absorption at the boundaries;

Chapter 5 showed that the change in sound speed resulting from the introduction of the particles at concentrations used in the experiments is small (less than a few tens of cm s^{-1} even at the highest concentrations). It is trivial to demonstrate that the volume change due to the addition of the particles at the concentrations used in these experiments is similarly small (volume fractions are typically much smaller than 10^{-3}) and it is reasonable to assume that the particles in suspension have little effect on the absorption properties of the walls. Particles that settle to the bottom of the volume may, however, affect the boundary losses, but attempts were made to make measurements with the majority of the particles in suspension.

Ideally, the reverberation time should be determined from the decay of a diffuse sound field, that is to say one in which the average energy density is the same throughout the entire volume and all directions of propagation are equally probable [61]. The onset of a diffuse sound field in an enclosure can be described by the Schroeder cut-off frequency [62], which gives an indication of the lowest frequency at which the modal density, i.e. the number of modes per unit bandwidth, is sufficient to constitute a diffuse field. The Schroeder cut-off frequency, f_s, may be written [62]

$$f_s = \left(\frac{c^3}{4 \ln 10}\right)^{\frac{1}{2}} \left(\frac{t_{60}}{V_{\text{enc}}}\right)^{\frac{1}{2}} \tag{6.4}$$

Ideally then, all experiments should be carried out at frequencies well above the Schroeder cut-off in order to ensure that the measurements are not influenced by modal structure in the sound field.

6.2.2 Preliminary investigations

Prior to converging on the design of the final experimental system (described in Section 6.2.3) two developmental systems were tested [54]. These served to prove the concept and reveal the critical features that were required of the final system.

In both a 1 m^{-3} plastic tank and a 0.03 m^{-3} glass tank the reverberation time was observed to decrease as the concentration of suspended sand grains was increased. The smaller volume of the glass tank was desirable as it enabled greater control of experimental conditions. However, the increased surface area to volume ratio of the smaller system resulted in a greater relative contribution by the losses at the boundaries. These development systems therefore indicated that the final configuration should be optimized in order to minimize wall losses. The ideal system should therefore have perfectly reflecting walls, which may be achieved in theory either with a pressure-release boundary condition or a perfectly rigid boundary. Of these the easiest to approximate to in practice is the pressure-release boundary, since an air-water interface is a good approximation to this. The final system therefore employed a thin-walled (30 μm) polythene bag containing around 0.016 m^3 of water, suspended from a frame and surrounded by air. This provided an approximation to the ideal situation in which a pressure-release surface surrounds the entire volume, leading to a pressure amplitude reflection coefficient close to -1. Measurements of decay rate with this arrangement confirmed that the wall-losses were much lower than in the glass tank, and all subsequent measurements were carried out using the suspended polythene bag.

6.2.3 Experimental system

The experimental system used to obtain the results presented in this chapter is shown schematically in Figure 6.1 [54] and Figure 6.2 shows a photograph of the apparatus.

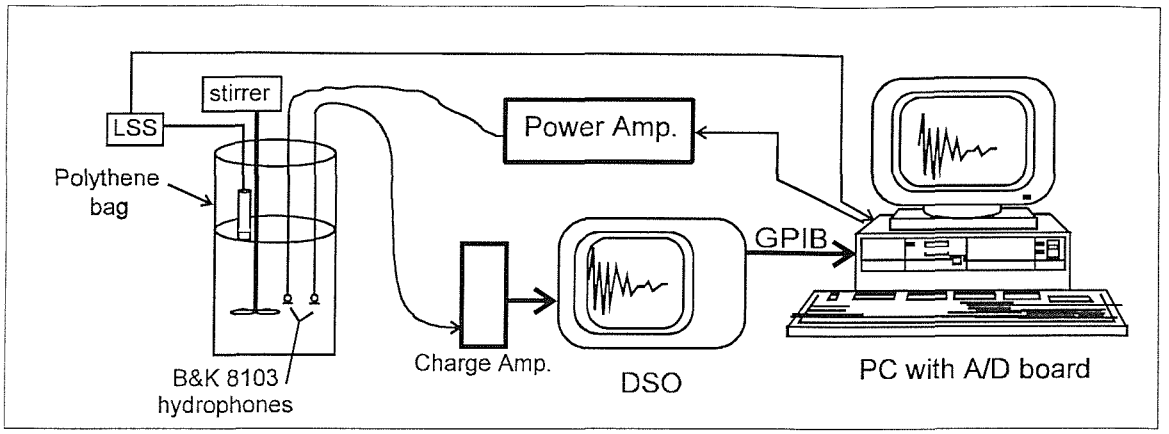

Figure 6.1. Schematic of the experimental apparatus used to measure absorption in dilute suspensions over the frequency range 50-150 kHz [54].

The signal generation, data acquisition and signal processing were all performed under the LabVIEW laboratory instrument management system, running on a personal computer (PC). The signal from the PC's digital-to-analogue converter (DAC) board was fed to a power amplifier driving a Brüel and Kjær (B&K) 8103 hydrophone. A second B&K 8103 hydrophone was used for the receiving transducer and the signal from this was amplified and fed to a LeCroy digital storage oscilloscope (DSO). The DSO was connected to the PC via a GPIB interface, and the data were transferred to the computer for storage and post processing. A mechanical stirring device (propeller) was used to resuspend particles that had settled out of suspension. This was removed from the water when the acoustic measurements were performed, as additional absorbing / reflecting surfaces complicate the acoustic system. The temporal variation in the concentration of the suspension was monitored using a Sea Tech light scattering sensor (LSS), and this was also removed from the volume during acoustic measurements. In later experiments the LSS was mounted horizontally on the outside of the bag, with its window in close contact with the side of the bag. The mating faces of the LSS window and the side of the bag were wetted to ensure good optical coupling. This configuration ensured that any spatial integrating inherent in the LSS measurements would be in the horizontal direction, not in the vertical where the concentration would be expected to be spatially varying after a finite period of settling.

The photograph (Figure 6.2) shows the polythene bag suspended from its mechanical support by means of fine wires attached to a metal hoop. The items dipping into the water are, from left to right, the LSS used to monitor the concentration of the suspended particles, the transmitting and receiving hydrophones and the propeller used to stir the water in order to suspend the particles. The diameter of the bag at the water surface is about 235 mm.

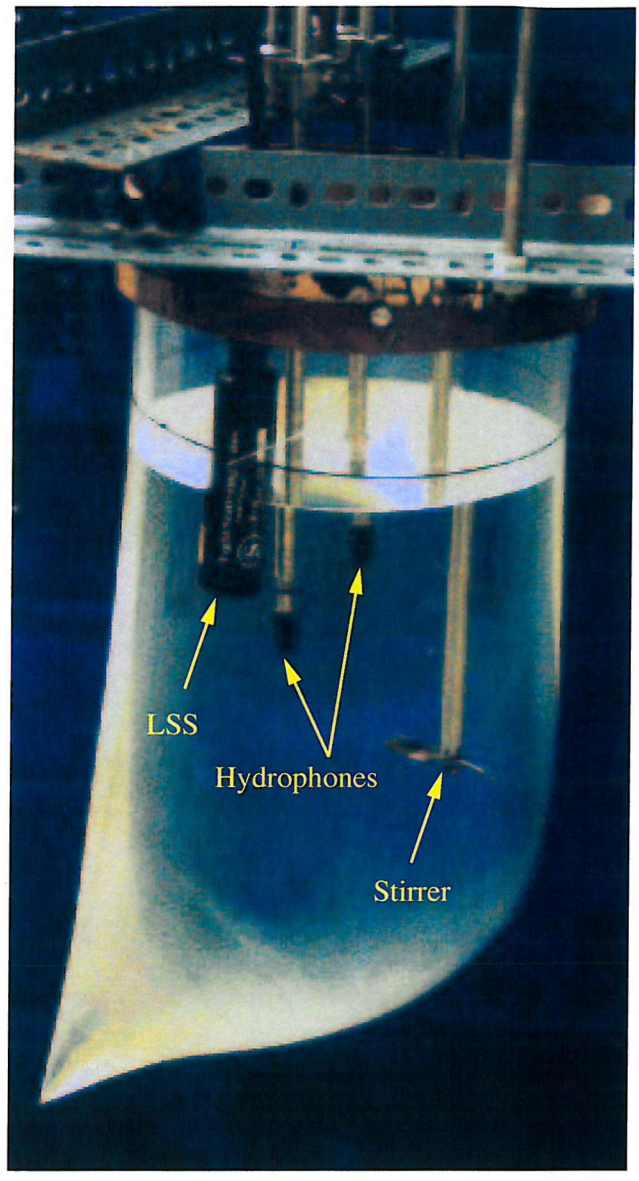

Figure 6.2. Photograph of the experimental apparatus [54]. This photograph is illustrative only, as the LSS and stirrer were removed during acoustic measurements. The majority of experiments were carried out with the LSS mounted horizontally on the outside of the bag (see text). Other instrumentation included pH, temperature and dissolved oxygen probes (not shown). The hydrophones are mounted in rigid tubes to prevent movement.

From Equation 6.4 the Schroeder cut-off frequency for the water volume held in the bag can be shown to be around 55 kHz for typically measured reverberation times, providing a lower limit on the frequency used for the tests. The cut-off frequency could be reduced to below 50 kHz by increasing the water volume to about 0.02 m^3, although this would mean approaching the strength limit of the bag.

Prior to acoustic measurements the water was passed through a reverse osmosis system and then filtered to remove any remaining particulate matter. This ensured that no particles of diameter greater than 0.22 μm remained in the water. The water was then degassed under partial vacuum in order to avoid the presence of bubbles which may be acoustically significant. The temperature and pH of the water were measured using a Jenway 3071 pH and temperature meter and these measurements were used to calculate the speed of sound in the ambient water. The level of dissolved oxygen was monitored throughout the experiments (between acoustic runs) using a Jenway 9010 dissolved oxygen probe attached to the 3071 meter. This was to ensure that the addition of the particles or the stirring process did not cause significant gas entrainment. The dissolved oxygen content was found to vary from 51% to 65% (expressed as a percentage of the saturation level) over the course of a measurement period, and no bubbles were observed.

In each series of experiments reverberation time measurements were first made in the nominally clear water in order to provide a reference measurement. Particles were then added in stages, in known quantities by mass, to enable a series of measurements to be made at varying concentrations[1].

Before each series of acoustic measurements the suspension was stirred by the mechanical stirrer until the spatial distribution of suspended particles appeared to be homogeneous. The time taken for this to occur was shown, by measurements made with the LSS, to be of the order of a few seconds. Care was taken to ensure that the particles that collect in the corners formed by the bottom seam of the bag were resuspended by the stirring. As the stirring takes place just before each set of acoustic measurements, the clear water reference measurements were also made on stirred water. This ensured that the reference signal used was obtained under conditions which most closely represented those experienced during the measurements made with the particles in suspension. It may be noted that stirring induces turbulence which can, in principle, lead to absorption. This issue is addressed in Section 6.3, where it is shown that the absorption due to turbulence in these experiments may be neglected.

The acoustic measurement itself consisted of first generating the sound field, then switching off the sound source and recording the decay of the reverberant sound field.

Two techniques for generating the sound field were investigated; an impulse and a long burst (20 ms) of uniform white noise. Both of these methods produce a broadband sound field. The advantage of using the long burst technique is that it gives sufficient time for a steady-state sound field to build up before the source is switched off, and the decaying sound field is also less prone to large perturbations resulting from direct reflections and particular modes of the volume. For these reasons the long burst generation method was used for the results presented in this chapter.

Typically a series of measurements consisted of emitting 10 noise bursts from the transmitting transducer and recording their responses via the receiver hydrophone, with the entire sequence

[1] The concentration is the spatial average over the volume, i.e. the mass of particles added divided by the volume of water.

lasting approximately 35 s. During this period the concentration, which changes as a result of the particles settling out, does not decay appreciably according to the estimates obtained using the LSS.

The decaying reverberant sound field measured by the receiving hydrophone demonstrates seemingly random fluctuations resulting from the interference between the many modes within the reverberating volume (see Figure 6.4 on Page 84). These fluctuations limit the accuracy with which the decay rate of the reverberant field may be determined from the measured decay curve. In order to improve the accuracy of the estimate of the reverberation time of a reverberating volume, it is usual practice to repeat the experiment many times and average the decay rates obtained from the individual measurements. This method is, however, inefficient owing to the large number of measurements which must be made in order to obtain an accurate estimate of the decay rate or reverberation time. This averaging also obscures any ping-to-ping variations in the decay rate and any temporal variation within the integration time, which can be long due to the requirement for a large number of measurements.

The decay rates were therefore determined by applying the method of integrated impulse response (IIR) [63] to the sound field from the time that the driving signal was switched off. This method was used, even for signals derived from non-impulsional sources, as it gives a decay curve which is equivalent to the average over infinitely many decay curves that would be obtained from exciting the volume with bandpass filtered noise.

The value of the IIR represents the ensemble average of the squared noise responses at time t after the onset of decay, which is equal to the squared tone-burst response integrated from time t to ∞. The practical implementation of this method is as follows. The response of the volume to the burst of random noise (which contains the frequency range of interest) is squared then backwards integrated from an upper time limit (some time before the response is exceeded by the background noise) to the lower time limit when the sound was cut off. This produces the IIR curve, the slope of which is determined from a linear regression over the linear part of the curve (where 'linear' here refers to straight lines on a log-linear plot). Typically, the lower time limit for the linear regression was some 10 ms after the sound was cut off and the upper limit was chosen depending on the rate of the decay.

Post-processing of the results also involved performing the IIR analysis at each of the desired frequency bands. The raw data were filtered using a Butterworth bandpass filter in 10 kHz bands over the frequency range 50 kHz to 150 kHz. Butterworth filters are characterized by an extremely flat passband response with sharp cut-offs. The data were also reduced into time bins which represented the r.m.s. value of the signal for a user-defined number of samples, typically 100. The sampling rate of the DSO was 500 kHz.

It will be noted that whilst these experiments are broadband, the theories described in Chapters 2 and 3 are obtained for a single insonifying frequency. However, under the assumption that the individual frequency components are linearly independent, the single-frequency models may be applied to the interpretation of the broadband measurements in each narrow band. In the following sections good agreement is obtained between the single-frequency calculations and the frequency-binned measurements, thus validating the assumption that the frequency components may be considered as linearly independent.

6.2.4 Particle concentration and size distribution

6.2.4.1 Light scattering sensor

Because the particles settle out of suspension over time, the LSS was used to monitor the concentration to ensure that it did not change significantly over the time taken for a series of acoustic measurements to be carried out. It is important here to note the limitations of such a device for quantitative measurements of suspended particle concentration. The LSS device emits light in the forward direction and detects the light which is backscattered from the medium. Whilst the intensity of the backscattered light depends upon the concentration of particles in suspension, it also depends upon the properties of the particles, such as their size, shape and complex refractive index. The LSS may be calibrated using a known concentration of the suspension of interest. However, in cases where the suspension contains particles with a range of sizes, larger particles will settle out of suspension quicker and the size distribution will therefore be time-varying, thus invalidating the calibration. It should be noted that the LSS was not used to obtain quantitative measurements of particle concentration for normalization of the attenuation measurements. This was done by careful weighing of the quantity of particles added and ensuring that all particles were in suspension.

The LSS only provides a relative measurement of the total concentration of suspended particles in the measurement volume, and does not provide any information on the sizes of the particles present. Since the particle size is an important parameter influencing the acoustic absorption by suspended particles, it is important to know the size distribution of the particles in suspension. Whilst this is possible with spherical particles, it is not a simple matter where non-spherical particles are used. This is discussed in the following sections.

6.2.4.2 Laser diffraction analysis

Laser diffraction analysis was used to determine the size distributions of particles used in the experiments. This technique uses the diffraction pattern of laser light scattered by a sample of particulate in suspension to infer the particle size distribution in the range 0.4 μm to 1000μm. It is important to note that, since this is not an *in-situ* measurement, it was not possible to measure the particle size distribution dynamically.

It is instructive to describe briefly the laser diffraction method of particle sizing, which exploits the fact that small particles in a laser beam scatter light in a characteristic pattern, i.e. the diffraction pattern. The details of the diffraction pattern depend upon the distribution of particle sizes contributing to the light scattering. Information about the particle size distribution can thus be inferred from the details of the light flux pattern.

A discussion of diffraction by a collection of spheres should be available in any standard reference on physical optics (e.g. [64]). The simplest flux pattern, that from a monomodal dispersion of spheres, consists of a central bright spot, known as the Airy disk, surrounded by concentric bright and dark rings whose intensity diminishes further from the centre of the diffraction pattern, that is to say at higher scattering angles. The scattering angles at which the diffraction maxima and minima occur depend on the size of the particles, with smaller particles leading to higher scattering angles. The particle size in such a monomodal dispersion of spheres can therefore be simply inferred from the scattering angles.

These scattering patterns obey the principle of linear superposition, meaning that the total scattering pattern for a mixture of two (or more) monomodal dispersions can be constructed by adding the intensities of the scattering patterns from each constituent monomodal dispersion. This allows the possibility of inferring the particle size distribution from sufficiently accurate measurements of the scattering pattern due to a multimodal dispersion of spherical particles.

The interpretation of laser diffraction measurements of particle size distribution becomes complicated when non-spherical particles are involved. The standard analysis yields the size distribution of spherical particles which would give the observed diffraction pattern. In principle it would be possible to infer the size distribution of particles of a different shape by inverting a forward model for the diffracted pattern obtained from forward scattering by such particles. However for highly irregular particles and suspensions containing many different particles, this becomes impractical. A more fundamental question is what exactly we mean by the size when discussing non-spherical particles. In general non-spherical particles cannot be described by a single number, such as the diameter of a sphere. The laser diffraction technique may be considered to yield an effective spherical diameter for optical scattering. Other particle sizing techniques are available which also yield effective spherical diameters for non-spherical particles. In order to compare with the measurements made by laser diffraction, measurements have also been made using two alternative techniques: gravitational sedimentation and centrifugal sedimentation.

6.2.4.3 Gravitational sedimentation

The gravitational sedimentation technique, described in Reference [65], is based on the measurement of the rate of settling of particles. This method yields the Stokes diameter of the particle, defined as the diameter of a sphere which has the same density and the same free falling velocity in a given fluid as the particle, within the viscous flow regime. From Stokes' equation the Stokes diameter may be written

$$d_{\mathrm{st}} = \left(\frac{18 \eta h_{\mathrm{s}}}{(\rho' - \rho) g t} \right)^{\frac{1}{2}} \tag{6.5}$$

where η is the molecular viscosity of the suspending fluid, h_{s} is the distance the particle falls in time t, ρ' and ρ are the densities of the particle and fluid, and g is the acceleration due to gravity. The time taken for the particle to reach its terminal velocity is negligible [65], and the free fall velocity is therefore taken to be $v_{\mathrm{s}} = h_{\mathrm{s}}/t$.

Stokes' equation is only valid in the region of viscous flow, which sets an upper limit on the particle size which may be determined by this technique. This limit is determined by the magnitude of the Reynolds number

$$Re = \frac{\rho v_{\mathrm{s}} d_{\mathrm{st}}}{\eta} \tag{6.6}$$

The Reynolds number should not exceed 0.25 if the error in the Stokes diameter is not to exceed 3% [65]. Setting $Re = 0.25$ and equating Equations 6.5 and 6.6 yields the following expression for the limiting Stokes diameter

$$d_{\mathrm{st}}|_{\max} = \left(\frac{4.5\eta^2}{(\rho' - \rho)\rho g}\right)^{\frac{1}{3}} \tag{6.7}$$

For example, for silica ($\rho' = 2650$ kg m^{-3}), sedimenting in water ($\rho = 1000$ kg m^{-3}; $\eta = 0.001$ Pa s) the limiting Stokes diameter is 65.3 μm.

The lower size limit is partly determined by the long settling times experienced by small particles, and partly by other motions which may be significant compared to the small settling velocities, such as Brownian motion, diffusion and convection currents which may be set up over long integration periods. For these reasons the use of gravitational sedimentation is not usually recommended for particles smaller than about 1 μm.

6.2.4.4 Centrifugal sedimentation

Some of the difficulties associated with the use of gravitational sedimentation for fine particles may be reduced by speeding up the settling time. This may be achieved through the use of centrifugal sedimentation techniques, described in [66].

As in the case of gravitational sedimentation the Stokes diameter is determined from Stokes' law (see Equation 6.5), but now the acceleration due to gravity is replaced by the centrifugal acceleration and the free fall velocity is replaced by the radial settling velocity to give

$$d_{\mathrm{st}} = \left(\frac{18\eta}{(\rho' - \rho)\omega_{\mathrm{c}}^2 r_{\mathrm{c}}}\frac{\mathrm{d}r_{\mathrm{c}}}{\mathrm{d}t}\right)^{\frac{1}{2}} \tag{6.8}$$

where r_{c} is the radial distance of the particle from the axis of the centrifuge, $\mathrm{d}r_{\mathrm{c}}/\mathrm{d}t$ is the radial settling velocity and ω_{c} is the rotation speed of the centrifuge.

Centrifugal sedimentation is usually used for particles up to a few microns in diameter, although this can easily be extended using more viscous suspending fluids and longer settling times. The lower limit on particle size is determined by the consideration that the radial displacement of the particles by Brownian motion during sedimentation should be much smaller than the displacement due to centrifugal motion. For a typical example (see [66]) the minimum Stokes diameter is less than 0.01 μm.

For the measurements of the size distributions of clay-like and marine sediment particles presented later in this chapter, the samples were dispersed in the suspension media and insonified with ultrasound (normally for one minute) to assist in dispersal and breaking up of agglomerates. Additionally, the sample portions used for the centrifugal sedimentation were dispersed using prolonged ultrasonics in an attempt to disseminate the aggregates and obtain a particle size distribution more representative of the discrete particles.

6.3 Turbulence

Since stirring is employed in the experiments to suspend the particles there is a degree of turbulence inherent in the measurement volume. It is therefore necessary to investigate the potential impact of this turbulence on the acoustic absorption to determine whether it is an important contribution to the total absorption coefficient being measured in the experiments.

Noir and George [67] calculated the amount of acoustic energy converted to turbulent kinetic energy for a plane wave propagating through an unbounded field of turbulence. Their approach has been used here to estimate the order of magnitude of the contribution to the acoustic absorption coefficient resulting from turbulence in the experiments. Their analysis is based on the interaction of two opposing phenomena. These are the perturbation of the turbulence field by the acoustic wave, leading to anisotropic Reynolds stresses, and the redistribution of turbulent kinetic energy as it cascades from the large scale to the dissipation scale, leading to a return to isotropy. As a result of these two effects, the Reynolds stress is not in phase with the acoustic field, and there is thus a net transfer of energy from the acoustic field to turbulent kinetic energy, corresponding to absorption of acoustic energy.

As the acoustic time scales are generally much shorter than the time scales associated with the turbulence, previous investigators assumed that there is no change in the turbulence structure over the time scale of the interaction, thus considering *frozen* turbulence. Noir and George, however, allowed the Reynolds stresses to fluctuate in response to the sound wave in their analysis, thus introducing *non-frozen* turbulence.

In terms of energy, the absorption of sound by turbulence produces additional turbulent kinetic energy, which is eventually dissipated by viscosity. The production term in the turbulent kinetic energy equation involves mean-flow gradients and the normal Reynolds stresses. A model of the coupling between the Reynolds stress and the mean flow then results in a time-average production of turbulent kinetic energy.

Unfortunately the analysis of Noir and George does not lend itself well to summarization without compromising clarity, so this section is necessarily limited to simply quoting their key results. For the complete argument the interested reader is referred to the original paper [67].

Assuming that the distortion of the turbulence field by the acoustic wave may be considered to be locally homogeneous, the analysis of Reference [67] yields the following result for the absorption coefficient due to turbulence, α_τ:

$$\alpha_\tau \simeq 20 \log(\mathrm{e}) \left(\frac{2.3 \epsilon_\mathrm{d}}{c^3} \right) \tag{6.9}$$

where ϵ_d is the dissipation rate of turbulent kinetic energy and c is the speed of sound. In cases where the acoustic wavelength is smaller than the largest length scale of the flow, as may be the case in the experimental system described here, the acoustic wavelength, λ, is taken to be the upper limit of the spatial scale, and the attenuation coefficient becomes

$$\alpha_\tau \simeq 20 \log(\mathrm{e}) \left[\frac{1.3 \epsilon_\mathrm{d}}{c^3} \ln \left(\frac{\lambda}{\eta_\mathrm{k}} \right) \right] \tag{6.10}$$

where η_k is the Kolmogorov length scale, the characteristic scale of the turbulent eddies at the smallest, dissipative end of the turbulent energy cascade process, given by

$$\eta_\mathrm{k} = \left(\frac{\nu^3}{\epsilon_\mathrm{d}} \right)^{1/4} \tag{6.11}$$

where ν is the kinematic viscosity of the fluid.

Both of the expressions for the coefficient of sound absorption by turbulence (Equations 6.9 and 6.10) clearly depend upon the dissipation rate, ϵ_d, of turbulent kinetic energy which, in the case of the experimental system discussed in this chapter, is not known. The predictions of these two equations are shown in Figure 6.3 as functions of this turbulent dissipation rate. The solid line shows the result of Equation 6.10, which assumes that the turbulence may be approximately characterized by an energy spectrum of the form

$$E(\kappa_e) \sim 1.5\epsilon_d^{2/3} k_e^{-5/3} \tag{6.12}$$

where k_e is the wavenumber of the turbulent eddies.

The dotted line shows the result of assuming that the turbulence is locally homogeneous (Equation 6.9). Note that the two equations give significantly different predictions of the attenuation coefficient as a result of the different assumptions made in each case [67]. Both models, however, predict that the attenuation coefficient is several orders of magnitude below the calculated viscous absorption coefficient and the measured attenuation coefficient presented in Section 6.4 over most of the range of dissipation rate shown.

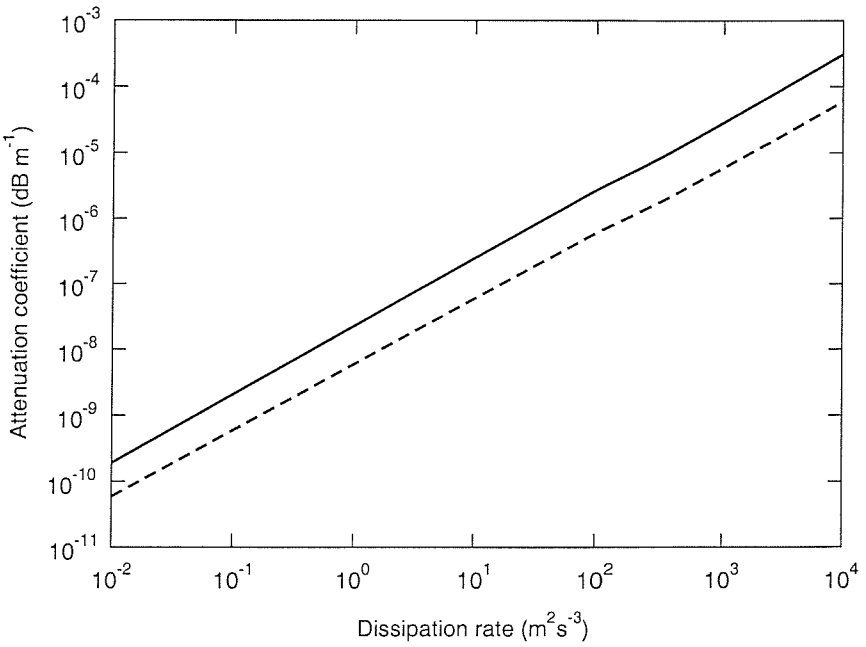

Figure 6.3. Predicted attenuation coefficient due to turbulence

Although it is not possible to predict accurately the turbulent dissipation rate in the experimental system, it is possible estimate an upper limit on the order of magnitude of this parameter, allowing us to estimate the maximum order of magnitude of the turbulence attenuation coefficient. Let us assume that the maximum rate at which turbulent kinetic energy is dissipated in the experimental system is equal to the rate at which energy is supplied to the system by the mechanical stirrer. In fact this will overestimate the dissipation rate, as we know from observations that the system remains turbulent after the stirrer has been switched off. The electrical power rating of the stirrer motor is 25 W. Let us assume that this power is coupled to the turbulence with an efficiency of 0.3 (an optimistic estimate), such that the maximum possible

rate at which turbulent kinetic energy is produced in the system is about 7.5 W. Recognizing that the units in which the dissipation rate is expressed (m^2s^{-3}) are dimensionally equivalent to Wkg^{-1} we can estimate that the upper limit of the turbulence dissipation rate in the 16 kg or so of water in the experimental system is less than 1 m^2s^{-3}. From Figure 6.3 we can therefore see that the upper limit on the turbulence absorption coefficient to be expected in the experimental system is of the order of 10^{-8} dBm^{-1}. This is several orders of magnitude smaller than the predicted viscous absorption coefficient and the measured absorption, suggesting that the phenomenon of sound absorption by turbulence may be neglected in the present series of measurements.

6.4 Results

In this section results of measurements made using three different categories of particles are presented in a logical order. Firstly results of measurements made using spherical glass particles are presented. These particles were chosen to enable direct comparisons to be made between measurements and the prediction of the models described in Chapter 2, which assume the particles to be spherical. Next to be presented are results from pure samples of clay-like particles. These particles are similar in form to particles found in natural, fine-particulate suspensions, but are much better characterized than natural samples and have known physical properties. Finally results are presented of measurements made with natural, marine sediment particles.

To help the reader understand the nature of the measurements it is perhaps helpful at this point to show an example of a measured reverberation decay curve.

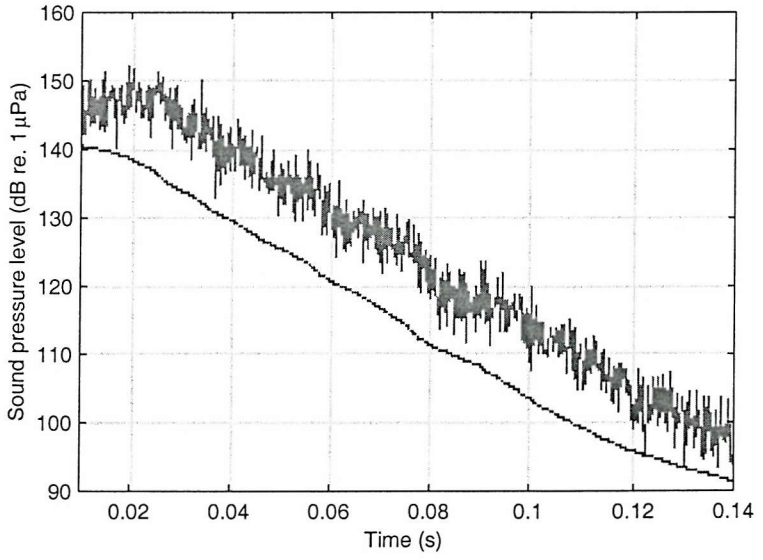

Figure 6.4. Typical binned time trace for reverberation time calculation (upper curve) and corresponding integrated impulse response (lower curve). Note that the vertical scale applies only to the time trace.

Figure 6.4 shows the binned time trace and integrated impulse response curve for a typical sample. The IIR curve clearly represents the decay rate of the sound energy in the volume. It should be noted that the vertical scale in Figure 6.4 relates only to the time trace, not to the IIR curve of which only the gradient is important. The reverberation time calculated for this trace

was 0.139 s and the figure illustrates that the magnitude of the decay curve drops by nearly 60 dB in the time shown.

6.4.1 Spherical particles

Initial measurements were made using spherical glass beads. This was to facilitate direct comparison with the predictions of the models of Chapter 2, which are based on the assumption of homogeneous spherical particles.

6.4.1.1 Scanning electron micrographs

Examples of the spherical glass particles are shown in the scanning electron microscope (SEM) images of Figures 6.5 and 6.6 These images show the high degree of sphericity of these particles.

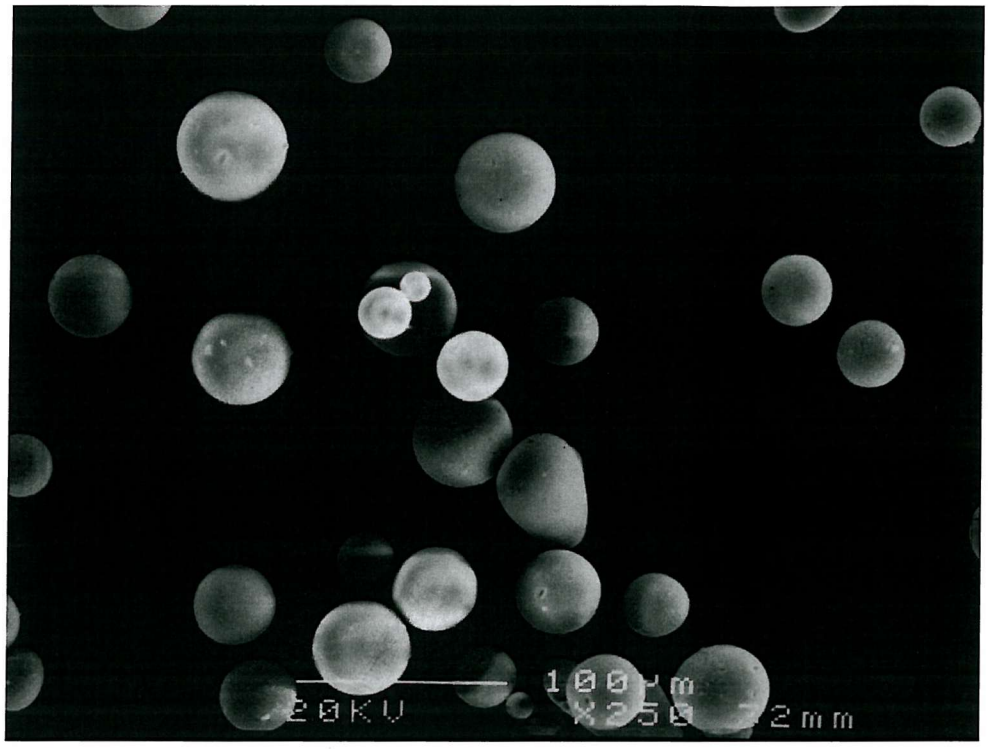

Figure 6.5. Scanning electron microscope image of glass particles taken with an original instrument magnification of ×250.

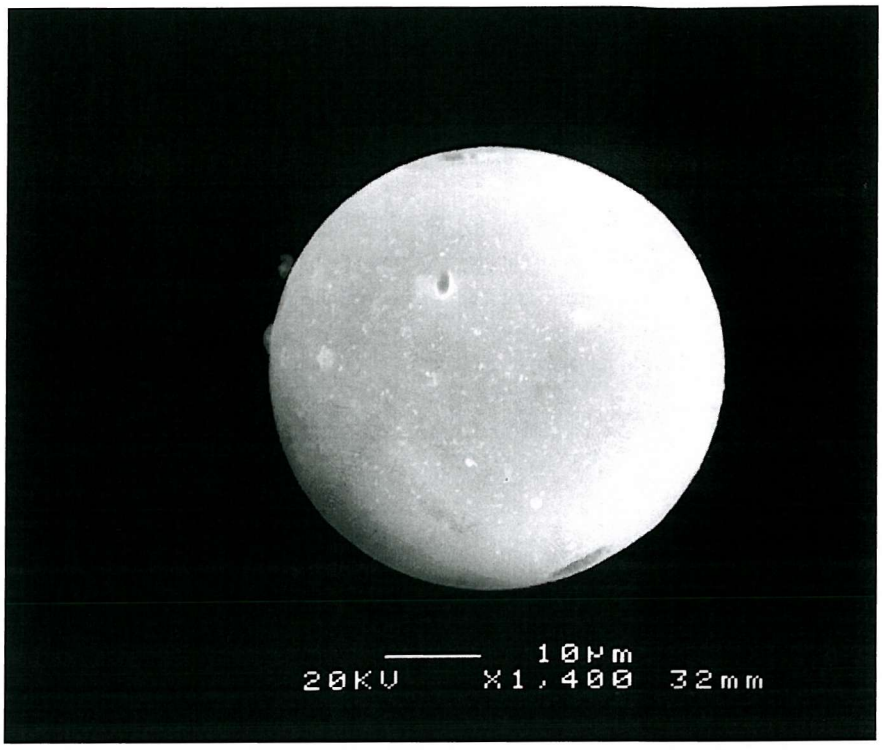

Figure 6.6. Scanning electron microscope image of glass particles - detail of area shown in Figure 6.5 with an original magnification of ×1400.

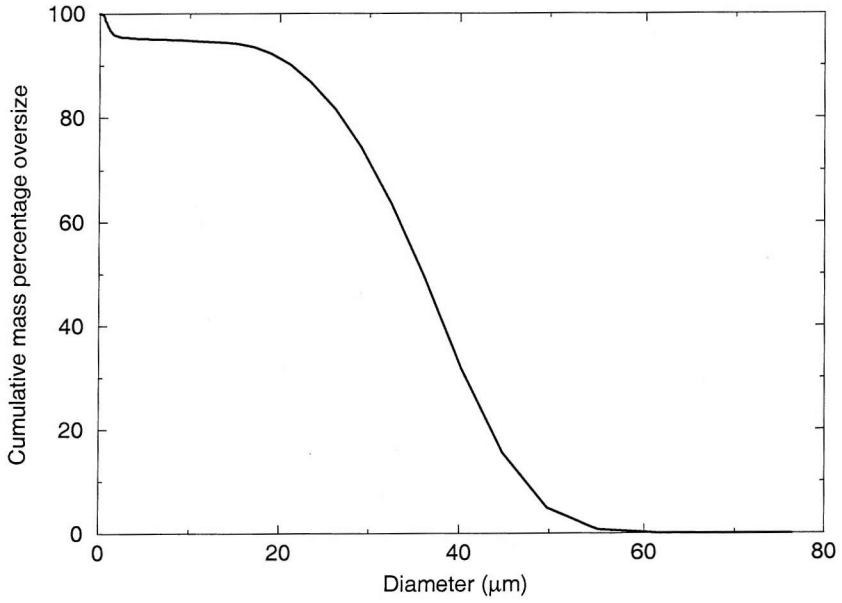

Figure 6.7. Size distribution of spherical glass particles measured by laser diffraction analysis.

6.4.1.2 Particle size distributions

Figure 6.7 shows the size distribution of these particles, measured using the laser diffraction analysis technique described on page 79, the measurements being made in the Department of Geology, University of Southampton.

6.4.1.3 Attenuation measurements

In order to provide a reference measurement, the decay rate of the reverberant sound field was first measured in particulate-free water. To this known quantities of particulate were then added in stages in order to measure the decay rate at various concentrations.

Figures 6.8 to 6.14 show the attenuation coefficient measured with increasing concentrations of suspended particles, as a function of frequency, normalized to a concentration of 1 kgm^{-3}. Also shown in each of these figures is the calculated viscous absorption coefficient obtained using the Urick expression (Equation 2.31) integrated over the measured particle size distribution shown in Figure 6.7.

The most significant contribution to the experimental error in the attenuation measurements was found to be a residual spatial dependence of the sound field. A series of reverberation measurements made with the hydrophones in different locations within the bag showed a 4% standard deviation in the reverberation time. The error bars shown on the experimental data plotted in this chapter are therefore derived from this 4% standard deviation in reverberation time, together with smaller contributions due to changes in water temperature over the duration of the measurements and errors in the mass of added particulate.

It is clear from these figures that the agreement between the experimental measurements and the theoretical predictions significantly improves as the concentration is increased. This is to be expected since at low concentrations the difference in the decay rates caused by the introduction of the particles is small, and this is reflected in the larger error bars on the low concentration data points. However, in all cases the theoretical curve lies within the error bars of the majority of the data points. At the highest concentrations the error bars are relatively small, and the fact that most of the experimental data lie on the theoretical curve to within this error indicates that the attenuation measurements are in agreement with the predictions of the Urick model for viscous absorption. It should be noted that, since the experimental technique is based on measurements of the decay of a reverberant sound field, sound that is scattered by the particles remains a contribution to the sound field in question and does not therefore represent a loss from the system. The model used for the theoretical predictions in this chapter does not therefore include the effects of sound scattering. The experimental measurements do, however, include any other dissipative processes in which sound is converted to other forms of energy (ultimately heat) as a result of the presence of the particles. Therefore the thermal absorption contribution discussed in Chapter 2 would also be included in the measured attenuation. The fact that the Urick model for visco-inertial absorption appears to predict the measured attenuation reasonably well suggests that, in the case under investigation, thermal absorption does not represent a significant contribution to the total dissipative attenuation coefficient, as predicted in Chapter 2.

It may be noted that an anomalously high attenuation at 50 kHz appears to be a common feature in Figures 6.8 to 6.14. It should, however, be remembered that the Schroeder cut-off

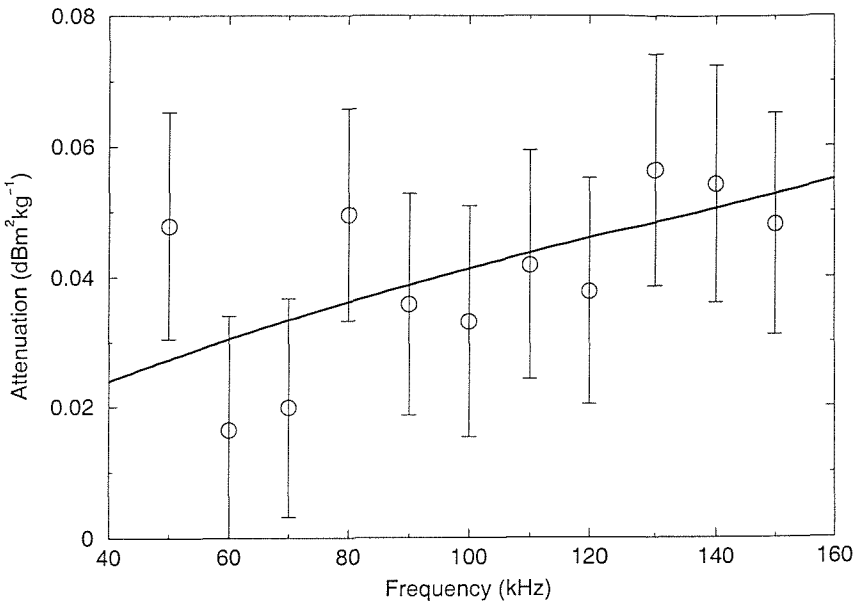

Figure 6.8. Normalized attenuation coefficient measured with a concentration of 0.50 kgm^{-3} (circles) compared with theoretical prediction (solid line).

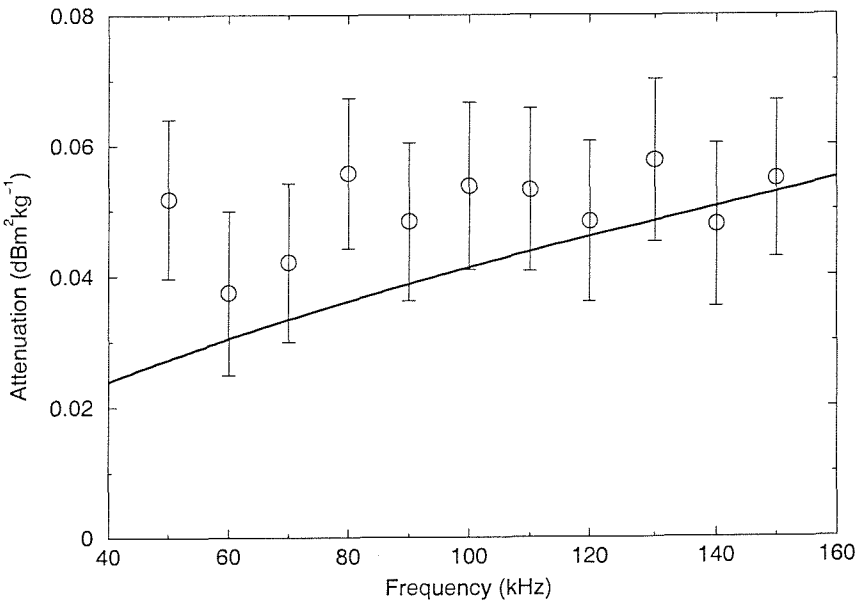

Figure 6.9. Normalized attenuation coefficient measured with a concentration of 0.75 kgm^{-3} (circles) compared with theoretical prediction (solid line).

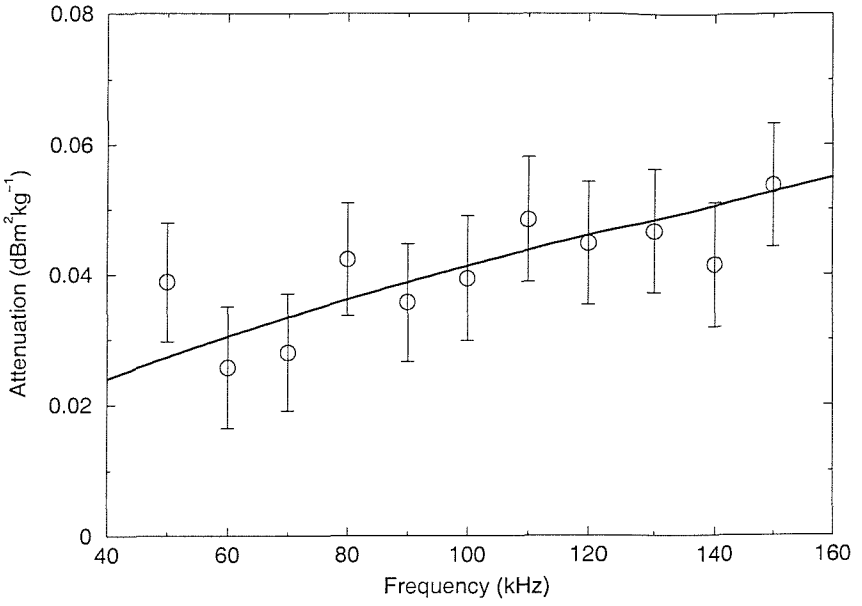

Figure 6.10. Normalized attenuation coefficient measured with a concentration of 1.00 kgm^{-3} (circles) compared with theoretical prediction (solid line).

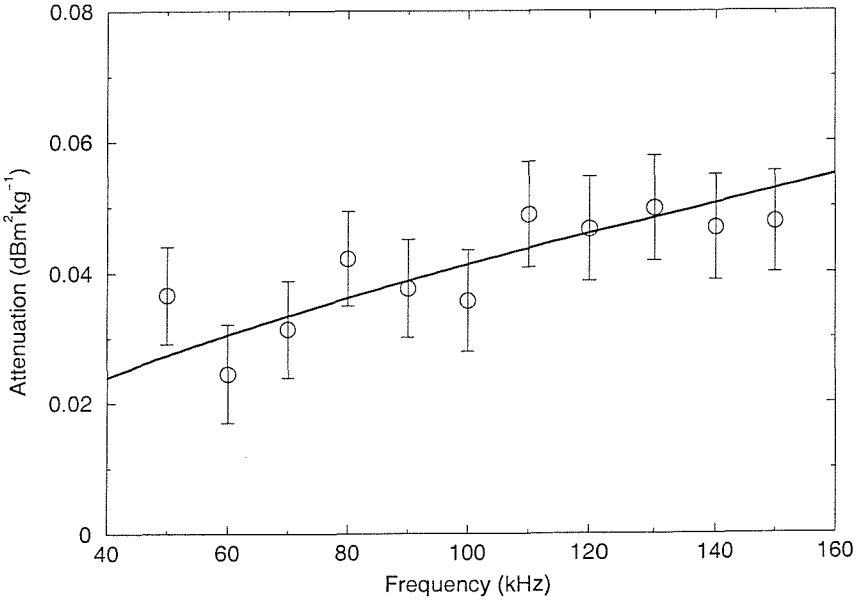

Figure 6.11. Normalized attenuation coefficient measured with a concentration of 1.25 kgm^{-3} (circles) compared with theoretical prediction (solid line).

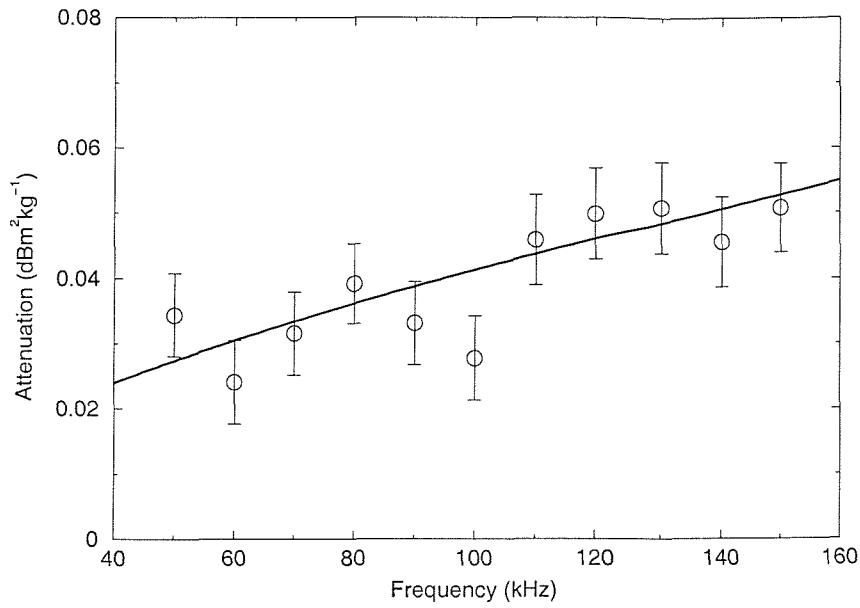

Figure 6.12. Normalized attenuation coefficient measured with a concentration of 1.50 kgm^{-3} (circles) compared with theoretical prediction (solid line).

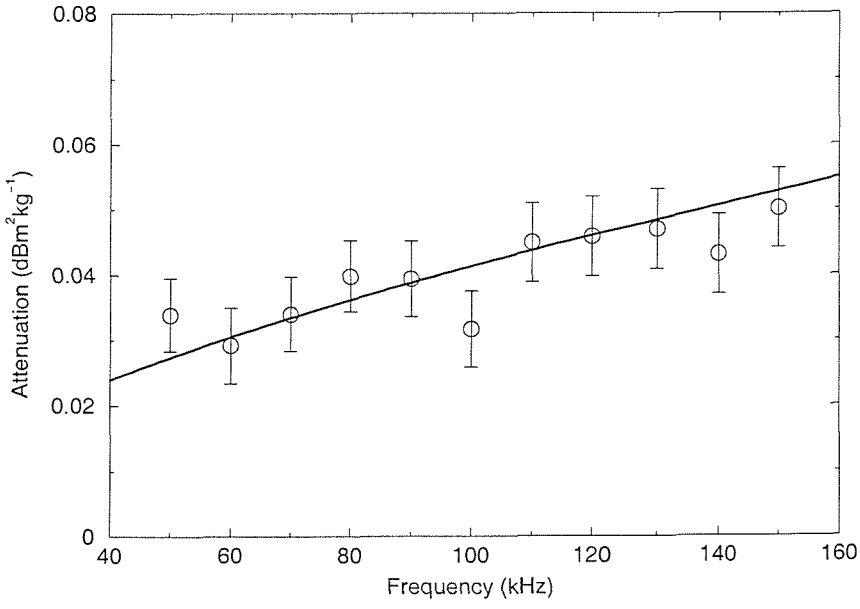

Figure 6.13. Normalized attenuation coefficient measured with a concentration of 1.75 kgm^{-3} (circles) compared with theoretical prediction (solid line).

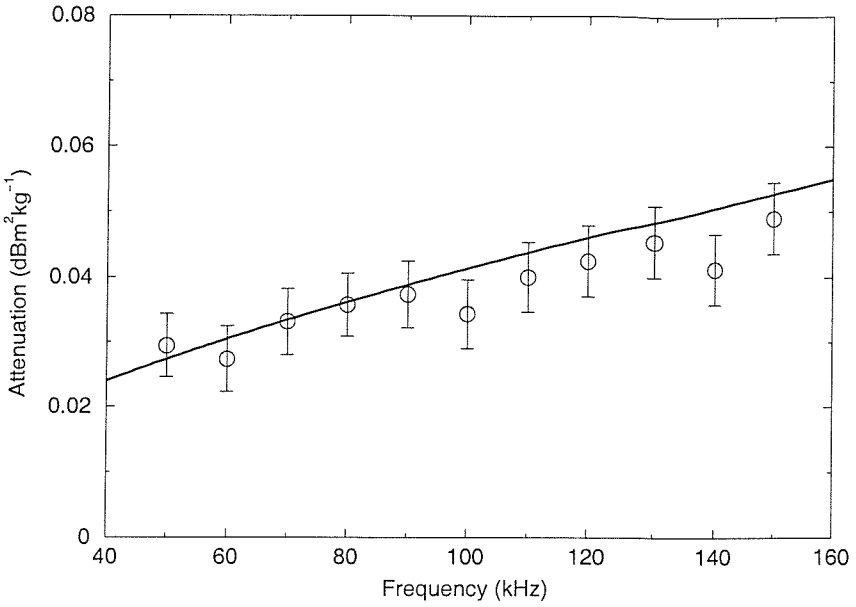

Figure 6.14. Normalized attenuation coefficient measured with a concentration of 2.00 kgm^{-3} (circles) compared with theoretical prediction (solid line).

frequency of the measurement volume is around 55 kHz, and it is therefore reasonable to assume that the sound field at 50 kHz is not truly diffuse, and some modal structure in the system may therefore be responsible for the observed anomalies.

6.4.1.4 Particle settling

An example of a LSS measurement is shown in Figure 6.15. This figure shows the variation in suspended particle concentration as a function of time, for a suspension with a nominal concentration of 1 kgm^{-3}. The trace clearly shows the time at which the stirrer was turned on and also demonstrates that the nominal concentration is reached very quickly. This indicates that the suspension is well mixed by that time. The stirrer was switched off at 20 s and the concentration shows a gradual decay from that time, as the particles settle out. The smooth curve in the figure is the result of a theoretical calculation of the concentration as a function of time based on considerations of the particles settling out at the Stokes settling velocity, v_s, given by (c.f. Equation 6.5)

$$v_s = \frac{(2a)^2 (\rho' - \rho) g}{18\eta} \tag{6.13}$$

where a is the radius of the particles, ρ' and ρ are the densities of the particles and suspending fluid, g is the acceleration due to gravity and η is the dynamic shear viscosity of the suspending fluid. The settling calculation was performed for each particle size in the distribution and the results show the total concentration of suspended particles at each time. Clearly the measurement displays some fluctuation in the concentration, but the general trend agrees reasonably well with the predicted concentration.

The size distribution of the suspended particles is shown in Figure 6.16. In this figure the solid

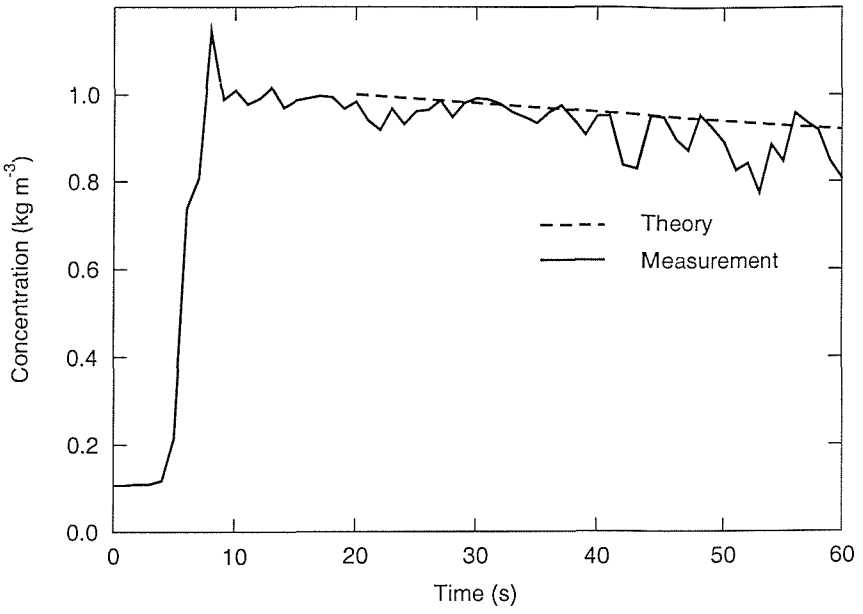

Figure 6.15. Temporal variation of particle concentration measured using the LSS, compared with prediction based on Equation 6.13.

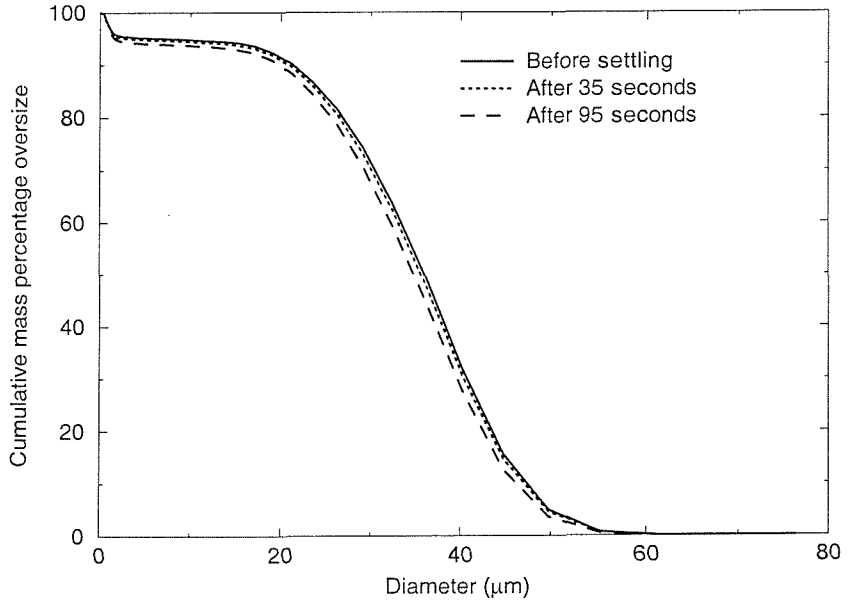

Figure 6.16. Temporal variation of particle size distribution predicted by Equation 6.13.

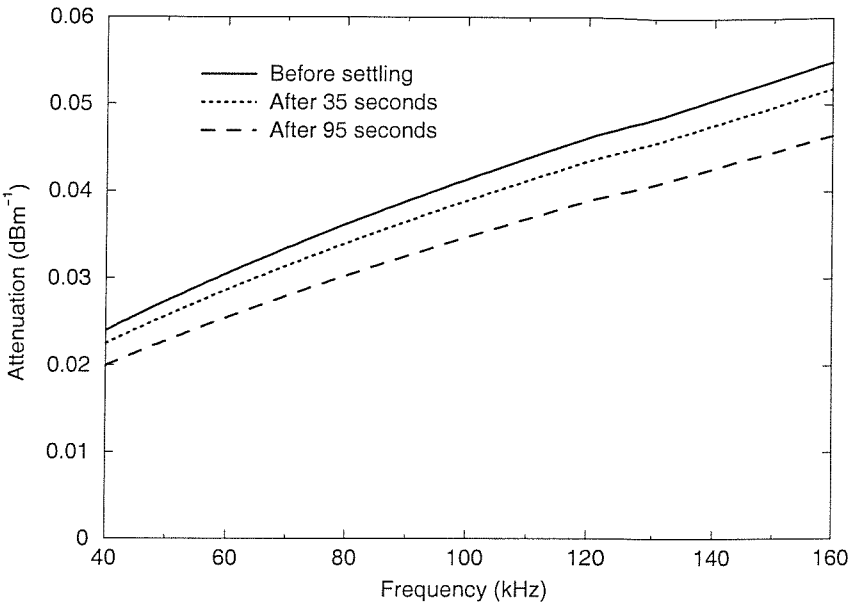

Figure 6.17. Calculated attenuation coefficient before and after particle settling based on the the particle size distributions shown in Figure 6.16.

curve denotes the distribution measured by laser diffraction analysis, and the dotted and dashed curves show the predicted distribution 35 s and 95 s later, respectively, calculated using the Stokes settling model described above. This figure shows that the size distribution shifts slightly towards smaller particles as the particles settle. This is to be expected since the larger particles sink more rapidly than the smaller particles. The lack of a dynamic measurement of the particle size distribution in the system meant that these predictions could not be tested experimentally, but as has already been shown the predictions of total concentration agreed well with the LSS measurements.

In order to investigate the effect of the settling out of the particles on the attenuation, the visco-inertial absorption coefficients were calculated for both the initial distribution and the predicted distributions after 35 s and 95 s of settling shown in Figure 6.16, assuming a total initial concentration of 1 kgm^{-3}. The results of these calculations are shown in Figure 6.17. The line-styles of the curves in this figure correspond to the those in Figure 6.16, such that the solid curve is the attenuation with the initial distribution, and the dotted and dashed curves show the attenuation with the predicted distributions after 35 s and 95 s of settling respectively. Clearly the attenuation reduces as the particles settle out, as expected. The acoustic measurements were all made within 35 s of the stirrer being switched off, and although the reduction in attenuation is noticeable after this time, it is relatively small and well within the experimental error of the measurement.

6.4.2 Clay-like particles

The preceding section showed how good agreement was obtained between measurements of absorption made with spherical particles and the Urick model for viscous absorption by spherical particles. The next stage in the experimental programme was to make measurements with

non-spherical particles to assess the applicability of the spherical models as the particles depart from being spherical.

For this purpose two samples of particulates were obtained from ECCI (English China Clays International, now Imerys). The first was a type of kaolin (china clay) with the trade name Speswhite, and the second was a form of calcium carbonate with the trade name Polcarb. Both of these samples were relatively pure and relatively well characterized industrial samples, allowing the study of absorption by non-spherical particles without the problems associated with using natural marine sediments of unknown composition and physical parameters.

6.4.2.1 Scanning electron micrographs

Figures 6.18 to 6.20 show scanning electron micrographs of the Speswhite particles. They were produced by DERA Bridgwater [68] using the following technique.

A clean brush was dipped into each of the samples and brushed across a carbon impregnated sticky tab attached to an aluminium stub. Any excess material was blown off using compressed air. The samples were then gold coated in a sputter coater in order to make them electrically conducting, before being examined on the scanning electron microscope at various magnifications.

Figure 6.18 shows a typical area of the sample, imaged at an original magnification of $\times 2000$. Obviously the magnification of the printed image differs from the the original instrument magnification, but the scale is indicated by the micron marker at the bottom right of the image.

Figures 6.19 and 6.20 show higher magnification ($\times 10000$) details of parts of the area shown in Figure 6.18.

It may be seen from these micrographs that the sample is composed of flat, very thin, plate-like flakes which aggregate together to form larger particles. This structure is typical of clay minerals. The difference between the plate thickness and length or width can clearly be seen in some cases. The whole sample appeared to be composed of these plate-like, flat, clay particles, with very little material from other origins, as expected for this nominally pure industrial sample.

Figures 6.21 to 6.23 show representative scanning electron micrographs of the Polcarb particles [68]. Figure 6.21 was obtained using an original instrument magnification of $\times 2000$ and Figures 6.22 and 6.23 show details of this region at an original magnification of $\times 10000$.

It may be seen that the form of the particles is different from the Speswhite particles shown in the previous images. Here there are few aggregates, and the particles are more angular and not plate-like. Some particles do appear to be composed of layers, but they are larger and appear thicker than the china clay flakes.

6.4.2.2 Particle size distributions

Figures 6.24 and 6.25 show particle size distributions for the Speswhite and Polcarb particles respectively, measured using laser diffraction analysis, gravitational sedimentation and centrifugal sedimentation [68].

Clearly there are very significant differences between the size distributions obtained using these different methods. This serves as an illustration of the fundamental difficulties of characterizing irregular particles. The laser diffraction technique may be considered to yield an effective optical

Figure 6.18. Scanning electron micrograph of Speswhite particles taken with an original instrument magnification of $\times 2000$.

Figure 6.19. Scanning electron micrograph of Speswhite particles taken with an original instrument magnification of $\times 10000$ - detail of area shown in Figure 6.18.

Figure 6.20. Scanning electron micrograph of Speswhite particles taken with an original instrument magnification of ×10000 - another detail of area shown in Figure 6.18

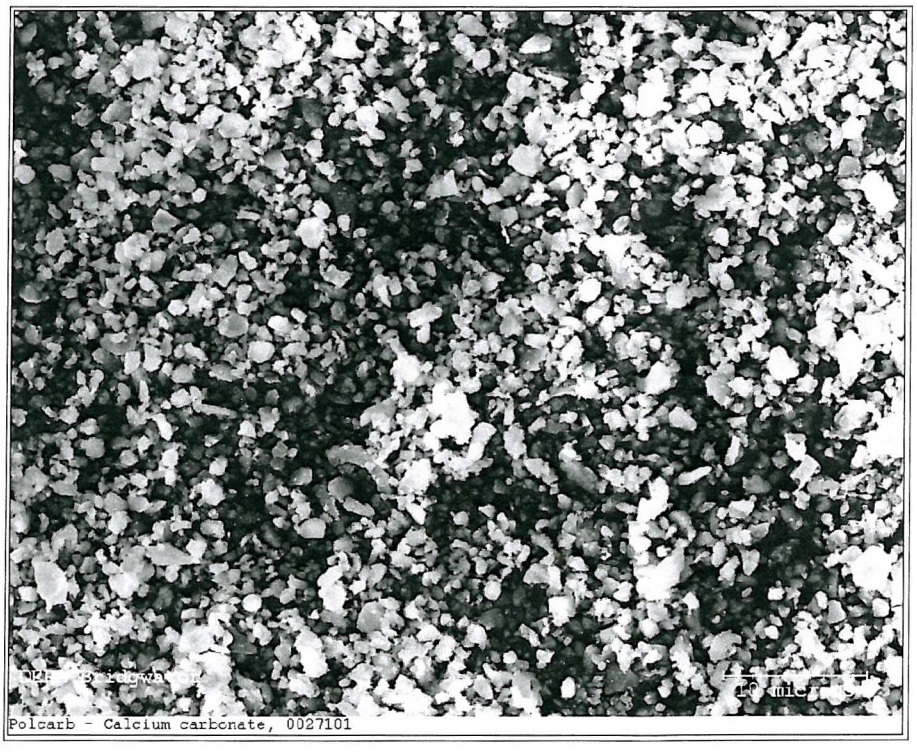

Figure 6.21. Scanning electron micrograph of Polcarb particles taken with an original instrument magnification of ×2000.

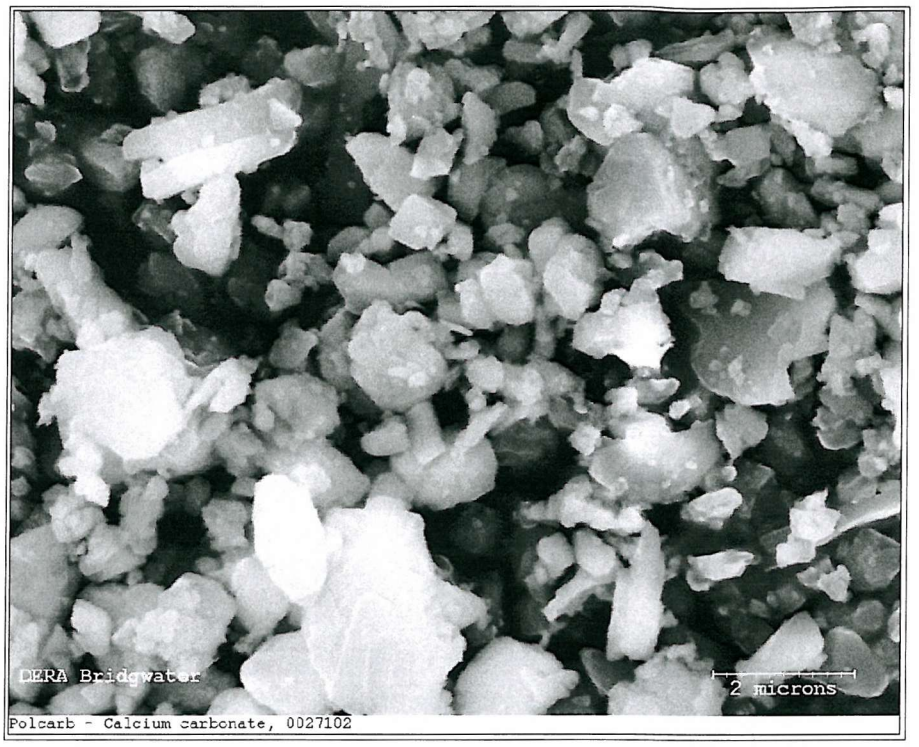

Figure 6.22. Scanning electron micrograph of Polcarb particles taken with an original instrument magnification of ×10000 - detail of area shown Figure 6.21.

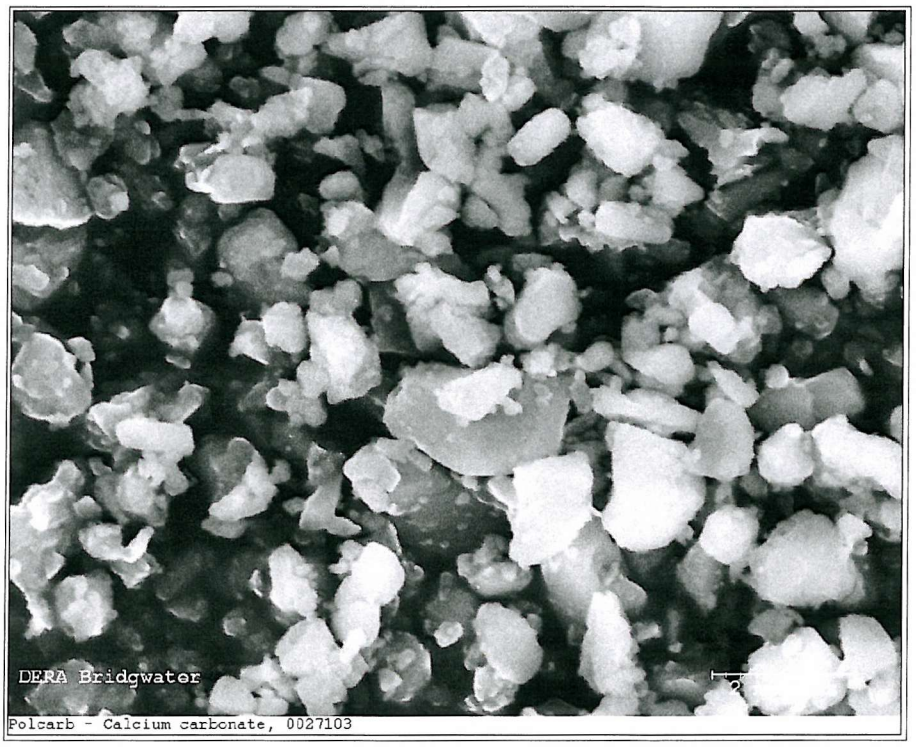

Figure 6.23. Scanning electron micrograph of Polcarb particles taken with an original instrument magnification of ×10000 - another detail of area shown in Figure 6.21.

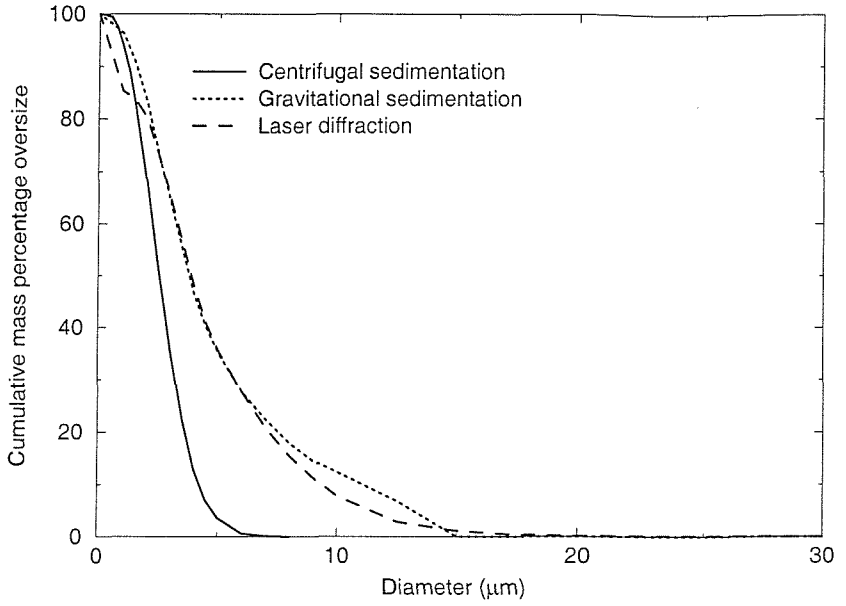

Figure 6.24. Size distribution of Speswhite particles measured by centrifugal sedimentation, gravitational sedimentation and laser diffraction.

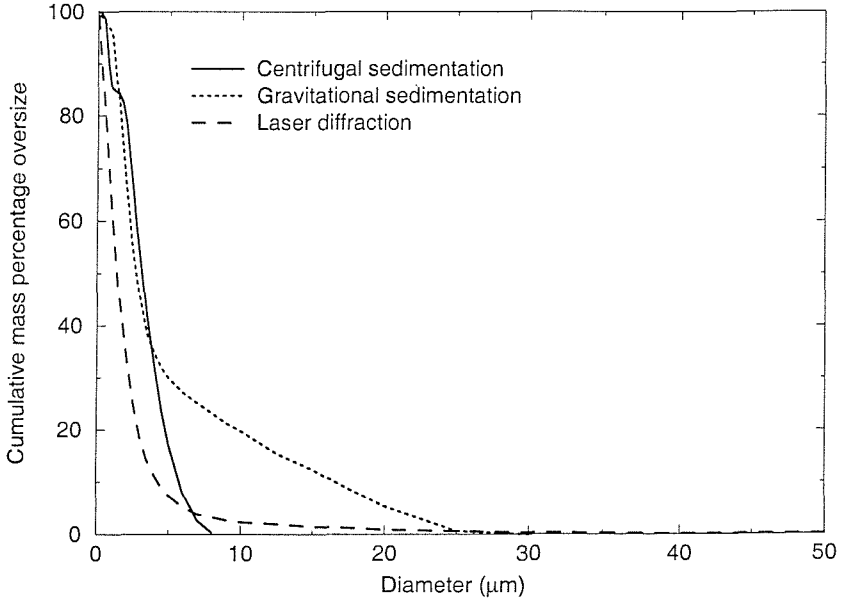

Figure 6.25. Size distribution of Polcarb particles measured by centrifugal sedimentation, gravitational sedimentation and laser diffraction.

scatterer dimension, since it gives the size distribution of spherical particles which would give the observed optical diffraction pattern. Both the gravitational and centrifugal sedimentation techniques use Stokes' law to determine particle size, and hence yield an effective Stokes diameter.

In the case of Speswhite in particular the centrifugal sedimentation measurement shows a strong bias towards smaller particles. Since samples used for the centrifugal sedimentation measurements were treated with prolonged ultrasound to break up aggregates this might possibly be an indication that there was some degree of aggregation of the Speswhite particles. This is consistent with the SEMs of the Speswhite particles, which do show some clumping of particles.

6.4.2.3 Attenuation measurements

Figure 6.26 shows the measured attenuation coefficient for the Speswhite (kaolin) particles as a function of frequency, normalized with respect to concentration. The symbols indicate measurements made at different concentrations. The measurements are binned at 10 kHz intervals over the range 50-150 kHz, but are shown offset slightly so that the individual error bars can be resolved.

Also shown on this graph is the attenuation predicted by Equation 2.31 for spherical particles using the three size distributions shown in Figure 6.24. These three predictions are in surprisingly close agreement with each other, given the apparent differences displayed by the size distributions measured by the different techniques. However, it must be remembered that over the relatively limited frequency range of the acoustic measurements the absorption is dominated by those particles whose size is close to the peak in the visco-inertial absorption (see Figure 4.3). As expected for these highly non-spherical particles, the prediction of the theory for spherical particles does not agree well with the measured attenuation.

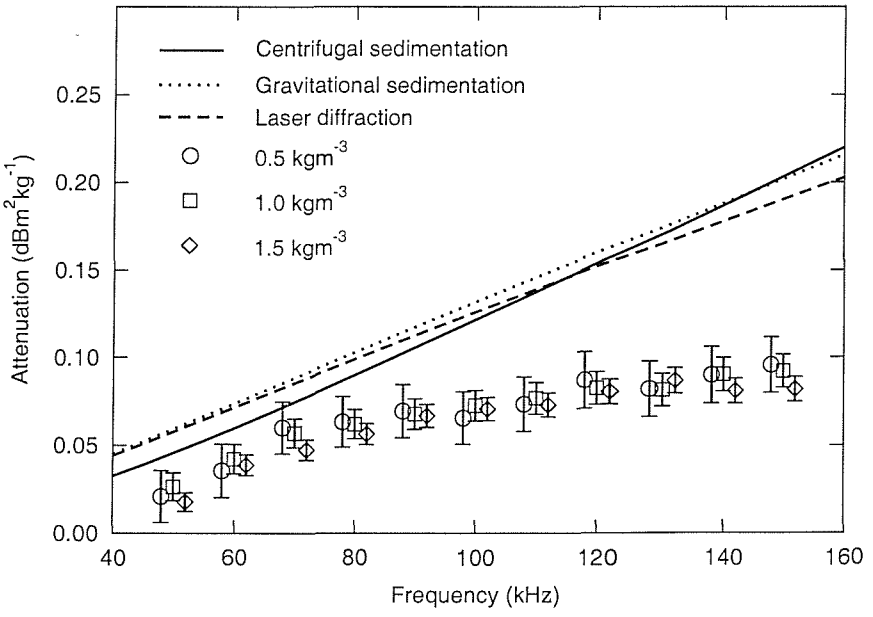

Figure 6.26. Normalized attenuation coefficient for Speswhite particles: experimental data and theoretical predictions assuming spherical particles. Data points have been offset in frequency to show individual error bars (see text).

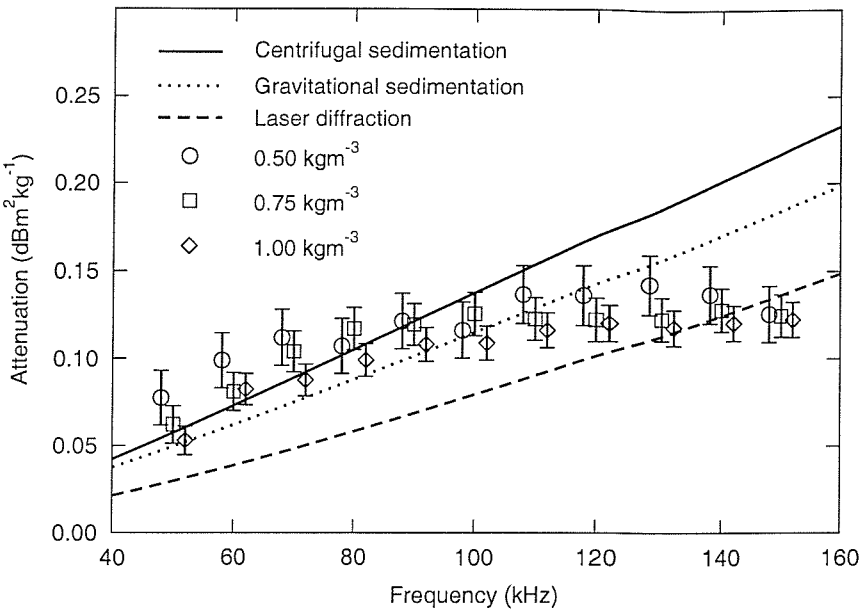

Figure 6.27. Normalized attenuation coefficient for Polcarb particles: experimental data and theoretical predictions assuming spherical particles. Data points have been offset in frequency to show individual error bars (see text).

Figure 6.27 shows the results of the measurements of attenuation with Polcarb (calcium carbonate) particles. Again, the symbols indicate measurements made at different concentrations, and the data have been normalized with respect to concentration. In this case the theoretical predictions using the size distributions yielded by the different sizing techniques show greater differences than in the case of the Speswhite. This would be because the size distributions have greater differences in the particle size range contributing most to the absorption, although this is not immediately apparent from visual inspection of the curves showing cumulative mass percentage oversize.

The measurements for Polcarb show much better agreement with the theoretical predictions than was the case for Speswhite. Although the theoretical curves do not have the same form for the frequency dependence as suggested by the data, the magnitude of the predicted absorption is close to the measured absorption over much of the frequency range. The fact that the Polcarb measurements agree better with the predictions of the spherical particle theory than the Speswhite measurements is not surprising, since inspection of the SEMs shows the Speswhite particles to be highly plate-like whereas the Polcarb particles, although certainly irregular and non-spherical, are closer to spheres in aspect ratio.

6.4.3 Marine sediments

The measurements with spherical particles described in Section 6.4 enabled the models to be tested in the idealized case. Moving to the Speswhite and Polcarb particles allowed investigations to be carried out with highly non-spherical particles in a relatively controlled way. The final part of the experimental study involved the use of real marine sediment particles from a seabed sediment core sample. This core was obtained in about 1600 m of water on the continental slope,

west of the Malin Shelf and comprises primarily soft grey clay.

6.4.3.1 Scanning electron micrographs

Figure 6.28 shows a SEM image of a typical sample of these sediment particles, imaged at an instrument magnification of ×2000 [68]. Figures 6.29 and 6.30 show details of the area shown in Figure 6.28, imaged at a magnification of ×10000. These figures show that the particles are highly irregular and highly variable, with a mixture of plate-like particles and more granular particles. This sample does appear to have similarities with the Speswhite sample, indicating that the sediment contains a significant component of clay-like particles. However, there also appear to be other types of particle present. Grains appear to range in size from fine silt (about 10 to 15 μm) to fine clays (about 0.5 to 1 μm). Although the SEM was not used to identify grain mineralogy, it is likely that the sample will comprise quartz, chlorite, calcite, feldspar and illite [69].

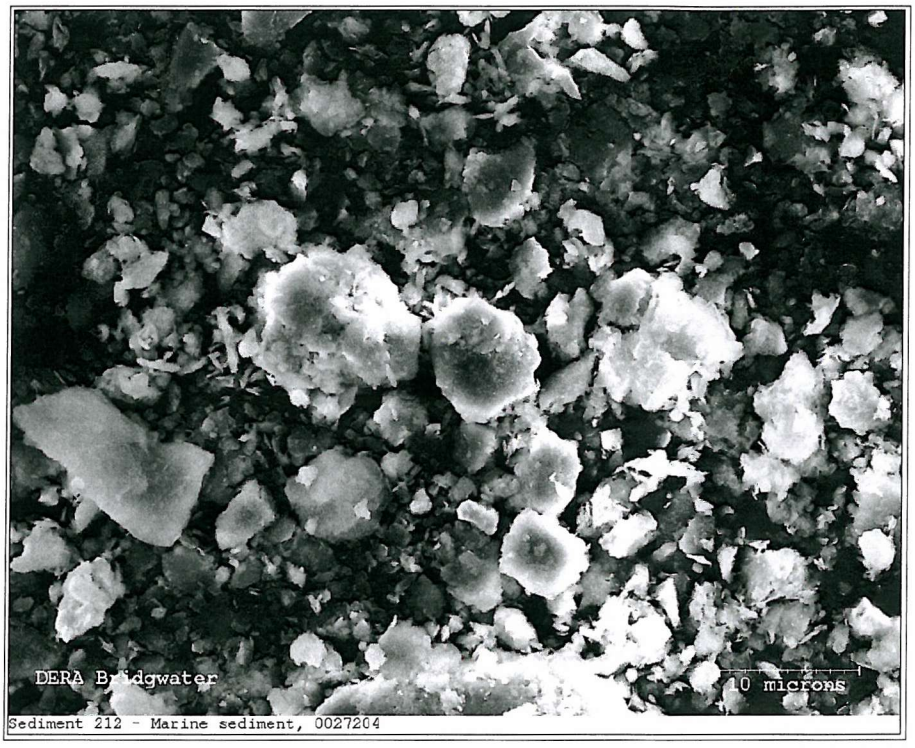

Figure 6.28. Scanning electron micrograph of sediment particles taken with an original instrument magnification of ×2000.

6.4.3.2 Particle size distributions

Figure 6.31 shows the size distribution of these particles, measured by laser diffraction analysis, centrifugal sedimentation and gravitational sedimentation. Again, the three techniques yield different results over much of the size range. As with the Speswhite the centrifugal sedimentation technique yields a size distribution biased towards smaller particles, indicating that there might be some aggregation of these particles. This is supported by the SEMs.

Figure 6.29. Scanning electron micrograph of sediment particles taken with an original instrument magnification of ×10000 - detail of the area shown in Figure 6.28.

Figure 6.30. Scanning electron micrograph of sediment particles taken with an original instrument magnification of ×10000 - another detail of the area shown in Figure 6.28.

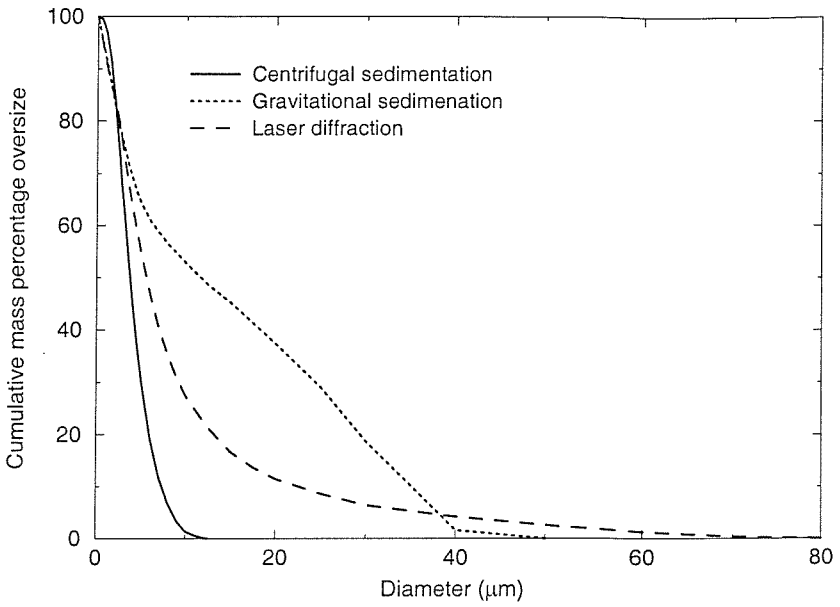

Figure 6.31. Size distribution of sediment particles measured by centrifugal sedimentation, gravitational sedimentation and laser diffraction.

6.4.3.3 Attenuation measurements

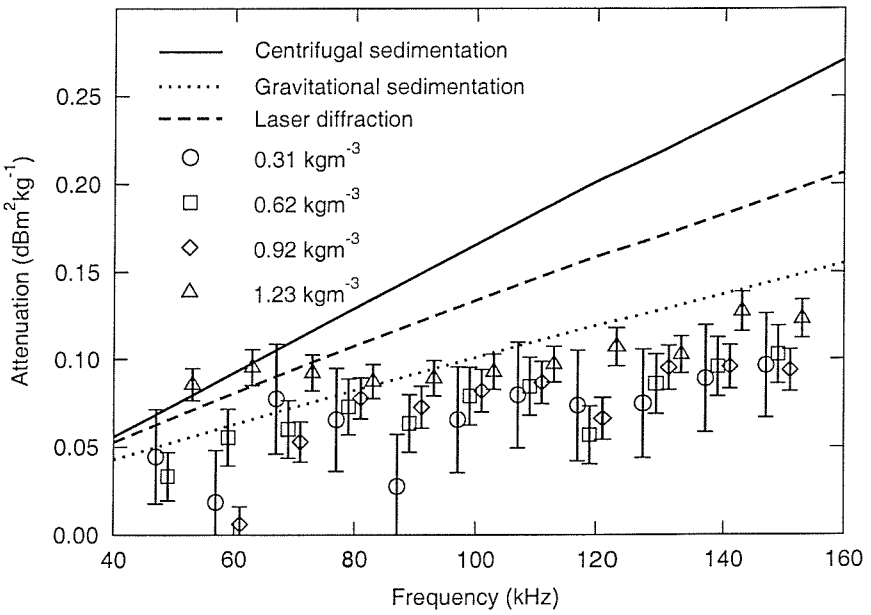

Figure 6.32. Normalized attenuation coefficient for marine sediment particles: experimental data and theoretical predictions assuming spherical particles.

Figure 6.32 shows the results of measuring the attenuation due to the sediment particles. As before, the symbols indicate measurements made at different concentrations and normalized with respect to concentration. It may be noted that there is a greater spread between measurements

made at different concentrations than was the case for Speswhite or Polcarb particles. This may be attributed to the greater uncertainty in the mass of sediment added to the test volume. In the cases of Speswhite and Polcarb the dry particulates were carefully weighed before being dispersed in water and added to the experimental system. In contrast to this the sediment particles were taken from a wet core sample leading to uncertainty in the dry mass of particles added. To estimate the water content of the core, samples of the wet sediment were weighed, dried and re-weighed. The resulting value for the water content was then used to estimate the dry mass of sediment particles added to the experiment. The variability in water content of the core is the major contribution to the variability observed in the normalized attenuation measurements.

The size distributions obtained using the three different techniques clearly lead to different predictions for the attenuation over the frequency range of the measurements. The theoretical curves generally overpredict the attenuation over most of the frequency range, although all three curves are within the experimental error in the range 50 to 70 kHz. The predictions based on the size distribution determined by gravitational sedimentation are within the experimental error of the majority of the data points, albeit at the upper end of the error bar. The predictions based on the centrifugal sedimentation measurements overpredict by the greatest margin. This may be explained by examination of Figure 6.31 which shows that the centrifugal sedimentation yields a size distribution which is strongly biased towards smaller particles. This may be because the sediment sample contains some flocs which are more likely to be broken up by the centrifugal technique than the other particle sizing methods.

The SEMs show that the sediment sample contains a high proportion of clay-like particles of similar form to the kaolin particles of the Speswhite sample. Given the poor agreement between the attenuation measurements for Speswhite and the predictions of the spherical particle model, it is perhaps surprising to find that the predictions of the model are reasonably close to the measured data for sediment particles (particularly using the gravitational sedimentation size distribution). It is likely that this is a consequence of ensemble averaging over many different particle shapes and sizes in the case of the natural sediment particles, as opposed to the pure samples of similarly shaped, highly non-spherical particles in the case of the Speswhite. This gives some encouragement that the spherical particle models may be of some use for predicting the attenuation from natural marine suspensions.

6.4.4 Application of the theory for non-spherical particles

The results in the previous sub-section showed the comparison between the predictions of Urick's equation, which assumes spherical particles, and measurements made with non-spherical particles. These results showed that the spherical model is of some limited use in providing estimates of the attenuation from the Polcarb and marine sediment particles. In the case of the highly non-spherical Speswhite particles, the spherical theory significantly overpredicts the attenuation.

A method for calculating the attenuation due to suspensions of oblate and prolate spheroids was described in Section 5.4. Since the degenerate form of an oblate spheroid is a thin circular disk it is appropriate to approximate the Speswhite plate-like particles as oblate spheroids.

In order to apply the method of Section 5.4 it is necessary to know the size distribution of the spheroids representing the particles. It is not appropriate to simply use the size distributions shown in the previous sub-section as these are distributions of Stokes diameters (equivalent

spheres). Therefore these distributions have been used to derive new distributions for spheroids.

The starting point for this process is the distribution of Stokes diameters obtained from gravitational sedimentation measurements. These were originally derived by applying Equation 6.5 to measurements of the fraction of particles which settle out of suspension as a function of time. Unfortunately the original time-domain data were not available but it was possible to recalculate them by inverting Equation 6.5 and applying it to the distributions of Stokes diameters. This gives the fraction of particles which settle out of suspension as a function of time. Now, if the settling velocity of spheroids is known as a function of their major and minor radii, these data can be used to derive a particle size distribution for the spheroids.

The steady-state settling velocity for spheroids may be obtained by equating the drag force on a spheroid (Equation 5.62) with the gravitational force and rearranging to give

$$v_s = \frac{4\pi a' b' \left(\rho' - \rho\right) g}{18\pi\eta K_{sf}} \tag{6.14}$$

The shape factors, K_{sf}, for oblate spheres with their axis of symmetry oriented parallel and perpendicular to the flow are given by Equations 5.72 and 5.76 respectively.

In this way the size distribution for Speswhite particles derived by gravitational sedimentation, shown in Figure 6.24, was used to calculate the size distribution of spheroids of given aspect ratio, $h = b'/a'$, which would give the same measured settling time history.

These particle size distributions were then used to calculate the attenuation spectrum due to the suspension of spheroids, using the approach described in Section 5.4. The attenuation measurements, as described in Section 6.2, employ an approximately diffuse field in which all directions of propagation are equally probable. Ideally, then, these calculations would be integrated over all orientations. However, the method only yields solutions for the two orthogonal cases, so the results presented below were obtained assuming equal concentrations of the two orthogonal orientations.

Figure 6.33 shows the comparison between the attenuation predicted using the oblate spheroid model and the measured attenuation for Speswhite particles. Predictions are for $h = 1$, i.e. for spherical particles, and $h = 1/30$ and $h = 1/40$ which is the range of typical aspect ratios of the Speswhite particles as quoted by the suppliers. The predictions for spheres, using the spheroidal model with $h = 1$, are in agreement with the predictions of the spherical model shown in Figure 6.26, and thus overestimate the attenuation. The predictions for the aspect ratios which are representative of the Speswhite particles, however, show excellent agreement with the measured attenuation. It is notable that this agreement is achieved without using any *a priori* knowledge of the attenuation measurements.

The spheroidal approach has also been applied to the Polcarb particles in exactly the same manner. However, inspection of Figures 6.21 to 6.23 shows that they are very angular and irregular. The spheroidal approach was therefore not expected to yield significantly improved agreement over the spherical model. Furthermore, no information was available on the aspect ratio, other than perhaps what could be inferred from the microscope images. Therefore calculations were performed for a number of different aspect ratios and those which gave predictions which were reasonably close to the measured data are shown in Figure 6.34. All that can really be concluded from this result is that the predictions of the spheroidal model for

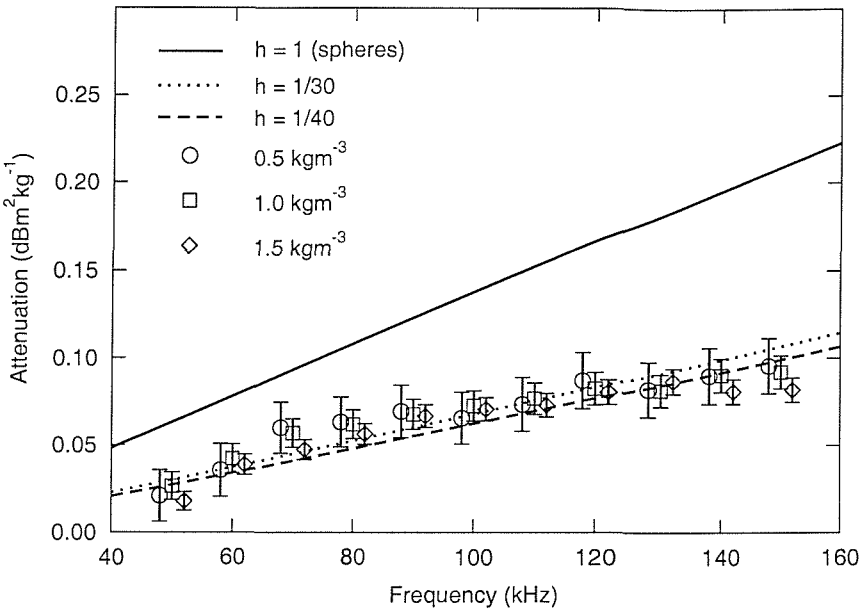

Figure 6.33. Normalized attenuation coefficient for Speswhite particles: experimental data and theoretical predictions using the model for spheroidal particles. The size distribution of the spheroids was derived from gravitational sedimentation measurements.

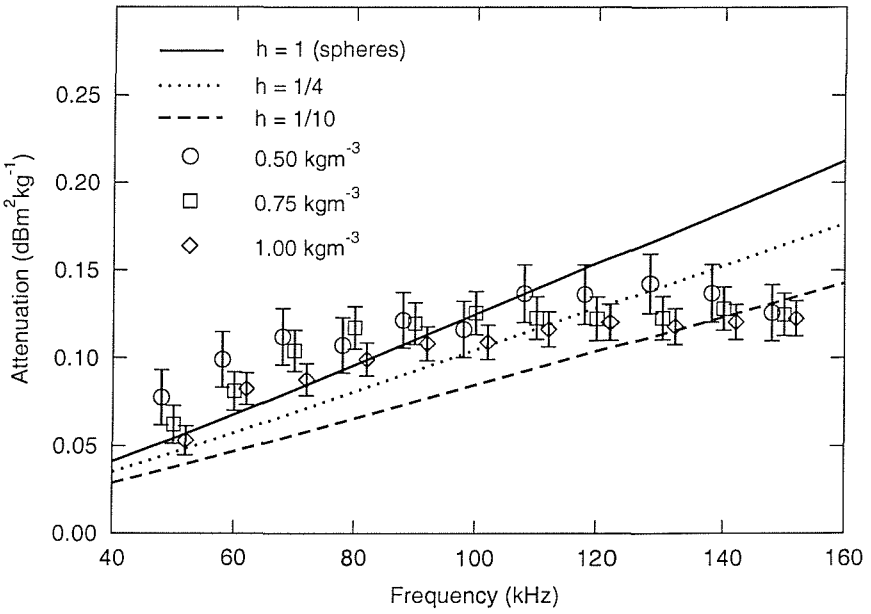

Figure 6.34. Normalized attenuation coefficient for Polcarb particles: experimental data and theoretical predictions using the model for spheroidal particles. The size distribution of the spheroids was derived from gravitational sedimentation measurements.

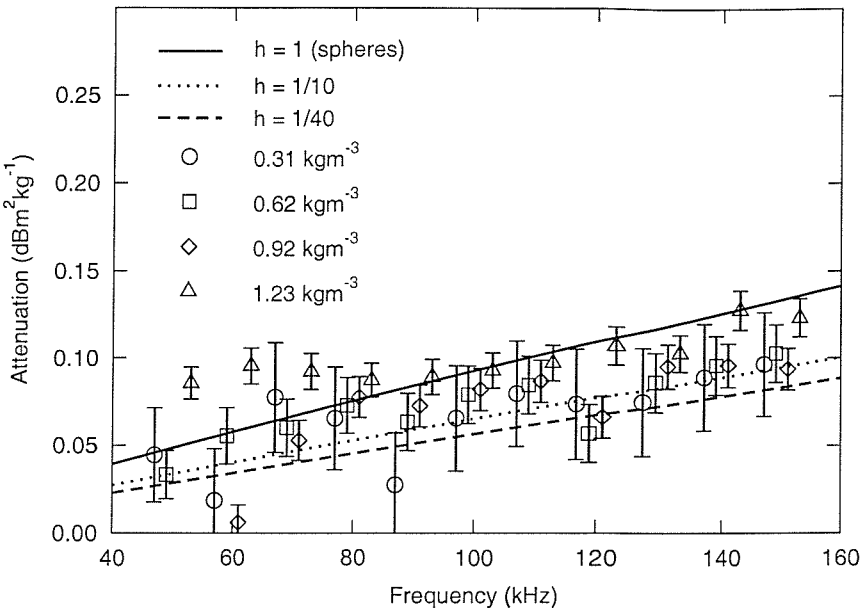

Figure 6.35. Normalized attenuation coefficient for marine sediment particles: experimental data and theoretical predictions using the model for spheroidal particles. The size distribution of the spheroids was derived from gravitational sedimentation measurements.

$0.1 \leq h \leq 1$ are neither better nor worse than the predictions of the spherical model. This is consistent with expectations, given the nature of the particles.

Finally, the spheroidal approach was applied to the natural marine sediment particles. Again, independent data on the aspect ratio were unavailable, although could potentially be estimated by detailed analysis of electron microscope imagery. Since the sediment samples contain a mixture of particles, some of which are granular and similar in form to the Polcarb particles, and others which are clay-like and similar to the Speswhite, calculations were performed for $h = 1$, $h = 1/10$ and $h = 1/40$. Owing to the spread in the measured data, all of these theoretical curves may be considered to lie broadly within the experimental error. However, the $h = 1/10$ curve lies closest to the centre of the dataset. Ideally, when faced with such a sample containing a distribution of particle shapes, the calculations should be integrated over a range of aspect ratios. In this case, however, data were not available to support this approach.

6.5 Summary and conclusions

The method of measuring the attenuation due to solid particles described in this chapter has been demonstrated to yield estimates of the attenuation due to spherical glass particles which are in agreement with the theoretical predictions of the Urick model for viscous absorption to within experimental error. From this it may be concluded that the experimental technique is suitable for the measurement of the acoustic attenuation coefficient in particulate suspensions over the range of parameters considered. It may also be concluded from the fact the the Urick model predicts the observed attenuation to within the measurement error that this attenuation is primarily due to viscous absorption, and that contributions from other dissipative processes, such as thermal absorption, are small.

Having validated the experimental method with the spherical glass particles, measurements were made with highly non-spherical particles of kaolin and calcium carbonate. With these non-spherical particles the method of obtaining the particle size distribution became an important issue, and three different particle sizing techniques were employed. Significant differences were observed in the particle size distributions yielded by the three techniques, leading to differences in the predicted attenuation.

The predictions of Urick's model for visco-inertial absorption by spherical particles, integrated over the size distributions obtained using the three particle sizing techniques, significantly overestimate the attenuation by the Speswhite particles. This poor agreement is to be expected since the plate-like kaolin particles are far from spherical. Agreement between the spherical particle model and the experimental data for Polcarb particles is much better, although the model fails to predict the observed frequency dependence in the attenuation. These calcium carbonate particles, while still highly irregular, are nearer to spheres than the kaolin particles, so the improved agreement is consistent with expectation.

The final series of measurements was made with natural marine suspension particles. Although the marine sediment sample contains a significant number of clay-like particles, in common with the kaolin sample, agreement between experiment and theory was much better in the case of the sediment particles. In particular the prediction based on the size distribution measured by gravitational sedimentation agrees with the attenuation measurements to within experimental error for most of the data points. However, there does appear to be a tendency for the model to overpredict the attenuation.

A model for acoustic attenuation by dilute suspensions of spheroidal particles has been used to predict the attenuation in suspensions of the three different particles. This model is most appropriate for the plate-like kaolin particles as the degenerate form of an oblate spheroid is a circular disk. The predictions of the model for oblate spheroids were found to be in excellent agreement with the measurements of attenuation by kaolin particles without requiring any *a priori* information about the attenuation measurements. Agreement between this model and the measurements made on calcium carbonate and marine sediment particles was less good, as expected due to the shape of these particles.

The experimental method uses stirring to suspend the particles and turbulence is therefore inherent in the test volume. Since it is possible that there could be a net transfer of acoustic energy to turbulent kinetic energy it was important to estimate the magnitude of this effect in order to determine whether this was a significant contribution to the total dissipative attenuation. A method was described in this chapter for estimating the order of magnitude of this turbulence attenuation coefficient. Calculations using this method based on estimates of maximum energy suggested that the turbulence attenuation coefficient in the experimental system was several orders of magnitude smaller than both the measured attenuation and the calculated viscous absorption coefficient. It is therefore concluded that turbulence is not a significant absorption mechanism in the experiments described in this chapter.

Thus far this thesis has described a theoretical and experimental investigation into the effects of dilute suspensions of mineral particles on acoustic propagation, within ranges of parameters which are pertinent to high frequency sonar systems operating in coastal waters. The next chapter goes on to apply this work to the problem of high frequency sonar performance prediction.

Chapter 7

Application to the sonar performance problem

7.1 Introduction

This thesis describes theoretical, computational and experimental investigations of visco-inertial dissipation by dilute particulate suspensions. One immediate application of this research is the determination of the effects of suspended particulate matter on the performance of high frequency acoustic sensors operating in shallow, turbid, coastal waters.

This chapter addresses this application of the research by including the additional attenuation due to suspended particles into a high frequency sonar detection model.

Shallow coastal waters are also likely to be characterized by persistent microbubbles throughout the water column, and these are likely to be acoustically significant. Therefore the effect of such bubble populations on the attenuation and phase speed have also been included in the work presented so that the magnitude of the effect may be compared with the magnitude of the effect of the solid particles.

7.2 Sonar detection model

7.2.1 Background

The sonar performance calculations presented in this chapter are based on a modified version of the SEARAY mine countermeasures sonar performance model.

SEARAY was originally implemented at the Naval Coastal Systems Center (NCSC), Panama City, Florida, and was based on a BASIC version of the MINERAY sonar simulation model developed and in use at the Applied Research Laboratories, University of Texas at Austin (ARL:UT).

The version which was modified in this work was Fortran version 1.4, obtained from the NATO Undersea Research Center (SACLANTCEN) along with a set of Matlab functions which serve as a graphical user interface to the underlying model.

7.2.2 Model operation

The operation of the SEARAY model is described in Reference [70]. The main elements of the model operation are summarized below.

SEARAY models the acoustic environment by using ray tracing to determine sound paths in a horizontally stratified water column. The signal to noise ratio along each ray is determined by calculating the directivity, absorption, geometric spreading loss, the effects of various noise and reverberation sources, and applying the active sonar equation

$$SNR = SL - 2TL + DI + TS - RL - NL \tag{7.1}$$

where

SL	=	Sonar source level
TL	=	One way transmission loss
DI	=	Directivity index
TS	=	Target strength
RL	=	Total reverberation level (bottom, surface and volume)
NL	=	Total noise level (ambient, flow, propeller, receiver)

These terms are discussed in the following sub-sections.

7.2.3 Source level and target strength

Both the source level and target strength are expressed in dB and are input by the user.

The source level is the sound pressure level of the source, measured at a distance of 1 m from the array. Sound pressure levels in SEARAY are expressed in dB re. 1 μbar, but all sound pressure levels in this thesis are expressed in the more conventional (in the UK) units of dB re. 1 μPa. Conversion from dB re. 1 μbar to dB re. 1 μPa is achieved by adding 100 dB.

The target strength is the ratio, in dB, of the scattered acoustic intensity to the incident acoustic intensity. The scattered and incident intensities are referenced to a point located 1 m from the centre of the target. As a result of this definition, positive target strengths are common. Some typical target strengths are given in Table 7.1.

Target	Aspect	TS (dB)
submarine	beam	3 to 25
submarine	bow-stern	0 to 10
mine	beam	0 to 10
mine	off-beam	-25 to 10
unsuited swimmer	any	-15

Table 7.1. Some typical target strengths (illustrative only) [71, 72].

7.2.4 Transmission loss

The transmission loss is the attenuation along the ray path, normally including losses at boundary interactions as well as geometric spreading and volume absorption. However, SEARAY models the seabed and sea surface as lossless reflectors.

For geometric spreading SEARAY models spherical spreading of wavefronts along the calculated ray paths. The effects of ray convergence and divergence are not calculated. These approximations are reasonable for the direct path scenarios for which the model is used.

Absorption of sound in seawater was discussed in Section 2.3. SEARAY provides two models for the absorption coefficient: Francois & Garrison [4] and Schulkin & Marsh [3]. The Francois & Garrison model, as described in Section 2.3, has been used here.

7.2.5 Directivity index

Most sonar systems employ directional arrays, which means that they transmit and receive over finite beam patterns rather than omni-directionally. This results in an *array gain* relative to an omnidirectional transmitter or receiver. In the special case where the signal is coherent and the noise is isotropic the array gain is referred to as the directivity index.

Three different routines for calculating the directivity index are used in the model, depending on the application and user choice. For the calculation of flow noise and ambient noise, which are independent of ray angle, the following approximation for the directivity is used

$$DI = \frac{B_\mathrm{h} B_\mathrm{v}}{4\pi} \tag{7.2}$$

where B_h and B_v are the horizontal and vertical beam-widths in radians.

For other applications within the model the beam-pattern is computed using either a bizonally shaded or Taylor shaded planar array [70].

7.2.6 Bottom reverberation

Bottom reverberation refers to sound that is scattered from the seabed and propagates to the receiver. This effect can have an important influence on sonar performance, especially in shallow water. The bottom reverberation level in dB is given by

$$RL_\mathrm{b} = SL - 40\log(r_\mathrm{r}) - 2\alpha r_\mathrm{r} + S_\mathrm{b} + 10\log(A_\mathrm{b}) \tag{7.3}$$

where SL is the sonar source level, α is the volume absorption coefficient, r_r is the range along the ray, S_b is the bottom scattering strength and A_b is the insonified area of the seabed.

The version of SEARAY used in this work provides four alternative models for computing the bottom scattering strength:

- McKinney-Anderson [73]
- Lambert's law [74]
- GESMA (Group d'Etudes Sous-Marines de l'Atlantique) [75]
- APL-UW (Applied Physics Laboratory, University of Washington) [76]

The McKinney-Anderson model was developed from data taken in shallow water over a frequency range of 12 to 290 kHz. Backscattering is a function of bottom type (m_b), grazing angle in radians (θ_g) and frequency in kHz (f_k). The bottom type is divided into four classes: 1 for mud; 2 for sand; 3 for gravel; 4 for rock. The bottom type can be any real number between 1 and 4 (e.g. 1.5 for mud and sand). The scattering strength is given by

$$S_\mathrm{b} = 10\log\left(2.53 \cdot C_\mathrm{b} \cdot f_\mathrm{k}^{3.2-0.8m_\mathrm{b}} \cdot 10^{2.8m_\mathrm{b}-12} + 10^{-4.5}\right) \tag{7.4}$$

UNIVERSITY OF SOUTHAMPTON LIBRARY

where

$$C_b = B_b \left(\sin\left(\theta_g + 0.19\right)\right)^{D_b} \tag{7.5}$$

$$B_b = 1 + 125e^{E_b} \tag{7.6}$$

$$D_b = m_b(\cos(\theta_g))^{16} \tag{7.7}$$

$$E_b = -2.64(m_b - 1.75)^2 - \left(\frac{50\cot^2\theta_g}{m_b}\right) \tag{7.8}$$

$$f_k = \text{frequency in kHz} \tag{7.9}$$

$$\theta_g = \text{grazing angle in radians} \tag{7.10}$$

Lambert's law computes scattering as a function of bottom type and grazing angle, and is frequency independent:

$$S_b = \mu_0 + 20\log(\sin(\theta_g)) \tag{7.11}$$

where θ_g is the grazing angle in radians and μ_0 is a constant depending on bottom type. Typical values of μ_0 are given in Table 7.2. This was the model used for the calculations presented in this chapter.

Bottom type	$\mu_0(dB)$
Mud	-29
Sand	-22
Gravel and rock	-15

Table 7.2. Typical values of Lambert's constant, μ_0.

The GESMA model is also based on bottom type and grazing angle and is independent of frequency:

$$S_b = \alpha_g + \beta_g \log(\theta_d) \tag{7.12}$$

where θ_d is the grazing angle in degrees and α_g and β_g are constants which depend on the bottom type. Typical values are given in Table 7.3

Bottom type	α_g	β_g
Mud	-60	13
Fine sand	-67	28
Sand	-47	21
Gravel	-37	21
Rock	-16	7

Table 7.3. Typical values of constants α_g and β_g in GESMA model.

The APL-UW model is based on seafloor sediment grain size and porosity and it depends on both grazing angle and frequency. This model is an empirical fit to data collected at 20 to 80 kHz and grazing angle from 5 to 90°. The expression for calculating the bottom scattering strength is more complicated than the preceding models, and as the APL-UW model has not been used in

this work the expression will not be reproduced here. The interested reader is referred to Reference [76].

A comparison of these four environmental sub-models for computing bottom scattering may be found in Reference [77].

7.2.7 Surface reverberation

The surface reverberation level is given by

$$RL_{\mathrm{s}} = SL - 40\log(r_{\mathrm{r}}) - 2\alpha r_{\mathrm{r}} + S_{\mathrm{s}} + 10\log(A_{\mathrm{s}}) \tag{7.13}$$

where S_{s} is the surface scattering strength and A_{s} is the insonified area of the sea surface.

The version of SEARAY used here provides three alternative sub-models for computing surface scattering strength:

- Chapman-Harris [78]
- Urick-Hoover [79]
- APL-84 [80]

The Chapman-Harris model is derived from measurements in the frequency range 400 Hz to 6.4 kHz and is a function of wind speed in knots (w), grazing angle in radians (θ_{g}) and frequency in kHz (f_{k}). The actual model implemented in SEARAY is a modified form of the Chapman-Harris model which has been extended to include data at higher frequencies:

$$S_{\mathrm{s}} = -51.3 + 20\log(1+w) + \frac{w\log(f_{\mathrm{k}}+0.1)}{15} + 10\Gamma\log(\tan\theta_{\mathrm{g}}) \tag{7.14}$$

where

$$\Gamma = \frac{4(w+2)}{w+1} + \left(2.5(f_{\mathrm{k}}+0.1)^{-1/3} - 4\right)(\cos\theta_{\mathrm{g}})^{1/8} \tag{7.15}$$

The Urick-Hoover model was developed from data measured at 60 kHz. The formula is independent of frequency but depends on both grazing angle and wind speed. The Urick-Hoover model has not been used here and the formula is therefore not reproduced. The APL-84 is an adaptation of the Urick-Hoover model, and has also not been used in this work.

7.2.8 Volume reverberation

The volume reverberation level is given by

$$RL_{\mathrm{v}} = S_{\mathrm{v}} + SL - 2TL + 10\log V_{\mathrm{v}} \tag{7.16}$$

where V_{v} is the insonified volume and S_{v} is the volume scattering strength given by

$$S_{\mathrm{v}} = -89 + 7\log f_{\mathrm{k}} \tag{7.17}$$

This scattering strength is representative of conditions in the body of the ocean under conditions of sparse marine life, and the presence of denser marine life such as is found in shallow, coastal environments may raise the volume scattering level by as much as 15 dB. The increase in scattering strength with increasing frequency accounts for the fact that as the wavelength gets smaller more forms of life become large with respect to the wavelength and thus become significant scatterers.

7.2.9 Ambient noise

The ambient noise model is a fit to the Knudsen curves [81] (based on empirical measurements) with a high frequency cut-off at the thermal noise limit of an omnidirectional hydrophone of unit efficiency [82, 83].

$$I_{\text{amb}} = \frac{10^{-7}}{f_{\text{k}}^3} + \frac{3 \cdot 10^{-2}}{1 + 10^4 \cdot f_{\text{k}}^4} + \frac{10^{-6} \cdot w^2}{1 + f_{\text{k}}^{5/3}} + 2.5 \cdot 10^{-12} \cdot f_{\text{k}}^2 \tag{7.18}$$

where I_{amb} is the ambient noise intensity, f_{k} is the frequency in kHz and w is the wind speed in knots.

The terms in Equation 7.18 account for: low frequency background noise (e.g. seismic activity); distant shipping noise; wind generated noise; and thermal noise, respectively. At frequencies above around 1 kHz the wind generated and thermal noise contributions dominate. Wind leads to generation of noise by the effects of wave splashing and the entrainment of air bubbles which subsequently oscillate, or *ring*. The ambient noise level increases with increasing wind speed for frequencies below about 300 kHz; at higher frequencies the wind speed dependence is negligible for wind speeds within normal ranges. Ambient noise levels decrease with increasing frequency at a rate of around 5 dB per octave until the thermal noise limit of the hydrophone is reached.

7.2.10 Flow, propellor and receiver noise

Hydrodynamic noise due to flow over a moving sonar housing is calculated using an expression developed at ARL:UT

$$NL_{\text{f}} = 56.6 + 10\log\left(10^{v_{\text{p}}/10} - 1\right) - 20\log(f_{\text{k}}) - 100 \tag{7.19}$$

where v_{p} is the platform speed in knots and f_{k} is the frequency in kHz.

The propeller noise level, NL_{p}, received by a sonar which trails behind the stern of a ship is calculated by subtracting transmission loss from a user-input propeller source level.

Receiver noise level, NL_{r} in SEARAY may be calculated from the ratio of the thermal noise voltage of the receiver to the receiver sensitivity [84]. Alternatively a user-input receiver noise level can be used.

7.3 Model limitations

The SEARAY model has a number of limitations of which users must be aware:

- The model calculates the SNR along the individual ray paths calculated by the ray tracing algorithm. Multipath interference effects are thus neglected. In some scenarios this may be perfectly adequate whilst in others it may be seen as a major limitation.
- The seafloor and sea surface are modelled as lossless reflectors. The number of interface reflections to include is set by the user.
- Sloping or rough bottoms cannot be modelled.
- The geometric spreading term is calculated assuming spherical spreading instead of performing a calculation based on ray convergence or divergence.
- The model is range-independent.

7.4 Model enhancements

As a result of the work described in this thesis, and other work by the author [85], the SEARAY sonar model has been enhanced in a number of respects in order to include the effects of suspended particulate matter and microbubbles.

7.4.1 Suspended particles

The additional attenuation due to visco-inertial absorption and scattering by suspended solid particles has been added to the volume absorption algorithm in SEARAY. This is used to compute the propagation loss in all propagating terms, including the signal, surface, bottom and volume reverberation and propagating noise terms. Visco-inertial absorption is computed by Equation 2.31 and scattering by Equation 2.45. The attenuation coefficient including physico-chemical absorption in seawater and visco-thermal absorption and scattering by suspended particles is given by Equation 2.3.

7.4.2 Microbubbles

As with solid particles, the presence of microbubbles in the water column leads to additional acoustic attenuation through thermal and viscous absorption and scattering. Unlike particles, however, resonant scattering can be important in the case of bubbles, and the scattering cross-section of a bubble near resonance may be very much larger than its geometric cross-section. Bubbles also cause the compressibility of the medium to be complex, resulting in dispersion.

The dispersion relation for a bubbly liquid may be written [86]

$$k_{\mathrm{b}}^2 = \frac{\omega^2}{c^2} + 4\pi\omega^2 \int_{a_0=0}^{\infty} \frac{a_0 n_{\mathrm{b}}(a_0) da_0}{\omega_0^2 - \omega^2 + 2ib\omega} \tag{7.20}$$

where k_{b} is the complex wavenumber for the bubbly liquid, ω is the angular frequency of the acoustic wave, c is the speed of sound in the ambient fluid, a_0 is the equilibrium bubble radius, ω_0 is the resonant frequency of bubbles having equilibrium radius a_0 and $n_{\mathrm{b}}(a_0)da_0$ is the number of bubbles per unit volume in the size range a_0 to $a_0 + da_0$ (it is conventional to take $da_0 = 1$ μm). The damping constant b is a summation of the viscous, thermal and radiation damping of the bubble, given by [86]

$$b = \frac{2\eta}{\rho a_0^2} + \frac{p_b}{2\rho a_0^2 \omega} \Im\Phi + \frac{\omega^2 a_0}{2c} \tag{7.21}$$

where ρ and η are the density and molecular viscosity of the ambient liquid, and p_b is the equilibrium gas pressure in the bubble. The complex term Φ is a thermal scaling factor given by

$$\Phi = \frac{3\gamma}{1 - 3(\gamma)\mathrm{i}\Xi \left[(\mathrm{i}/\Xi)^{1/2} \coth (\mathrm{i}/\Xi)^{1/2} - 1 \right]} \tag{7.22}$$

in which

$$\Xi = \frac{\chi_g}{\omega a_0^2} \tag{7.23}$$

where χ_g is the gas thermal diffusivity and γ is the ratio of the specific heat of the gas at constant pressure to that at constant volume.

The phase speed c_b and attenuation coefficient α_b for the bubbly liquid may be obtained from the real and imaginary parts of the complex wavenumber (Equation 7.20) using the following relation

$$k_b = \frac{\omega}{c_b} + \frac{\mathrm{i}\alpha_b}{10 \log \mathrm{e}^2} \tag{7.24}$$

The attenuation coefficient α_b is added to the volume loss term in SEARAY and the phase speed c_b is used to modify the sound speed profile.

7.4.3 Water column properties

In order to include the additional effects of suspended particles and microbubbles into the model the density and viscosity of the water must be known. However, these are not available in the original version of the model as they were not explicitly required. Instead the water column is described in terms of a single sound speed profile (SSP) or a single temperature profile, together with a constant value of salinity or a single salinity profile. Note that whilst salinity profiles are supported by the model itself they are not currently implemented in the user interface.

In the case where the temperature profile is supplied by the user, the SSP is computed using the Del Grosso equation [87] for sound speed as a function of temperature, salinity and depth. Where the SSP is given, the temperature profile is calculated using the Del Grosso equation inverted to give temperature as a function of sound speed, salinity and depth.

The simplest way to provide the additional parameters of density and viscosity would be to make these user inputs to the model. However, this would inevitably lead to inconsistencies between water column properties, as both density and viscosity depend on temperature, salinity and depth. Temperature in particular has been shown [88] (see Appendix A) to affect strongly the attenuation due to suspended particles in seawater. The new version of SEARAY has therefore been enhanced to compute density and viscosity profiles using the temperature profile (user supplied or calculated from the SSP) and salinity value available in the original version of the model. This approach ensures that all of the water column properties are consistent with each other. The expressions used to calculate density and viscosity as functions of temperature,

pressure and salinity are given in Appendix A.

7.5 Results

In this section some example results from the enhanced version of SEARAY, described in the preceding sections, are presented.

The basic situation which is modelled here is a typical shallow water, high frequency sonar scenario. A monostatic sonar system, i.e. one in which the source and receiver are co-located, is placed at a depth of 10 m in 40 m of water, with a 3° downward tilt angle. The sonar source emits a 1 ms pulse with a centre frequency of 100 kHz and a bandwidth of 4 kHz, with a source level of 220 dB re. 1 μPa. The transmitting array has horizontal and vertical beam-widths of 90° and 10° respectively, whilst the corresponding beam-widths of the receiver array are 10° and 1.5°. Both the transmitting and receiving arrays are Taylor shaded[1] and the projector has a side-lobe level of 8 dB whilst the receiver has a side-lobe level of 18 dB. The receiver noise level is 49 dB re. 1 μPa and the target strength is -23 dB.

The water-column is isothermal, with a temperature of 15°C and salinity of 35 on the practical salinity scale at all depths. The wind speed is 7 knots and the bottom type is mud. The volume absorption coefficient of seawater is calculated using the Francois-Garrison expression (Equation 2.4), surface scattering by Chapman-Harris (Equation 7.14) and bottom scattering by Lambert's law (Equation 7.11).

Figure 7.1 shows the ray paths calculated by SEARAY for the above scenario, together with the SSP. This shows the SSP and resultant ray paths in the absence of bubbles. Under the isothermal and isohaline conditions modelled here, the sound speed increases slowly with depth due to the increasing hydrostatic pressure. This results in a weakly upward refracting environment as evidenced by the ray paths shown in the figure.

Figure 7.2 shows the sound pressure levels for the most significant terms in the active sonar equation (Equation 7.1) calculated by SEARAY for the scenario described above. The three terms omitted from this plot are the ambient noise level, flow noise level and propeller noise level. All of these terms, like the receiver noise level (shown), are independent of target range and all three are significantly lower than the receiver noise. It may be noted that the bottom reverberation level is cut off at small ranges. Examination of the ray trace in Figure 7.1 reveals that this is because no rays have interacted with the seabed at the earliest ranges.

For sonar performance assessment the important terms are the total background level, consisting of the sum of noise and reverberation levels, the signal level and, ultimately, the signal to noise ratio. These are shown, for the scenario considered here in Figure 7.3. In this plot the total background level and the signal level are plotted in dB re. 1 μPa whilst the signal to noise ratio, which is the ratio of the other two terms, is in dB.

Figure 7.4 shows the same SNR, along with corresponding curves for the same basic scenario but including either suspended particles, bubbles, or both. For the purposes of this illustrative example the particulate suspension chosen was simply a monodisperse suspension of quartz-like, spherical particles with a radius of 1 μm and a concentration of 0.2 kgm^{-3} at all depths.

[1] Taylor shading: array elements are weighted according to a Taylor series to achieve desired beam-patterns.

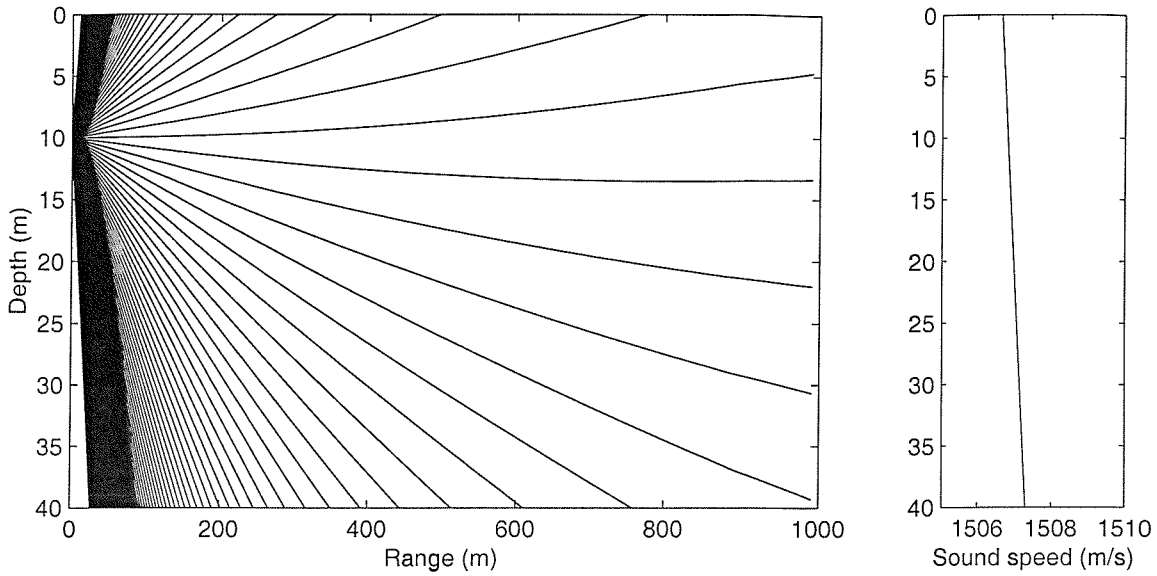

Figure 7.1. Ray paths calculated by SEARAY with SSP shown on the right. See text for the model parameters used in this calculation.

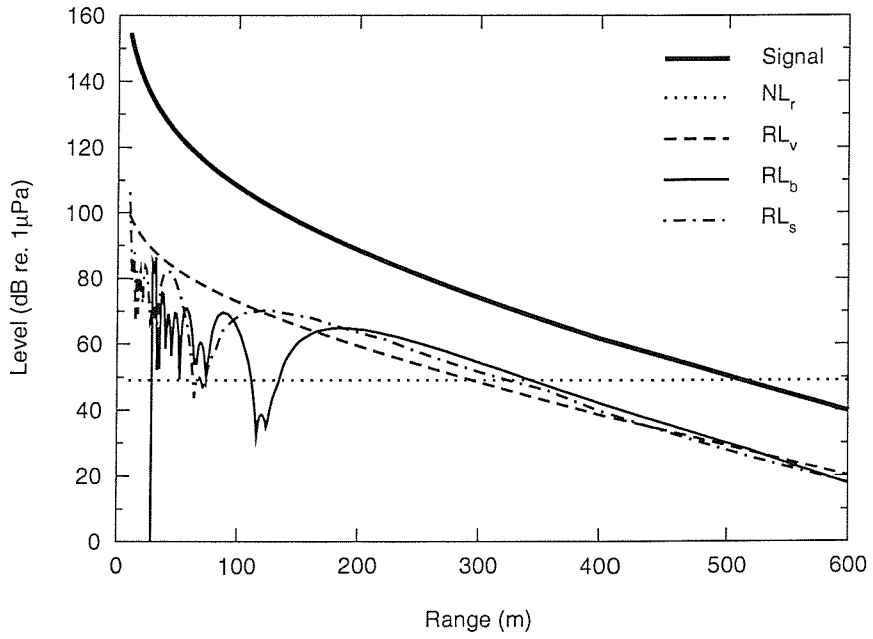

Figure 7.2. Levels calculated by SEARAY. See text for the model parameters used in this calculation.

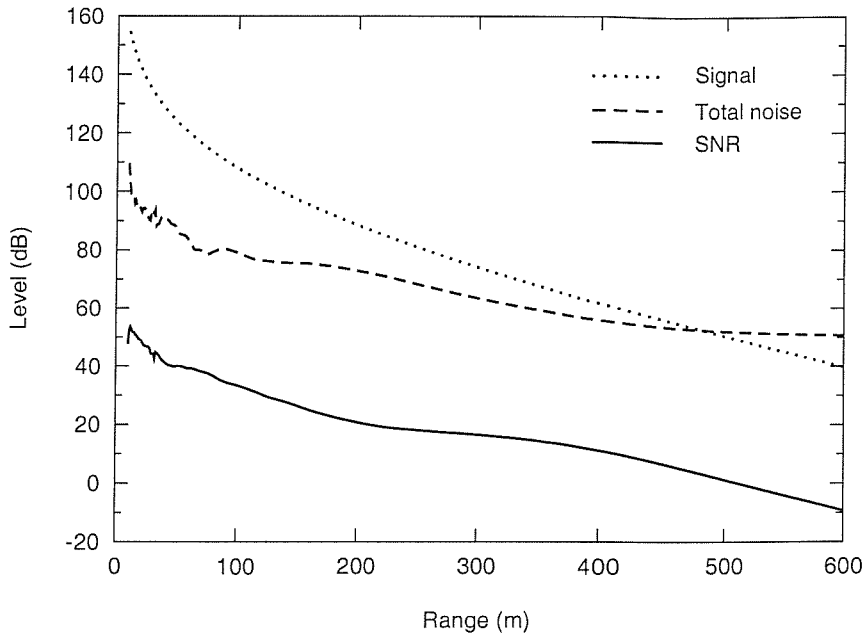

Figure 7.3. Signal level, total noise level (noise + reverberation) and the SNR for the scenario described in the text. The signal and noise levels are in dB re. 1 μPa, whilst the SNR is a simple ratio in dB.

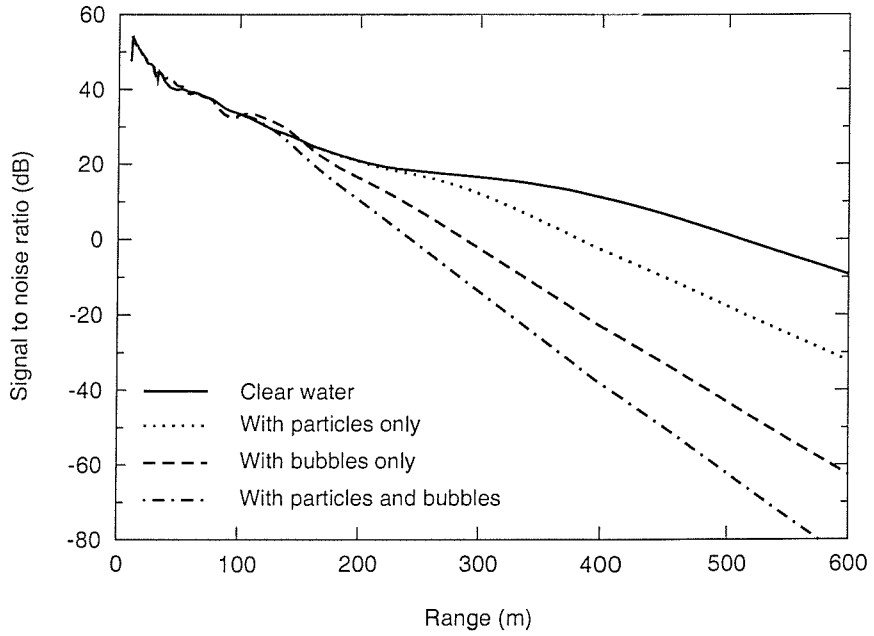

Figure 7.4. The effect of suspended particles and microbubbles on the SNR for the scenario described in the text.

The bubble population modelled here is more complicated, including both a distribution of sizes and a depth dependence. The bubble spectrum, containing bubbles with radii in the range 10 μm to 200 μm, is given by [89]

$$n_{\mathrm{b}}(a_0)da_0 = \begin{cases} K_1(a_0/60)^{-2}(d)^{-1/2} & \text{for } 200\ \mu\mathrm{m} > \mathrm{a}_0 > 60\ \mu\mathrm{m} \\ K_2(a_0/60)^{-4}\mathrm{e}^{d/L_{\mathrm{b}}} & \text{for } 10\ \mu\mathrm{m} < \mathrm{a}_0 < 60\ \mu\mathrm{m} \end{cases} \tag{7.25}$$

where $L_{\mathrm{b}} \approx 7$ m is the e-folding depth for small bubbles, d is depth in metres and K_1 and K_2 are constants which depend on time of day and season. Here the constants were chosen as $K_1 = 382.7$ and $K_2 = 298.8$ to give an approximate fit to measurements of bubble spectra made in near-calm, isothermal, coastal waters [90, 91].

Figure 7.4 shows that these suspended particle and bubble populations have a significant effect on the SNR in this modelled scenario. If it is assumed that the detection range for this particular sonar system is defined as the range beyond which the SNR drops below 0 dB then it may be seen from the figure that the detection range would be in excess of 500 m in clear water. This drops to less than 400 m in the presence of the chosen population of suspended particles and is reduced to less than 300 m in the presence of the modelled bubble population. If both suspended particles and bubbles are included in the model then the detection range is less than 250 m. Note that for a real sonar system the lowest SNR at which detection is possible depends on a number of factors, including the signal processing, and the specified probability of detection and probability of false alarm.

7.6 Proposal for estuarine measurements

7.6.1 Introduction

In this section a speculative proposal for monitoring suspended sediment flux through an estuary mouth is discussed. The relationship between the propagation loss for a high frequency active sonar and the concentration of suspended particulate matter presents the possibility of inferring path-integrated suspended sediment concentration from measurements of transmission loss across an estuary. Measurements of this nature have a range of applications in the field of environmental monitoring and management of the coastal zone.

Current acoustic techniques for measuring *in-situ* suspended sediment concentrations exploit backscattering at frequencies of 1 MHz and above. As a consequence they are local measurements, typically operating over ranges of 1 m or less. In contrast the proposed method presents the opportunity of yielding path-integrated concentrations over ranges of the order of 100 m.

7.6.2 Proposed method

A practical implementation of a trans-estuary transmission loss measurement would probably consist of a projector array located near one side of a river mouth or estuary, with a receiver array placed on the opposite side. The transmitter would ideally project a narrow beam, in both vertical and horizontal directions, in order to avoid multipath issues, whilst the receiver would have a wider beam-pattern to ensure that source-receiver alignment does not present too much of

a problem. A single hydrophone may even suffice for the receiver.

An extension to this technique may employ a vertical array of receiver hydrophones, with the projector using beam-forming to scan the launch angle in the vertical plane. This will give transmission loss measurements for a series of chords in the vertical plane, which may be processed to yield 2D estimates of sediment flux.

7.6.3 Worked example

In order to illustrate the potential of the proposed technique, an example calculation is presented. This calculation was carried out using the sonar performance model discussed in Section 7.2. As described in that section the model is a monostatic target detection model, so the calculation presented here is for a monostatic geometry, rather than the bistatic case described above which may be more appropriate for practical measurements. Nevertheless, the monostatic calculation will serve to illustrate the key points. In this geometry the source and receiver are co-located on one side of the estuary, and an inert target is place on the opposite side. The transmission loss in this case must be calculated over both the outgoing and reflected paths.

The scenario modelled here has the projector and receiver arrays co-located at depths of 10 m or 20 m in 40 m of water. The projector has a horizontally directed beam with a 3 dB beam-width of 1° in both vertical and horizontal directions, and a source level of 220 dB re. 1 μPa. For simplicity the receiver beam-width is the same, although in practice the receiver would probably employ a wider beam, possibly even omni-directional, as discussed above. A target with target strength of 0 dB is at a range of 100 m and at the same depth as the projector and receiver arrays.

The water column is isovelocity before the effects of microbubbles on the phase speed are taken into account. For simplicity, the suspended particle population used in this illustrative example is a depth-independent, monomodal suspension of 1 μm particles of density 2600 kgm^{-3}. A depth-dependent [89] distribution of microbubbles with equilibrium radii in the range $10 - 200$ μm was used, with coefficients chosen to approximate at-sea bubble density measurements [90, 91]. This bubble population is appropriate for the persistent background bubble population.

Figure 7.5 shows how the level of the received signal would vary with the mass concentration of suspended particles, with and without the chosen bubble population, for sonar and target depths of 10 m and 20 m. Only one line is plotted for the case where bubbles were not included in the calculation as there was no significant difference between the results for the two depths in the absence of bubbles. It is clear from this graph that even a calm water bubble population has a significant effect on the proposed measurement. At a sonar depth of 10 m the bubbles result in an additional reduction of the signal level of 24 dB. Even at a depth of 20 m the additional two-way transmission loss is 4.7 dB. The consequence of this is that if the effect of the bubbles is not taken into account a signal level of, say, 120 dB re. 1 μPa might be taken to infer a path-averaged particle concentration of about 0.36 kgm^{-3}, whereas the signal level in the presence of the bubble population corresponds to a concentration of 0.2 kgm^{-3}. In a practical measurement of this nature the effects of a static bubble population could be calibrated out. However it is likely that the bubble population may be sufficiently dynamic to preclude this. In such circumstances care would be required to ensure that the interpretation of the measurements accounted for both the particles and the bubble populations correctly. *A priori* knowledge of the

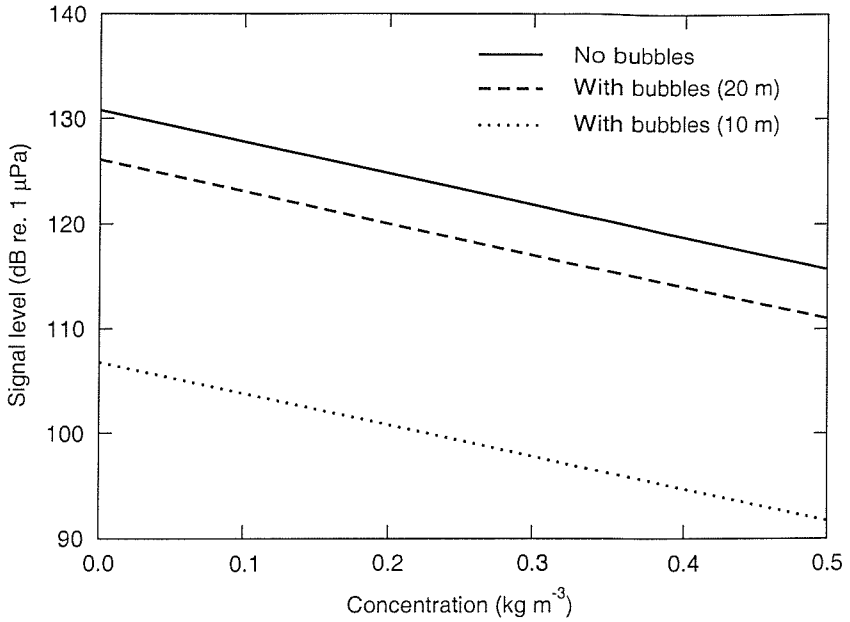

Figure 7.5. Variation in signal level with suspended particle concentration. Results are shown for a simulations with and without a bubble population. In the bubbly case results are shown for source/receiver depths of 10 m and 20 m (see text for full details).

bubble population may also be exploited to optimize transmission measurements of the form discussed here. For example, it is clear that the effect of bubbles is greater near the surface, where their number density is highest.

7.7 Summary and conclusions

This chapter describes, for the first time, the inclusion of the additional attenuation due to visco-inertial absorption and scattering by suspended mineral particles into a sonar performance model.

In addition to including the effects of solid particles on the volume attenuation, the effects of microbubbles distributed throughout the water column on both the volume absorption coefficient and the sound speed profile have been taken into account.

Illustrative, example results from this enhanced sonar model have been presented. These results demonstrate that the presence of suspensions of solid particles and microbubbles can have a significant effect on the signal to noise ratio, resulting in shorter detection ranges for high frequency active sonars.

Also presented in this chapter is a somewhat speculative proposal for exploiting the relationship between suspended particle concentration and the signal level in an active sonar operating in a turbid environment. It is proposed and demonstrated numerically by a modelled example, that a properly designed and calibrated system based on measurements of direct path transmission loss could be used to monitor suspended sediment mass flux through an estuary.

Chapter 8

Discussion

8.1 Summary and conclusions

The aim of the research described in this thesis was to elucidate the physics of, and provide a methodology for enabling the quantitative predictions of the effects of dilute suspensions of marine particles on high frequency sonar.

Suspended particles can influence the performance of high frequency sonars by contributing to the total attenuation coefficient and by modifying the sound speed. In Chapter 2 the theory of sound absorption and scattering by suspended particles was investigated, and numerical models based on these theories were described. Three attenuation mechanisms associated with the suspended particles were investigated; visco-inertial absorption, thermal absorption and scattering. Of these, visco-inertial absorption was shown to be the dominant effect over the range of frequency and particle size of interest, with scattering becoming important as the frequency and particle size increases, i.e. as the scattering parameter ka increases. Thermal absorption was shown not to be important for mineral particles over the parameter range of interest. The visco-inertial absorption contribution to the attenuation coefficient may be modelled using a simple expression based on Stokes' law for viscous drag and the scattering contribution may be modelled using a simple heuristic approach.

A more complete mathematical model of the relevant phenomena is provided by the Allegra-Hawley model, discussed in Chapter 3. This model solves the Helmholtz equations for the six waves (compression, shear and thermal waves in both phases) generated when a plane wave impinges on an elastic, thermally-conducting sphere suspended in a viscous, thermally-conducting fluid. This approach implicitly accounts for visco-inertial absorption, thermal absorption and scattering, allows the phase speed in the suspension to be determined and facilitates the effects of multiple scattering to be estimated. The disadvantages of this model include numerical difficulties in computing the solution and its complexity, which obscures physical insight. Therefore the AH model has only been used here to validate the more intuitive models for absorption and scattering. Comparison between these models indeed showed that the simpler models provide a good approximation to the more complete model over the range of parameters considered. Furthermore, this comparison confirms that thermal absorption is not important for mineral particles suspended in water.

In Chapter 5 a wave equation for acoustic propagation in suspensions was described. From this approach the acoustic wavenumber in the suspension may be determined, from which the phase

speed and attenuation coefficient can be inferred. It is demonstrated that the visco-inertial absorption coefficient arising from this method is equivalent to Urick's equation discussed in Chapter 2. It is further shown that the sound speed calculated from the wave equation is not the same as that which may naively be obtained from the bulk averaging of density and compressibility, due to the fact that the sound speed depends not only on the bulk properties but also on the inertial part of the complex drag on the particles. Calculations of the phase speed in aqueous suspensions of mineral particles showed that the change in phase speed, and hence refraction, due to natural suspensions may normally be neglected for the purpose of high frequency sonar performance modelling. The primary advantage of formulating the wave equation in this way is that it facilitates the task of accounting for non-spherical particles by employing correct expressions for the drag force. Consequently a model is described for the calculation of attenuation in dilute suspensions of oblate and prolate spheroids.

In order to validate the models and investigate their applicability to non-spherical particles a laboratory measurement technique was developed. Measurement of absorption by dilute suspensions in a laboratory-scale experiment was found to be challenging and a novel experimental arrangement was adopted to overcome the difficulties. The results of measurements made using spherical glass particles were found to be in very good agreement with the predictions of the Urick equation for visco-inertial absorption. Comparisons between this model and measurements made with non-spherical particles did not yield such good agreement, as was to be expected. In particular, the model for spherical particles significantly overpredicted the attenuation for kaolin particles, which are plate-like in form. In the cases of calcium carbonate particles, which are granular, and natural marine sediment particles, which have a distribution of shapes, the agreement was moderate. These experiments highlighted the fundamental issue of how the size distribution for non-spherical particles should be interpreted. Three techniques were employed for measuring particle size distribution: gravitational sedimentation; centrifugal sedimentation; and laser diffraction. Differences were observed between the particle size distributions obtained using these techniques due to a combination of factors including the fact that the methods measure different physical properties, have different limitations and are interpreted in different ways. For the purpose of performing the acoustic attenuation calculations it is expected that the sedimentation methods should yield the most appropriate size distribution as the parameter measured (Stokes settling velocity) is directly related to the drag. However, the settling velocity is usually interpreted assuming the particles to be spherical.

Since the kaolin particles are very plate-like and the degenerate form of an oblate spheroid is a thin disk, results from the model for attenuation by oblate spheroids were compared with the attenuation measurements for kaolin particles. In order to achieve this the size distribution obtained by gravitational sedimentation for these particles was re-analysed using expressions for the Stokes drag on oblate spheroids to yield the size distribution for oblate spheroids which gave the same settling time history. The attenuation due to oblate spheres was then calculated assuming this size distribution, together with the aspect ratio quoted by the suppliers of the particles. This resulted in excellent agreement between theory and measurements. It is therefore concluded that this model for attenuation by oblate spheroids may be used to predict the visco-inertial absorption in dilute suspensions of clay particles. Predictions of the spheroid model were also compared with the measurements obtained with calcium carbonate particles and marine sediment particles, although the agreement was not significantly better than that

obtained using the spherical models. This is to be expected for calcium carbonate as the shapes of the granular particles are not approximated well by oblate spheroids. The marine sediments are composed of a distribution of particle shapes, and a model should therefore include such a shape distribution or, in the case of the spheroidal model, a distribution of aspect ratios. Lack of such data in this case would have made such an exercise pointless.

The effects considered in Chapter 2 depend upon the viscosity, sound speed and density of the suspending fluid and, in the case of seawater, these parameters all depend in turn on the temperature, salinity and hydrostatic pressure. In Appendix A an investigation into the effects of temperature, salinity and pressure on the attenuation coefficient of seawater containing suspended mineral particles is presented. This investigation demonstrates that, over the range to be found globally, the ambient temperature has a significant effect on the attenuation coefficient of seawater containing suspended mineral particles and the local sea temperature should therefore be taken into account when calculating the attenuation coefficient for high frequency sonar performance predictions. The effect of salinity variations over the range found in the natural environment are shown to be less important and the effect of hydrostatic pressure is found to be insignificant for water depths in the shallow, coastal environments of interest for high frequency sonar performance predictions. The expressions presented in Chapter 2 and Appendix A enable the attenuation coefficient in seawater containing suspended solid particles to be calculated as a function of temperature, salinity, pressure, acoustic frequency, particle size, particle density and particle compressibility.

Finally, the stated aim of the research presented in this thesis was to elucidate the physics of, and provide a methodology for enabling quantitative prediction of the effects of dilute suspensions of marine particles on high frequency sonar. The elements for achieving the first part of this aim were established in Chapters 2 to 6, and calculations of sonar performance were finally presented in Chapter 7. These calculations demonstrated, for the first time, the inclusion of the effects of suspended particulate matter in sonar performance calculations. It was thus demonstrated that suspended particles can have a significant effect on the detection range of a high frequency active sonar operating in turbid coastal environments. The enhanced sonar model which was used for these calculations was also applied to the problem of measuring path-integrated attenuation across an estuary. It was thus demonstrated how, in principle, direct path acoustic propagation measurements across an estuary might be used to monitor sediment flux.

8.2 Further work

Any good piece of research raises questions and presents opportunities for further research. It is possible to see how the research described here may be carried forward beyond the scope of this thesis.

In order for the work presented in this thesis to be of practical use in sonar performance prediction, it is necessary to have some means of measuring or predicting the suspension properties in the environment. This presents several opportunities for further research, including investigating in-water acoustic and optical techniques for estimating suspended sediment properties, as well as techniques based on the inversion of remotely sensed measurements of water-leaving radiance spectra. The author is engaged in research in these areas, but this is beyond the scope of this thesis.

The prediction of high frequency sonar performance in coastal waters is a complicated problem, and the effect of suspended particles is only one element of the larger problem. Other effects include the influence of microbubbles which are prevalent in coastal waters, the effects of bottom topography, the propagation of acoustic energy into the seabed and scattering of energy from the bed, the scattering of sound from the sea surface, and so on. Each of these effects should be investigated at a level of detail similar to that of this thesis in order to produce a model that is capable of predicting, with any accuracy, the performance of high frequency sonars operating in turbid coastal waters. To this end the effects of microbubbles on the volume attenuation coefficient and phase speed have been included in the sonar performance model described in Chapter 7. This was described briefly in that chapter but a full treatment is outside the compass of this thesis.

Another interesting line of investigation is the possibility of inverting measurements of transmission loss across, say, a river mouth or estuary, in order to estimate suspended particle load. There would be a significant amount of work in doing justice to such a study, and it is therefore beyond the scope of the current investigation. However, some preliminary calculations are presented in Section 7.6. It is suggested that this topic may make a suitable investigation for a future Ph.D. thesis.

Finally there is significant scope for further research on the subject of absorption by non-spherical particles. The model for absorption by oblate spheroids described in Section 5.4 proved very successful in predicting the measured absorption due to the plate-like kaolin particles discussed in Chapter 6. However, whilst both the spherical and spheroidal models yield approximate agreement with the measurements for the more granular calcium carbonate particles and the natural sediment particles, further work is required. To do justice to this problem requires significant theoretical development on the subject of oscillatory drag on these irregular particle shapes and careful experimental studies including complete characterization of the particulate samples. This subject is also recommended as a further Ph.D. investigation.

Appendix A

The effect of temperature, pressure and salinity

A.1 Introduction

Shallow coastal environments are highly variable, with temperature varying both seasonally and as a result of diurnal heating locally, as well as exhibiting large variations with geographic location. Salinity also varies greatly, from nearly fresh water in river estuaries to highly saline water in very warm, shallow seas such as the Persian Gulf or Dead Sea. The variation in the attenuation of sound in clear seawater with temperature, pressure (or depth) and salinity is well established, and is accounted for in the various empirically derived formulae for the attenuation coefficient of seawater [1–5]. The attenuation by suspended particles will also depend on temperature, pressure and salinity, since it depends on the compression wave speed, density and viscosity of the seawater, which all depend on temperature, pressure and salinity. In this chapter suitable expressions are employed for density, viscosity and sound speed in seawater as a function of temperature, salinity and pressure in order to investigate the variation in the attenuation coefficient of seawater containing suspended particles over the ranges of these parameters found in the environment.

Microbubbles which are prevalent in shallow water environments will also contribute to the total attenuation, and this effect will also depend on temperature, pressure and salinity. It is also possible that the bubble population itself may be influenced by these parameters. These effects are not within the scope of the present investigation.

A.2 Viscosity

Matthäus [92] gives a formula for calculating the molecular viscosity, η (Pas) of seawater as a function of temperature $\Theta(^\circ\mathrm{C})$, salinity S (measured on the practical salinity scale) and pressure p (dbar), which is valid for $0^\circ\mathrm{C} \leq \Theta \leq 30^\circ\mathrm{C}$, $0 \leq S \leq 36$ and 1 dbar $\leq p \leq 1000$ dbar. By employing summation notation his formula may be expressed in the following form

$$\eta(S,\Theta,p) = 0.1\left[\sum_i p^i \sum_j Q_{ij}\Theta^j + S\sum_k R_k\Theta^k\right] \tag{A.1}$$

where Q_{ij} and R_k are coefficients obtained by fitting to experimental data. These coefficients are given in Table A.1.

The kinematic viscosity used in Equation 2.31 is given by $\nu = \eta/\rho$.

	$j=0$	$j=1$	$j=2$	$j=3$
Q_{0j}	$1.79 \cdot 10^{-2}$	$-6.1299 \cdot 10^{-4}$	$1.4467 \cdot 10^{-5}$	$-1.6826 \cdot 10^{-7}$
Q_{1j}	$-1.8266 \cdot 10^{-7}$	$1.3817 \cdot 10^{-8}$	$-2.6363 \cdot 10^{-10}$	0
Q_{2j}	$9.8972 \cdot 10^{-12}$	$-6.3255 \cdot 10^{-13}$	$1.2116 \cdot 10^{-14}$	0
R_j	$2.4727 \cdot 10^{-5}$	$4.8429 \cdot 10^{-7}$	$-4.7172 \cdot 10^{-8}$	$7.5986 \cdot 10^{-10}$

Table A.1. Coefficients for the calculation of viscosity.

A.3 Sound speed

The recommended [93] formula for computing sound speed in seawater as a function of temperature, pressure and salinity is that of Chen & Millero. Recent studies [94] have shown that, in fact, the Del Grosso [87] sound speed equation is more accurate than the Chen & Millero expression for high hydrostatic pressures corresponding to depths greater than about 1000 m. However, in the current investigation we are concerned with shallow water environments, and it is therefore appropriate to use the recommended Chen & Millero expression.

[95]. Using summation notation as for viscosity, their formula may be written

$$c(S,\Theta,p) = C_{\mathrm{w}}(\Theta,p) + A_{\mathrm{w}}(\Theta,p)S + B_{\mathrm{w}}(\Theta,p)S^{3/2} + D_{\mathrm{w}}(p)S^2 \tag{A.2}$$

with

$$C_{\mathrm{w}}(\Theta,p) = \sum_i p^i \sum_j C_{ij}\Theta^j \tag{A.3}$$

$$A_{\mathrm{w}}(\Theta,p) = \sum_i p^i \sum_j A_{ij}\Theta^j \tag{A.4}$$

$$B_{\mathrm{w}}(\Theta,p) = \sum_i p^i \sum_j B_{ij}\Theta^j \tag{A.5}$$

$$D_{\mathrm{w}}(p) = \sum_i D_i p^i \tag{A.6}$$

The coefficients C_{ij}, A_{ij}, B_{ij} and D_i are given in Table A.2. This expression is valid for $0°\mathrm{C} \leq \Theta \leq 40°\mathrm{C}$, $0 \leq S \leq 40$ and $0\ \mathrm{dbar} \leq p \leq 10000\ \mathrm{dbar}$.

A.4 Density

The expressions for the density of seawater as a function of temperature, pressure and salinity used here are taken from reference [93]. These are based on the international equation of state for seawater diluted with pure water or concentrated by evaporation [96,97], which is valid for $-2°\mathrm{C} \leq \Theta \leq 40°\mathrm{C}$, $0 \leq S \leq 42$ and $0\ \mathrm{dbar} \leq p \leq 10000\ \mathrm{dbar}$.

	$j=0$	$j=1$	$j=2$	$j=3$	$j=4$	$j=5$
A_{0j}	1.389	$-1.262 \cdot 10^{-2}$	$7.164 \cdot 10^{-5}$	$2.006 \cdot 10^{-6}$	$-3.21 \cdot 10^{-8}$	0
A_{1j}	$9.4742 \cdot 10^{-5}$	$-1.2580 \cdot 10^{-5}$	$-6.4885 \cdot 10^{-8}$	$1.0507 \cdot 10^{-8}$	$-2.0122 \cdot 10^{-10}$	0
A_{2j}	$-3.9064 \cdot 10^{-7}$	$9.1041 \cdot 10^{-9}$	$-1.6002 \cdot 10^{-10}$	$7.988 \cdot 10^{-12}$	0	0
A_{3j}	$1.100 \cdot 10^{-10}$	$6.649 \cdot 10^{-12}$	$-3.389 \cdot 10^{-13}$	0	0	0
B_{0j}	$-1.922 \cdot 10^{-2}$	$-4.42 \cdot 10^{-5}$	0	0	0	0
B_{1j}	$7.3637 \cdot 10^{-5}$	$1.7945 \cdot 10^{-7}$	0	0	0	0
C_{0j}	1402.388	5.03711	$-5.80852 \cdot 10^{-2}$	$3.3420 \cdot 10^{-4}$	$-1.478 \cdot 10^{-6}$	$3.1464 \cdot 10^{-9}$
C_{1j}	0.153563	$6.8982 \cdot 10^{-4}$	$-8.1788 \cdot 10^{-6}$	$1.3621 \cdot 10^{-7}$	$-6.1185 \cdot 10^{-10}$	0
C_{2j}	$3.1260 \cdot 10^{-5}$	$-1.7107 \cdot 10^{-6}$	$2.5974 \cdot 10^{-8}$	$-2.5335 \cdot 10^{-10}$	$1.0405 \cdot 10^{-12}$	0
C_{3j}	$-9.7729 \cdot 10^{-9}$	$3.8504 \cdot 10^{-10}$	$-2.3643 \cdot 10^{-12}$	0	0	0
D_0	$1.727 \cdot 10^{-3}$	-	-	-	-	-
D_1	$-7.9836 \cdot 10^{-6}$	-	-	-	-	-

Table A.2. Coefficients for the calculation of sound speed.

The density of seawater may be written

$$\rho(S,\Theta,p) = \frac{\rho(S,\Theta,0)}{1 - p/B(S,\Theta,p)} \tag{A.7}$$

where $B(S,t,p)$ is the bulk modulus.

Using summation notation as before, the density at $p = 0$ may be expressed

$$\rho(S,\Theta,0) = \rho_{\mathrm{w}} + S\sum_i b_i\Theta^i + S^{3/2}\sum_j c_j\Theta^j + d_0S^2 \tag{A.8}$$

where

$$\rho_{\mathrm{w}} = \sum_i a_i\Theta^i \tag{A.9}$$

and coefficients a_i, b_i, c_i and d_i are given in Table A.3.

The bulk modulus is given by

$$B(S,t,p) = B(S,t,0) + P_{\mathrm{B}}p + Q_{\mathrm{B}}p^2 \tag{A.10}$$

where

$$B(S,t,0) = B_{\mathrm{B}} + S\sum_i f_i\Theta^i + S^{3/2}\sum_j g_j\Theta^j \tag{A.11}$$

$$P_{\mathrm{B}} = P_{\mathrm{w}} + S\sum_i i_i\Theta^i + j_0S^{3/2} \tag{A.12}$$

$$Q_{\mathrm{B}} = Q_{\mathrm{w}} + S\sum_i l_i\Theta^i \tag{A.13}$$

$$B_{\mathrm{B}} = \sum_i e_i\Theta^i \tag{A.14}$$

$$P_{\mathrm{w}} = \sum_i h_i \Theta^i \tag{A.15}$$

and

$$Q_{\mathrm{w}} = \sum_i k_i \Theta^i \tag{A.16}$$

Again, the coefficients are listed Table A.3.

	$j=0$	$j=1$	$j=2$	$j=3$	$j=4$	$j=5$
a_i	999.842594	$6.793952 \cdot 10^{-2}$	$-9.095290 \cdot 10^{-3}$	$1.001685 \cdot 10^{-4}$	$-1.120083 \cdot 10^{-6}$	$6.536332 \cdot 10^{-9}$
b_i	$8.24493 \cdot 10^{-1}$	$-4.0899 \cdot 10^{-3}$	$7.6438 \cdot 10^{-5}$	$-8.2467 \cdot 10^{-7}$	$5.3875 \cdot 10^{-9}$	0
c_i	$-5.72466 \cdot 10^{-3}$	$1.0227 \cdot 10^{-4}$	$-1.6546 \cdot 10^{-6}$	0	0	0
d_i	$4.8314 \cdot 10^{-4}$	0	0	0	0	0
e_i	19652.21	148.4206	−2.327105	$1.360477 \cdot 10^{-2}$	$-5.155288 \cdot 10^{-5}$	0
f_i	54.6746	−0.603459	$1.09987 \cdot 10^{-2}$	$-6.1670 \cdot 10^{-5}$	0	0
g_i	$7.944 \cdot 10^{-2}$	$1.6483 \cdot 10^{-2}$	$-5.3009 \cdot 10^{-4}$	0	0	0
h_i	3.239908	$1.43713 \cdot 10^{-3}$	$1.16092 \cdot 10^{-4}$	$-5.77905 \cdot 10^{-7}$	0	0
i_i	$2.2838 \cdot 10^{-3}$	$-1.0981 \cdot 10^{-5}$	$-1.6078 \cdot 10^{-6}$	0	0	0
j_i	$1.91075 \cdot 10^{-4}$	0	0	0	0	0
k_i	$8.50935 \cdot 10^{-5}$	$-6.12293 \cdot 10^{-6}$	$5.2787 \cdot 10^{-8}$	0	0	0
l_i	$-9.9348 \cdot 10^{-7}$	$2.0816 \cdot 10^{-8}$	$9.1679 \cdot 10^{-10}$	0	0	0

Table A.3. Coefficients for the calculation of density.

A.5 Results

The attenuation in turbid seawater has been calculated using the Francois & Garrison expression (Equation 2.4) for absorption in clear seawater together with the expressions for attenuation due to absorption and scattering by a suspension of spherical particles (Equations 2.31 and 2.45). The sound speed, density and viscosity of seawater used in these equations were calculated using the expressions in Sections A.2, A.3 and A.4, as functions of temperature, salinity and pressure. Results are thus presented for attenuation in turbid seawater as a function of temperature, salinity and pressure, over the ranges

$$0°\mathrm{C} \leq \Theta \leq 30°\mathrm{C}$$

$$0 \leq S \leq 35$$

$$1 \text{ dbar} \leq p \leq 900 \text{ dbar}$$

It has been assumed that the variation in the bulk compressibility and density of solid mineral particles can be considered to be negligible compared with the variation of the physical properties of the seawater within these parameter ranges.

It may be seen from Section 2.3 that only the boric acid relaxation is dependent on pH. Since we are interested in frequencies well above the boric acid relaxation frequency, this is not an

important attenuation mechanism and the effect of pH on the attenuation may be neglected. All results presented in this chapter were calculated using a pH of 8.0.

Figure A.1 shows the attenuation as a function of temperature and salinity for $p = 1$ dbar, $f = 1$ MHz, $a = 1$ μm, $M = 1$ kgm^{-3}. This figure shows that for the given parameters, the attenuation decreases significantly as the temperature is increased. Over the range $0°\text{C} \leq \Theta \leq 30°\text{C}$ the attenuation in dBm^{-1} changes by a factor of approximately 1.24 for a salinity of 35, whilst in fresh water (S=0) the factor is approximately 1.4. The variation with salinity is less significant, but it is notable that there is a positive variation with salinity at the upper end of the temperature range, whilst the opposite is true at the lower end of the temperature range. Figure A.2 is similar to Figure A.1, but with a pressure of 900 dbar. The similarity between these figures indicates that pressure does not have a very significant impact on attenuation over the range of parameters studied here.

Figures A.3 and A.4 show the attenuation as a function of salinity and pressure for $\Theta = 0°\text{C}$ and $\Theta = 30°\text{C}$ respectively, with $f = 1$ MHz, $a = 1$ μm, $M = 1$ kgm^{-3}. Temperature clearly has a significant effect on the attenuation as noted in Figures A.1 and A.2 These figures demonstrate that the effect of pressure on the attenuation over the range 0 to 900 dbar is small and, since for shallow water applications we are generally only interested in water depths of order 100 m or less (p up to about 100 dbar), the effect on the attenuation of pressure variation with depth may be neglected. This is supported by Figures A.5 and A.6, which show that there is little variation in attenuation with pressure over the entire temperature range considered, for salinities of 35 and 0 respectively.

Figures A.7 and A.8 show the variation in attenuation with frequency and particle radius, for temperatures of 30°C and 0°C respectively and Figure A.9 shows the difference between these two cases. The peak occurring in the small a region of Figures A.7 and A.8 is due to viscous absorption, which peaks when the skin depth (e-folding length) of the viscous shear waves in the fluid is of the order of the particle size. The increase in absorption at large a is due to scattering, which becomes important as the frequency and particle size become large, i.e. with increasing ka. There is clearly a significant difference between these cases in terms of both the overall magnitude of the absorption, with a maximum difference of over 0.5 dBm^{-1}, and also in the position of the viscous absorption peak along the particle radius axis at a given frequency. It is this shift in the absorption peak which leads to the negative regions of the difference plot. From Figures A.7 and A.8 it can be seen that the absorption peak moves towards smaller particles as the temperature is increased. This may be understood in terms of the kinematic viscosity, ν and the skin depth of the viscous shear waves, $\delta_\text{v} = \sqrt{2\nu/\omega}$. As the temperature increases, the viscosity decreases, and hence δ decreases. Since the absorption peak occurs when $\delta_\text{v} \sim a$, the peak would be expected to shift to smaller a as δ decreases. Therefore the peak should shift to smaller a as the temperature increases, as observed.

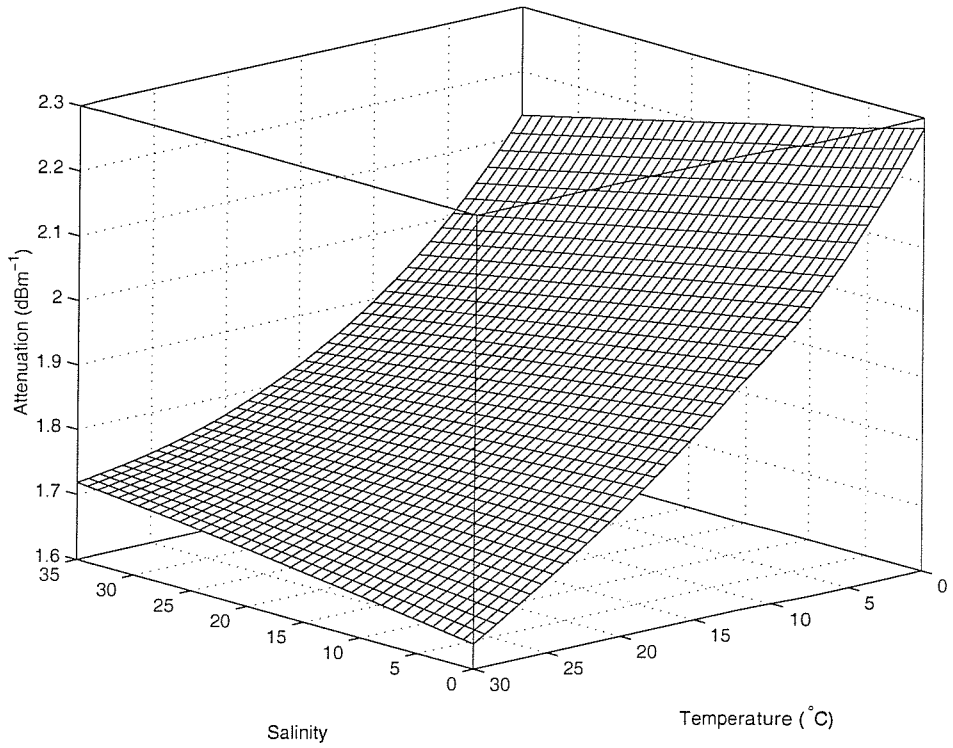

Figure A.1. Attenuation as a function of temperature and salinity for $p = 1$ dbar, $f = 1$ MHz, $a = 1$ μm, $M = 1$ kgm^{-3}.

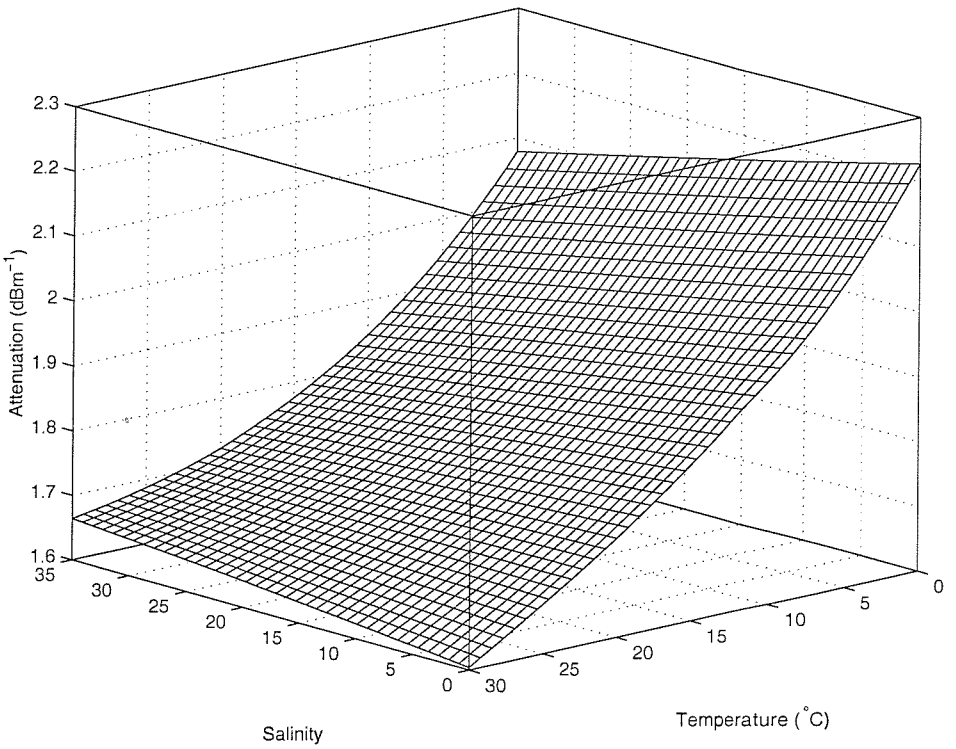

Figure A.2. Attenuation as a function of temperature and salinity for $p = 900$ dbar, $f = 1$ MHz, $a = 1$ μm, $M = 1$ kgm^{-3}.

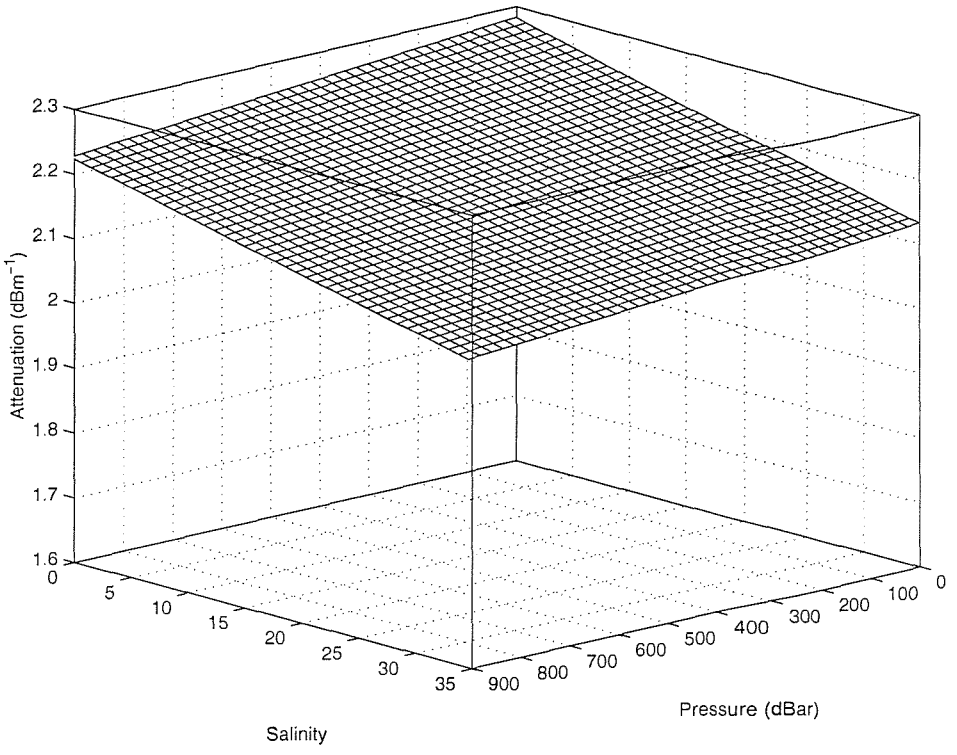

Figure A.3. Attenuation as a function of pressure and salinity for $\Theta = 0°\mathrm{C}$, $f = 1$ MHz, $a = 1$ μm, $M = 1$ kgm^{-3}.

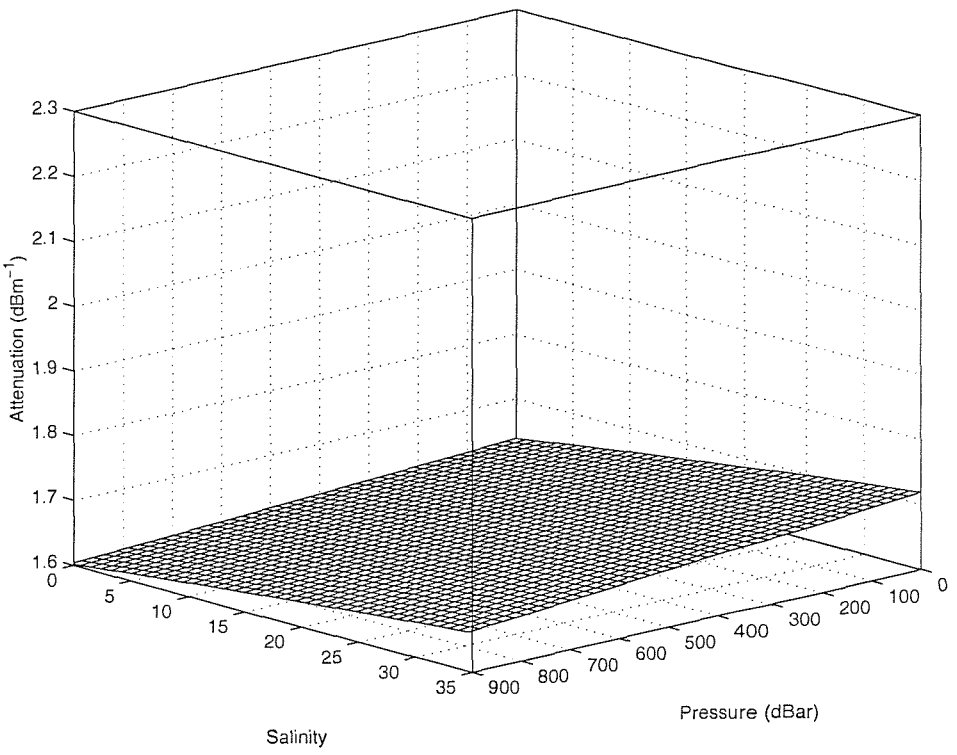

Figure A.4. Attenuation as a function of pressure and salinity for $\Theta = 30°\mathrm{C}$, $f = 1$ MHz, $a = 1$ μm, $M = 1$ kgm^{-3}.

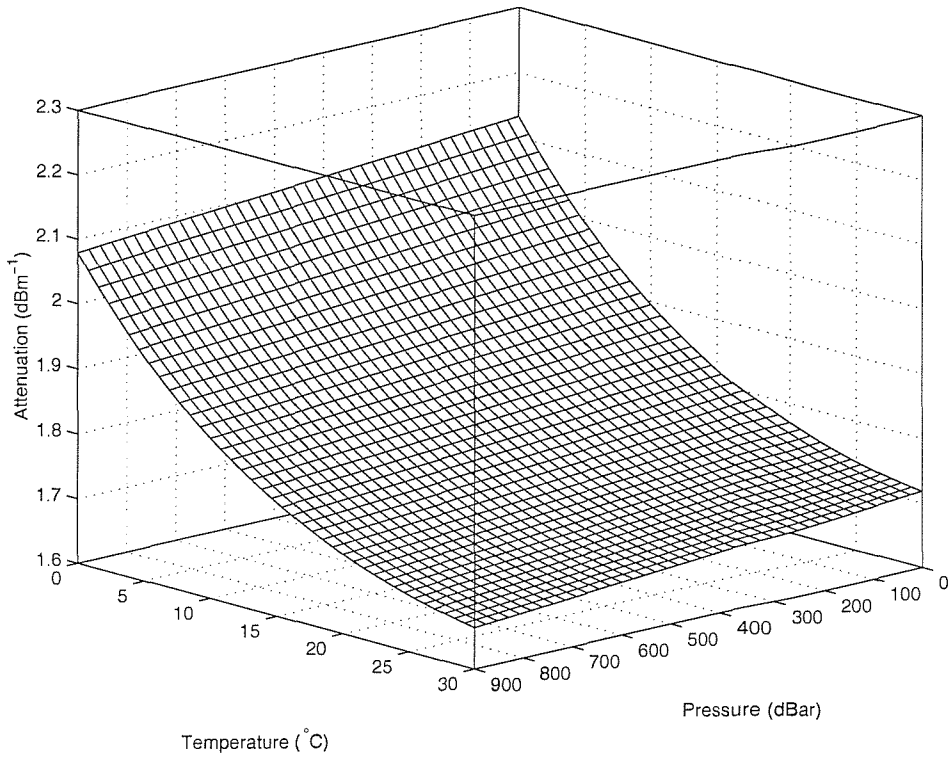

Figure A.5. Attenuation as a function of pressure and temperature for $S = 35$, $f = 1$ MHz, $a = 1$ μm, $M = 1$ kgm^{-3}.

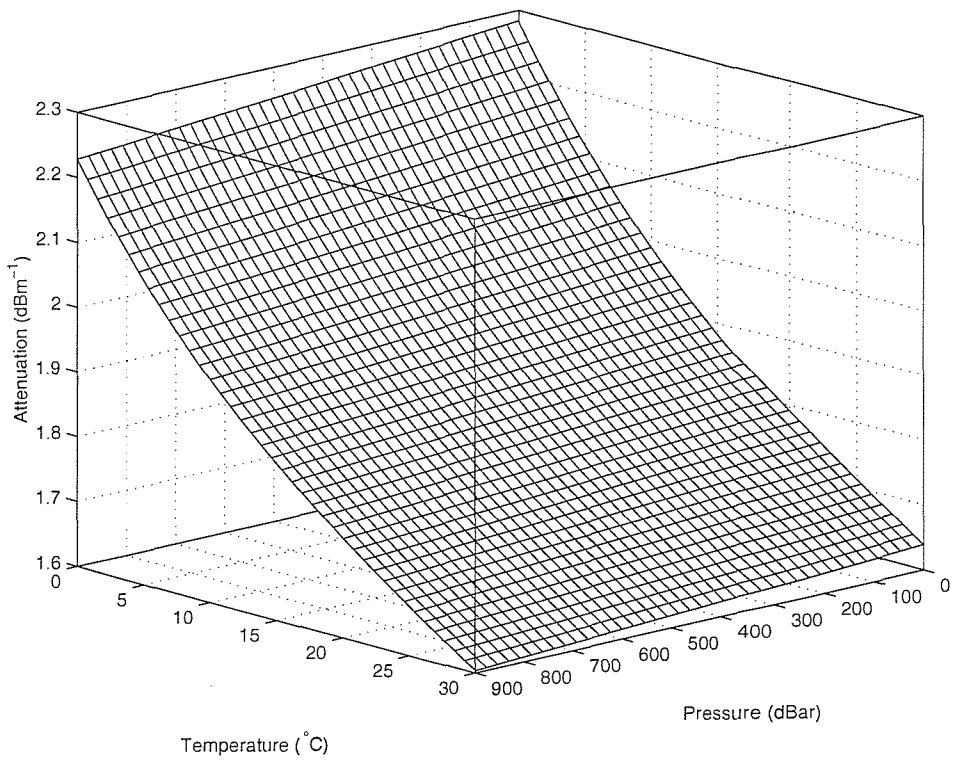

Figure A.6. Attenuation as a function of pressure and temperature for $S = 0$, $f = 1$ MHz, $a = 1$ μm, $M = 1$ kgm^{-3}.

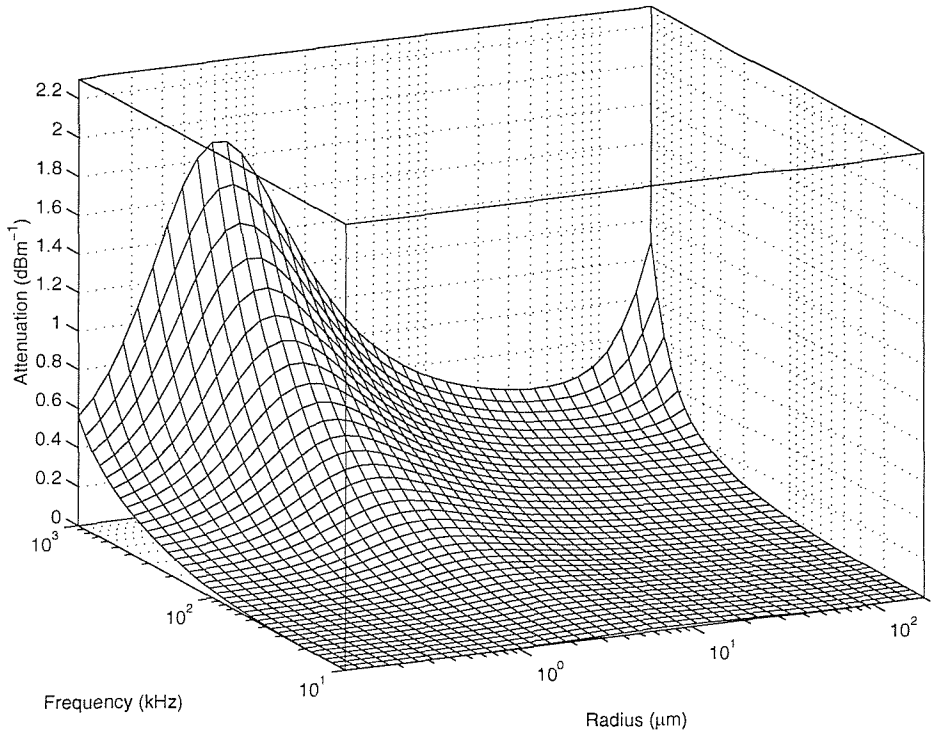

Figure A.7. Attenuation as a function of frequency and particle radius for $\Theta = 30°\mathrm{C}$, $S = 35$, $p = 1$ dbar, $M = 1\ \mathrm{kgm}^{-3}$.

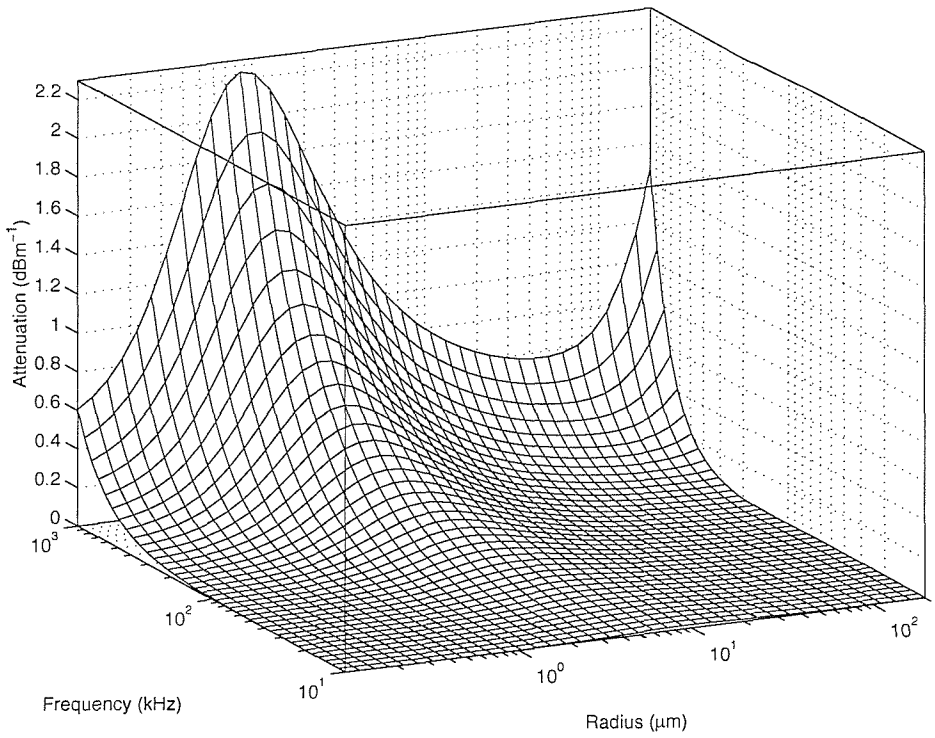

Figure A.8. Attenuation as a function of frequency and particle radius for $\Theta = 0°\mathrm{C}$, $S = 35$, $p = 1$ dbar, $M = 1\ \mathrm{kgm}^{-3}$.

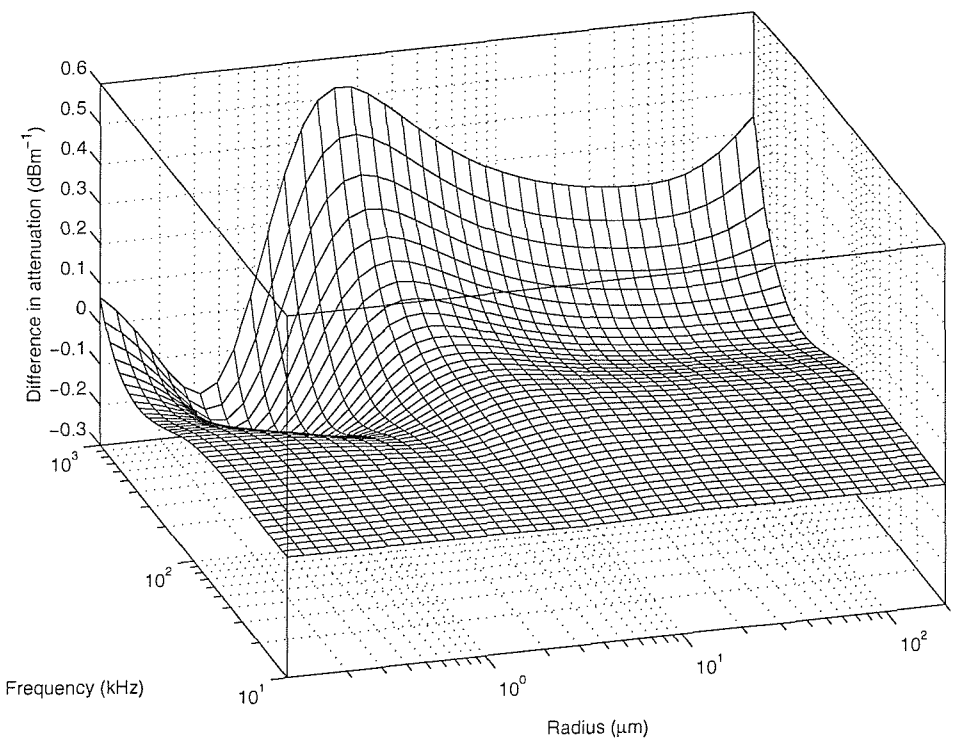

Figure A.9. Difference between attenuation at $\Theta = 0°C$ and $\Theta = 30°C$, for $S = 35$, $p = 1$ dbar, $M = 1$ kgm^{-3}.

A.6 Summary and conclusions

A method has been described for including the effects of temperature, pressure and salinity into the formula for calculating total attenuation by seawater containing dilute suspensions of solid mineral particles (Equation 2.3). This involves the substitution of suitable expressions for sound speed, density and viscosity as functions of temperature, pressure and salinity into the formulae for the attenuation contributions due to scattering and viscous absorption by suspended particles. Combined with the Francois & Garrison expression for the absorption coefficient of clear seawater, this gives the capability for calculating the total absorption coefficient of seawater containing solid particles as a function of temperature, salinity, pressure, frequency, particle size, particle concentration and the density and bulk compressibility of the solid particles.

Results presented have shown that over the range of values found in the environment, temperature has the most significant impact on the attenuation coefficient of turbid water, whilst the effect of salinity is less significant and the effect of pressure may normally be neglected in the shallow water environments of interest.

Future sonar models applied to high frequency acoustic devices operating in shallow, coastal waters should include the effects of suspended particulate matter on the attenuation coefficient and these results suggest that the local salinity and particularly temperature should be taken into account in such calculations. The method presented in this appendix can be used to carry out these calculations.

Whilst experimental validation of the dependencies predicted by these calculations is highly desirable, it should be recognized that the expressions for density, viscosity, sound speed and clear-water absorption are all empirically derived. It may be possible to include temperature and salinity dependencies in laboratory measurements of viscous absorption by aqueous suspensions of mineral particles, such as those described in Chapter 6.

Appendix B

Attenuation, dispersion and the Kramers-Kronig relations

B.1 Introduction

The Kramers-Kronig relations [98, 99] may be used to describe the relationship between the frequency dependence of the attenuation and the frequency dependence of the phase speed in a dispersive medium. This leads to the possibility of an independent method for determining the attenuation in suspensions in which the attenuation spectrum is inferred from measurements of dispersion.

B.2 Theory

The Kramers-Kronig relations for acoustic waves in the linear regime may be written [100, 101]

$$\kappa_{\mathrm{r}}(\omega) - \kappa_{\mathrm{r}}(\infty) = \frac{2}{\pi} \int_0^\infty \frac{\omega' \kappa_{\mathrm{i}}(\omega')}{\omega'^2 - \omega^2} d\omega' \tag{B.1}$$

$$\kappa_{\mathrm{i}}(\omega) = -\frac{2\omega}{\pi} \int_0^\infty \frac{\kappa_{\mathrm{r}}(\omega') - \kappa_{\mathrm{r}}(\infty)}{\omega'^2 - \omega^2} d\omega' \tag{B.2}$$

where κ_{r} and κ_{i} are the real and imaginary parts of the dynamic compressibility respectively.

The acoustic wavenumber for a dispersive medium may be written

$$k = \frac{\omega}{c(\omega)} + \frac{\mathrm{i}\alpha(\omega)}{10 \log \mathrm{e}^2} \tag{B.3}$$

where c is the phase velocity and α is the total attenuation coefficient. The following analysis involves only this total attenuation coefficient and does not depend on the details of the attenuation mechanisms (i.e. absorption, scattering, or a combination of the two). The effect on the incident wave is the same regardless of whether the energy removed is immediately dissipated or scattered and subsequently dissipated to heat, and in either case the effect may be represented by a phenomenological compressibility $\kappa(\omega)$ which obeys Equations B.1 and B.2.

If the real part of the wavenumber is much greater than the imaginary part, such that $\alpha(\omega)c(\omega)/\omega \ll 1$, the real and imaginary parts of the compressibility may be directly related to

the attenuation and phase velocity such that

$$c(\omega) \simeq \frac{1}{[\rho\kappa_{\mathrm{r}}(\omega)]^{1/2}} \tag{B.4}$$

and

$$\frac{\alpha(\omega)}{10\log \mathrm{e}^2} \simeq \tfrac{1}{2}\rho c(\omega)\kappa_{\mathrm{i}}(\omega) \tag{B.5}$$

Using Equations B.1 and B.4 the dispersion at a specified frequency may be obtained from a knowledge of the attenuation at all frequencies. Conversely, if the dispersion is known at all frequencies the attenuation at any particular frequency may be found from Equations B.2 and B.5.

The practical application of Equations B.1 and B.2 is hindered by the fact that they are non-local in frequency. That is to say that determination of dispersion at a single frequency requires knowledge of the attenuation at *all* frequencies, and determination of attenuation at a single frequency requires knowledge of the dispersion at *all* frequencies. Of more practical use are the nearly-local approximate forms of the dispersion-attenuation relationships which may be obtained under the assumptions that the attenuation and dispersion are sufficiently small and do not change rapidly over the frequency range of interest. The validity of these assumptions is discussed in [101].

The nearly-local relationships are

$$\frac{\alpha(\omega)}{10\log \mathrm{e}^2} \simeq \left(\frac{\pi\omega^2}{2c_{\mathrm{ref}}^2}\right)\frac{dc(\omega)}{d\omega} \tag{B.6}$$

and

$$\Delta c(\omega) = c(\omega) - c_{\mathrm{ref}} \simeq \frac{2c_{\mathrm{ref}}^2}{\pi}\int_{\omega_{\mathrm{ref}}}^{\omega} \frac{\alpha(\omega')}{(10\log \mathrm{e}^2)\omega'^2}\,d\omega' \tag{B.7}$$

where ω_{ref} is some convenient reference frequency and $c_{\mathrm{ref}} \equiv c(\omega_{\mathrm{ref}})$ is the phase velocity at this reference frequency.

Consequently, measurements of dispersion over a finite frequency range can be used to infer the attenuation in that range through the application of Equation B.6.

B.3 Example calculation

In order to investigate the feasibility of using the Kramers-Kronig approach to infer attenuation from measurements of dispersion it is necessary to determine how dispersive the suspensions under investigation are. Equation B.7 has been used to calculate the dispersion due to a 1 kgm^{-3} suspension of the glass beads used for the measurements described in Chapter 6. The attenuation was calculated using the particle size distribution shown in Figure 6.7, using the Urick equation for viscous absorption and the high pass equations for scattering. These models have been validated experimentally for this suspension (Figures 6.8 to 6.14)

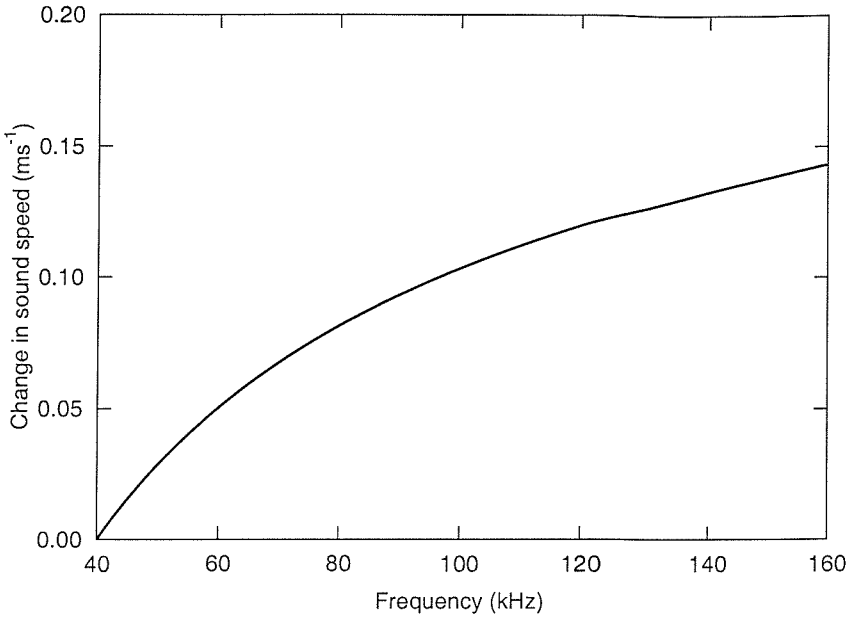

Figure B.1. Calculate dispersion due to a 1 kgm^{-3} suspension of glass beads.

Figure B.1 shows the calculated dispersion for this example. Clearly the suspension is weakly dispersive, and measurement of this dispersion with sufficient accuracy to enable the attenuation to be determined accurately will be experimentally challenging.

For comparison, the change in phase speed resulting from variations in temperature has been calculated using the Chen & Millero sound speed equation [95] with salinity $S = 0$ and depth $d = 0$. Figure B.2 shows the change in sound speed, Δc, as a function of the temperature difference $\Delta\Theta = \Theta - \Theta_0$ for three the reference temperatures, $\Theta_0 = 10°\text{C}, 15°\text{C}, 20°\text{C}$. Clearly temperature changes of less than 0.1°C result in sound speed changes in excess of those expected as a result of dispersion over the frequency range of the measurements, again indicating that measurement of this weak dispersion is experimentally difficult.

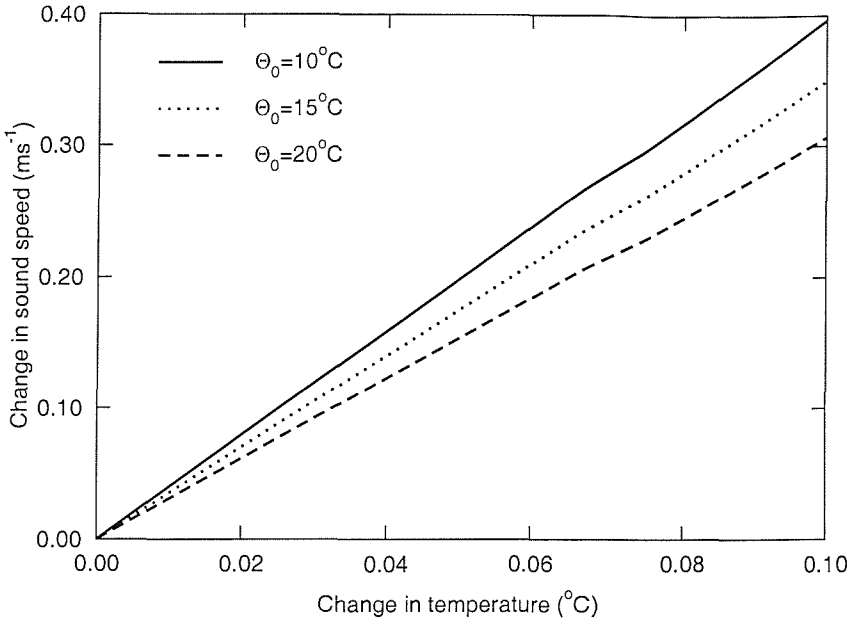

Figure B.2. Calculated change in phase speed due to temperature variations.

B.4 Experimental design

The determination of attenuation from dispersion in weakly dispersive fluids requires very accurate measurements of phase speed. One potential technique for achieving the desired accuracy may be to determine directly the difference between the phase velocity of the test fluid and a reference fluid, such as pure, degassed water, which may be assumed to be non-dispersive. This technique was proposed in Reference [102].

Figure B.3 shows a schematic of the apparatus which might be used for making such measurements. A test vessel, divided in half by a thin, acoustically transparent film membrane, holds the test liquid on one side of the membrane and a reference liquid on the other. This vessel is submerged in a temperature bath to ensure thermal stability. The source transducer is located in the liquid on one side of the membrane, whilst the receiving transducer is located on the other side. The two transducers are mounted on a sliding assembly such that their separation is fixed but they can be moved accurately relative to the membrane by means of a micrometer positioning system. This means that the transducers may be moved from a position where propagation between the transducers is entirely in the reference liquid, through to a position where propagation is entirely in the test liquid. In this way, using time-of-flight measurements between transducers, the difference in phase speed between the test liquid and the reference liquid may be accurately determined.

One of the advantages of this technique is that, by measuring the phase speed difference between the test fluid and the reference fluid rather than measuring the phase speed directly, the effect of temperature on the phase speed may be eliminated.

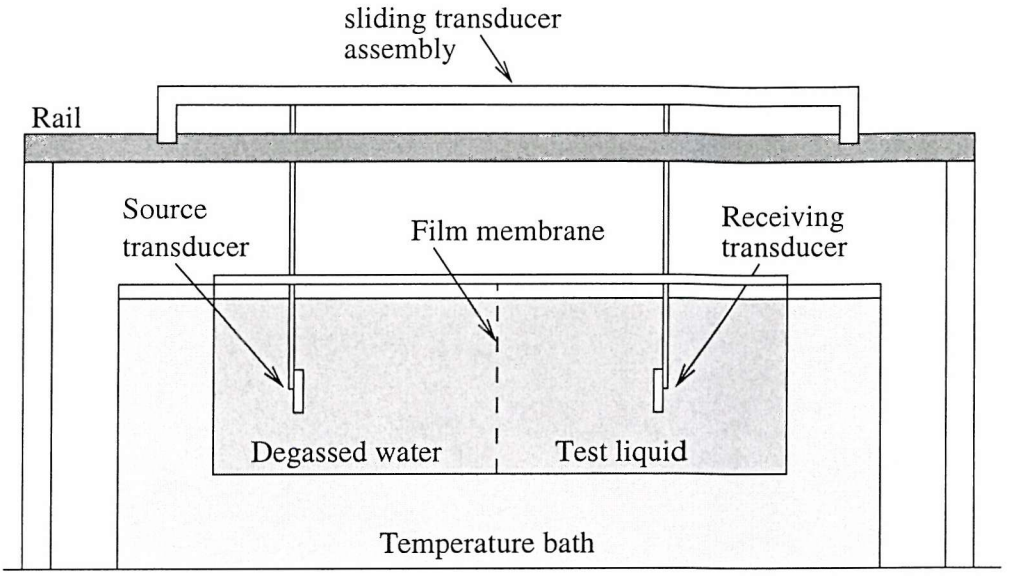

Figure B.3. Experimental arrangement for the measurement of dispersion [102]

B.5 Summary and conclusions

In this appendix an independent method for determining the attenuation in dilute suspensions has been proposed. This technique is based on measurement of phase speed dispersion and use of the Kramers-Kronig relations to determine the attenuation from the dispersion.

This approach requires very accurate measurements of velocity dispersion and is therefore experimentally challenging. In particular, it has been demonstrated that small changes in temperature could potentially swamp the effects of dispersion.

Finally, an experimental configuration for measuring phase speed dispersion with the required accuracy has been proposed.

List of publications

The following relevant papers and reports were contributed to or written by the author during the course of the research described in this thesis.

Peer-reviewed academic journals:

(i) Heathershaw A D, Richards S D and Thorne P D, Acoustic absorption and scattering by suspended sediments in turbid coastal waters, *Journal of Defence Science*, 1996, **1**, 200-206. [103]

(ii) Richards S D, Heathershaw A D and Thorne P D, The effect of suspended particulate matter on sound attenuation in seawater, *Journal of the Acoustical Society of America*, 1996, **100**, 1447-1450. [104]

(iii) Richards S D, The effect of temperature, pressure and salinity on sound attenuation in turbid seawater, *Journal of the Acoustical Society of America*, 1998, **103**, 205-211. [88]

(iv) Richards S D, Brown N R and Leighton T G, Turbidity in future high frequency sonar performance models, *Journal of the Acoustical Society of America*, 1998, **103**, 2900. [57]

(v) Brown N R, Leighton T G, Richards S D and Heathershaw A D, Measurement at low ultrasonic frequencies of absorption due to suspended particulate matter, *Journal of the Acoustical Society of America*, 1998, **103**, 2900. [58]

(vi) Brown N R, Leighton T G, Richards S D and Heathershaw A D, Measurement of viscous sound absorption at 50-150 kHz in a model turbid environment, *Journal of the Acoustical Society of America*, 1998, **104**, 2114-2120. [56]

(vii) Richards S D and Leighton T G, High frequency sonar performance predictions for littoral operations - The effect of suspended sediments and microbubbles, *Journal of Defence Science*, (In press), 2002. [85]

(viii) Richards S D, Leighton T G and Brown N R, Visco-inertial absorption in dilute suspensions of irregular particles, *Proc. Roy. Soc. Lond. A*, (In review), 2002. [60]

(ix) Richards S D, Leighton T G and Brown N R, Sound absorption from non-spherical particles suspended in water: Comparison of measurements with predictions based on various particle sizing techniques, in preparation for *Journal of the Acoustical Society of America*. [105]

(x) Richards S D, Leighton T G and Brown N R, Ultrasonic absorption in a dilute suspension of natural marine sediment particles and its effect on sonar performance, in preparation for *IEEE Journal of Oceanic Engineering*. [106]

Other journals:

(i) Richards S D and Leighton T G, Sonar performance in coastal environments: Suspended solid particles and microbubbles, *Acoustics Bulletin*, Jan/Feb, 2001. [107]

Peer-reviewed conference proceedings:

(i) Brown N R, Leighton T G, Richards S D and Heathershaw A D, Boundary and volume losses in a diffuse sound field near the atmosphere/ocean boundary, *Proceedings of Sea Surface Sound 97, Southampton, UK*, 1997, 123-132. [55]

(ii) Richards S D and Leighton T G, Acoustic sensor performance in coastal waters: solid suspensions and bubbles, in *Acoustical Oceanography*, Editors Leighton T G, Heald G J, Griffiths H D, Griffiths G, *Proceedings of the Institute of Acoustics*, **23**, Part 2, 2001, 399-406. [108]

Other conference proceedings:

(i) Richards S D, Sound attenuation by suspended particles in turbid coastal waters, *Ocean Modelling Workshop, FNMOC, Monterey, California, USA*, 1996. [109]

(ii) Hewitt R N, Richards S D and Heathershaw A D, Modelling the transport of suspended sediment in coastal waters and its effect on sound propagation, *22nd General Assembly of the European Geophysical Society, Vienna, Austria*, 1997. [110]

(iii) Richards S D, Hewitt R N and Heathershaw A D, The effect of sediment plumes on sonar performance, *Proceedings of IEE Conference on Electronics in Oceanography, Southampton, UK*, 1997, 67-72. [111]

(iv) Richards S D, Heathershaw A D, Hewitt R N, Brown N R and Leighton T G, The effect of suspended particles on the performance of minehunting sonars in turbid coastal water, *Proceedings of Undersea Defence Technology, Hamburg, Germany*, 1997, 171-174. [112]

(v) Richards S D, Heathershaw A D, Brown N R and Leighton T G, The effect of suspended particulate matter on the performance of high frequency sonars in turbid coastal waters, *Proceedings of NATO SACLANTCEN conference on High Frequency Acoustics in Shallow Water, Lerici, Italy*, 1997, 443-450. [113]

(vi) Brown N R, Leighton T G, Richards S D and Heathershaw A D, Sound absorption by suspended particulate matter, *Proceedings of NATO SACLANTCEN conference on High Frequency Acoustics in Shallow Water, Lerici, Italy*, 1997 75-82. [54]

(vii) Richards S D, Rapid Environmental Assessment of Turbidity for Sonar Performance Prediction, *Ocean Modelling Workshop, DERA Haslar, Gosport, UK*, 1997. [114]

(viii) Brown N R, Leighton T G, Richards S D and Heathershaw A D, Measurement at low ultrasonic frequencies of absorption due to suspended particulate matter, *Proceedings of the Joint Meeting of the 16th International Congress on Acoustics and the 135th Meeting of the Acoustical Society of America, Seattle, WA, USA*, 1998, 1347-1348. [58]

(ix) Richards S D, Brown N R and Leighton T G, Turbidity in future high frequency sonar performance models, *Proceedings of the Joint Meeting of the 16th International Congress on Acoustics and the 135th Meeting of the Acoustical Society of America, Seattle, WA, USA*, 1998, 1349-1350. [57]

(x) Richards S D, Brown N R and Leighton T G, Characterisation of propagation parameters for high frequency sonar in turbid coastal waters, *Proceedings of the 4th European Conference on Underwater Acoustics, Rome, Italy*, 1998, 709-714. [59]

(xi) Richards S D and Leighton T G, Acoustic propagation in bubbly and turbid environments, *Proceedings of the International Conference on Acoustics, Noise and Vibration, Montreal, Quebec, Canada*, 2000. [115]

(xii) Richards S D and Leighton T G, Sonar performance in turbid and bubbly environments, *Program of the 140th Meeting of the Acoustical Society of America, Newport Beach, CA, USA*, 2000, 2562, (abstract). [116]

(xiii) Richards S D, Leighton T G and White P R, High frequency sonar variability in littoral environments: irregular particles and bubbles, submitted to *Submitted to First Pan-American/Iberian Meeting on Acoustics, Cancun, Mexico*, 2002.

Reports:

(i) Richards S D, Heathershaw A D, An investigation of viscous absorption of sound energy in turbid seawater at mine-hunting frequencies, *DRA Report DRA/SS(PS)/CR96021*, 1996. [117]

(ii) Richards S D, Hewitt R N, Acoustic properties of turbid coastal waters: Year 2 progress report, *DERA Report DERA/SS(PS)/CR97014*, 1997. [118]

(iii) Richards S D, Acoustic properties of turbid coastal waters : Year 3 interim progress report, *DERA Report DERA/SS/PS/CR980061*, 1998. [119]

(iv) Richards S D and Hewitt R N, Final report on the acoustic properties of turbid coastal waters, *DERA Report DERA/S&P/UWS/CR980133*, 1998. [120]

(v) Richards S D, A review of acoustic techniques to characterize suspended particles, *QinetiQ Working Paper QINETIQ/S&E/SCS/WP020262*), 2002. [121]

(vi) Richards S D, High Frequency Sonar Performance in Shallow Water: CRP Fellowship Final Summary Report, *QinetiQ Report QINETIQ/S&E/SCS/CR021097*), 2002. [122]

(vii) Richards S D, High Frequency Sonar Performance in Shallow Water: Suspended Particles and Microbubbles, *QinetiQ Working Paper QINETIQ/S&E/SCS/WP021051*), 2002. [123]

References

[1] F H Fisher and V P Simmons. Sound absorption in sea water. *J. Acoust. Soc. Am.*, 62:558–564, 1977.

[2] W H Thorpe. Deep ocean sound attenuation in the sub and low kilocyle per second range. *J. Acoust. Soc. Am.*, 42:648–654, 1965.

[3] M Schulkin and H W Marsh. Sound absorption in seawater. *J. Acoust. Soc. Am.*, 34:864–865, 1962.

[4] R E Francois and G R Garrison. Sound absorption based on ocean measurements: Part I: Pure water and magnesium sulfate contributions. *J. Acoust. Soc. Am.*, 72:896–907, 1982.

[5] R E Francois and G R Garrison. Sound absorption based on ocean measurements: Part II: Boric acid contribution and equation for total absorption. *J. Acoust. Soc. Am.*, 72:1879–1890, 1982.

[6] E L Lewis. The practical salinity scale 1978 and its antecedents. *IEEE J. Oceanic Engr.*, OE-5:3–8, 1980.

[7] R G Perkin and E L Lewis. The practical salinity scale 1978. *IEEE J. Oceanic Engr.*, OE-5:9–16, 1980.

[8] F Culkin and P Ridout. Salinity: Definitions, determinations and standards. *Sea Technology*, 30:47–49, 1989.

[9] C T J Sewell. On the extinction of sound in a viscous atmosphere by small obstacles of cylindrical and spherical form. *Phil. Trans. Roy. Soc. London*, 210:239–270, 1910.

[10] P S Epstein. *Contributions to applied mechanics, Theodore von Kármán Anniversary Volume.* California Institute of Technology, 1941.

[11] H Lamb. *Hydrodynamics.* Dover Publications, New York, sixth edition, 1945.

[12] R J Urick. The absorption of sound in suspensions of irregular particles. *J. Acoust. Soc. Am.*, 20:283–289, 1948.

[13] G G Stokes. On the effect of internal friction of fluids on the motion of pendulums. *Transactions of the Cambridge Philosophical Society*, IX, 1851.

[14] J J Faran, Jr. Sound scattering by solid cylinders and spheres. *J. Acoust. Soc. Am.*, 23:405–418, 1951.

[15] A E Hay and D G Mercer. On the theory of sound scattering and viscous absorption in aqueous suspensions at medium and short wavelengths. *J. Acoust. Soc. Am.*, 78:1761–1771, 1985.

[16] I K Bjørnø and L Bjørnø. Modelling of multiple scattering in suspensions. In *Proc. 3rd European Conference on Underwater Acoustics, Heraklion, Crete, Greece, 24-28th June, 1996*, pages 87–92, 1997.

[17] G C Gaunaurd, H Huang, and H C Strifors. Acoustic scattering by a pair of spheres. *J. Acoust. Soc. Am.*, 98:495–507, 1995.

[18] R K Johnson. Sound scattering from a fluid sphere revisited. *J. Acoust. Soc. Am.*, 61:375–377, 1977.

[19] J Sheng and A E Hay. An examination of the spherical scatterer approximation in aqueous suspensions of sand. *J. Acoust. Soc. Am.*, 83:598–610, 1988.

[20] H Überall. Surface waves in acoustics. In *Physical Acoustics*, volume X, pages 1–60. Academic Press, 1973.

[21] P D Thorne, L Hayhurst, and V F Humphrey. Scattering by non-metallic spheres. *Ultrasonics*, 30:15–20, 1992.

[22] P D Thorne, K R Waters, and T J Brudner. Acoustic measurements of scattering by objects of irregular shape. *J. Acoust. Soc. Am.*, 97:242–251, 1995.

[23] J W Lord Rayleigh Strutt. *Theory of Sound*, volume 2. Dover, New York, 2nd edition, 1945.

[24] M A Isakovich. On propagation of sound in emulsions. *Zh. Eksperim. i Teor. Fiz.*, 18:907, 1948. In Russian.

[25] P S Epstein and R R Carhart. The absorption of sound in suspensions and emulsions I. Water fog in air. *J. Acoust. Soc. Am.*, 25:553–565, 1953.

[26] J R Allegra and S A Hawley. Attenuation of sound in suspensions and emulsions: Theory and experiments. *J. Acoust. Soc. Am.*, 51:1545–1564, 1971.

[27] A E Hay and R W Burling. On sound scattering and attenuation in suspensions with marine applications. *J. Acoust. Soc. Am.*, 72:950–959, 1982.

[28] P C Waterman and R Truell. Wave propagation through an assembly of spheres IV. Relations between different multiple scattering theories. *J. Math. Phys.*, 2:512–537, 1961.

[29] P Lloyd and M V Berry. Multiple scattering of waves. *Proc. Phys. Soc.*, 91:678–688, 1992.

[30] M Abramowitz and I A Stegun, editors. *Handbook of Mathematical Functions with Formulas, Graphs and Mathematical Tables.* Number 55 in National Bureau of Standards Applied Mathematics Series. United States Department of Commerce, 1965.

[31] S Temkin and R A Dobbins. Attenuation and dispersion of sound by particulate-relaxation processes. *J. Acoust. Soc. Am.*, 40:317–324, 1966.

[32] C L Morfey. Sound attenuation by small particles in a fluid. *J. Sound Vib.*, 8:156–170, 1968.

[33] N A Gumerov, A I Ivandaev, and R I Nigmatulin. Sound waves in monodisperse gas-particle or vapour-droplet mixtures. *J. Fluid. Mech.*, 193:53–74, 1988.

[34] T S Margulies and W H Schwartz. A multiphase continuum theory for sound wave propagation through dilute suspensions of particles. *J. Acoust. Soc. Am.*, 96:319–331, 1994.

[35] A H Harker and J A G Temple. Velocity and attenuation of ultrasound in suspensions of particles in fluids. *J. Phys. D: Appl. Phys.*, 21:1576–1588, 1988.

[36] R L Gibson and M N Toksoz. Viscous attenuation of acoustic waves in suspensions. *J. Acoust. Soc. Am.*, 85:1925–1934, 1989.

[37] C M Atkinson and H K Kyotomaa. Acoustic wave speed and attenuation in suspensions. *Int. J. Multiphase Flow*, 18:577–592, 1992.

[38] J M Evans and K Attenborough. Coupled phase theory for sound propagation in emulsions. *J. Acoust. Soc. Am.*, 102:278–282, 1997.

[39] A K Holmes. private communication, June 2002.

[40] G W C Kaye and T H Laby. *Tables of Physical and Chemical Constants.* Longman, fifteenth edition, 1982.

[41] K Kranck. Particulate matter grain-size characteristics and flocculation in a partially mixed estuary. *Sedimentology*, 28:107–114, 1981.

[42] A S Ahuja. Formulation of wave equation for calculating velocity of sound in suspensions. *J. Acoust. Soc. Am.*, 51:916–919, 1972.

[43] A S Ahuja. Wave equation and propagation parameters for sound propagation in suspensions. *J. Appl. Phys.*, 44:4863–4868, 1973.

[44] A D Pierce. *Acoustics: an introduction to its physical principles and applications.* Acoustical Society of America, New York, 1994. pp 187.

[45] A S Ahuja and W R Hendee. Effects of particle shape and orientation on propagation of sound in suspensions. *J. Acoust. Soc. Am.*, 63:1074–1080, 1978.

[46] R P Kanwall. Drag on an axially symmetric body vibrating slowly along its axis in a viscous fluid. *J. Fluid. Mech.*, 19:631–636, 1964.

[47] J Happel and H Bremner. *Low Reynolds Number Hydrodynamics.* Prentice-Hall, Englewood Cliffs, NJ, 1965.

[48] P D Thorne and S C Campbell. Backscattering by a suspension of spheres. *J. Acoust. Soc. Am.*, 92:978–986, 1992.

[49] P D Thorne and P J Hardcastle. Acoustic measurements of suspended sediments in turbulent currents and comparison with *in-situ* samples. *J. Acoust. Soc. Am.*, 101:2603–2614, 1997.

[50] P D Thorne, P J Hardcastle, and R L Soulsby. Analysis of acoustic measurements of suspended sediments. *J. Geophys. Res.*, 98:899–910, 1993.

[51] P D Thorne and D M Hanes. A review of acoustic measurements of small-scale sediment processes. *Cont. Shelf. Res.*, 22:603–632, 2002.

[52] P A Chinnery, V F Humphrey, and J D Zhang. Low frequency acoustic scattering by a cube: Experimental measurements and theoretical predictions. *J. Acoust. Soc. Am.*, 101:2571–2582, 1997.

[53] P D Thorne, S B Sun, J D Zhang, II K Bjørnø, and T Mazoyer. Measurements and analysis of acoustic backscattering by elastic cubes and irregular polyhedra. *J. Acoust. Soc. Am.*, 102:2705–2713, 1997.

[54] N R Brown, T G Leighton, S D Richards, and A D Heathershaw. Sound absorption by suspended particulate matter. In *High Frequency Acoustics in Shallow Water*, pages 75–82, Italy, 1997. NATO SACLANT Undersea Research Center.

[55] N R Brown, T G Leighton, S D Richards, and A D Heathershaw. Boundary and volume losses in a diffuse acoustic field near the atmosphere / ocean boundary. In *Proc. Sea Surface Sound 97, 21-24 July*, pages 123–132, 1997.

[56] N R Brown, T G Leighton, S D Richards, and A D Heathershaw. Measurement of viscous sound absorption at 50-150 kHz in a model turbid environment. *J. Acoust. Soc. Am.*, 104:2114–2120, 1998.

[57] S D Richards, N R Brown, and T G Leighton. Turbidity in future high frequency sonar performance models. In *Proc. Joint Meeting of the International Congress on Acoustics and the Acoust. Soc. Am., Seattle, WA, 20 - 26th June 1998*, pages 1349–1350, 1998.

[58] N R Brown, T G Leighton, S D Richards, and A D Heathershaw. Measurement at 50-150 KHz of acoustic absorption due to suspended particulate matter. In *Proc. Joint Meeting of the International Congress on Acoustics and the Acoust. Soc. Am., Seattle, WA, 20 - 26th June 1998*, pages 1347–1348, 1998.

[59] S D Richards, N R Brown, and T G Leighton. Characterisation of propagation parameters for high frequency sonar in turbid coastal waters. In *Proc. 4th European Conference on Underwater Acoustics, Rome, Italy, 21 - 25th September 1998*, pages 709–714, 1998.

[60] S D Richards, T G Leighton, and N R Brown. Visco-inertial absorption in dilute suspensions of irregular particles. *Proc. Roy. Soc. Lond. A*, 2002. In review.

[61] L E Kinsler, A R Frey, A B Coppens, and J V Sanders. *Fundamentals of Acoustics.* Wiley, New York, third edition, 1982.

[62] A D Pierce. *Acoustics: an introduction to its physical principles and applications.* Acoustical Society of America, New York, 1994.

[63] M R Schroeder. New method of measuring reverberation time. *J. Acoust. Soc. Am.*, 37:409–412, 1965.

[64] E Hecht. *Optics.* Addison Wesley, 1974.

[65] BS3406 Part 2. *British Standard Methods for Determination of Particle Size Distribution. Part 2: Recommendations for Gravitational Liquid Sedimentation Methods for Powders and Suspensions*, 1984.

[66] BS3406 Part 6. *British Standard Methods for Determination of Particle Size Distribution. Part 6: Recommendations for Centrifugal Liquid Sedimentation Methods for Powders and Suspensions,*

1985.

[67] D T Noir and A R George. Absorption of sound by homogeneous turbulence. *J. Fluid Mech.*, 86:593–608, 1978.

[68] S Foran and J Irvine. Particle characterisation and scanning electron microscopy (SEM) of china clay, calcium carbonate and sediment samples. Technical Report DERA/CBSTS/TN002089, DERA Bridgwater, March 2000.

[69] S G Healy. Private communication, 2001.

[70] S M Tuovila. Searay sonar simulation model. TN 946-88, NCSC, March 1989.

[71] R J Urick. *Principles of Underwater Sound.* McGraw-Hill, 3rd edition, 1983.

[72] A D Waite. *Sonar for Practising Engineers.* Thomson Marconi Sonar Ltd., 2nd edition, 1998.

[73] C M McKinney and C D Anderson. Measurements of backscattering of sound from the ocean bottom. *J. Acoust. Soc. Am.*, 36:158–163, 1964.

[74] M A Gensane. A statistical study of acoustic signals backscattered from the sea bottom. *IEEE J. Ocean. Eng.*, 14:84–93, 1989.

[75] S Guyonic. Analysis of reverberation level and statistics of two different bottom types from 15 to 40 kHz. Technical Report 1916, GESMA, Brest, 1991.

[76] J R Ventura. HFEAM high frequency environmental acoustic model. Technical Report TD 10 114, Naval Underwater Systems Centre, Newport, RI, 1992.

[77] P Caprais and A Lombardi. Development of a SACLANTCEN MCM sonar performance model. Technical Report SM 315, SACLANTCEN, 1996.

[78] R P Chapman and J H Harris. Surface backscattering strength measured with explosive sound sources. *J. Acoust. Soc. Am.*, 34:1592–1597, 1962.

[79] R J Urick and R M Hoover. Backscattering of sound from the sea surface. *J. Acoust. Soc. Am.*, 28:1038–1042, 1956.

[80] S O McConnell. Formatting strategy for NAVOCEANO acoustic survey. Technical Report TM2-82, Applied Physics Laboratory, University of Washington, 1992.

[81] V O Knudsen, R S Alford, and J W Emling. Underwater ambient noise. *J. Marine. Res.*, 3:410–429, 1948.

[82] R H Mellen. The thermal noise limit in the detection of underwater acoustic signals. *J. Acoust. Soc. Am.*, 24:478–480, 1952.

[83] V M Albers. *Underwater Acoustic Handbook 2.* Penn State Press, 1965.

[84] C D Motchenbacher and F C Fitchen. *Low Noise Electronic Design.* Wiley, 1973.

[85] S D Richards and T G Leighton. High frequency sonar performance predictions for littoral operations - the effect of suspended sediments and microbubbles. *Journal of Defence Science*, 2002. In press.

[86] K W Commander and A Prosperetti. Linear pressure waves in bubbly liquids: Comparison between theory and experiments. *J. Acoust. Soc. Am.*, 85:732–746, 1989.

[87] V A Del Grosso. New equation for the speed of sound in natural waters (with comparisons to other equations). *J. Acoust. Soc. Am.*, 56:1084–1091, 1974.

[88] S D Richards. The effect of temperature, pressure and salinity on sound attenuation in turbid seawater. *J. Acoust. Soc. Am.*, 103:205–211, 1998.

[89] H Medwin and C S Clay. *Fundamentals of Acoustical Oceanography.* Academic Press, 1998.

[90] H Medwin. *In-situ* measurements of bubble populations in coastal waters. *J. Geophys. Res.*, 75:599–611, 1970.

[91] H Medwin. *In-situ* measurements of microbubbles at sea. *J. Geophys. Res.*, 82:971–976, 1977.

[92] W Matthäus. Die viskosität des meerwassers. *Beiträde zur Meereskunde*, 29:93–107, 1972. In German.

[93] N P Fofonoff and R C Millard, Jr. Algorithms for computation of fundamental properties of seawater. *Unesco Technical Papers in Marine Science*, 44, 1983.

[94] J L Spiesberger and K Metzger. New estimates of sound speed in waer. *J. Acoust. Soc. Am.*, 89:1697–, 1991.

[95] C Chen and F J Millero. Speed of sound in seawater at high pressures. *J. Acoust. Soc. Am.*, 92:1129–1135, 1977.

[96] F J Millero, C Chen, A Bradshaw, and K Schleicher. A new high pressure equation of state for seawater. *Deep Sea Res.*, 27A:255–264, 1980.

[97] F J Millero and A Poisson. Summary of data treatment for the unesco one atmosphere equation of state for seawater. *Deep Sea Res.*, 28A:625–629, 1981.

[98] R Kronig. On the theory of dispersion of X-rays. *J. Opt. Soc. Am.*, 12:547, 1926.

[99] R Kronig and H A Kramers. Absorption and dispersion in X-ray spectra. *Zeits. f. Phys.*, 48:174, 1928.

[100] M O'Donnell, E T Jaynes, and J G Miller. General relationships between ultrasonic attenuation and dispersion. *J. Acoust. Soc. Am.*, 63:1935–1937, 1978.

[101] M O'Donnell, E T Jaynes, and J G Miller. Kramers-Kronig relationship between ultrasonic attenuation and phase velocity. *J. Acoust. Soc. Am.*, 69:696–701, 1981.

[102] E L Carstensen. Measurement of dispersion of velocity of sound in liquids. *J. Acoust. Soc. Am.*, 26:858–861, 1954.

[103] A D Heathershaw, S D Richards, and P D Thorne. Acoustic absorption and scattering by suspended sediments in turbid coastal waters. *Journal of Defence Science*, 1:200–206, 1996.

[104] S D Richards, A D Heathershaw, and P D Thorne. The effect of suspended particulate matter on sound attenuation in seawater. *J. Acoust. Soc. Am.*, 100:1447–1450, 1996.

[105] S D Richards, T G Leighton, and N R Brown. Sound absorption from non-spherical particles suspended in water: Comparison of measurements with predictions based on various particle sizing techniques. *J. Acoust. Soc. Am.*, 2002. In preparation.

[106] S D Richards, T G Leighton, and N R Brown. Ultrasonic absorption in a dilute suspension of natural marine sediment particles and its effect on sonar performance. *IEEE J. Ocean. Eng.*, 2002. In preparation.

[107] S D Richards and T G Leighton. Sonar performance in coastal environments: Suspended sediments and microbubbles. *Acoustics Bulletin*, 26 (1):10–17, 2001.

[108] S D Richards and T G Leighton. Acoustic sensor performance in coastal waters: Solid suspensions and bubbles. In T G Leighton, G J Heald, H D Griffiths, and G Griffiths, editors, *Acoustical Oceanograpy*, volume 23 of *Proceedings of the Institute of Acoustics*, pages 399–406, Bath, 2001. Bath University Press.

[109] S D Richards. Sound attenuation by suspended particles in turbid coastal waters. Presented to UK/US Ocean Modelling Workshop, FNMOC, Monterey, California, 8th-10th October, 1996.

[110] R N Hewitt, S D Richards, and A D Heathershaw. Modelling the transport of suspended sediment in coastal waters and its effect on sound propagation. Presented to 22nd General Assembly of the European Geophysical Society, Vienna, 21st - 25th April, 1997.

[111] S D Richards, R N Hewitt, and A D Heathershaw. The effect of sediment plumes on sonar performance. In *Proc. IEE Conference on Electronics in Oceanography, Southampton Oceanography Centre, 23-25th June, 1997*, pages 67–72, 1997.

[112] S D Richards, A D Heathershaw, R N Hewitt, N R Brown, and T G Leighton. The effect of suspended particles on the performance of minehunting sonars in turbid coastal water. In *Proc. Undersea Defence Technology, Hamburg, Germany, 24th - 27th June 1997*, pages 171–174, 1997.

[113] S D Richards, A D Heathershaw, N R Brown, and T G Leighton. The effect of suspended particulate matter on the performance of high frequency sonars in turbid coastal waters. In *High Frequency Acoustics in Shallow Water*, pages 443–450, Italy, 1997. NATO SACLANT Undersea Research Center.

[114] S D Richards. Rapid environmental assessment of turbidity for sonar performance prediction.

Presented to UK/US Ocean Modelling Workshop, DERA Haslar, Gosport, UK, 28th-29th October, 1996.

[115] S D Richards and T G Leighton. Acoustic propagation in bubbly and turbid environments. In *Proceedings of the International Conference on Acoustics, Noise and Vibration*, 2000. Still in press as of May 2002.

[116] S D Richards and T G Leighton. Sonar performance in bubbly and turbid environments. In *Program of the 140th Meeting of the Acoustical Society of Americal, Newport Beach, CA*, page 2562, 2000.

[117] S D Richards and A D Heathershaw. An investigation of viscous absorption of sound energy in turbid seawater at mine-hunting frequencies (U). Technical Report DRA/SS(PS)/CR96021, DRA Winfrith, March 1996.

[118] S D Richards and R N Hewitt. Acoustic properties of turbid coastal waters : Year 2 progress report. Technical Report DERA/SS(PS)/CR97014, DERA Winfrith, March 1997. UK RESTRICTED.

[119] S D Richards. Acoustic properties of turbid coastal waters : Year 3 interim progress report. Technical Report DERA/SS/PS/CR980061, DERA Winfrith, March 1998.

[120] S D Richards and R N Hewitt. Final report on the acoustic properties of turbid coastal waters. Technical Report DERA/S&P/UWS/CR980133, DERA Winfrith, March 1998.

[121] S D Richards. A review of acoustic techniques to characterize suspended particles. Technical Report QINETIQ/S&E/SCS/WP020262, QinetiQ Winfrith, March 2002.

[122] S D Richards. High frequency sonar performance in shallow water: CRP Final summary report. Technical Report QINETIQ/S&E/SCS/CR021097, QinetiQ Winfrith, June 2002.

[123] S D Richards. High frequency sonar performance in shallow water: Suspended particles and microbubbles. Technical Report QINETIQ/S&E/SCS/WP021051, QinetiQ Winfrith, June 2002.

Index

Addendum

The following comments are added to clarify points raised by the examiners. The author is grateful to Dr. Victor Humphrey (University of Bath) and Professor Chris Morfey (University of Southampton).

(i) The experimental data were filtered using Butterworth bandpass filters, as described on Page 78. These were 2nd order Butterworth filters, giving a roll-off of 12 dB per octave outside of the pass-band. The consequence of the relatively gentle roll-off associated with low order filters is that each frequency bin will contain some out-of-band data. If these experiments were repeated it would be wise to use higher order filters. However, it will be noted that the frequency dependence of the attenuation isn't great, so this is not expected to affect the results greatly.

(ii) The upper time limit for the integration in the method of integrated impulse response (see Page 78) was determined manually by visually checking the linearity of the resulting IIR curve. As the reverberation level approaches the noise level, the IIR curve departs from linearity. The upper time limit for the integration was chosen such that this departure from linearity was not apparent in the IIR curve.

(iii) The typical reverberation time for clear water samples in the experimental configuration described in Chapter 6 was around 300 ms.

(iv) The Schroeder cut-off frequencies for the test volume were typically in the range 50 kHz to 75 kHz, depending on the reverberation time.

(v) All error bars on measurements of absorption coefficient represent one standard error.

(vi) Each calculation of reverberation time was based on the average of ten sets of ten noise bursts, with the hydrophones in fixed positions.

(vii) No averaging over measurements made at different locations in the volume was carried out. Instead a 4% standard error in the reverberation time was included in the error analysis to account for the measured spatial variation in the reverberation time.

(viii) The oblate spheroid analysis of the measurements with non-spherical particles assumed that half of the particles are orientated edgewise to the sound field and half are oriented broadside. However, it will be noted that there are three orthogonal spatial axes, which may be resolved into one broadside direction and two edgewise directions. It would therefore be more correct to assume that two thirds of the particles are orientated edgewise to the sound field and one third broadside to the field.